SPERRY
FLIGHT SYSTEMS

FINAL REPORT
AN EVALUATION OF REACTION WHEEL EMITTED VIBRATIONS FOR LARGE SPACE TELESCOPE

PREPARED FOR

NASA/MSFC

HUNTSVILLE, ALABAMA

JANUARY 1976

SPERRY FLIGHT SYSTEMS IS A DIVISION OF SPERRY RAND CORPORATION

PRINTED IN U.S.A. JANUARY 1976 PUB. NO. 71-0824-00-00

TABLE OF CONTENTS

LIST OF ILLUSTRATIONS

SECTION 1.0

INTRODUCTION AND BACKGROUND

The Large Space Telescope (LST) is to be a free-flying autonomous astronomical observatory that is to be launched in late 1982 by the Space Transportation System into a nominal 500 kilometer circular earth orbit. The telescope will employ a 2.4 meter diffraction limited primary mirror, and require a pointing stability of .005 arc-second rms for a duration of up to 10 hours. This pointing stability is equivalent to maintaining a line of sight fixed within a 5-inch diameter circle in Los Angeles when it emanates from an origin in New York City (neglecting earth's curvature). Because of the stringent pointing requirements, it became evident that the Momentum Exchange Actuator (MEA) required would have to possess a very smooth torque response and emit very small reaction forces and torques to the spacecraft. Cost studies and a vehicle redefinition from a 3.0 to 2.4 meter design indicated that reaction wheels may be used instead of Control Moment Gyros (CMG) for the MEA. However, reaction wheels present the problem of operation over a range of speeds (typically +2000 to -2000 rpm) and consequently generating emitted vibration over a corresponding range of frequencies. If any of the frequencies excite structural or appendage resonances, the probability of achieving the required pointing stability goal is jeopardized. CMGs, on the other hand, operate at only one spin speed which can be selected to be at a point where no resonances exist. Additional problems over reaction wheels encountered by CMGs are the gimbal axis friction characteristics and higher cost.

It was readily apparent that if reaction wheels were to be used, emitted vibration signature data for LST type units would be required to evaluate their feasibility in this precision pointing application. No vibration frequency spectrum data existed, however, on LST type reaction wheels since a mission with such a stringent pointing requirement had not been attempted before. Hence, this study was created with the broad objectives of gathering data on existing wheels and supplying the data in a form which could be related by NASA and the prime contractors to image motion and pointing stability.

OBJECTIVES

The study had the following specific objectives:

1. Measure typical reaction wheel emitted vibrations (forces and torques) about three orthogonal axes during constant speed operation, and during acceleration and deceleration.

2. Provide the measured data and a reaction wheel, if possible, to the Support System Module Prime Contractors for use in their Phase B studies and dynamic tests.

3. Make predictions of the emitted vibration levels for an LST ball bearing and magnetic bearing reaction wheel.

4. Perform tests on the RW 101H duplex pair ball bearings to determine their friction-spring characteristics near zero speed and determine their Dahl model parameter values.

To achieve these objectives, three Sperry units were tested.

- Fleet Satellite Communication RWA (FSC) - A seven ft-lb-sec reaction wheel using a ball bearing suspension system.
- Sperry Model Magnetic Bearing (MMB) - A laboratory development model of a radially passive, axially active magnetic bearing using a 5-pound rotor.
- High Energy Astonomical Observatory RWA (HEAO) - A thirty ft-lb-sec reaction wheel using a ball bearing suspension system very similar to the FSC RWA.

APPROACH

Each unit's rotor was first placed on a Schenck-type RS-5 dynamic balance machine and balanced to a value that was considered representative of the best balance level that could be achieved in a repeatable fashion. It would do no good to spend an extraordinary amount of time achieving a balance which was exceptional, but could not be repeated for production units. The FSC and MMB were then tested over a 5000 rpm range for emitted accelerations on a freely suspended mount. This provided data of the unit's performance for an isolated type mounting interface. The HEAO Engineering Model RWA, which was borrowed from the HEAO program for these tests, was not tested in a freely suspended configuration, since it was available for only a short time.

The FSC RWA was loaned to Lockheed after this testing effort for a joint IR&D study of emitted vibrations in a Lockheed 2.4 meter Dynamic Test Vehicle.

On return to Sperry, the FSC RWA was tested for emitted forces and torques on the Sperry hard mount, three-axis emitted vibration fixture. The MMB wheel was tested immediately after the FSC tests. A program delay ensued after this while waiting for the HEAO RWA to be made available for the three-axis tests.

In parallel, a limited analysis and data reduction effort was undertaken to verify test results by comparing them to predictions using existing RWA mathematical models. The majority of the data and observed phenomena has been explained by this analysis, but the scope of this study did not allow for the detailed type analysis which will be required to identify the causes of all the anomalies noted.

This final report concludes the study by presenting descriptions of the units tested and the test setups, typical test data and frequency spectrums, data analysis, and predictions of the emitted vibration from LST type reaction wheels.

SECTION 2.0

SUMMARY AND CONCLUSIONS

This study has measured emitted force and torque vibration data in three axes for three Sperry reaction wheels. Data has been taken for both hard and soft mounts; tests were conducted at constant speeds and during runup-rundown over a 0 to 5000 rpm range. A FSC, 7 ft-lb-sec and HEAO, 30 ft-lb-sec ball bearing reaction wheel and a Model Magnetic Bearing were tested. Data analysis was conducted to identify the principal resonances in the 10 to 120 Hz region. Although some particular phenomena remain unexplained, in general good agreement is attained between the analytical predictions and test data. Predictions have also been made of the expected emitted vibrations for an LST sized ball bearing and magnetic bearing reaction wheel using engineering judgment and the test data obtained during the study. Additional tests were also run on the 101H duplex bearing pairs used in the reaction wheel suspension to determine bearing stiffness characteristics in the pre-breakaway zero speed region.

The following conclusions have been drawn from the effort described above.

1. The Sperry three-axis, hard-mount, emitted-vibration measurement fixture provides an efficient means for measuring small reaction wheel force and torque signatures during both constant speed run and runup-rundown conditions. Emitted vibrations can be accurately measured over a range of 10 to 120 Hz with force and torque resolutions of .006 lb_f and .009 in.-lb_f respectively.

2. High amplitude level force and torque dynamic resonances exist in both ball and magnetic bearing wheels. The amplitudes at these resonances are considerably higher than the unbalance forces and are not easily controlled by design. The reaction wheels should be designed and mission operations planned such that those resonant frequencies are avoided during fine pointing.

3. At low speeds, below the dynamic resonances, the radial emitted vibration is proportional to frequency squared and agrees well with the measured readings obtained during wheel balancing. The HEAO RWA was balanced to .005 oz-in. static and .04 oz-$in.^2$ dynamically.

4. The 101H bearing retainer forces are small and almost negligible in comparison to the rotor unbalance forces in the ball bearing reaction wheels.

5. No significant forces or torques at harmonics of wheel speed are present in the ball bearing reaction wheels.

6. Existing dynamic mathematical models for reaction wheels do not predict all the three-axis interactions and gyroscopic effects measured. Prior to the LST application, reaction wheel vibration requirements were moderate and simple static and dynamic models were sufficient. Although most resonant frequencies in the 0 to 120 Hz range can be predicted, existing models are not capable of predicting their amplitudes. A model which includes the bearing-shaft interface, motor type and interactions, housing compliances, and structural damping factors needs to be developed.

7. Additional resonances are created when the reaction wheel is freely isolated, and present reaction wheel models do not completely explain all of them.

8. Below the dynamic gyroscopic resonant frequency, the magnetic bearing has very low emitted vibration. The only additional vibrations beside wheel speed were at harmonic frequencies and of low amplitude.

9. The 101H ball bearing set at very low speed behaves as a continuous, nonlinear spring element opposing shaft rotation. Torsional stiffness is very low (less than 5 ft-lb/radian).

SECTION 3.0

RECOMMENDATIONS FOR FURTHER STUDY

During the course of this study as tests were run, data was gathered, and certain questions were answered, many more questions were raised regarding the characteristics of reaction wheels which may be used on the LST. To answer many of these questions a significant amount of further work is necessary. This section lists some of Sperry's recommendations for further study.

It is realized that parallel LST Phase B vehicle definition studies are being conducted by three Prime Contractors, and conclusions from their studies and their use of the data within this report may place higher or lower priorities on these recommendations. For instance, if it is decided to use a HEAO type RWA for a low cost approach, the recommendations relating to ball bearing wheels will take on more importance, whereas, if it is considered that a magnetic bearing wheel must be used, then the ball bearing RWA suggestions have less importance.

Recommendations

1. Develop a more complete and detailed mathematical model for the HEAO type reaction wheel. Identify and quantify the causes for the 23 and 38 Hz gyroscopic resonances such that both frequency and amplitude levels can be accurately predicted. Determine if a technique for tuning out these resonances can be implemented. Include in the model such things as the case and mounting characteristics, the bearing-rotor shaft interface, the motor characteristics, and a more detailed flexible rotor.

This effort would include detailed computer simulations, as well as testing the HEAO RWA at both the individual piece part and subassembly level, and at the fully assembled unit level.

2. Determine the influence of environment on balance stability. Using an existing reaction wheel, such as HEAO, evaluate the RWA emitted vibration before and after shuttle level vibrations. Evaluate the effects of temperature variations on the emitted vibration levels. Evaluate the repeatability from runup to runup, and the effect of the earth's gravity field on vibration by placing the spin axis horizontal and vertical.

3. Retrofit a HEAO RWA with a dc motor and determine its influence on emitted vibrations compared to an ac motor. Develop the electronics necessary to provide smooth control over the LST speed range and through zero speed. Explore the possibility of using a common set of microprocessor electronics to control a 4- or 5-skewed reaction wheel system, thereby enabling dc motors to be used at a minimum complexity increase over ac motor control.

4. Build a magnetic bearing reaction wheel and test the emitted vibration. The MMB tested in this study does not completely represent an LST magnetic bearing RWA since the housing and rotor dynamics are absent. Therefore, a more representative unit should be built and tested. The radial spring constant should be made adjustable in three steps such that an evaluation can be made of emitted vibrations for very weak and very strong radial springs. A detailed mathematical model should also be developed for the wheel and emitted vibration predictions compared to actual test data.

SECTION 4.0

DESCRIPTION OF UNITS TESTED

The principal features, construction and performance characteristics of the three momentum devices which were tested for emitted vibrations during the study are described in this section. Specifically, they were the Fleet Satellite Communications (FSC) MWA, the High Energy Astronomy Observatory (HEAO) RWA, and a prototype Model Magnetic Bearing (MMB) Assembly.

4.1 FLEET SAT COM MWA

The Fleet Sat Com MWA is the second of a growing family of applications of the mid-range Sperry Model 15 series momentum wheel assemblies. At 7 foot-pound-seconds of momentum it weighs 12.3 pounds and uses a nominal steady power of 6 watts.

In January 1973 Sperry began development of the long life (5 years) biased momentum wheel for the Fleet Sat Com program, a military communication satellite developed by TRW Systems Group for the U.S. Navy via a SAMSO prime contract. Two wheels in each spacecraft will be launched nonoperating. One will be held in standby as a redundant element and the other will be brought up to a nominal operating speed of 3100 rpm. Control torques of ±15 ounce-inches will be available within a speed range from 2635 to 3565. The first unit was delivered to TRW in October 1973. Two life test units were delivered in March 1973. Three other Model 15 life test units have been operating at Sperry since September 1973. The FSC Life Test Unit, Serial No. SLU-2, retained at Sperry, was refurbished and rebalanced for this study evaluation.

Long life and confidence for long life were specific design goals. To this end, the same bearings (101H Duplex Pair) and lubrication system (Andok C grease and V79 oil) were used that have been employed so successfully in the Model 400 MWA. The 400 MWA was developed as an operational flight device for the TRW Model 35 Spacecraft in 1968, and to date a number of these units has accrued over 8000 hours of successful flight operation. Improved labyrinth seals and larger supplies of lubricant provide additional confidence in a life greater than 5 years. Loss of lubricant by evaporation has been calculated to be less than 3 percent over a 5-year period.

The cross sectional view in Figure 4.1-1 shows several characteristics of the device. The aluminum housing, machined as a conical structure with circumferential ribs, provides a lightweight enclosure with good heat conduction. The ac induction spin motor is the same as those used in previous designs with the exception that the number of wire turns has been reduced to provide higher torque output (±15 ounce-inches over speed and voltage range).

Thermistors near both bearing pairs provide bearing and motor temperature monitoring. A rotor speed sensor, adjustable from outside the housing, produces a signal when a shaped indentation in the rotor rim passes by. The signal provides both magnitude and direction of rotor information. A five-sided optical cube provides an angular momentum vector alignment reference to an accuracy of .02 degree.

As in all Sperry momentum exchange devices, the Fleet Sat Com MWA is designed to operate with its inertia wheel spinning in a vacuum. No backfilling of the unit with gas is required. This capability allows higher speed operation without the penalizing power drain associated with windage drag. The result is significantly lower weight and power consumption. A valve is provided on the Fleet Sat Com unit which enables the housing to be vented to space to completely avoid pressure increases due to long term outgassing of internal components.

Table 4.1-1 summarizes the performance characteristics of the unit tested. For the LST study the FSC MWA was run over a speed range of 0 to 5000 rpm, and the unit was balanced to .001 ounce-inch static and .01 ounce-inch^2 dynamic.

4.2 HEAO RWA

The HEAO RWA is derived from the Sperry Model 15 Series which includes a 15 foot-pound-second reaction wheel used on the Canadian Communication Technology Satellite (CTS), and the 7 foot-pound-second FSC MWA described above. A cross-sectional view of the HEAO RWA is shown in Figure 4.2-1, a photograph in Figure 4.2-2, and its characteristics are summarized in Table 4.2-1.

The HEAO contract with TRW was started at Sperry in November 1974. The HEAO Engineering Model Unit has successfully passed all the performance and environmental tests and is the unit employed for this evaluation. Qualification and flight unit fabrication has been approved. Four HEAO RWA's will be used in a skewed array on HEAO-B Spacecraft--they will operate over a ±2000 RPM speed range.

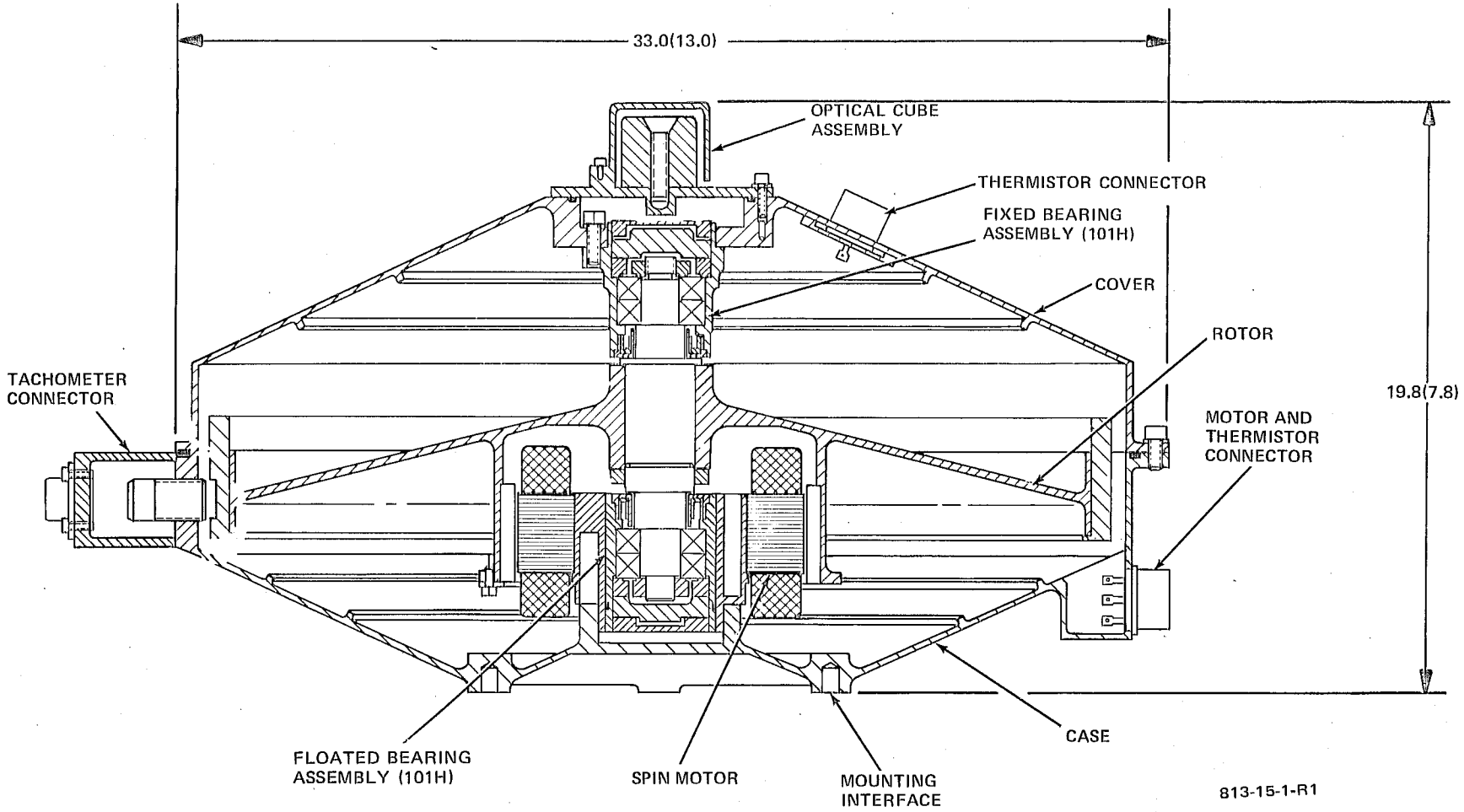

DIMENSIONS IN CENTIMETERS (INCHES)

Figure 4.1-1
Fleet Sat Com MWA

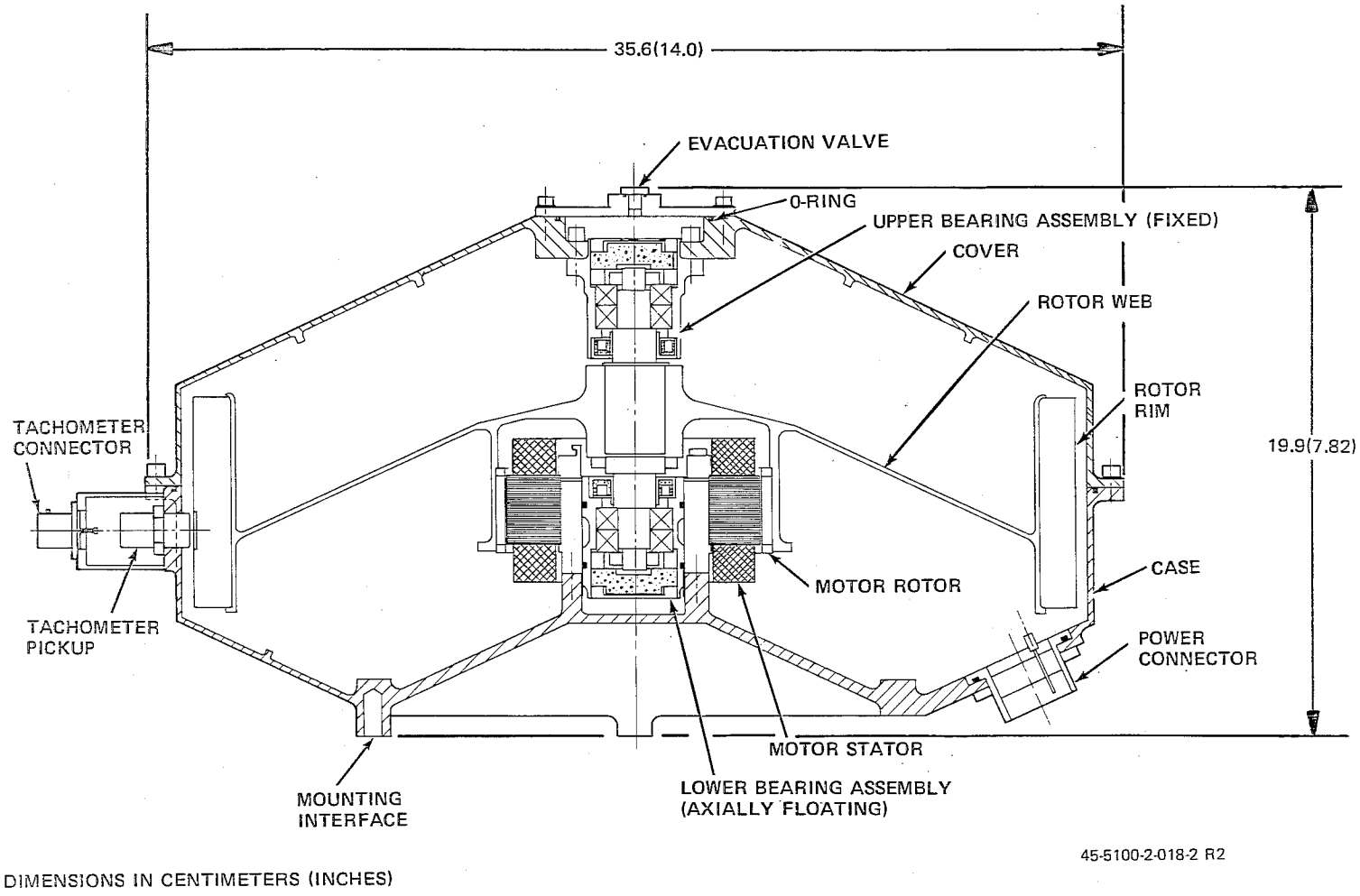

Figure 4.2-1
HEAO RWA Cross-Sectional View

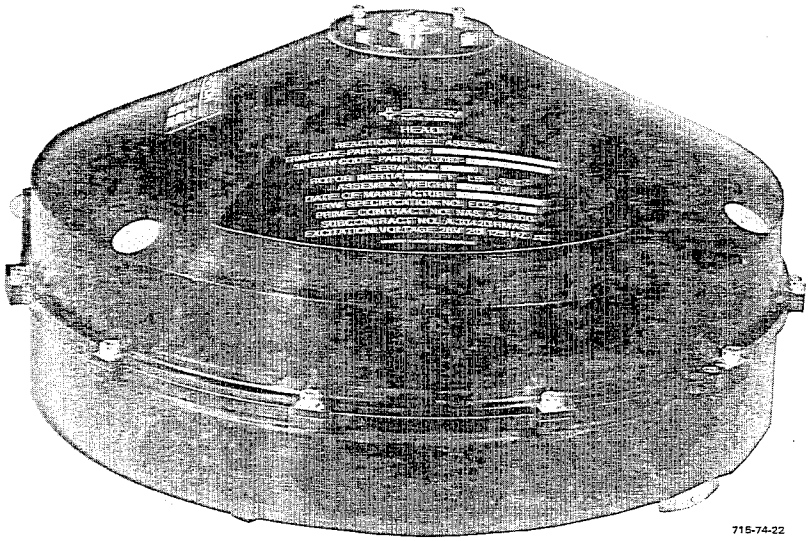

Figure 4.2-2
HEAO RWA

TABLE 4.1-1

FLEET SAT COM BIASED MOMENTUM WHEEL ASSEMBLY

Parameter	Value		Units	
Biased Angular Momentum	9.5	7	n-m-sec	ft-lb-sec
Rotor Speed at 7 ft-lb-sec	325	3100	rad/sec	rpm
Speed Range	276 to 373	2635 to 3565	rad/sec	rpm
Rotor Outer Diameter	28.55	11.24	cm	inches
Total Weight	5.58	12.3	kg	lb
Rotor Weight	2.40	5.3	kg	lb
Output Torque, Minimum Over Speed Range	.12	17	n-m	oz-in.
Drag Torque, Maximum at 3100 RPM	.01	1.5	n-m	oz-in.
Wheel Unbalance,* Maximum Static	7.2×10^{-6}	.01	kg-m	oz-in.
Wheel Unbalance,* Maximum Dynamic	1.8×10^{-6}	.10	$kg\text{-}m^2$	$oz\text{-}in.^2$
Run Power, Maximum at 3100 rpm	6	6	watts	watts
Spin Vector to Mount Alignment	$.436 \times 10^{-3}$	.025	rad	deg
Inertias				
Rotor Polar	.0290	.0214	$n\text{-}m\text{-}sec^2$	$ft\text{-}lb\text{-}sec^2$
Rotor Transverse	.0151	.0112	$n\text{-}m\text{-}sec^2$	$ft\text{-}lb\text{-}sec^2$
Unit Spin Axis, I_{ZZ}	.054	.040	$n\text{-}m\text{-}sec^2$	$ft\text{-}lb\text{-}sec^2$
Transverse Y Axis, I_{YY}	.034	.025	$n\text{-}m\text{-}sec^2$	$ft\text{-}lb\text{-}sec^2$
Transverse X Axis, I_{XX}	.035	.026	$n\text{-}m\text{-}sec^2$	$ft\text{-}lb\text{-}sec^2$

*For this study, the FSC RWA was balanced to better values.

TABLE 4.1-1 (cont)

FLEET SAT COM BIASED MOMENTUM WHEEL ASSEMBLY

Parameter	Value	Units	
Spin Motor Type	2ϕ ac induction	--	--
Bearing Type	Barden 101H Angular Contact Duplex Pair (DF)	--	--
Speed Pickoff	Magnetic (5 to 100% of speed range)	--	--
Design Life	7 7	years	years

TABLE 4.2-1

HEAO REACTION WHEEL ASSEMBLY

Parameter	Value		Units	
Angular Momentum	±40.67	±30	n-m-sec	ft-lb-sec
Rotor Speed at 30 ft-lb-sec	209	2000	rad/sec	rpm
Rotor Outer Diameter	32.02	12.61	cm	inches
Total Weight	13.4	29.5	kg	lb
Rotor Weight	9.5	21	kg	lb
Output Torque, Minimum Over Speed Range	.12	17	n-m	oz-in.
Drag Torque, Maximum at 2000 rpm	.01	1.5	n-m	oz-in.
Wheel Unbalance,* Maximum Static	7.2×10^{-6}	.01	kg-m	oz-in.
Wheel Unbalance,* Maximum Dynamic	1.8×10^{-6}	.10	$kg\text{-}m^2$	$oz\text{-}in.^2$
Run Power, Maximum at 2000 rpm	10	10	watts	watts
Spin Vector to Mount Alignment	4.36×10^{-4}	.025	rad	deg

*For this study, the HEAO RWA was balanced to better values. The values in the table represent typical balance.

TABLE 4.2-1 (cont)

HEAO REACTION WHEEL ASSEMBLY

Parameter	Value		Units	
Inertias				
Rotor Polar	.196	.144	$n\text{-}m\text{-}sec^2$	$ft\text{-}lb\text{-}sec^2$
Rotor Transverse	.113	.083	$n\text{-}m\text{-}sec^2$	$ft\text{-}lb\text{-}sec^2$
Spin Motor Type	2ϕ ac induction		--	--
Bearing Type	Barden 101H Angular Contact Duplex Pair (DF)		--	--
Speed Pickoff	Magnetic (5 to 100% of speed range)		--	--
Design Life	5	5	years	years

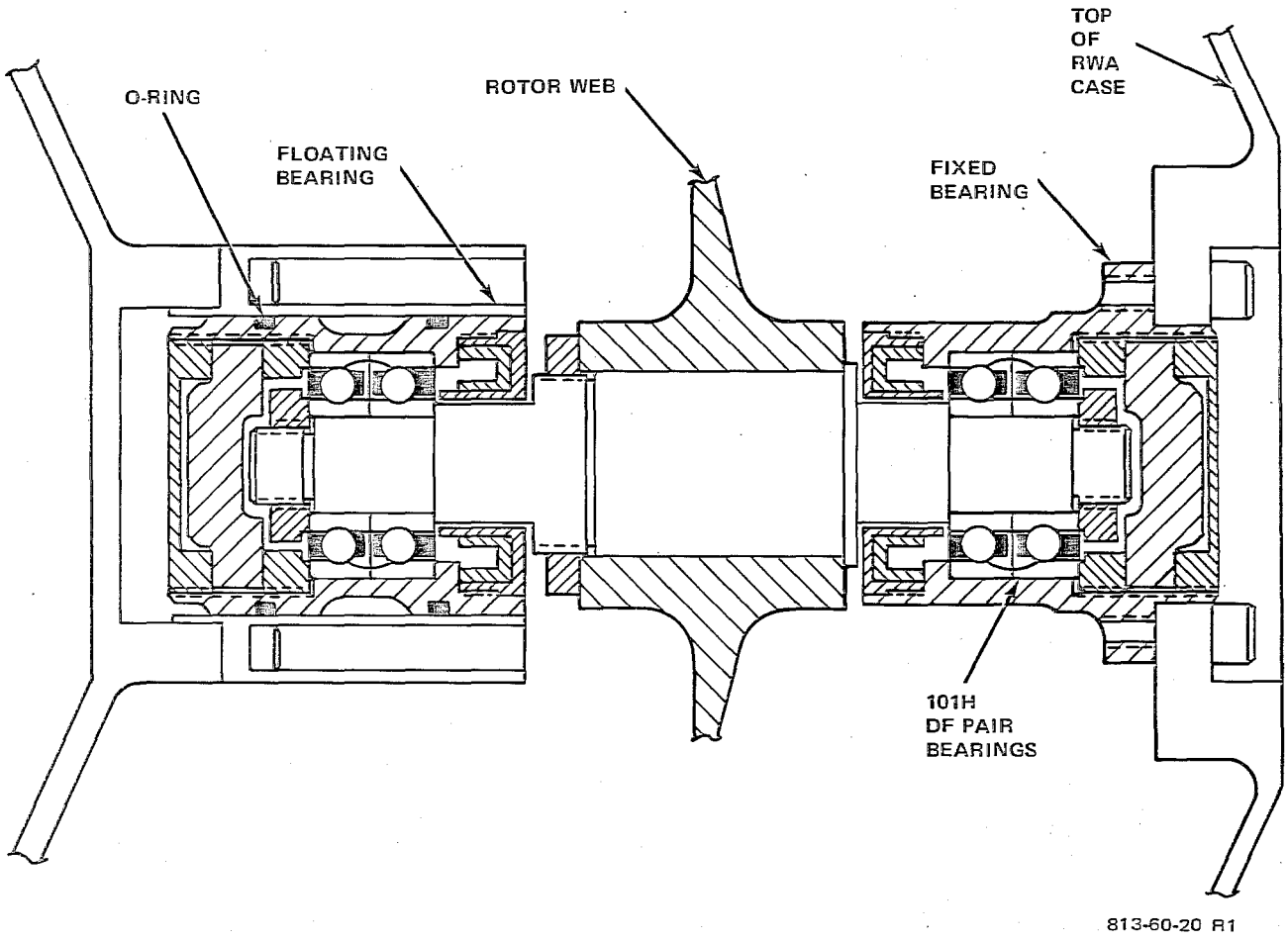

Figure 4.2-3
Suspension System Cross-Section

The rotor is of bimetal construction with a 17-4PH stainless steel rim thermally fitted to an aluminum web. A thermal fit is also employed at the rotor hub section to provide a steel shaft for material compatibility with the spin bearings. This construction technique is identical to that used in the Model 400 and Model 15 MWA rotors and has demonstrated its ability to maintain a stable interface through environmental extremes. The conical section web employed in this unit ensures an axial rotor stiffness that is approximately 5 times that of the bearing and housing combination. Therefore, vibration at the first axial resonance of the rotor rim does not cause large deflections in the web itself. This, in turn, ensures low web stresses and enhances rotor balance stability with environmental loadings.

The housing is made in two parts machined from 6061 aluminum alloy plate stock. Ribs are provided to strengthen the structure and prevent localized buckling due to evacuation and environmental loads. In addition, the symmetrical cross-sections ensure an accurate bore alignment for support of the rotor and bearing assembly. Sealing is achieved with two o-rings as shown, and a vent valve is provided for evacuation.

The bearing configuration shown in Figure 4.2-3 consists of two duplexed DF pairs of 101H bearings preloaded in cartridges. Axial support for the rotor is given by the fixed cartridge. Both bearing pairs share the radial load. The lower cartridge is axially floated in a sleeve so that differential expansions due to vibration and/or temperature can occur without affecting the bearing pair internal preload. This is a necessary feature for long life operation of a unit that must operate evacuated on the ground as well as in space and over a large temperature range.

The physical interface between the floated cartridge and the housing sleeve consists of a silver plated steel cartridge inside a titanium sleeve aided by two o-rings. The grooves that contain these rings are slightly larger than regular o-ring grooves so that the ring can compress completely. This allows a radial clearance of only .0003 inch between cartridge and sleeve which assures accurate H vector alignment. The o-rings provide two important primary functions, the effectiveness of which has been proven in M-15 RWA testing. First they reduce the direct metal-to-metal contact during environmental vibration so that the

rapid relative motion between cartridge and sleeve does not cause galling. Second, the relative motion that is caused under vibration environments is damped significantly by the viscous shear of the oil provided in the interface. The magnitude of damping afforded is sufficient to reduce the 101H bearing load by nearly 2 to 1 over a non-o-ring interface. The material combination in the cartridge and sleeve provides thermal compatibility and high wear resistance.

The spin bearing lubrication system supplies lubrication from several reservoirs. The largest of these is a sintered nylon reservoir vacuum impregnated with Teresso V-79 oil. The remaining lubricant supply is provided by an Andok C grease pack within the bearings. The lubricant finds its way into the ball working area by passive means. No mechanical mechanism or actuation system is used. Lubricant is supplied by the natural phenomenon of condensation from vapor and by capillary action. These processes have no failure mode as long as an adequate quantity of lubricant is available, and it functions by the demand of the bearing itself. This avoids starving or oversupply that can occur in mechanically actuated systems. Lubricant loss by vaporization is sufficiently retarded by the labyrinth seals. These seals provide lubricant protection even in the event of a hard vacuum exposure.

The loss of the primary lubricant over a period of 1 year on the ground and 5 years in space has been calculated to be 3.4 percent. The lubricant is identical to that used in the Model 400 MWA, which has demonstarted several years of operation in space as a vented assembly, and more than 3 years on the ground under continuous vacuum pumping.

Speed and rotational direction information is provided by a passive magnetic-slug pickoff which produces an electrical pulse once per rotor revolution. Speed information is available from 5 to 100 percent of rated speed.

The spin motor is of the same configuration as that currently used in the FSC RWA. It is a two-phase, six-pole ac induction motor with a bifilar winding. The unit features an extremely rugged squirrel cage rotor coupled with a proven stator insulation system capable of extended life in the extreme of space environment.

A thermistor is mounted on the sleeve between the motor and the floating bearing pair to provide temperature data for telemetry monitoring purposes.

For this study the HEAO RWA was run over a ±3000 rpm speed range and a balance of .005 ounce-inch static and .04 ounce-inch^2 dynamic was achieved. This level of static unbalance is equivalent to removing .0225 gram from the rim of a perfectly balanced wheel, and that corresponds to drilling a hole of 1/16 inch diameter by 1/18 inch deep in the steel rim - a small amount of metal! Alternately, this corresponds to a lateral shift of the principal axis from the spin axis of 15.2 microinches - a very small distance.

4.3 MODEL MAGNETIC BEARING (MMB) WHEEL

The MMB was constructed by Sperry in 1972 as a laboratory model to verify design approaches and obtain test data prior to the design and fabrication of a large 400 foot-pound-second magnetic bearing momentum wheel assembly. The model used a three-loop bearing configuration and was mounted within a very stiff test housing (or fixture). Figure 4.3-1 is a photograph of the MMB and Figure 4.3-2 shows a cross-sectional detail of the bearing. The model consists of a shaft mounted on two magnetic bearings (radially passive, axially active), with back-up ball bearings being provided for touchdown. An ac induction motor is used for spin-up. Samarium-cobalt magnets establish a quiescent flux between axially opposed soft iron rings, the flux being modulated suitably to provide axial support. Radial damping is provided by cementing copper wires in the pole-face grooves at the magnetic gaps. Eddy current proximeters are used both for axial position sensing and for monitoring radial displacements, as well as providing a speed indication.

Table 4.3-1 lists the principal characteristics of the MMB.

Axial Control Loop - The rotor is suspended by a simple, axially active, radially passive magnetic bearing system. Axial motion is sensed by an eddy current proximeter. Absolute positioning accuracy is not important but high resolution is needed to obtain the high servo loop bandwidth required to stabilize the statically unstable axial motion due to the rotor magnetics.

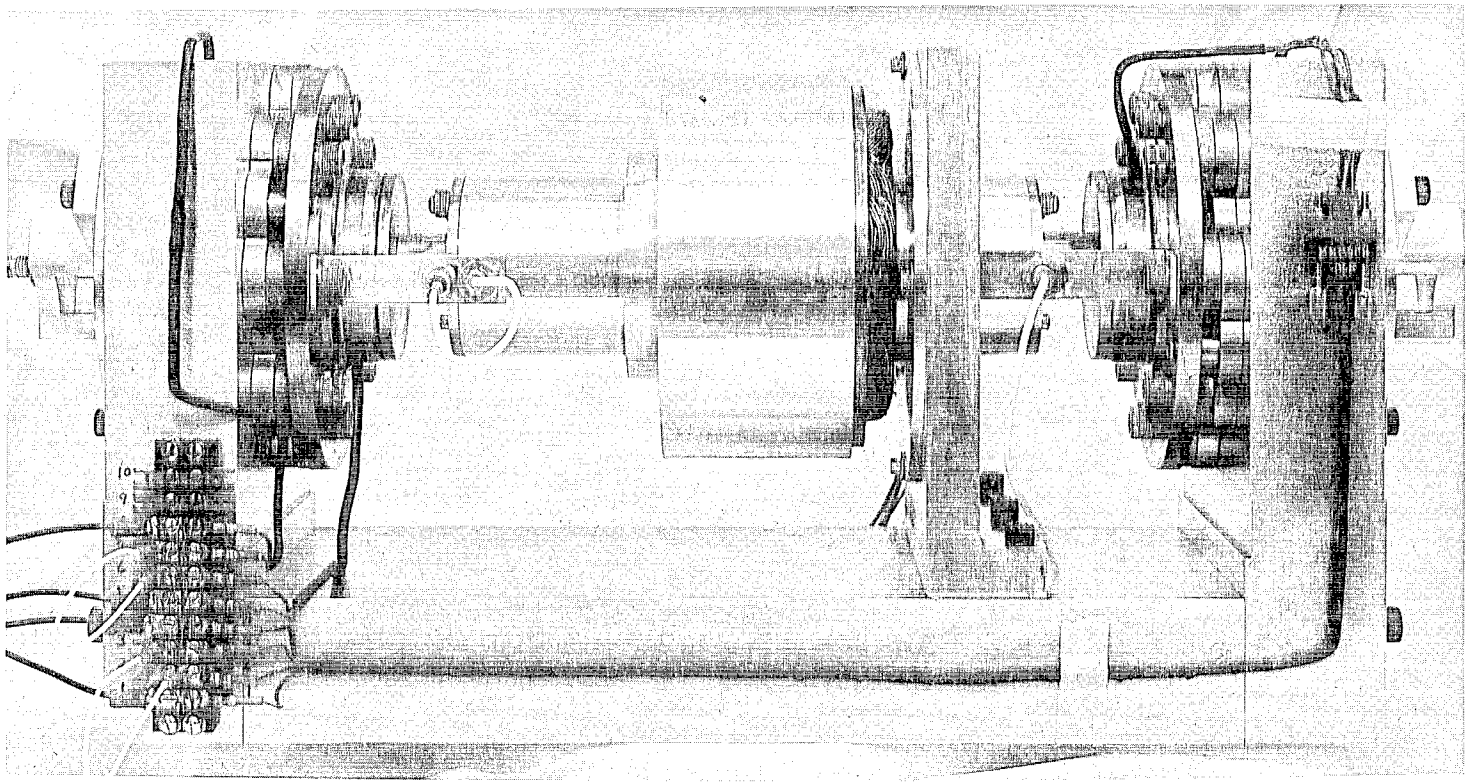

813-45-41

Figure 4.3-1
Model Magnetic Bearing

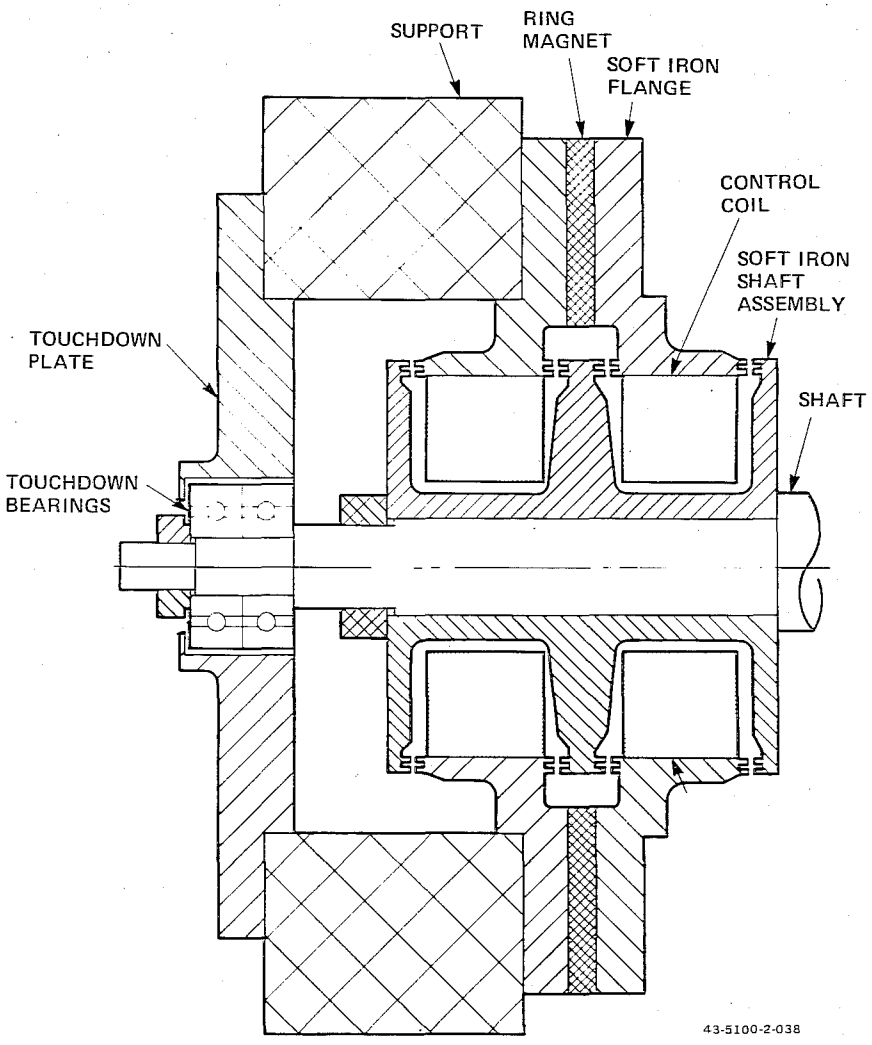

Figure 4.3-2
Magnetic Bearing Sectional View

TABLE 4.3-1

MMB WHEEL CHARACTERISTICS

Parameter	Value		Units	
Angular Momentum	.916	.676	n-m-s	ft-lb-sec
Rotor Speed at .916 (n-m-s)	520	5000	rad/sec	rpm
Rotor Outer Diameter	10.8	4.25	cm	in.
Total Weight	14.2	31.4	kg	lb
Rotor Weight	1.71	4.2	kg	lb
Drag Torque at 520 rad/sec	4.9×10^{-4}	.07	n-m	oz-in.
Rotor Unbalance				
Static	1.4×10^{-6}	.002	kg-m	oz-in.
Dynamic	1.8×10^{-7}	.01	$kg\text{-}m^2$	$oz\text{-}in.^2$
Spin Motor Type	2ϕ, ac induction		--	--
Radial Stiffness (Positive)	3731	330	n/cm	lb/in.
Axial Stiffness (Active)	11,298	1000	n/cm	lb/in.
Axial Unbalance Stiffness	-27,115	-2400	n/cm	lb/in.
Gap Flux Density	.43	4300	tesla	gauss
Radial Gap Length	.063	.025	cm	in.
Axial Gap Length	.030	.012	cm	in.
Rotor Polar Inertia	.0018	.0013	$n\text{-}m\text{-}sec^2$	$ft\text{-}lb\text{-}sec^2$
Rotor Transverse Inertia	.0058	.0043	$n\text{-}m\text{-}sec^2$	$ft\text{-}lb\text{-}sec^2$
Unit Spin Axis, I_{ZZ}	.057	.042	$n\text{-}m\text{-}sec^2$	$ft\text{-}lb\text{-}sec^2$
Transverse Y Axis, I_{YY}	.176	.130	$n\text{-}m\text{-}sec^2$	$ft\text{-}lb\text{-}sec^2$
Transverse X Axis, I_{XX}	.164	.121	$n\text{-}m\text{-}sec^2$	$ft\text{-}lb\text{-}sec^2$
Life	No Requirement (Laboratory Model Only)			

Dynamic Response - The radial restoring stiffness of the passive magnetics creates an instability in the axial direction as a consequence of Earnshaw's Theorem. The net force in the axial direction is approximately a linear function of axial displacement for small displacements from the equilibrium position. The axial equation of motion of the magnetically suspended rotor is therefore

$$M\ddot{z} - K_u z = F_c + F_{ext}$$

where

z = axial displacement from the equilibrium position

M = rotor mass

K_u = magnetic unbalance stiffness

F_c = rotor axial control force

F_{ext} = rotor axial external force

A block diagram of the axial control system is shown in Figure 4.3-3, and the root locus in Figure 4.3-4.

Axial stability can be obtained by controlling the current to the control coils to generate forces in the proper direction. Thus, if the control force includes rate-plus-displacement feedback given by

$$F_c = -B\dot{z} - Kz$$

then the axial equation of motion becomes

$$M\ddot{z} + B\dot{z} + (K - K_u)\, z = F_{ext}$$

This equation indicates that system stability can be obtained for $K > K_u$, which gives a net static stiffness of $(K - K_u)$ and results in a power loss under external axial loads. In practice, the rate sensor may be avoided by using lead compensation of the position signal.

In addition to the lead compensation, a minor loop integrator has been added (shown by dashed lines in Figure 4.3-3), in order that the unbalance stiffness of the passive magnetics can be used to advantage in overcoming external loads. The integrator provides zero average power in the coils under steady axial loads. The integrator also enables long-term, low-power operation by correcting for drift in any of the electronics components, including the position sensor. With integral feedback, the static axial stiffness is negative. The root locus of this system is shown in Figure 4.3-5.

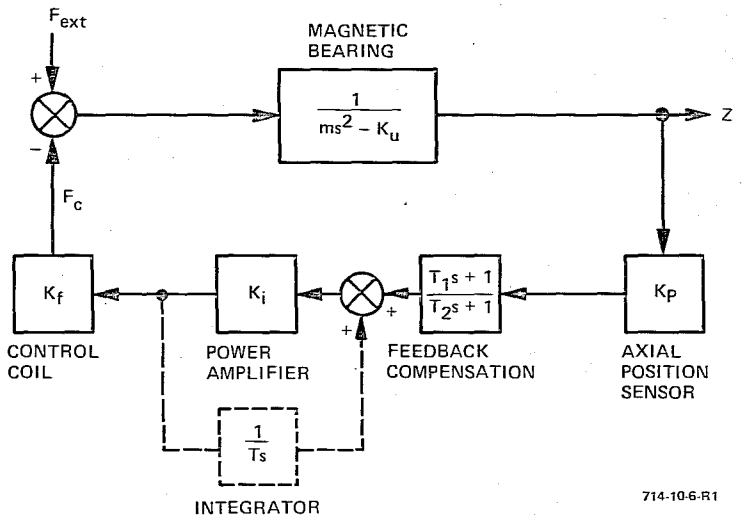

Figure 4.3-3
Magnetic Bearing Block Diagram

$$F_c = K \frac{(T_1s + 1)}{(T_2s + 1)} Z$$

- POSITION STIFFNESS = $(K - K_u)$
- POWER LOSS UNDER STEADY LOAD

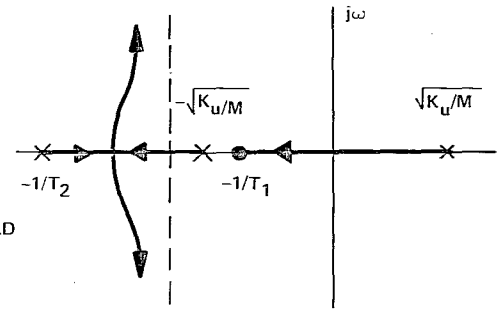

Figure 4.3-4
Root Locus Without Integrator

- INTEGRAL REGENERATIVE FEEDBACK

$$F_c = K \frac{(T_1s + 1)}{(T_2s + 1)} \frac{(Ts)}{(Ts - 1)}$$

- NEGATIVE STIFFNESS = $-K_u$
- ZERO POWER LOSS UNDER STEADY AXIAL LOADS
- COMPENSATES FOR ELECTRONICS AND SENSOR DRIFT

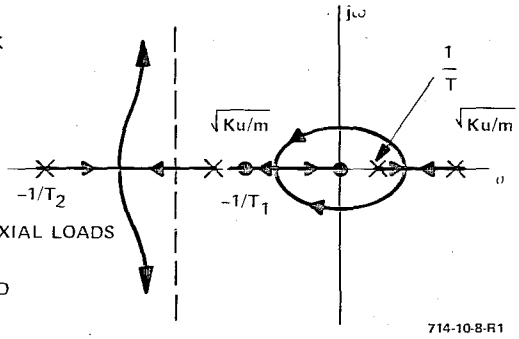

Figure 4.3-5
Root Locus With Integrator

SECTION 5.0

THREE-AXIS (HARD MOUNT) VIBRATION TESTS

5.1 TEST SETUP DESCRIPTION

The fixture used to measure the emitted vibrations was designed to simultaneously measure forces along three principal axes, and moments about these axes. The design simply consists of a mounting interface ring (approximately 33 inches O.D. and 26 inches I.D.) suspended by four vertical and four horizontal flexure/transducer combinations. Figure 5.1-1 illustrates the design. The flexures are designed to hold the fixture resonances as high as possible above the unit operating frequencies to minimize fixture-related amplification of the emitted vibration signature. They can also be designed to support the loads imposed by torque output from the test unit if such testing is desirable.

A detailed photograph of the fixture is shown in Figure 5.1-2. Three horizontal and two vertical flexures are visible supporting the mounting ring. The force transducers are Kistler model 903 quartz load washers and are installed with each of the eight flexures. The darker "tub" mounted in the mounting ring is an adapter for mounting the small reaction wheels tested during this program. Kistler model 503 charge amplifiers are employed to convert the charge signals from the transducers to voltage signals.

The forces and moments about the center of gravity of the force-moment fixture mounting ring are obtained by combining the eight-force transducer signals as follows:

$$F_x = F_1 + F_2 + F_3 + F_4$$

$$F_y = F_8 - F_6$$

$$F_z = F_7 - F_5$$

$$M_x = -R_2(F_5 + F_6 + F_7 + F_8)$$

$$M_y = R_1 (F_4 - F_2)$$

$$M_z = R_1 (F_3 - F_1)$$

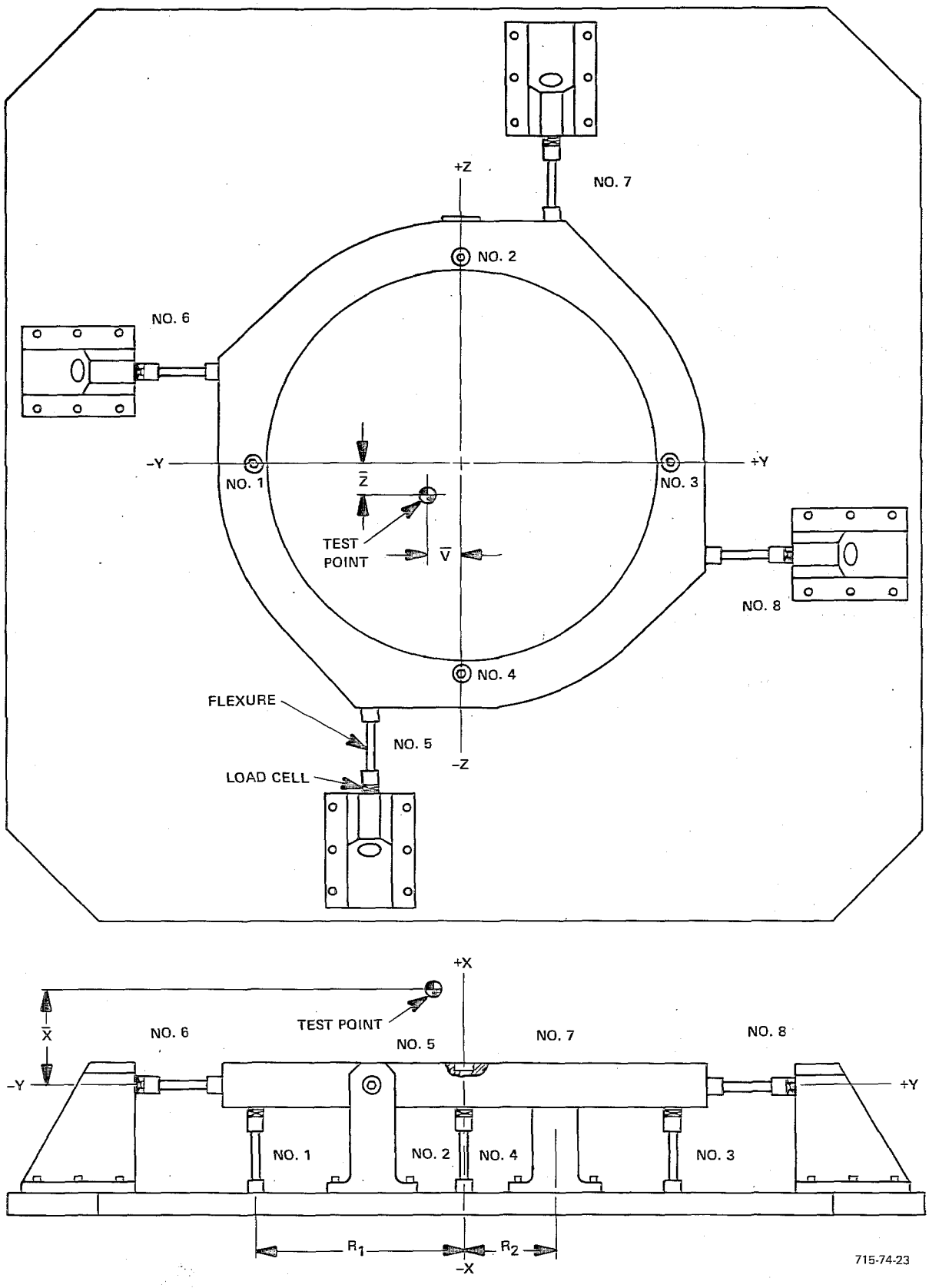

Figure 5.1-1
I.V. Fixture Schematic

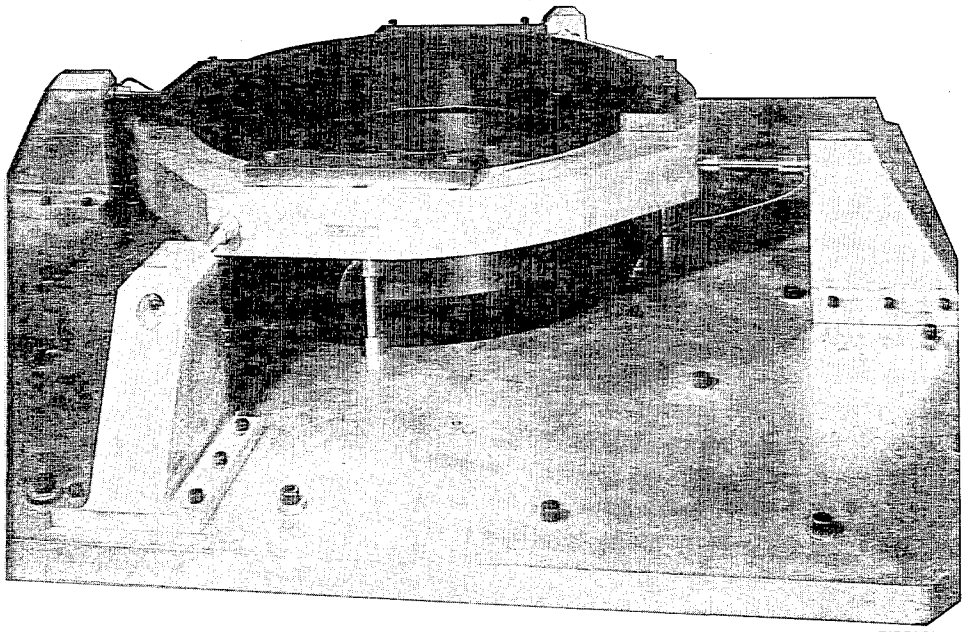

Figure 5.1-2
Induced Vibration Fixture

The forces acting through any point selected on the test specimen or fixture are identical to those given above. The moments about that point need to be transformed if the point does not coincide with the center of gravity of the fixture mounting ring. These transfer equations are:

$$M_x^1 = M_x + F_y \bar{z} - F_z \bar{y}$$

$$M_y^1 = M_y + F_z \bar{x} - F_x \bar{z}$$

$$M_z^1 = M_z + F_x \bar{y} - F \bar{x}$$

where $\bar{x}$, $\bar{y}$ and $\bar{z}$ are transfer components shown in Figure 5.1-1. These summing operations are performed by analog circuitry employing operational amplifiers.

In use, the fixture is mounted on a background noise isolation system shown in Figure 5.1-3. Two large seismic masses are employed in this system. The primary mass (~ 17,000 pounds) is set below floor level and separated from ground by air gaps on the sides and a 1-foot bed of sand on the bottom. The secondary seismic mass (~ 10,000 pounds) is suspended on pneumatic isolators mounted on the primary seismic mass. Portions of two of these isolators are visible in the figure. The unit mounting fixture hard-mounts to the secondary mass. This double system provides a higher degree of isolation than either isolated mass alone. Figures 5.1-4 through 5.1-7 present the background noise characteristics of the fixture with the unit under test nonoperating. The frequency range from 0 to 25 Hz is shown for both the force and moment axes, and is presented in Figures 5.1-4 and 5.1-5. Frequencies up to 200 Hz are shown in Figures 5.1-6 and 5.1-7. This combination isolation system enables the measurement of induced forces and moments down to .006 lbf and .009 in.-lbf, respectively in the frequency ranges of interest. Even the maximum background noise peaks are no greater than .051 lbf and .093 in.-lbf at 7.5 Hz.

The IV fixture calibration is accomplished electronically by matching the gain of each of the charge amplifiers to its respective force transducer so as to produce the desired volt per pound scale factor of load applied to the fixture. Provision is made to accomplish this scaling function at the charge amplitude level rather than through external calibration by application of known loads. This calibration is then statically checked by application of accurately known

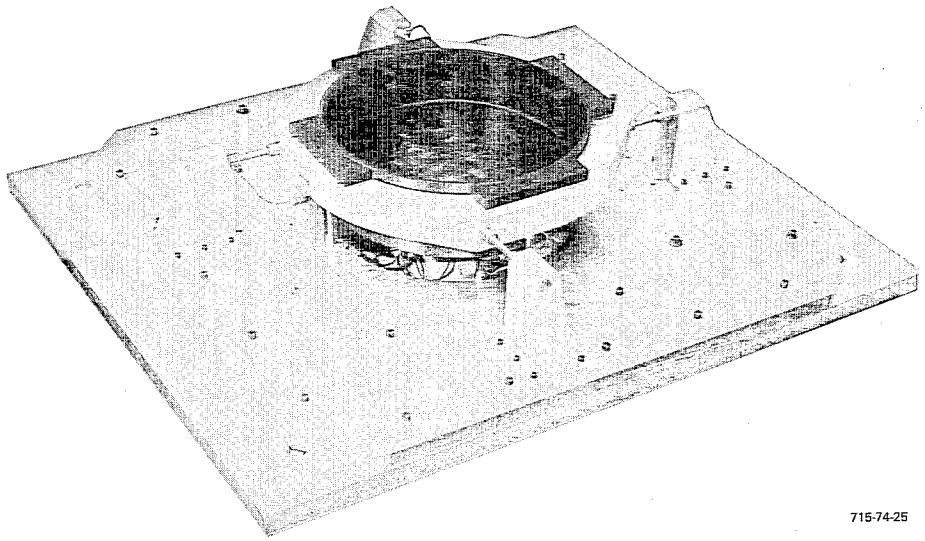

Figure 5.1-3
Background Noise Isolation System

Figure 5.1-4
Background Noise (0-25 Hz) RWA OFF

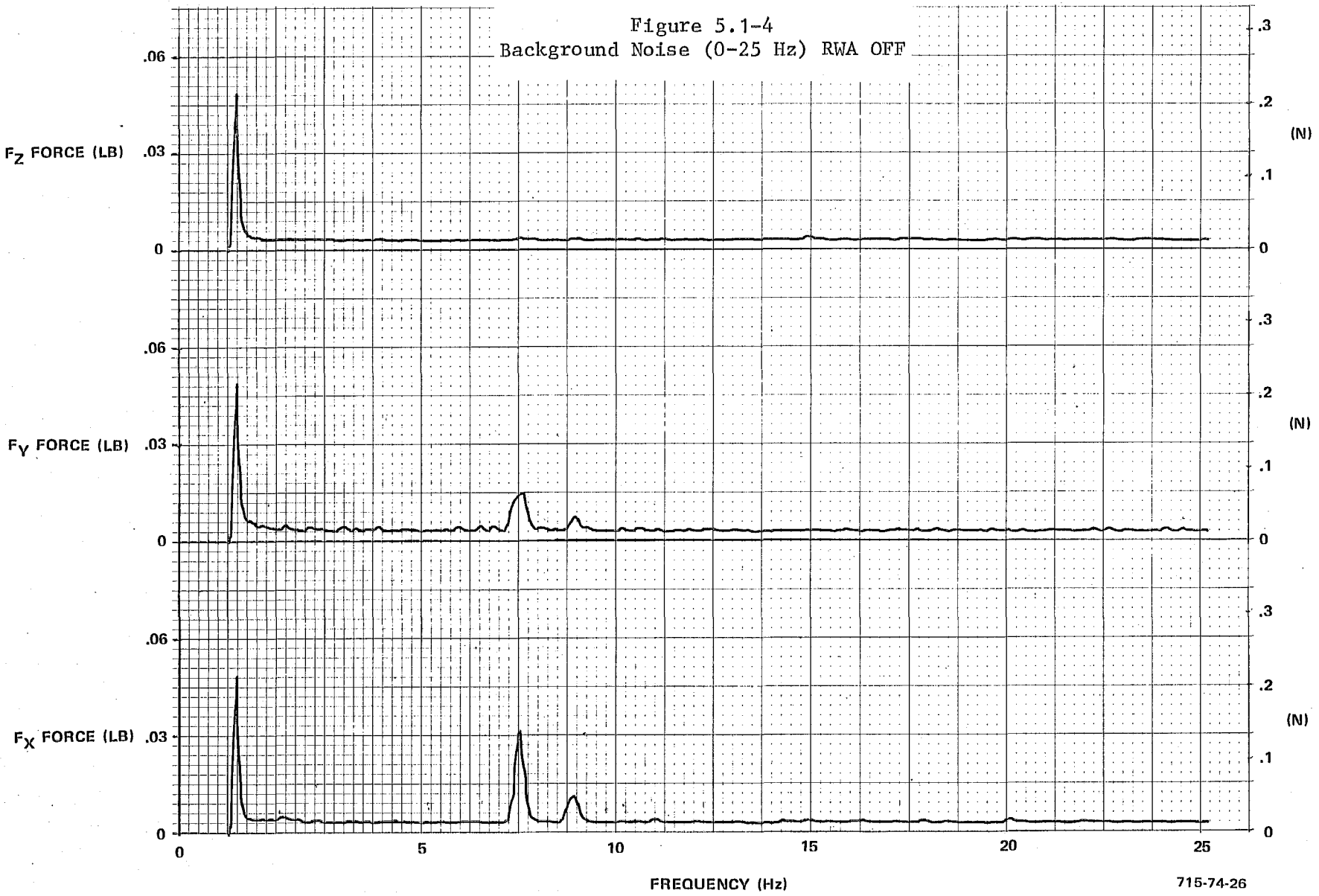

Figure 5.1-5
Background Noise (0-25 Hz) RWA OFF

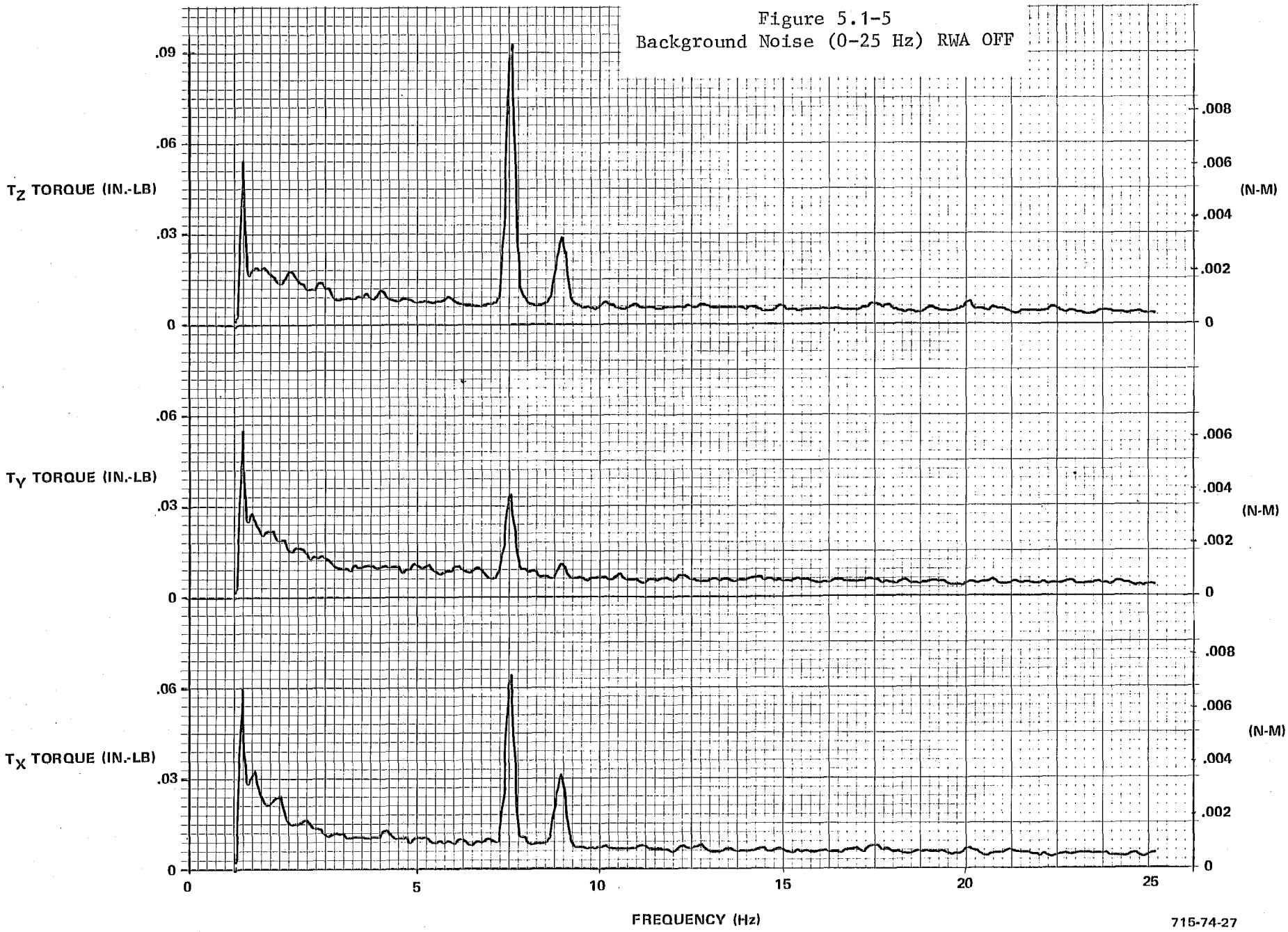

715-74-27

Figure 5.1-6
Background Noise Rotor Stopped

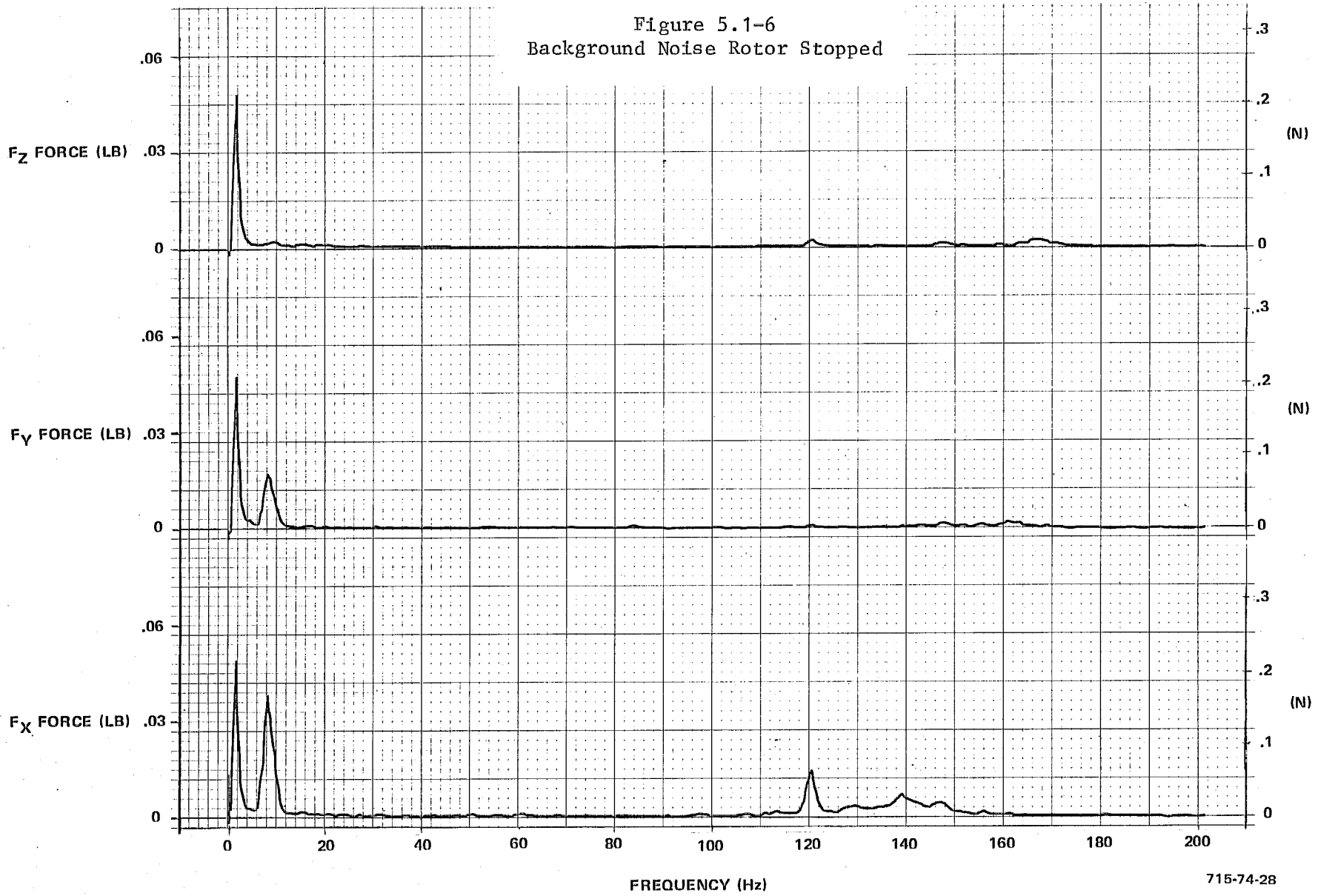

Figure 5.1-7
Background Noise Rotor Stopped

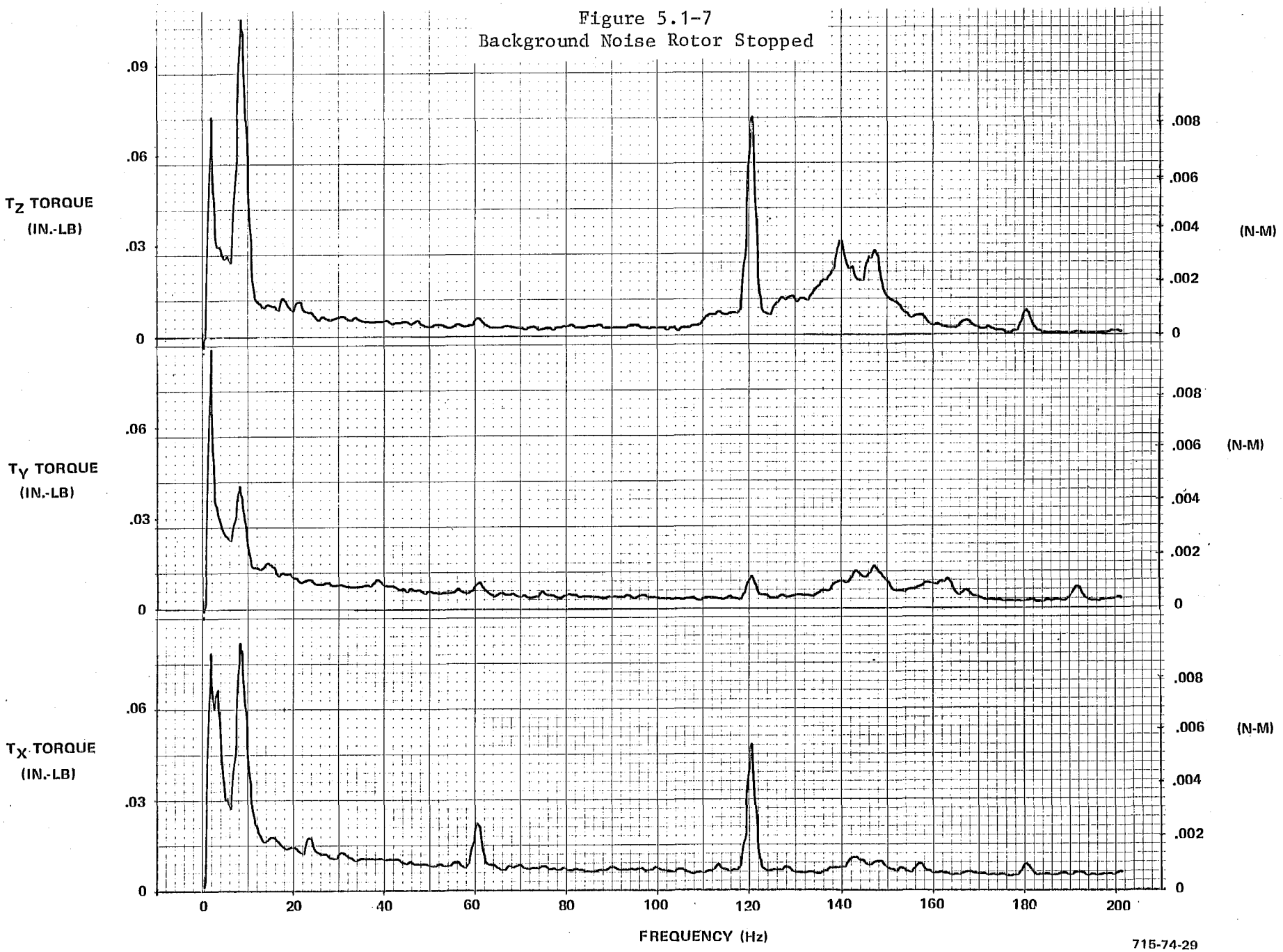

715-74-29

static loads to each of the six fixture axes and monitoring the output of the fixture electronics. Because the side axis stiffness of the fixture flexures is not entirely negligible, this initial static calibration is not correct. The static load application data is then analyzed in order to determine the proper gains to apply in each of the fixture electronic summing networks to compensate for the load sharing. These gains are then incorporated in the fixture electronics and the static loading tests repeated as a verification of results. Test results have shown this compensation technique to be very effective. The indicated side loading losses average around 3 percent on forces and 6 percent on moments with a maximum loss of 5 and 10 percent respectively. Crosstalk between axes is also typically held below these levels.

Upon completion of static calibration, the unit to be tested is mounted on the fixture for system dynamic transmissibility testing. Figures 5.1-8 and 5.1-9 show the model magnetic bearing test wheel and the Fleet Sat Com (FSC) reaction wheel mounted to the fixture. The HEAO RWA which is very similar to the FSC wheel, only slightly larger, was mounted in the same fixture for its tests. To check the system transmissibility, the unit under test is not operating and is excited with constant magnitude forces and moments over the frequency range of interest. This excitation is accomplished through the use of a small electromagnetic vibration exciter. The exciter is suspended from above on a mount of very low natural frequency so the mount does not enter into the system dynamics. A connecting rod between the exciter and the unit is cemented to the unit under test so as to allow transmission of the input force excitation. The exciter is oriented and attached such that, for force axis characterization, the input force acts through the center of gravity of the unit along the line of the axis being tested. For moment calibration, the input force is aligned to produce a moment about the axis under test. The exciter is driven by a sine wave signal which is swept through the desired frequency range at a constant sweep rate by a Spectral Dynamics SD104A-5 sweep oscillator. The output of an accelerometer mounted to the vibrating exciter is monitored and the amplitude of the sine wave varies as required to maintain a constant acceleration at the exciter. Knowing the mass of the exciter and the constant acceleration it is experiencing, the force being applied to the test unit is constant and of known magnitude. The output force or moment signal, as measured by the induced vibration fixture, is analyzed by a Spectral Dynamics SD101B dynamic analyzer which is tuned to the excitation frequency by the same sweep oscillator that drives the exciter. The resultant filtered signal is

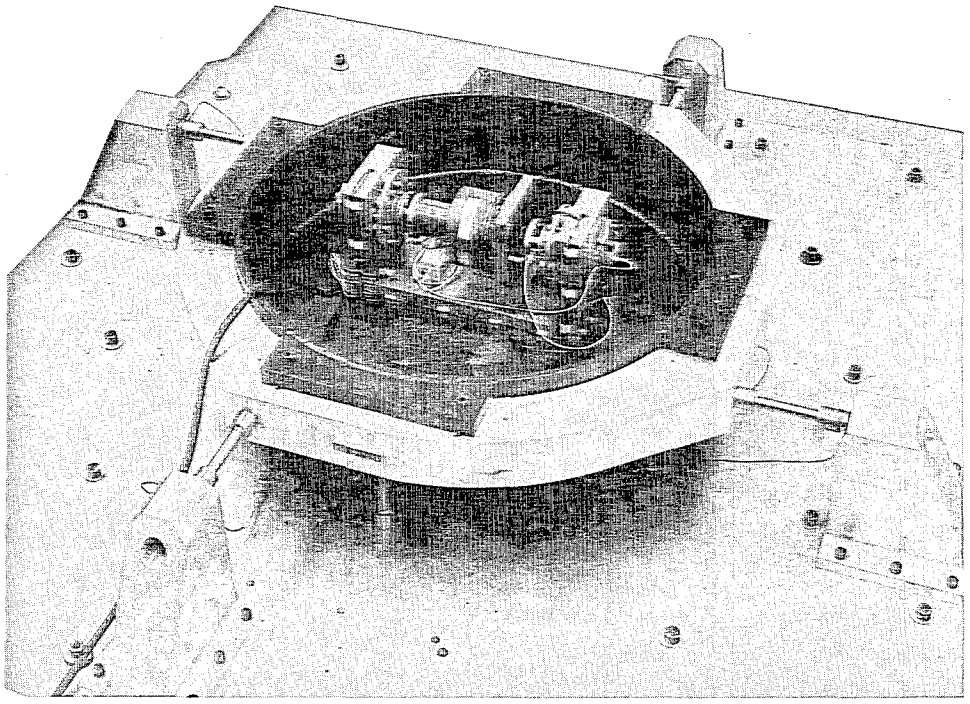

Figure 5.1-8
Magnetic Bearing Test Rotor on Induced Vibration Fixture

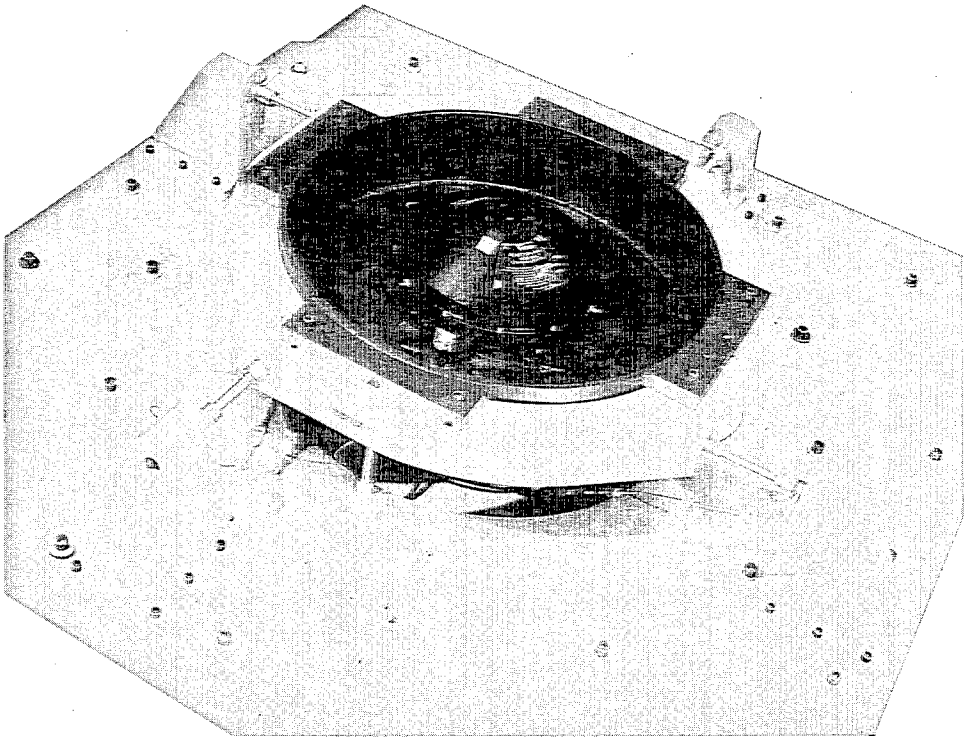

Figure 5.1-9
Fleet Sat Com Reaction Wheel on Induced Vibration Fixture

recorded on an X-Y plotter. Figures 5.2-1 and 5.2-2, respectively, illustrate typical force and moment axis characterization test output plots. Each of the six axes is analyzed for each of the axis excitation tests, so the response of three axes is normally shown on each of the plots. In the region where the system has a transmissibility of one, the measured output force is level and of the same magnitude as the input. As resonant frequencies of the mechanical system (the combination of the fixture and unit under test) are approached, the transmissibility builds and then peaks at the resonant frequencies. This series of tests provides the information required to analyze the actual force and moment excitations recorded from an operating reaction wheel at each particular excitation frequency.

Figure 5.2-3 shows the Model Magnetic Bearing Wheel being calibrated.

5.2 FSC TEST RESULTS

The 45 tests performed on the Fleet Sat Com MWA on the hard mount vibration fixture are listed in Table 5.2-1. The principal curves necessary to show the vibration signatures of the MWA are included and discussed in this section.

Calibration - Figures 5.2-1, 5.2-2 and 5.2-4 show some typical dynamic calibration runs. A freely suspended .25 pound force exciter (Ling, Model 203) was used to input sinusoidal forces and moments into the MWA case when mounted within the emitted vibration fixture. The response of the test fixture's three forces and three moments were recorded.

Figure 5.2-1 shows the three-axis force responses for an F_z axis force input. Note that over the frequency range of interest (20 to 100 Hz) the F_z force is nearly constant at .25 pound and no cross coupling is evident in the other two axes. At 123 Hz a small response is seen due to the FSC rotor web resonance, and above 150 Hz the vibration fixture resonances show up.

The torque responses, Figures 5.2-2 and 5.2-4, show a similar response with the 123 Hz web resonance more pronounced.

Figure 5.2-1
FLTSATCOM
Emitted Vibration
Fixture Calibration
F_Z Input = .25 lbf
Speed = 0 RPM

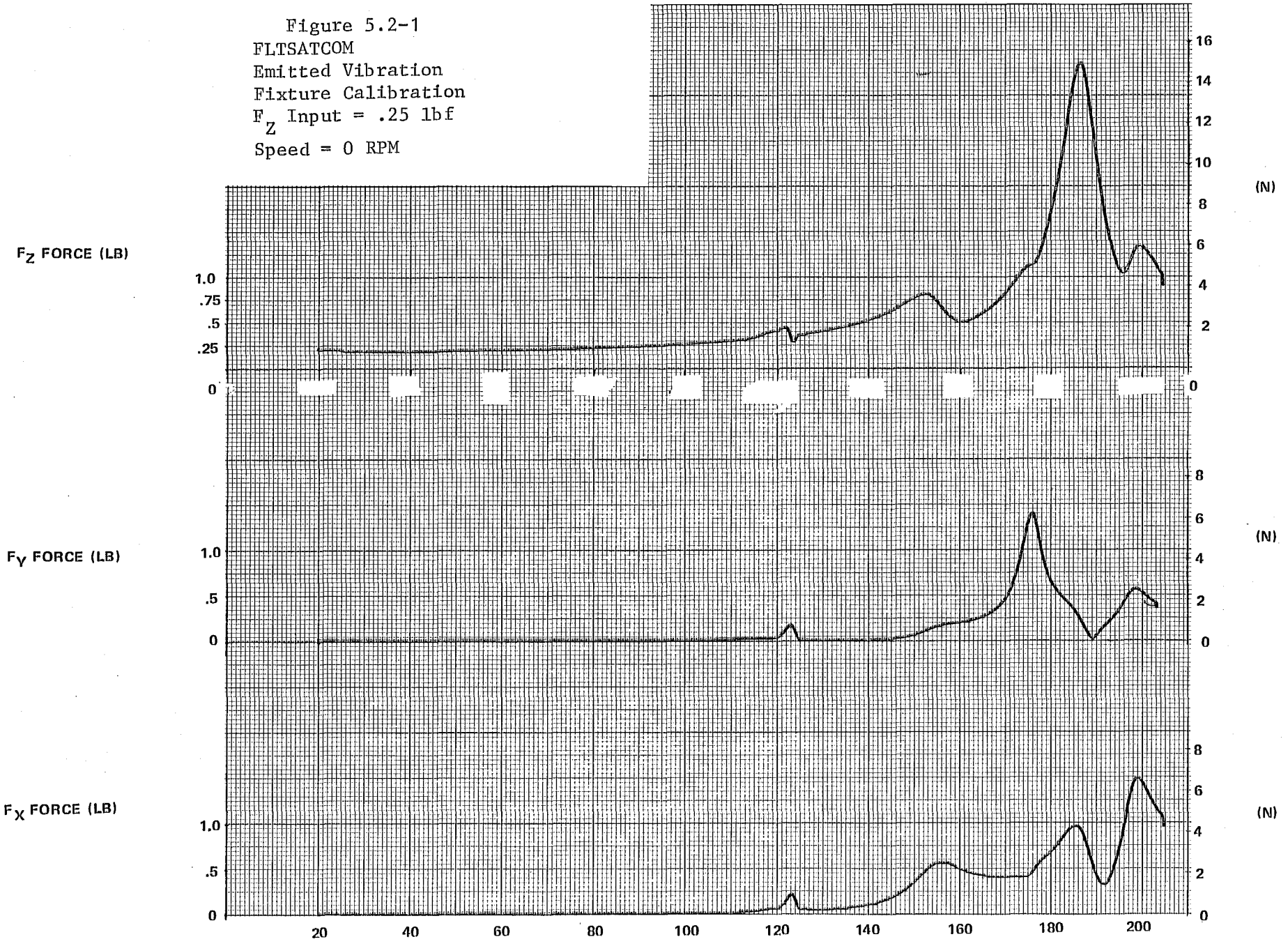

715-74-32

Figure 5.2-2
FLTSATCOM
Emitted Vibration
Fixture Calibration
T_X Input = 1 in.-lbf
Speed = 0 RPM

715-74-33

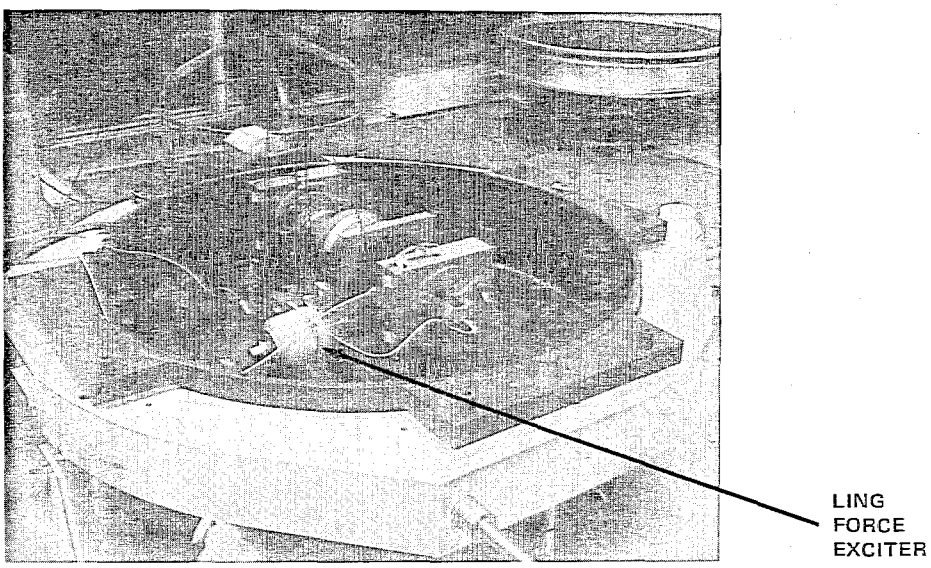

Figure 5.2-3
Model Magnetic Bearing Dynamic Calibration

Figure 5.2-4
FLTSATCOM
Emitted Vibration
Fixture Calibration
T_Z Input = 1 in.-lbf
Speed = 0 RPM

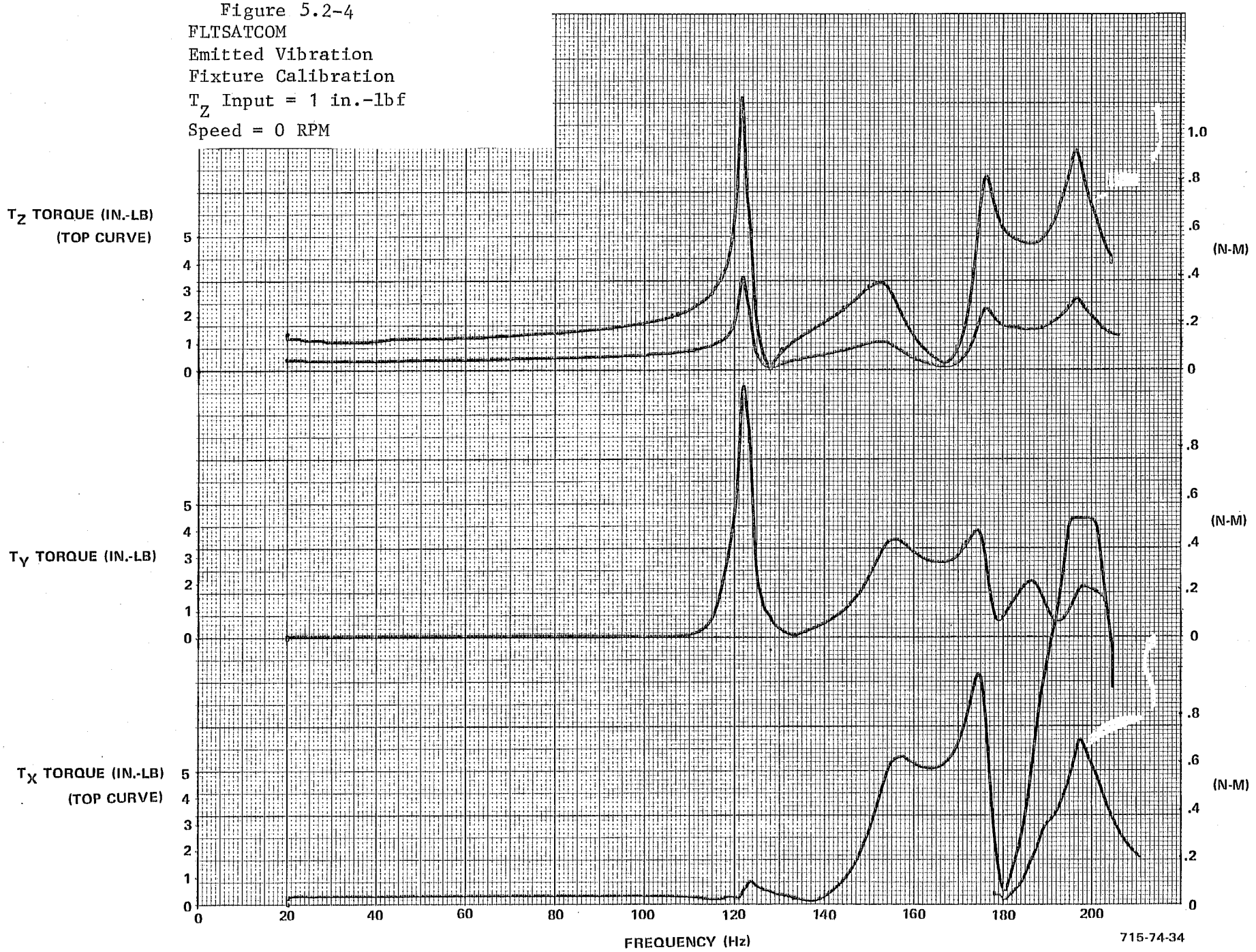

Peak Hold Runup - Figures 5.2-5 through 5.2-7 show some typical wheel runup response envelopes. These curves were obtained by using the peak hold mode of a Spectral Dynamics SD330 Real Time Analyzer with a 1.2-Hz bandwidth (1.25 second memory cycle). In this mode, the time signature is sampled every memory cycle, analyzed with a Fast Fourier Transform technique, and the amplitude at each frequency compared to that of the previous sample - the larger or peak of the two values at each frequency is retained and held for the next comparison. In this manner, the highest value seen during a runup at each frequency is maintained and the curve represents an envelope of the peak forces and torques.

Figure 5.2-5 shows the three forces transmitted. A dotted curve of radial (F_y or F_z) force corresponding to .001 ounce-inch static unbalance is plotted and matches the data reasonably over the speed (0 to 83.3 Hz) range. A peak at 34 Hz possibly due to the bearing retainer, and a peak at 74 Hz due to the gyroscopic effect of axial runout (discussed in the appendix) can be seen. This peak at 74 Hz is characteristic of the ball bearing momentum and reaction wheels and is present in both the FSC and HEAO RWA, although it occurs at a lower frequency in the HEAO wheel. Note that the force along the spin axis is the largest at .34 pound, compared to radial forces of approximately .1 pound.

Figure 5.2-6 shows the radial, T_y, and axial, T_x, torques emitted during runup. Approximately equal amplitude 74 Hz peaks of 1.1 inch-pound occur in the radial and axial direction.

Tracking Filter Runup - Figures 5.2-7 through 5.2-10 show some typical responses from the FSC MWA when a tracking filter is used. A Spectral Dynamics SD101B Dynamic Analyzer with a 1.5-Hz bandwidth filter was used, and the filter's center frequency was maintained at a frequency corresponding to wheel speed. Therefore, only the frequency components at wheel speed were recorded as the wheel ran up. This has the effect of showing mainly the unbalance components and gyroscopic resonance and filtering out the harmonics of wheel speed. The frequency range of the curves is 0 to 83.3 Hz, corresponding to 0 to 5000 rpm.

Figures 5.2-7 and 5.2-8 show peak axial and radial 74-Hz forces of .4 pound and .14 pounds respectively.

Figures 5.2-9 and 5.2-10 show peak axial and radial torques of 1.4 inch-pounds.

Figure 5.2-5
FLTSATCOM
Emitted Vibration
Runup
Peak Hold
Speed = 0-5000 RPM

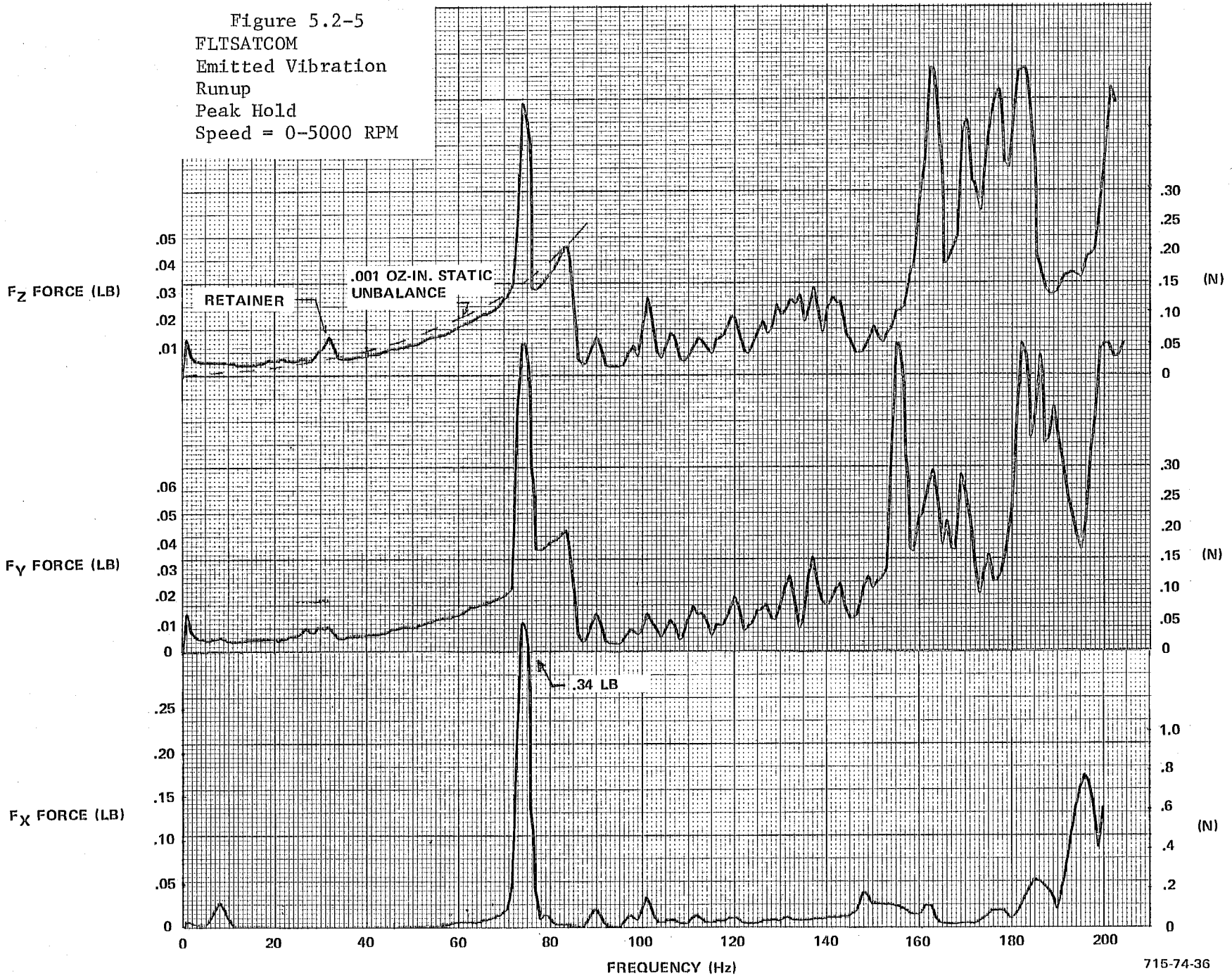

715-74-36

Figure 5.2-6
FLTSATCOM
Emitted Vibration
Runup
Peak Hold
Speed = 0-5000 RPM

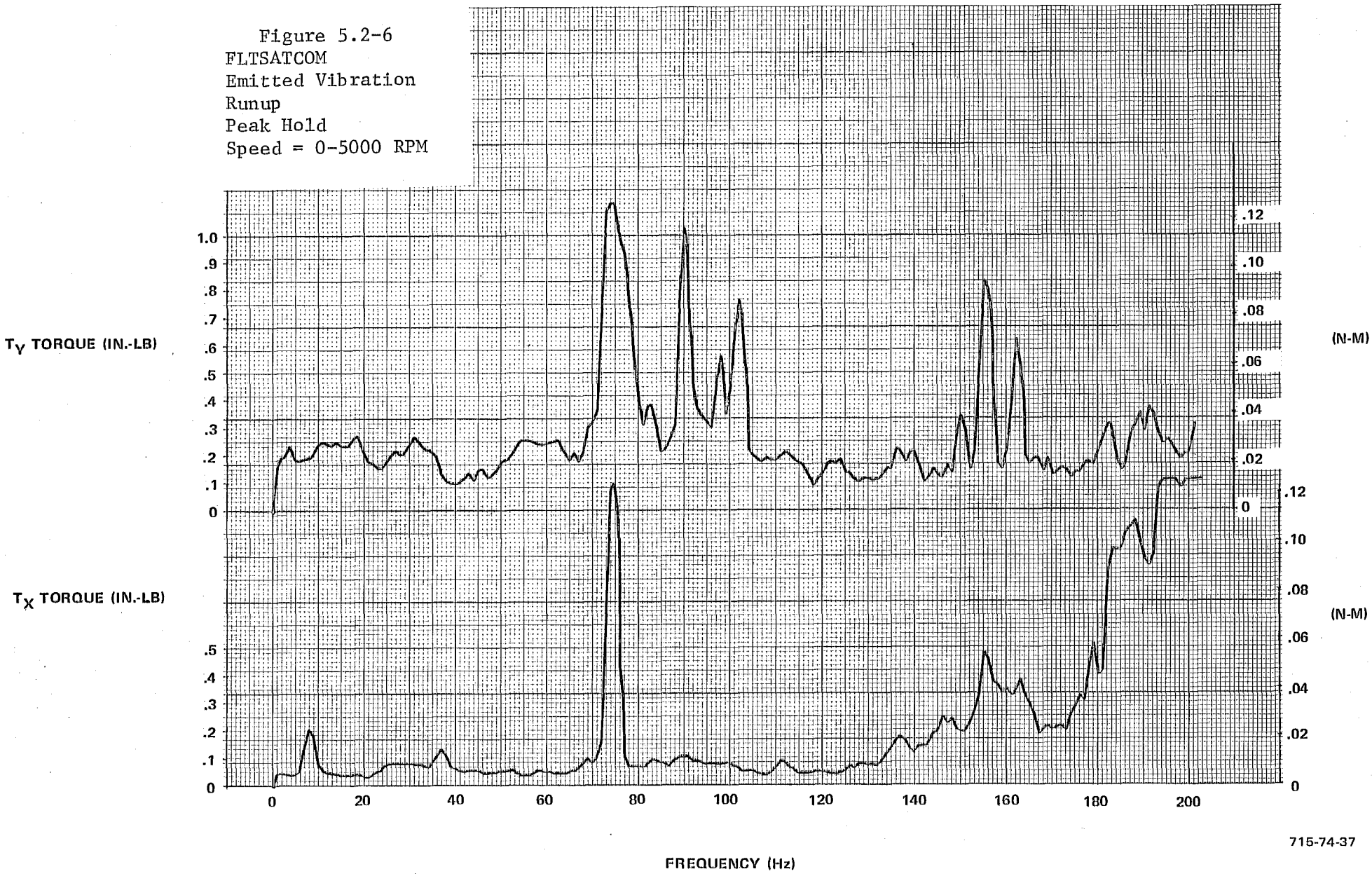

715-74-37

Figure 5.2-7
FLTSATCOM
Emitted Vibration
Runup
Tracking Filter
Speed = 0-5000 RPM

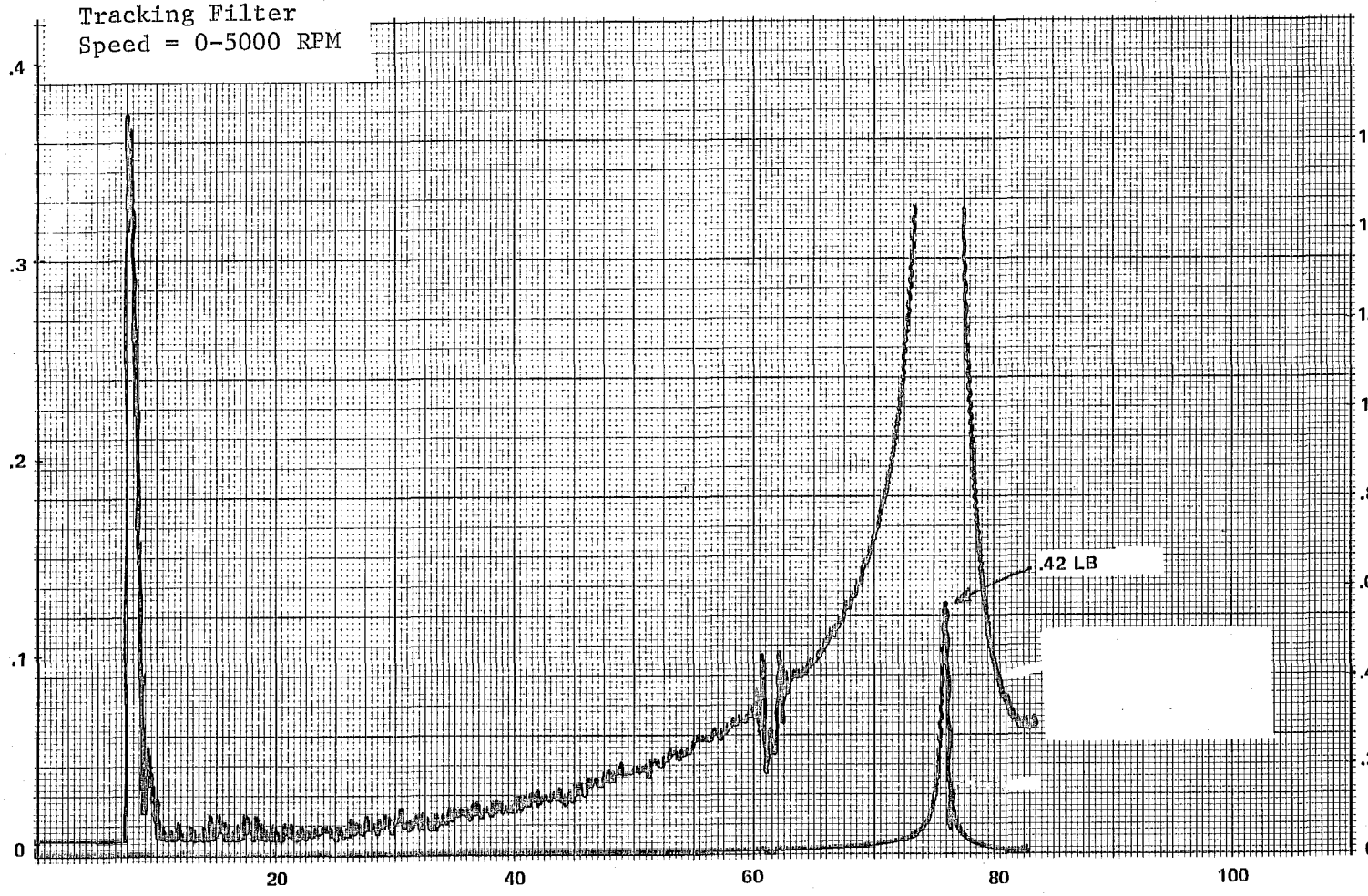

F_X FORCE (LB)
(TOP CURVE)

(N)

FREQUENCY (Hz)

715-74-38

Figure 5.2-8
FLTSATCOM
Emitted Vibration
Runup
Tracking Filter
Speed = 0-5000 RPM

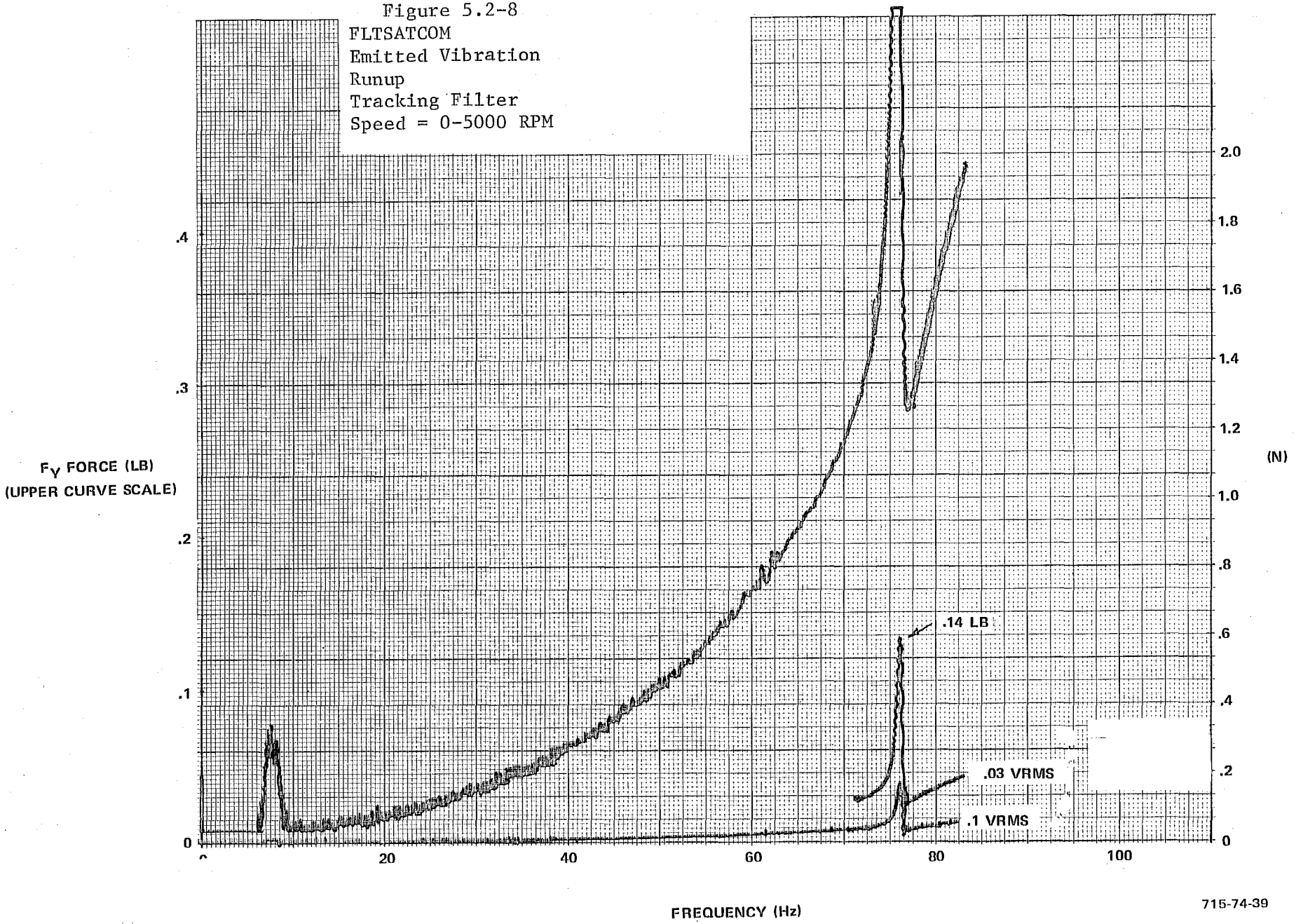

715-74-39

Figure 5.2-9
FLTSATCOM
Emitted Vibration
Runup
Tracking Filter
Speed = 0-5000 RPM

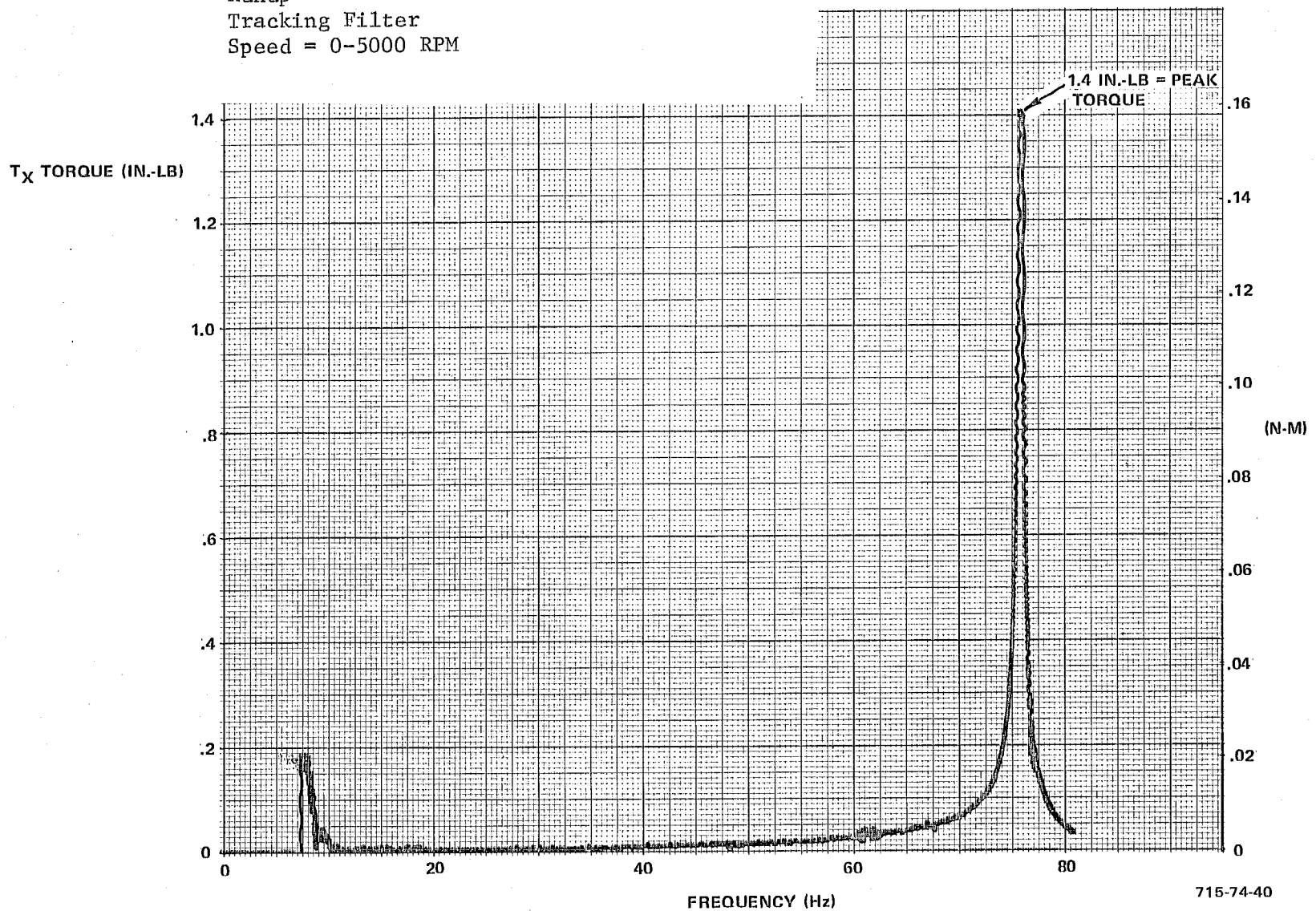

Figure 5.2-10
FLTSATCOM
Emitted Vibration
Runup
Tracking Filter
Speed = 0-5000 RPM

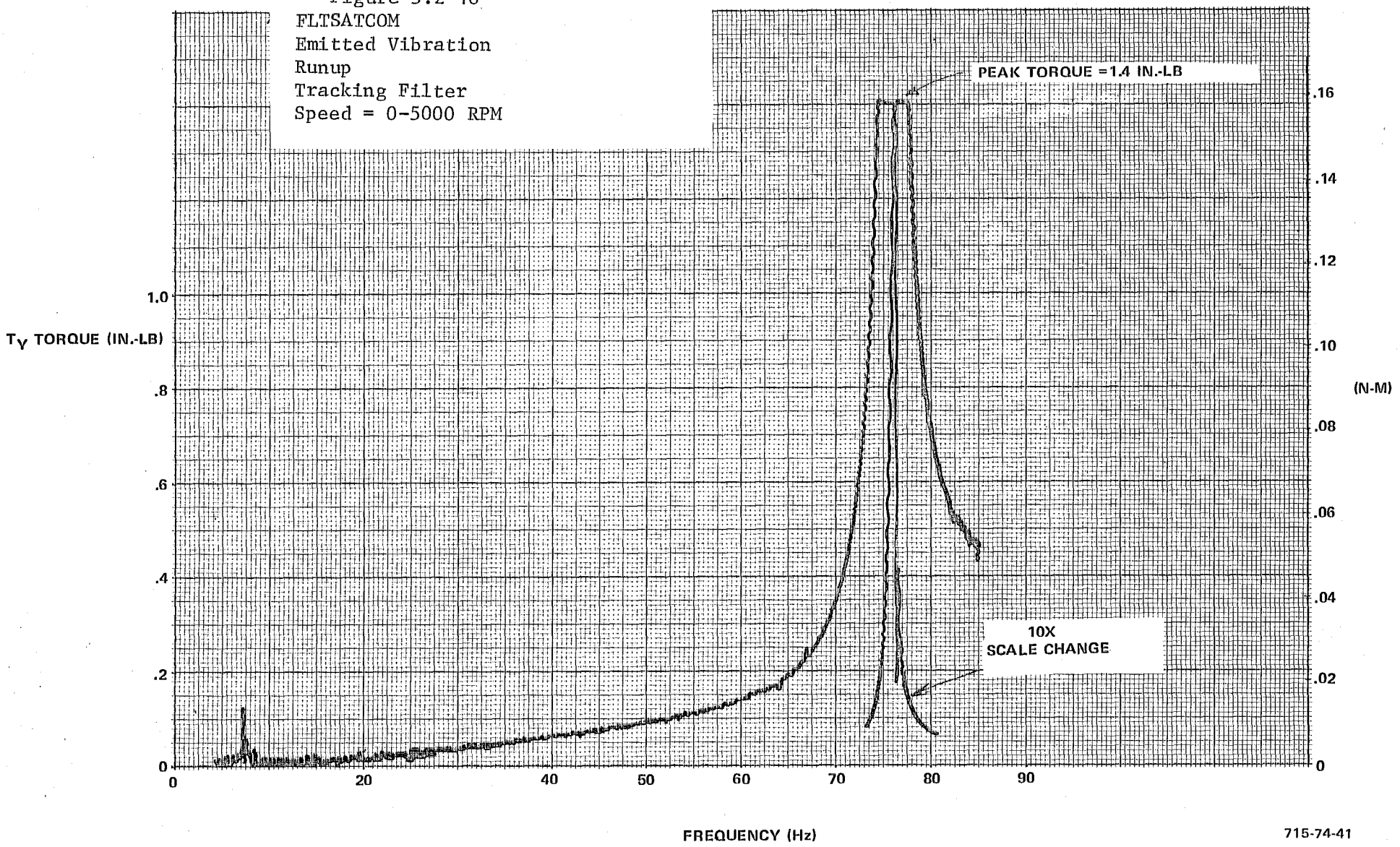

715-74-41

TABLE 5.2-1

FLEET SAT COM TESTS

Run No.	Response Axis						Rotor Speed (rpm)	Type of Run
	F_x	F_y	F_z	T_x	T_y	T_z		
1	X	X	X				0	Fixture Calibration, F_x input
2				X	X	X	0	Fixture Calibration, F_x input
3	X	X	X				0	Fixture Calibration, F_y input
4				X	X	X	0	Fixture Calibration, F_y input
*5	X	X	X				0	Fixture Calibration, F_z input
6				X	X	X	0	Fixture Calibration, F_z input
*7				X	X	X	0	Fixture Calibration, T_x input
8	X	X	X				0	Fixture Calibration, T_x input
9				X	X	X	0	Fixture Calibration, T_y input
10	X	X	X				0	Fixture Calibration, T_y input
*11				X	X	X	0	Fixture Calibration, T_z input
12	X	X	X				0	Fixture Calibration, T_z input
13	X	X	X				1000	Constant Speed (1 minute peak hold)
14				X	X	X	1000	Constant Speed (1 minute peak hold)
*15	X	X	X				1500	Constant Speed (1 minute peak hold)
*16				X	X	X	1500	Constant Speed (1 minute peak hold)
17	X	X	X				2000	Constant Speed (1 minute peak hold)
18				X	X	X	2000	Constant Speed (1 minute peak hold)
19	X	X	X				2500	Constant Speed (1 minute peak hold)
20				X	X	X	2500	Constant Speed (1 minute peak hold)
*21	X	X	X				3000	Constant Speed (1 minute peak hold)
*22				X	X	X	3000	Constant Speed (1 minute peak hold)
23	X	X	X				3500	Constant Speed (1 minute peak hold)
24				X	X	X	3500	Constant Speed (1 minute peak hold)
25	X	X	X				4000	Constant Speed (1 minute peak hold)
26				X	X	X	4000	Constant Speed (1 minute peak hold)
27	X	X	X				4500	Constant Speed (1 minute peak hold)
28				X	X	X	4500	Constant Speed (1 minute peak hold)
*29	X	X	X				5000	Constant Speed (1 minute peak hold)

* = Denotes that run data is included in this report.

TABLE 5.2-1 (cont)

FLEET SAT COM TESTS

Run No.	Response Axis						Rotor Speed (rpm)	Type of Run
	F_x	F_y	F_z	T_x	T_y	T_z		
*30				X	X	X	5000	Constant Speed (1 minute peak hold)
*31	X	X	X				0-5000	Runup, peak hold
32	X						0-5000	Runup, peak hold
*33		X	X				0-5000	Runup, peak hold
*34				X	X		0-5000	Runup, peak hold
35	X	X	X				5000-1500	Coastdown, peak hold
36				X	X	X	5000-1500	Coastdown, peak hold
37		X	X				5000-0	Power down, peak hold
38	X	X					5000-0	Power down, peak hold
39				X	X	X	5000-0	Power down, peak hold
*40				X			0-5000	Runup, Tracking Filter
*41					X		0-5000	Runup, Tracking Filter
42						X	0-5000	Runup, Tracking Filter
*43	X						0-5000	Runup, Tracking Filter
*44		X					0-5000	Runup, Tracking Filter
45			X				0-5000	Runup, Tracking Filter

Constant Speed - Figures 5.2-11 through 5.2-16 show typical constant speed signatures for the FSC forces and torques. These runs are taken by maintaining the wheel at a constant speed for 1 minute and taking data with the Spectral Dynamics Real Time Analyzer, Model SD330, in the peak hold mode. Curves for 1500, 3000, and 5000 rpm are included in this report.

Figure 5.2-15 shows the three emitted forces at a constant speed of 5000 rpm. A low frequency 8-Hz resonance is present due to the isolated pad fundamental isolation frequency. At 32 Hz in the F_y and F_z radial axis the 101H bearing retainer force can be seen. The rotor static unbalance is present in both radial axes at 83.3 Hz. Beyond 140 Hz, higher order test fixture resonant frequencies are present and the data is not valid in this region.

Figure 5.2-11
FLTSATCOM
Emitted Vibration
Constant Speed
1 Min Peak Hold
Speed = 1500 RPM

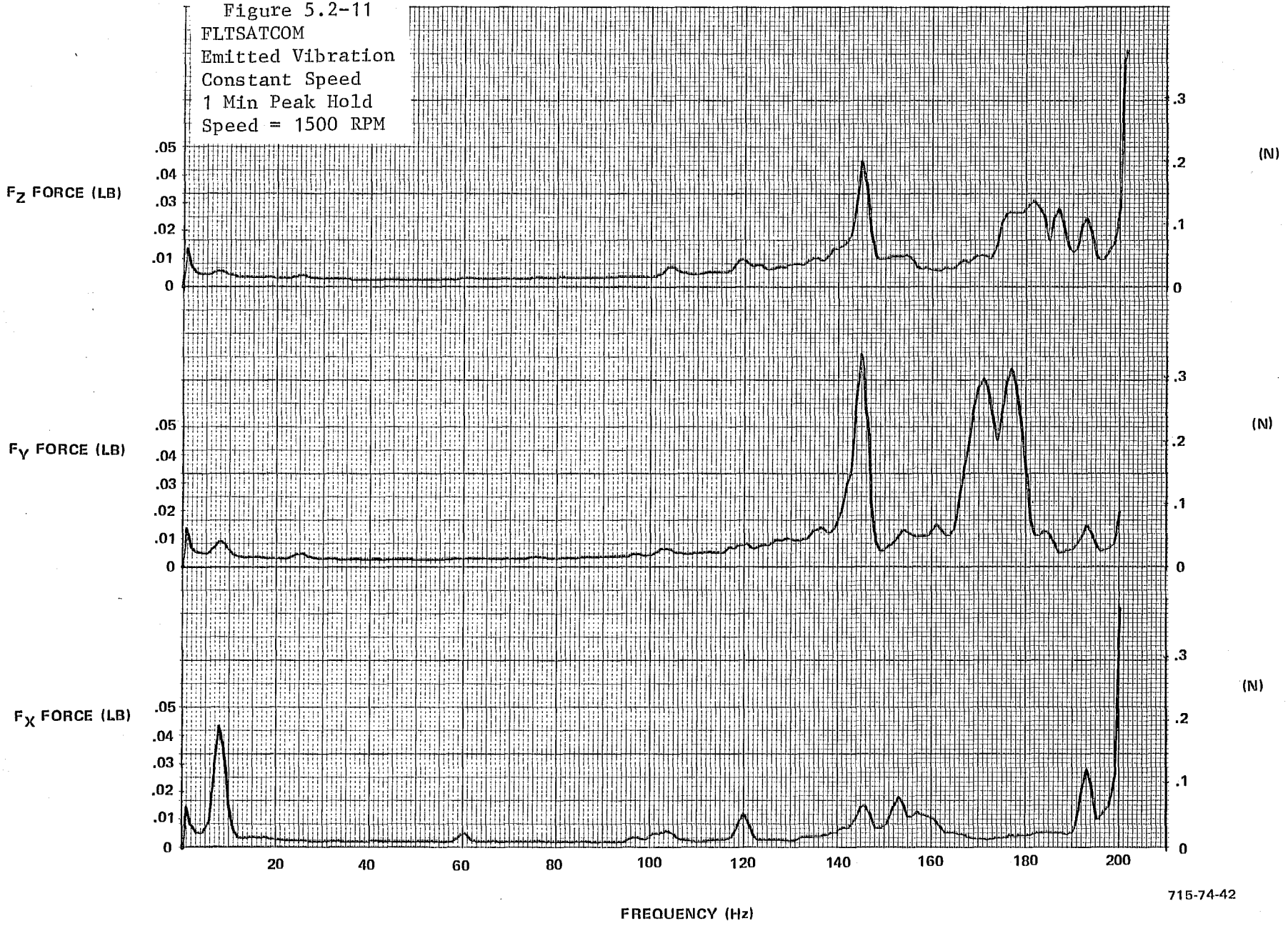

Figure 5.2-12
FLTSATCOM
Emitted Vibration
Constant Speed
1 Min Peak Hold
Speed = 1500 RPM

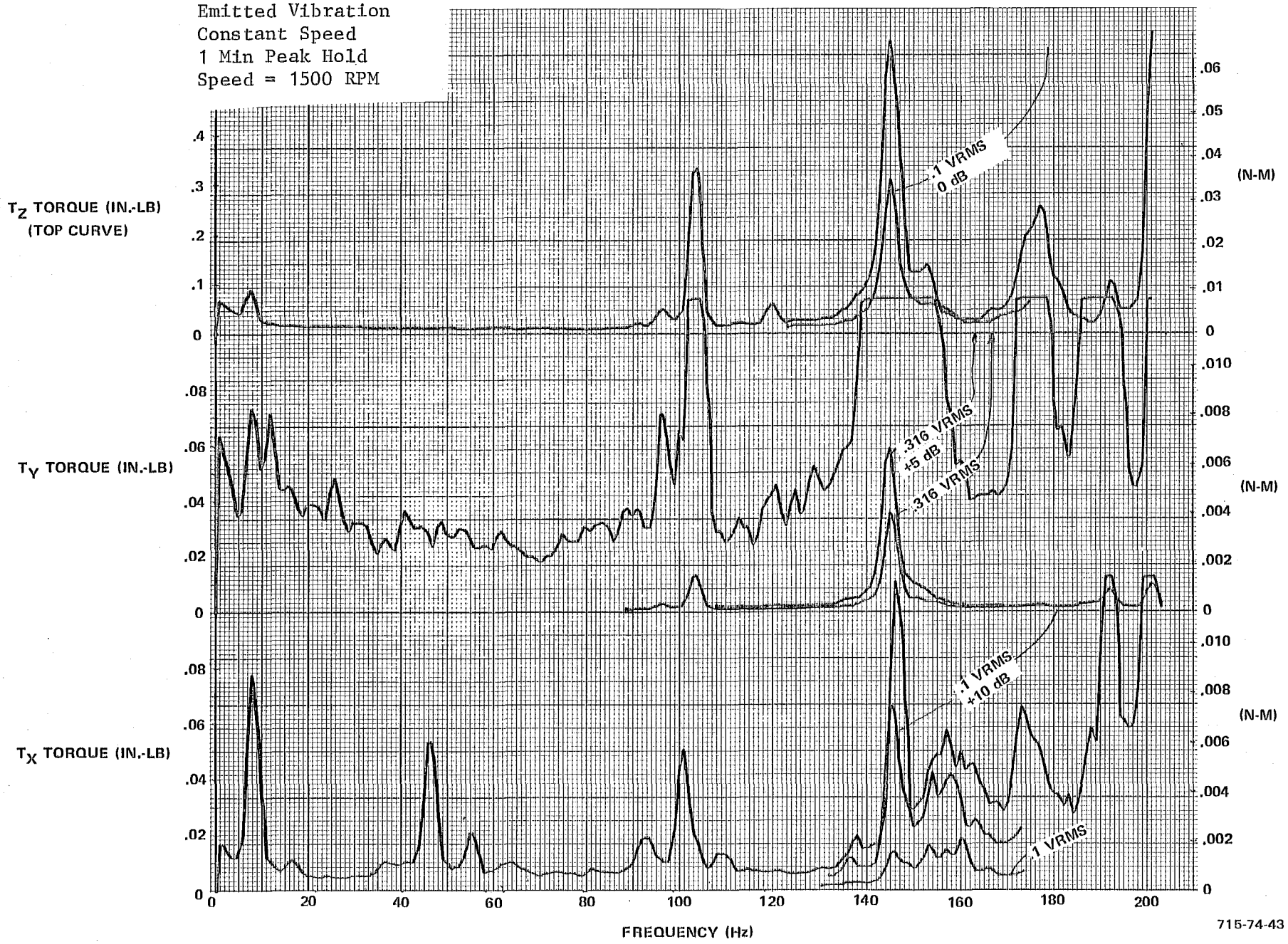

Figure 5.2-13
FLTSATCOM
Emitted Vibration
Constant Speed
1 Min Peak Hold
Speed = 3000 RPM

Figure 5.2-14
FLTSATCOM
Emitted Vibration
Constant Speed
1 Min Peak Hold
Speed = 3000 RPM

715-74-45

Figure 5.2-15
FLTSATCOM
Emitted Vibration
Constant Speed
1 Min Peak Hold
Speed = 5000 RPM

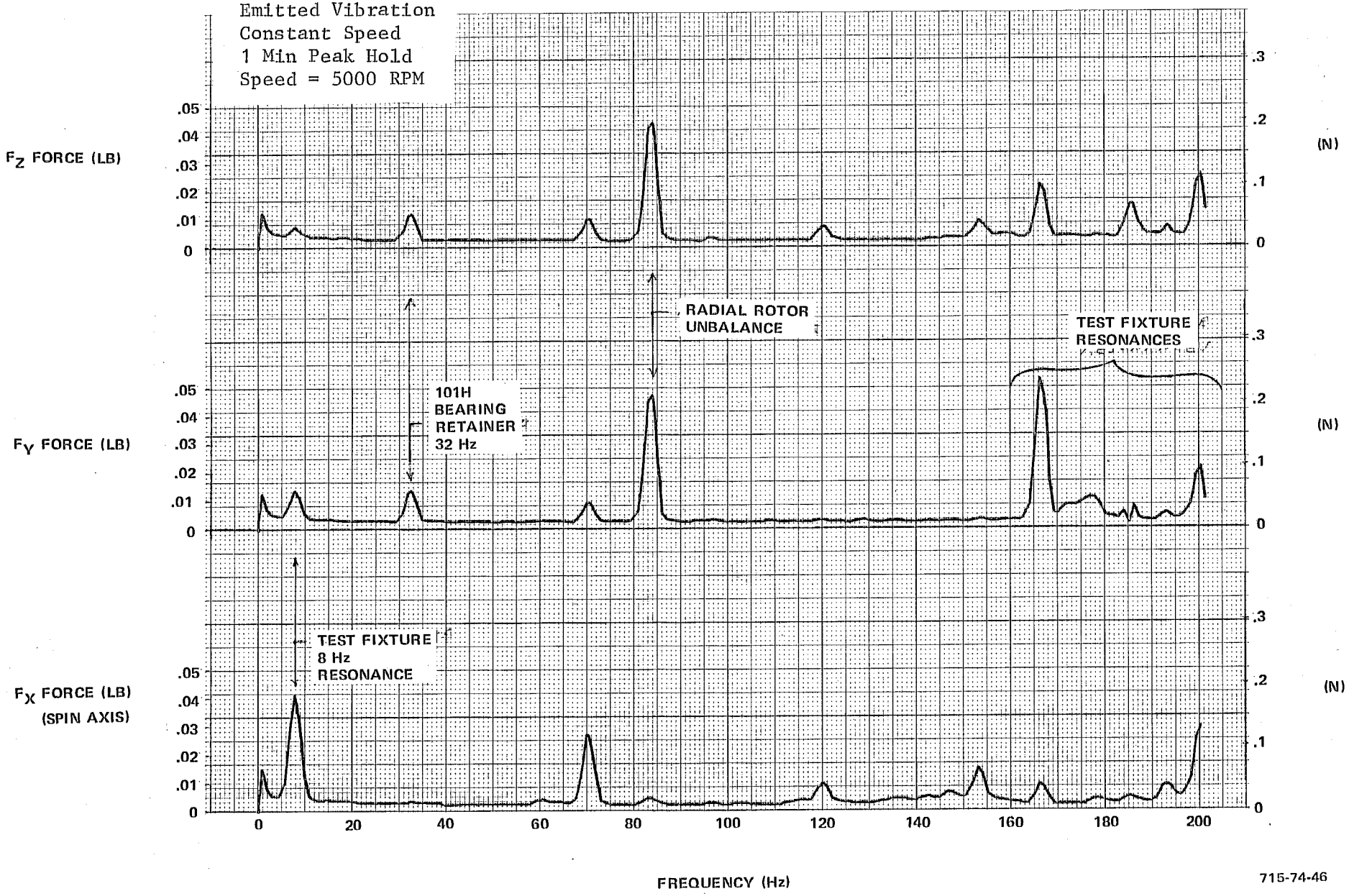

715-74-46

Figure 5.2-16
FLTSATCOM
Emitted Vibration
Constant Speed
1 Min Peak Hold
Speed = 5000 RPM

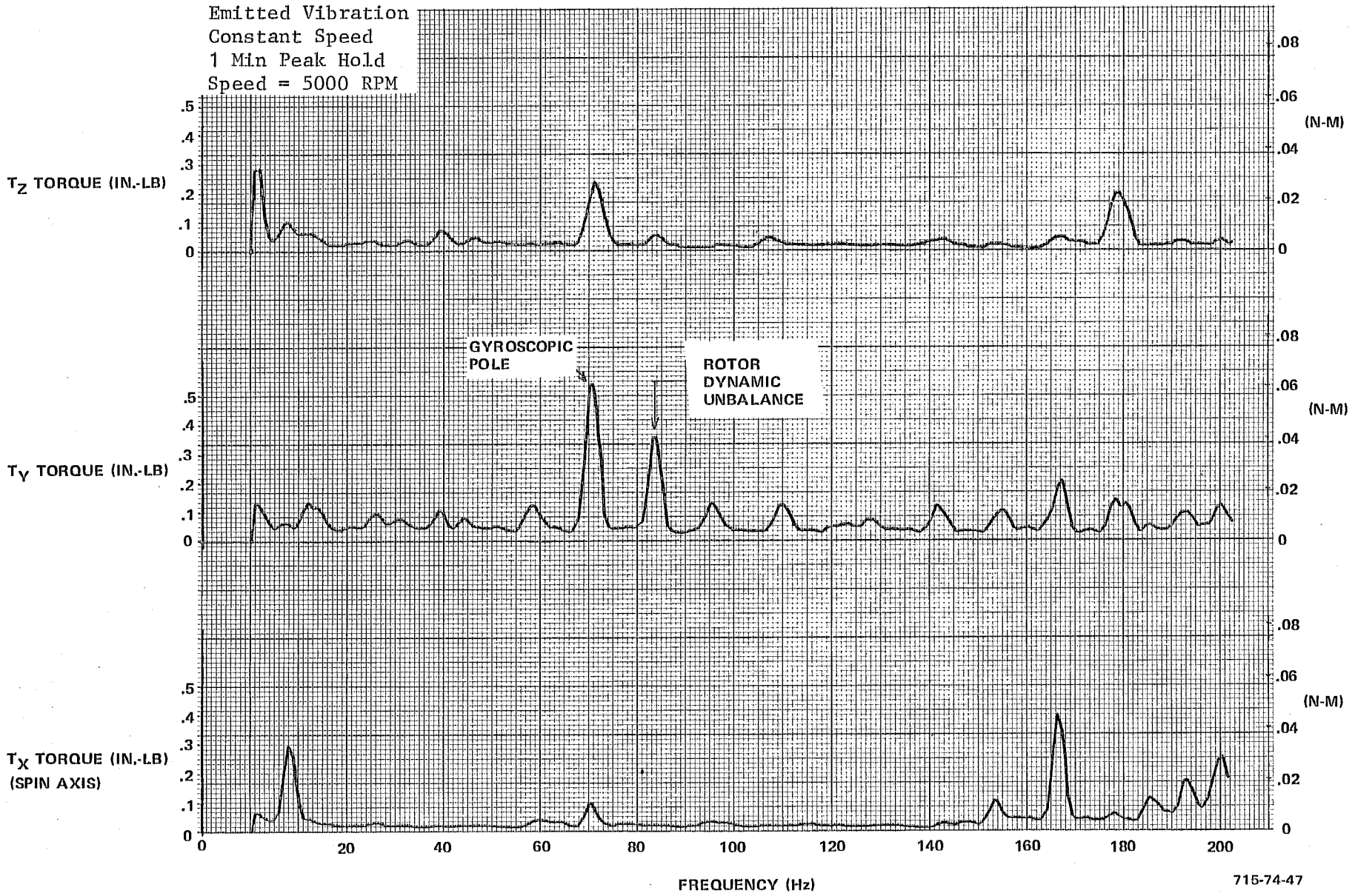

Figure 5.2-16 shows the three emitted torques at a constant speed of 5000 rpm. The largest torque is at 72 Hz and is .55 inch-pound.

Note in Figure 5.2-13 and 5.2-14 that no significant harmonic of the fundamental 50-Hz frequency exists at 100 Hz.

5.3 HEAO TEST RESULTS

The 47 tests performed on the HEAO RWA on the hard mount vibration fixture are listed in Table 5.3-1. The data which shows the principal vibration signatures of the RWA are included and discussed in this section. The HEAO tests were restricted to a maximum speed of 3000 rpm since this was the maximum speed considered to be used by an LST RWA at the time the testing was performed.

Calibration - Figures 5.3-1 and 5.3-2 show some typical dynamic calibration data. A freely suspended .25-pound force exciter was used, the same as described in Paragraph 5.2.

Figure 5.3-1 shows the three-axis force responses for an F_z axis force input. Note that little cross coupling exists over the 10-to-100 Hz frequency range of interest and the F_z force is approximately constant at .25 pound. At 66 Hz the rotor web resonance can be seen in the F_z axis response. This effect can be better seen in the T_y axis response of Figure 5.3-2. Another peak at 46 Hz can be seen in the T_x axis, but this may be caused by the rotor being free to rotate about its axis within the housing.

Peak Hold Runup - Figures 5.3-3 through 5.3-6 show some typical HEAO RWA runup response envelopes. These curves were obtained using the same technique described in Paragraph 5.2. The frequency range of 0 to 100 Hz was recorded with a .6-Hz bandwidth (2.5 second memory cycle).

Figures 5.3-3 and 5.3-4 show the axial and radial forces transmitted from the RWA during a rundown from 3000 to 0 rpm. Runup responses look very similar and are not included. Both curves show a 38-Hz resonance which is due to the gyroscopic effect of axial runout. The axial force of .09 pound slightly exceeds the radial force of .07 pound at this frequency. Figure 5.3-4 shows a static unbalance of .0056 ounce-inch and a dashed curve corresponding to this unbalance matches the data closely. Higher frequency content is present in the 70- to 90-Hz region, but is unexplained with the existing limited complexity RWA models.

Figure 5.3-1
HEAO RWA Tests
Emitted Vibration
Fixture Calibration
F_Z Input = .25 LBF
Speed = 0 RPM

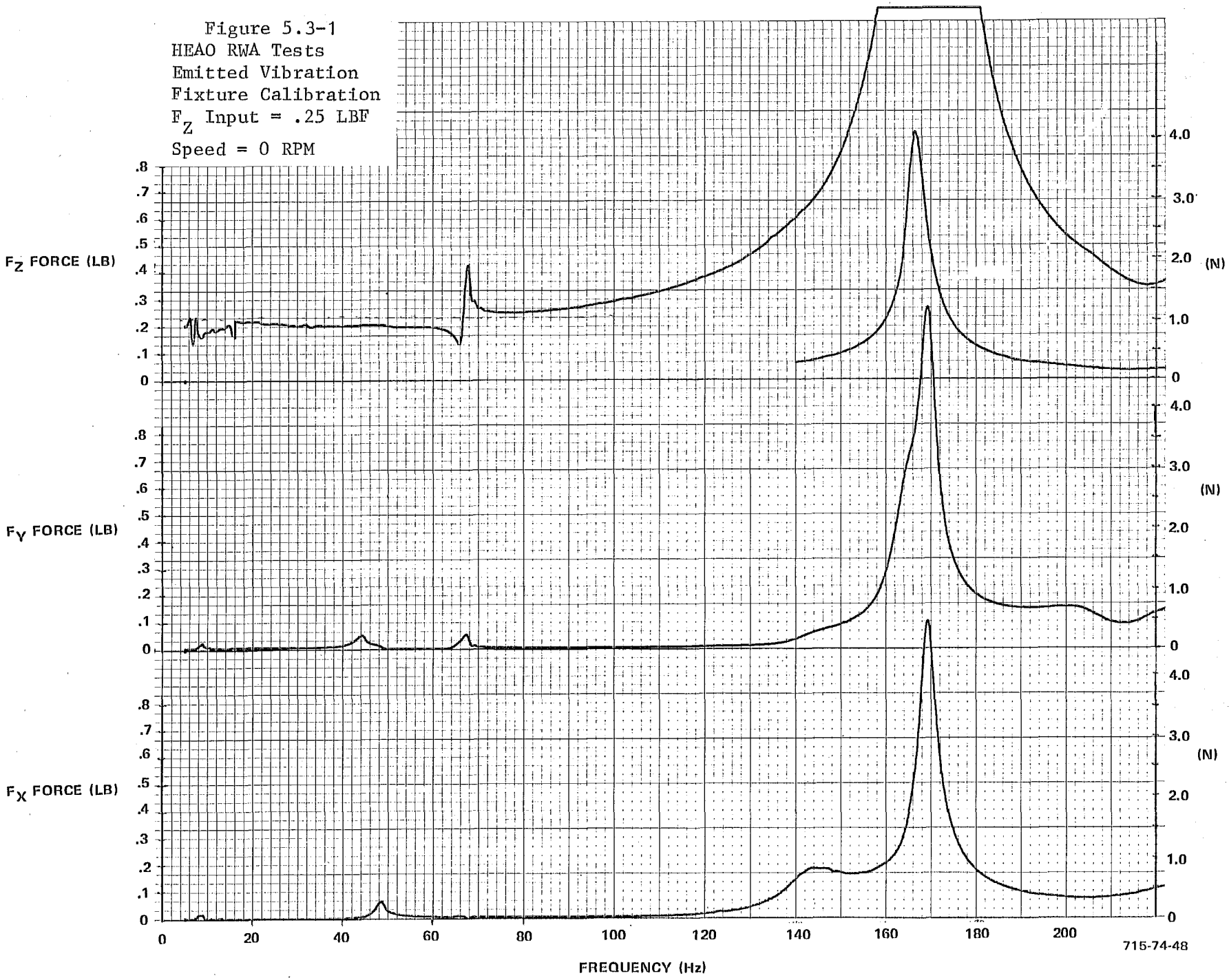

Figure 5.3-2
HEAO RWA Tests
Emitted Vibration
Fixture Calibration
F_Y Input = .25 LBF
Speed = 0 RPM

Figure 5.3-3
HEAO RWA Tests
Emitted Vibration
Power Down
Peak Hold
Speed = 3000-0 RPM

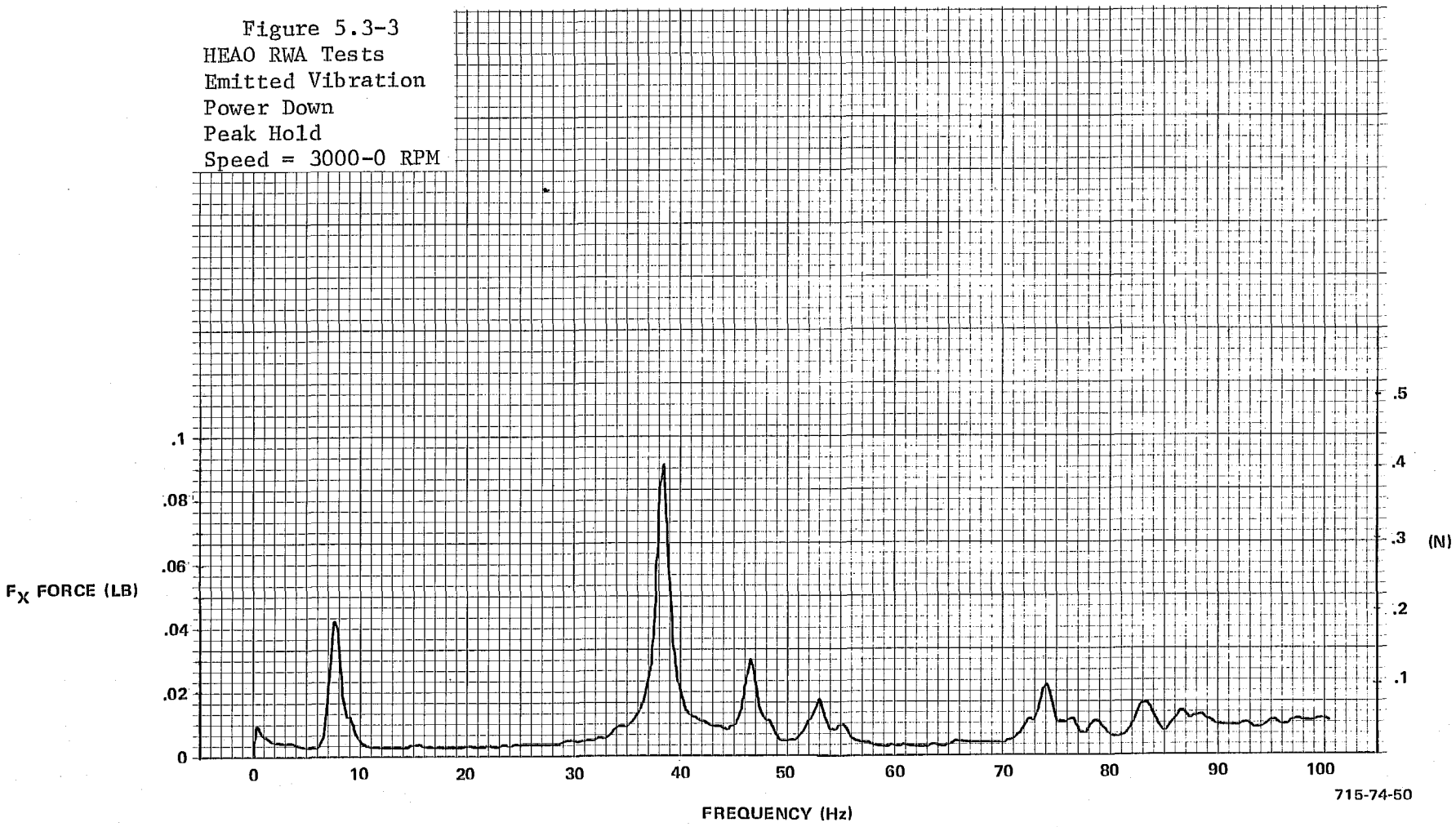

Figure 5.3-4
HEAO RWA Tests
Emitted Vibration
Power Down
Peak Hold
Speed = 3000-0 RPM

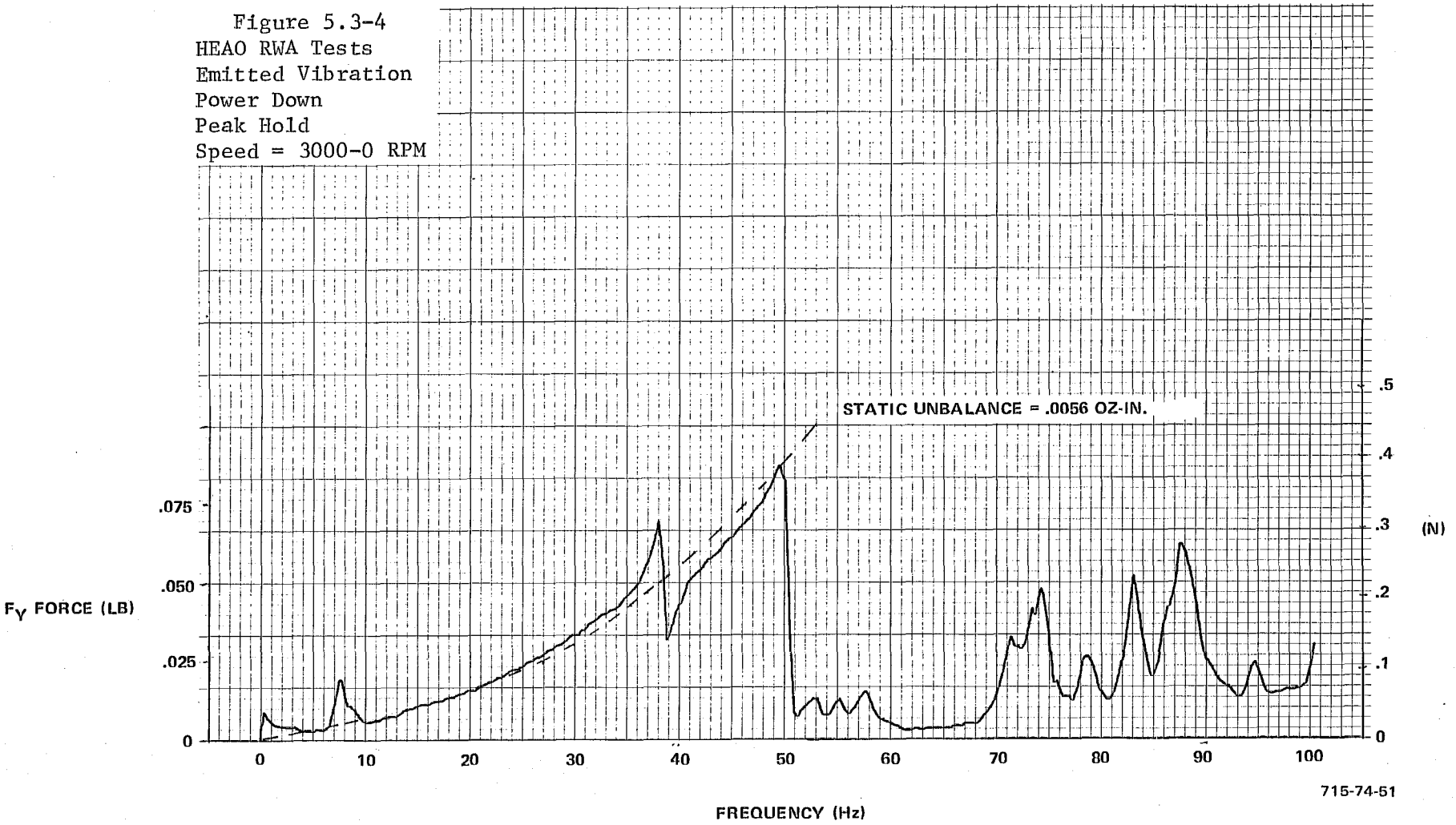

Figure 5.3-5
HEAO RWA Tests
Emitted Vibration
Runup
Peak Hold
Speed = 0-3000 RPM

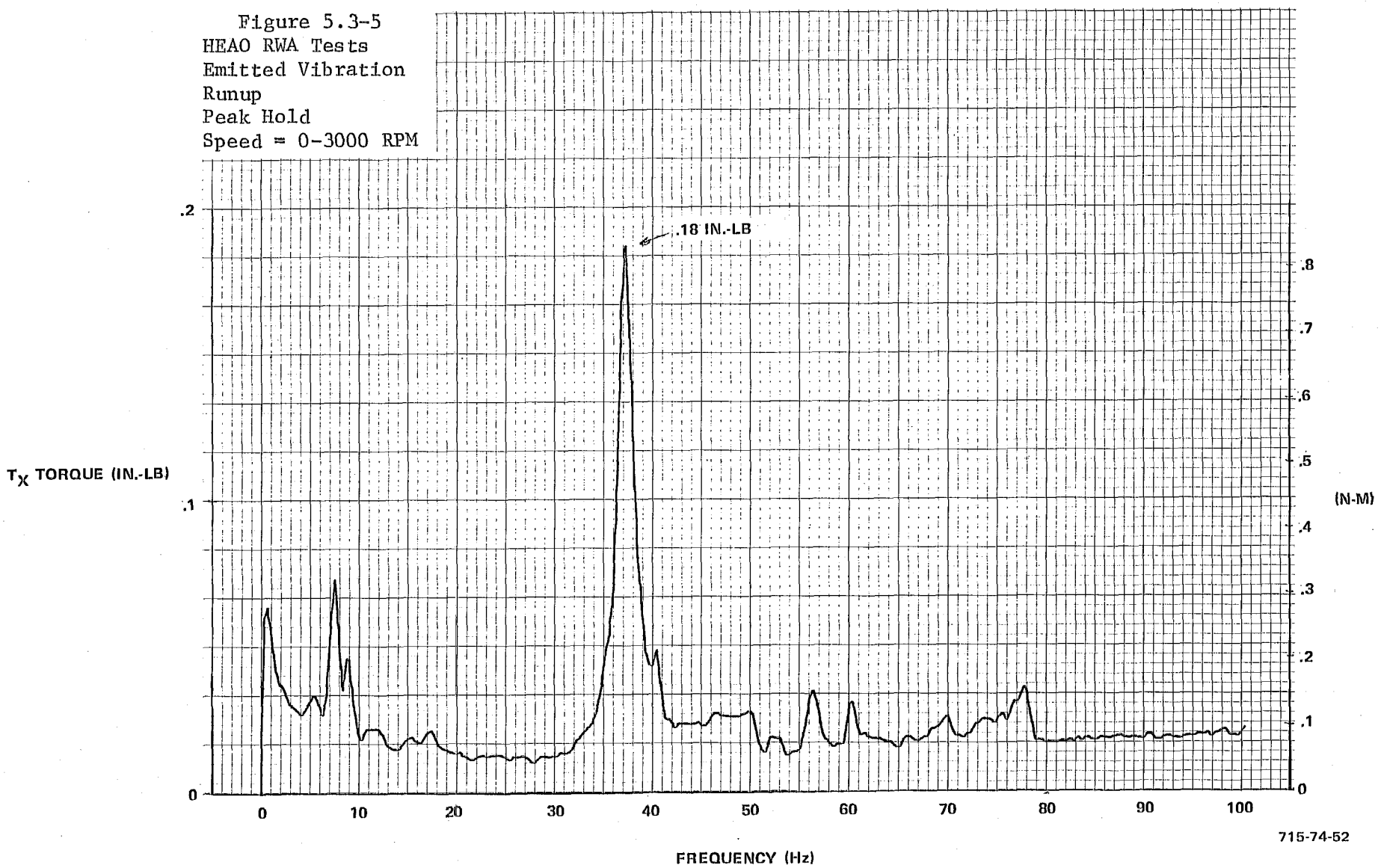

Figure 5.3-6
HEAO RWA Tests
Emitted Vibration
Runup
Peak Hold
Speed = 0-3000 RPM

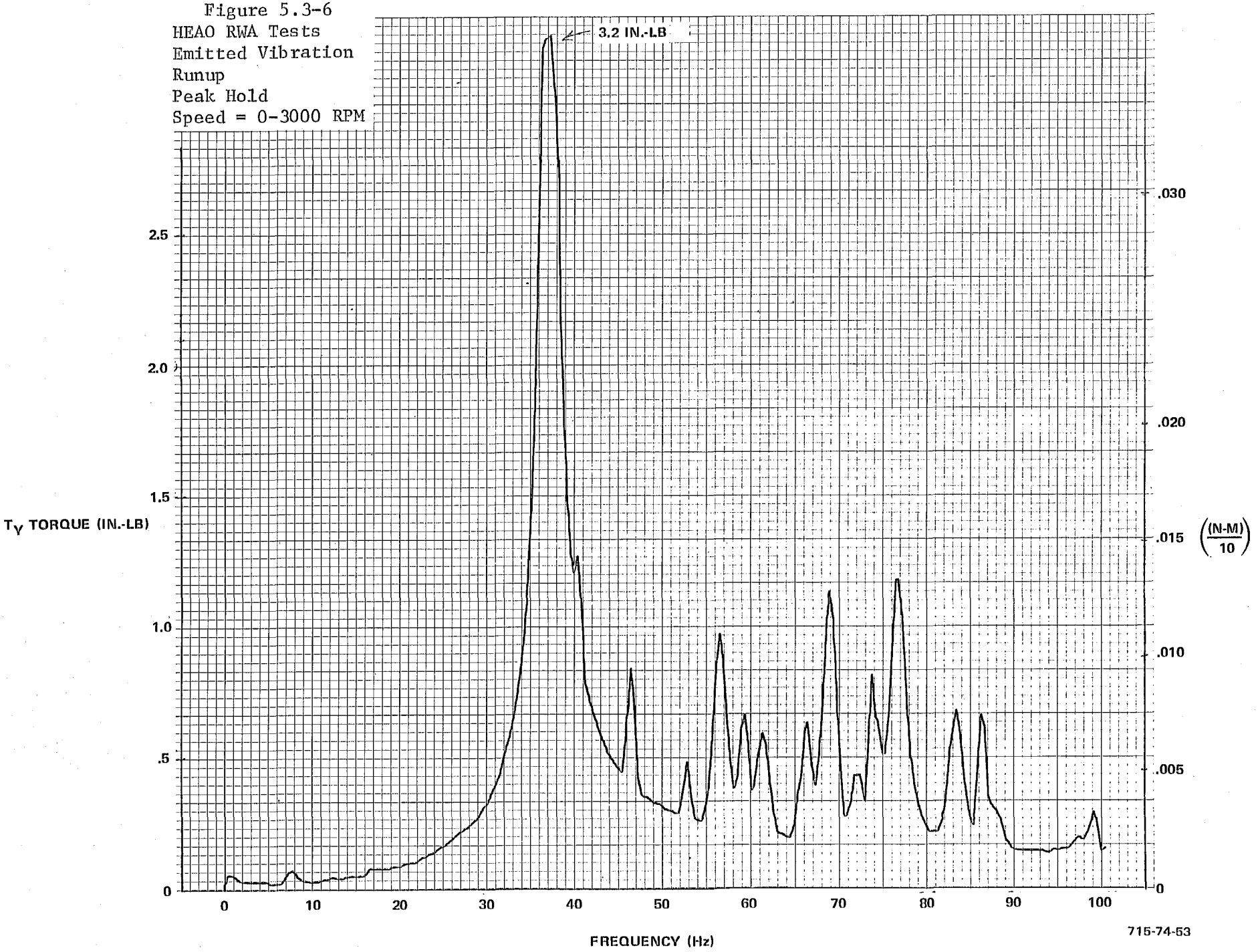

TABLE 5.3-1

HEAO RWA TESTS

Run No.	Response Axis						Rotor Speed (rpm)	Type of Run
	F_x	F_y	F_z	T_x	T_y	T_z		
1	X	X	X				0	Fixture Calibration, F_x Input
2				X	X	X	0	Fixture Calibration, F_x Input
3	X	X	X				0	Fixture Calibration, F_y Input
*4				X	X	X	0	Fixture Calibration, F_y Input
*5	X	X	X				0	Fixture Calibration, F_z Input
6				X	X	X	0	Fixture Calibration, F_z Input
*7	X						0-3000	Runup, F_x Input, Tracking Filter
*8	X						3000-0	Power Down, F_x Input, Tracking Filter
*9		X					0-3000	Runup, F_y Input, Tracking Filter
*10		X					3000-0	Power Down, F_y Input, Tracking Filter
*11			X				0-3000	Runup, F_z Input, Tracking Filter
*12			X				3000-0	Power Down, F_z input, Tracking Filter
13		X					3000-0	Coast Down, F_y, Tracking Filter
*14				X			0-3000	Runup, T_x Input, Tracking Filter
15				X			3000-0	Power Down, T_x Input, Tracking Filter
16					X		0-3000	Runup, T_y Input, Tracking Filter
*17					X		3000-0	Power Down, T_y Input, Tracking Filter
18						X	0-3000	Runup, T_z Input, Tracking Filter
*19						X	3000-0	Power Down, T_z Input, Tracking Filter
20	X	X	X				0	Background Noise (0-25 Hz)
21				X	X	X	0	Background Noise (0-25 Hz)
22	X	X	X				0	Background Noise (0-200 Hz)
23				X	X	X	0	Background Noise (0-200 Hz)
*24	X	X	X				500	Constant Speed (1 minute peak hold)
*25				X	X	X	500	Constant Speed (1 minute peak hold)
26	X	X	X				1000	Constant Speed (1 minute peak hold)
*27	X	X	X				1000	Constant Speed (1 minute peak hold)
*28				X	X	X	1000	Constant Speed (1 minute peak hold)
*29	X	X	X				1500	Constant Speed (1 minute peak hold)

* = Denotes that run is included in this report.

TABLE 5.3-1 (cont)

HEAO RWA TESTS

Run No.	Response Axis						Rotor Speed (rpm)	Type of Run
	F_x	F_y	F_z	T_x	T_y	T_z		
*30				X	X	X	1500	Constant Speed (1 minute peak hold)
31	X	X	X				2000	Constant Speed (1 minute peak hold)
32	X	X	X				2000	Constant Speed (1 minute peak hold)
33				X	X	X	2000	Constant Speed (1 minute peak hold)
34				X	X	X	2000	Constant Speed (1 minute peak hold)
*35	X	X	X				3000	Constant Speed (1 minute peak hold)
36	X	X	X				3000	Constant Speed (1 minute peak hold)
*37				X	X	X	3000	Constant Speed (1 minute peak hold)
38				X	X	X	3000	Constant Speed (1 minute peak hold)
39		X						Rundown, F_y input
40	X	X	X				2000	Reverse direction, Constant Speed
41				X	X	X	2000	Reverse direction, Constant Speed
*42				X			0-3000	Runup, Peak Hold
*43					X		0-3000	Runup, Peak Hold
44						X	3000-0	Power Down, Peak Hold
*45	X						3000-0	Power Down, Peak Hold
*46		X					3000-0	Power Down, Peak Hold
47			X				0-3000	Runup, Peak Hold

Figures 5.3-5 and 5.3-6 depict the axial and radial torques transmitted from the RWA during runup. The 38-Hz resonance is prominent in both curves, and is .18 inch-pound axially and 3.2 inch-pounds radially. Additional higher order peaks are evident between 50 and 90 Hz; these are unexplained by the existing models.

Tracking Filter Response - Figures 5.3-7 through 5.3-15 depict the emitted forces and torques from the HEAO RWA during runup to 3000 rpm and rundown from 3000 rpm. Runup and rundown data is included since a difference can be seen in the responses (i.e., Figures 5.3-7 and 5.3-10).

Figure 5.3-7
HEAO RWA Tests
Emitted Vibration
Runup
F_X Input Tracking Filter
Speed = 0-3000 RPM

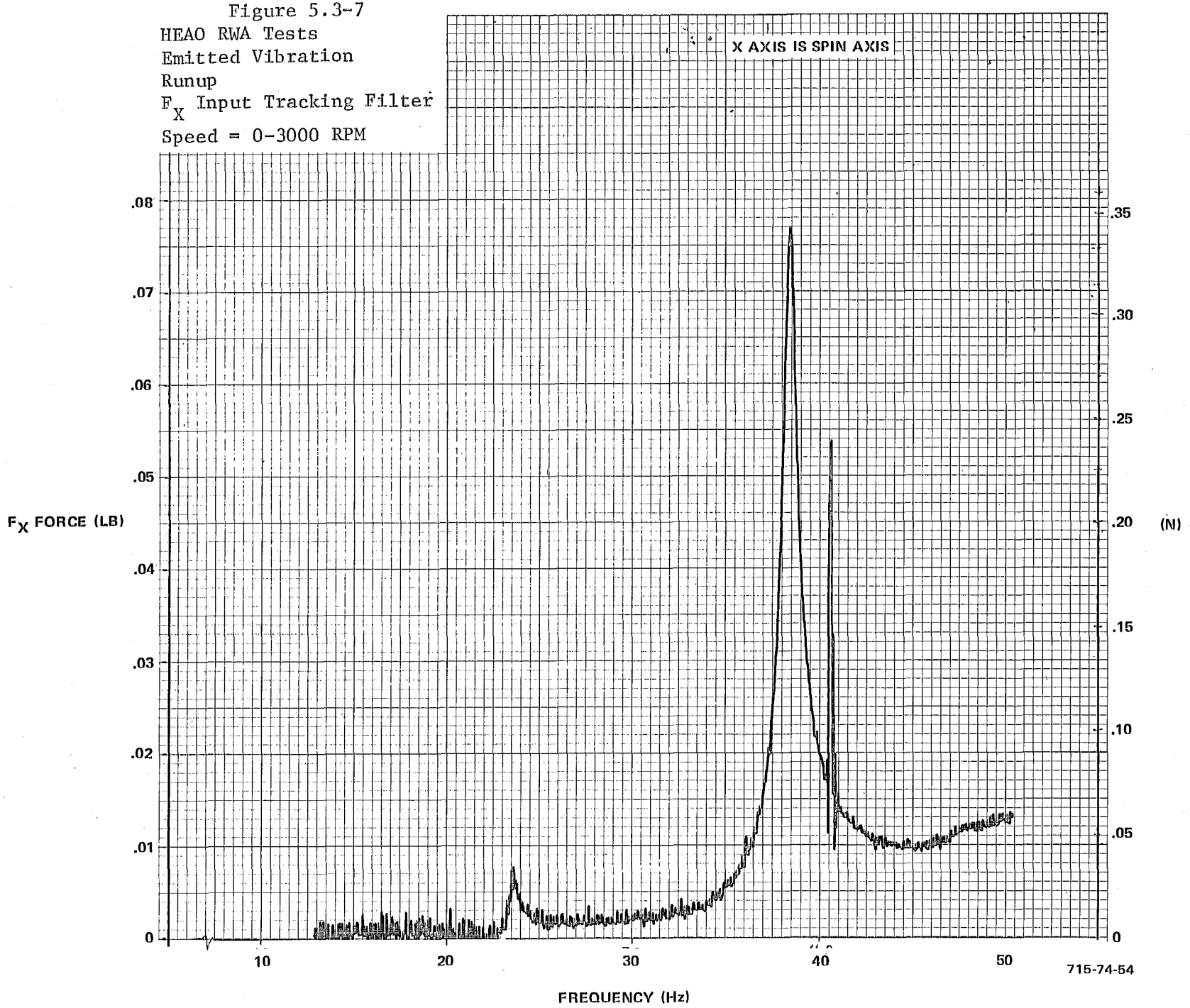

Figure 5.3-8
HEAO RWA Tests
Emitted Vibration
Runup
F_Y Input, Tracking Filter
Speed = 0-3000 RPM

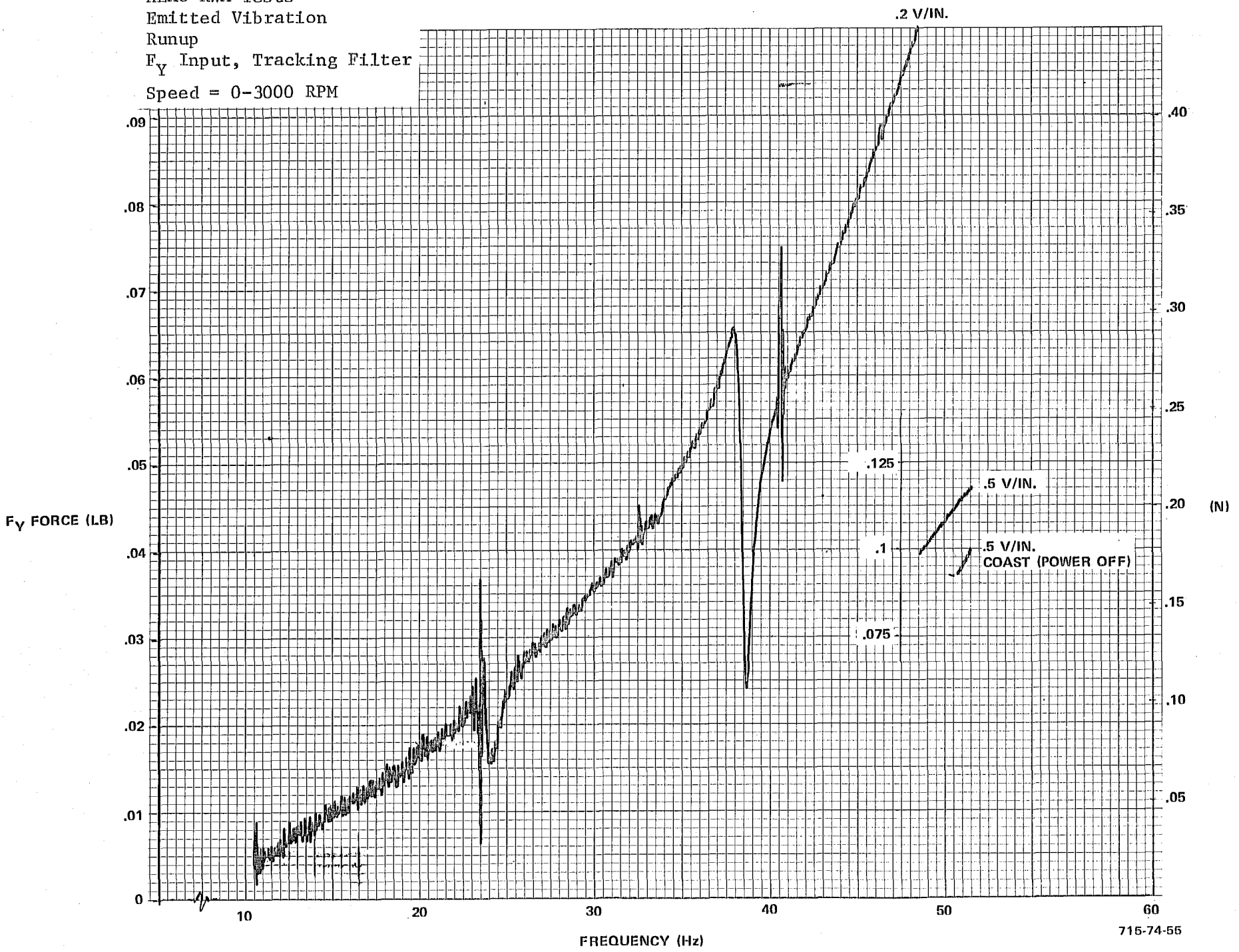

Figure 5.3-9
HEAO RWA Tests
Emitted Vibration
Runup
F_Z Input, Tracking Filter
Speed = 0-3000 RPM

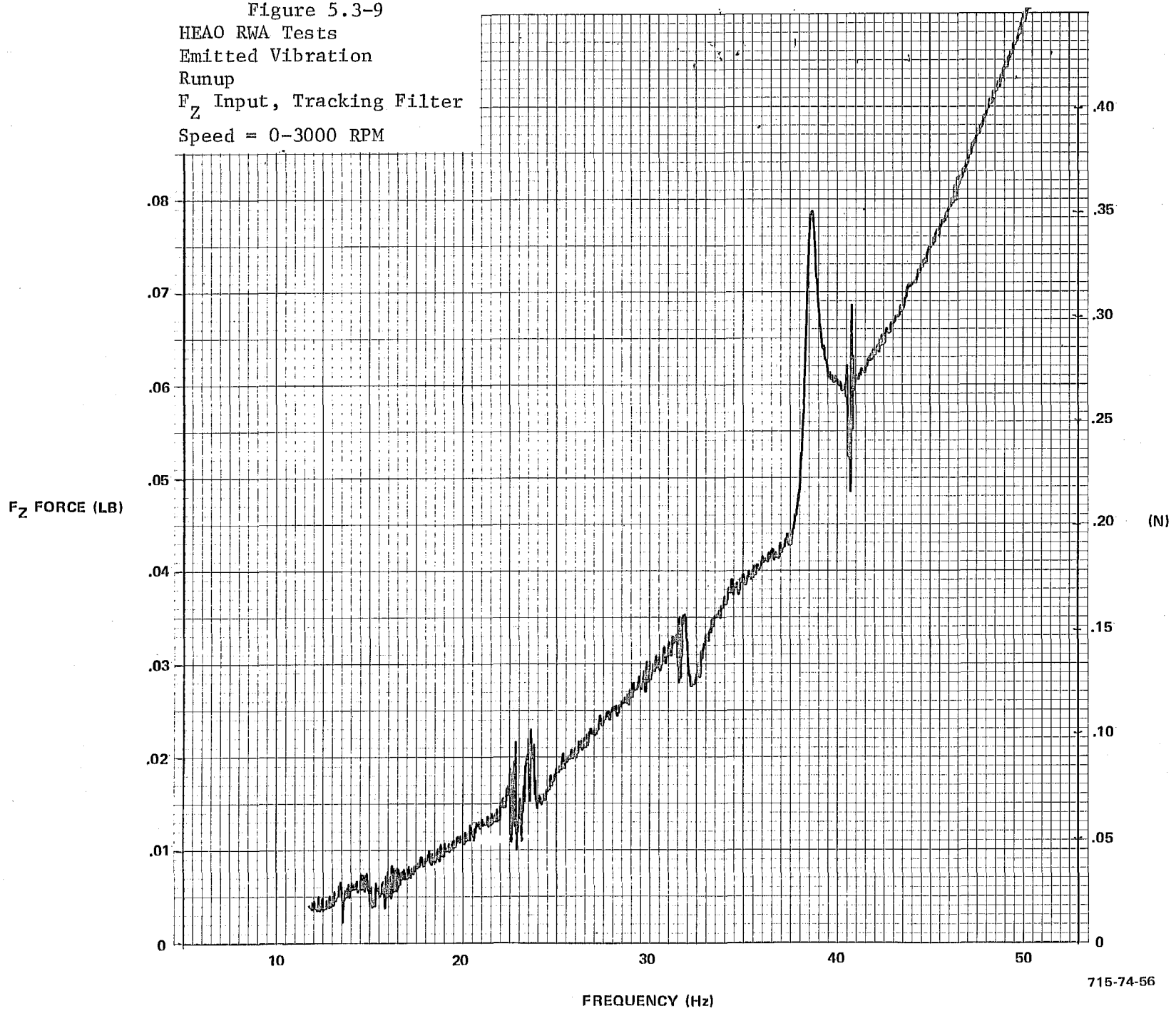

Figure 5.3-10
HEAO RWA Tests
Emitted Vibration
Power Down
F_X Input, Tracking Filter
Speed = 3000-0 RPM

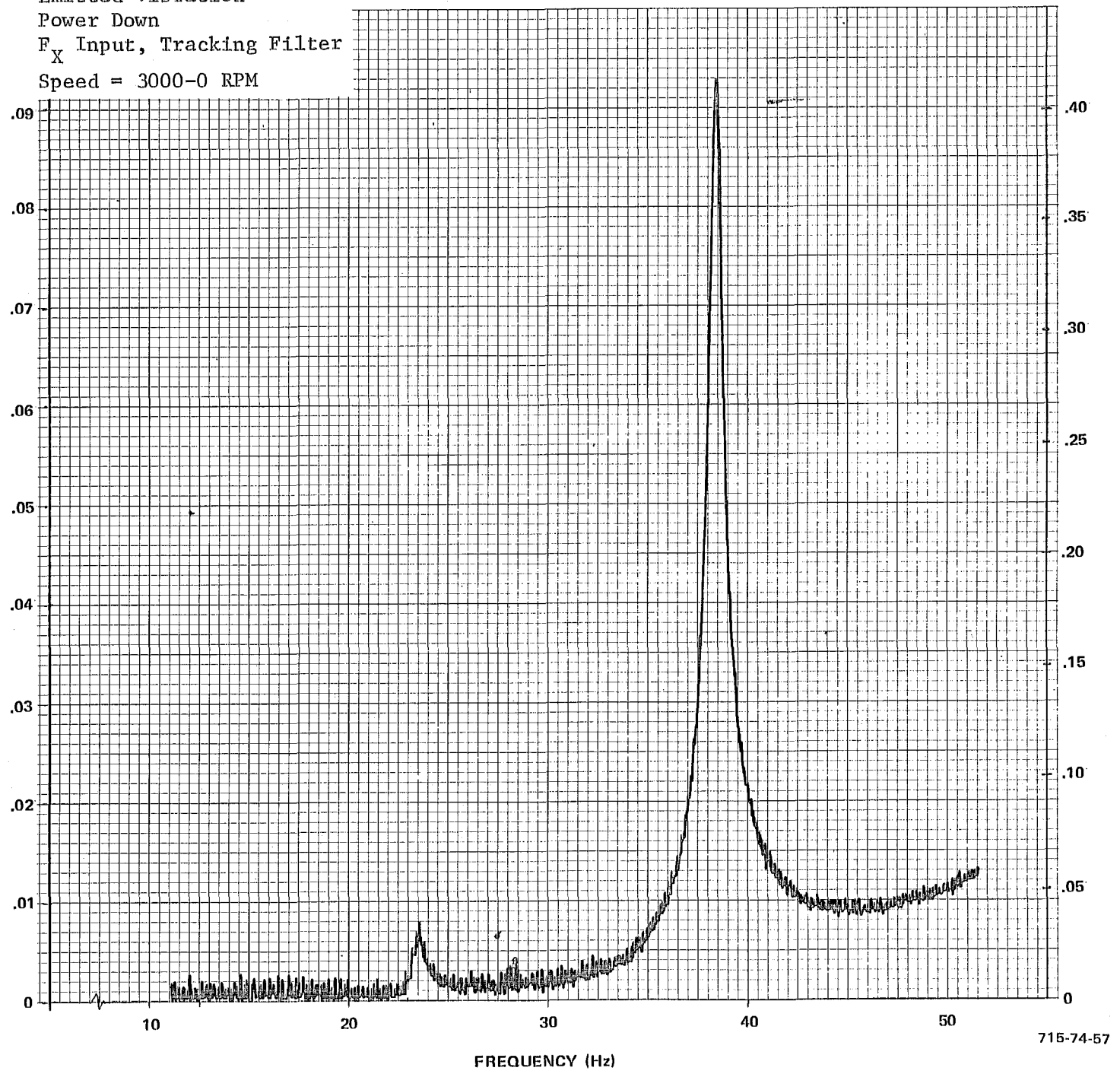

Figure 5.3-11
HEAO RWA Tests
Emitted Vibration
Power Down
F_Y Input, Tracking Filter
Speed = 3000-0 RPM

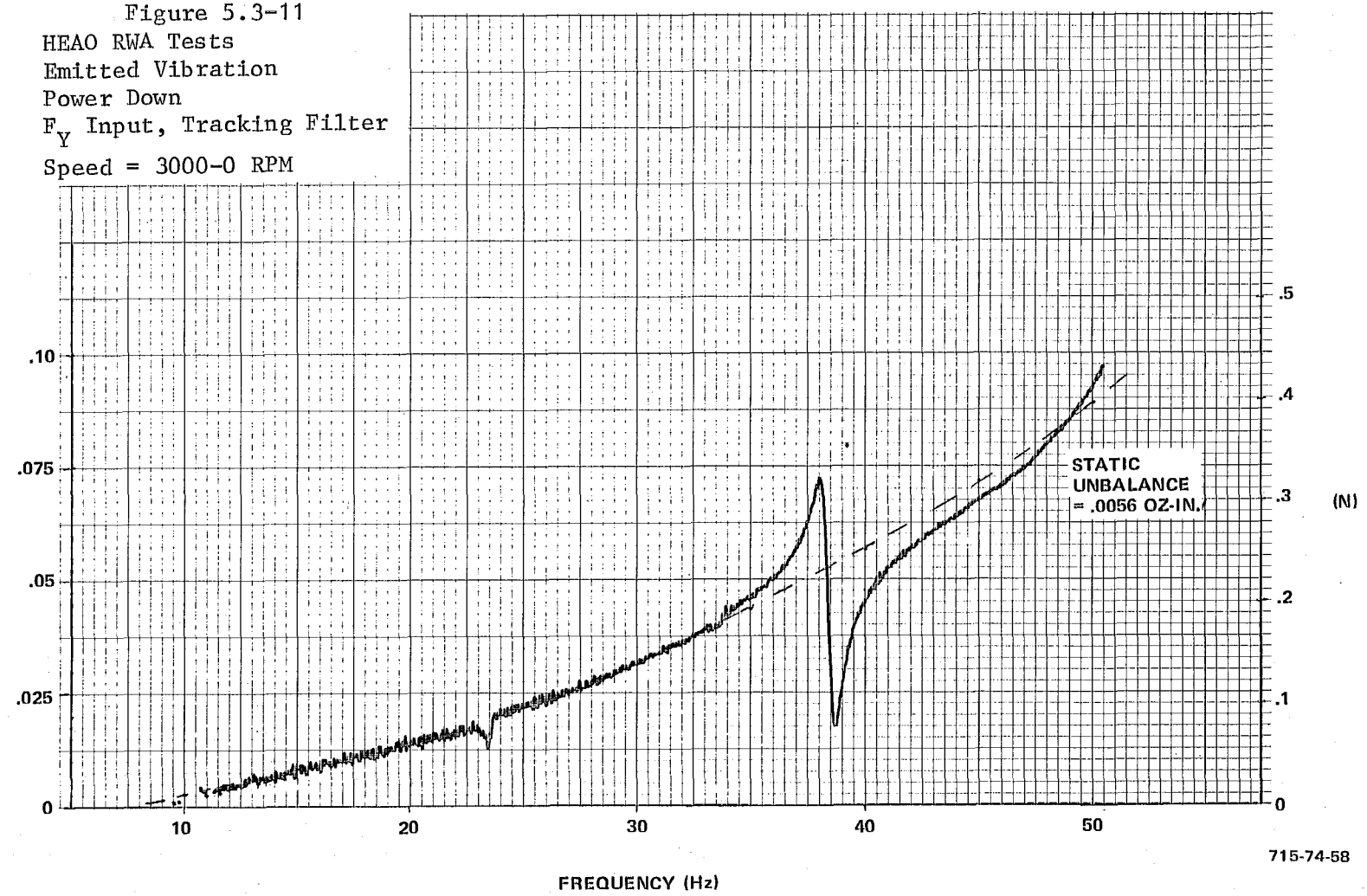

F_Y FORCE (LB)

FREQUENCY (Hz)

Figure 5.3-12
HEAO RWA Tests
Emitted Vibration
Power Down
F_Z Input, Tracking Filter
Speed = 3000-0 RPM

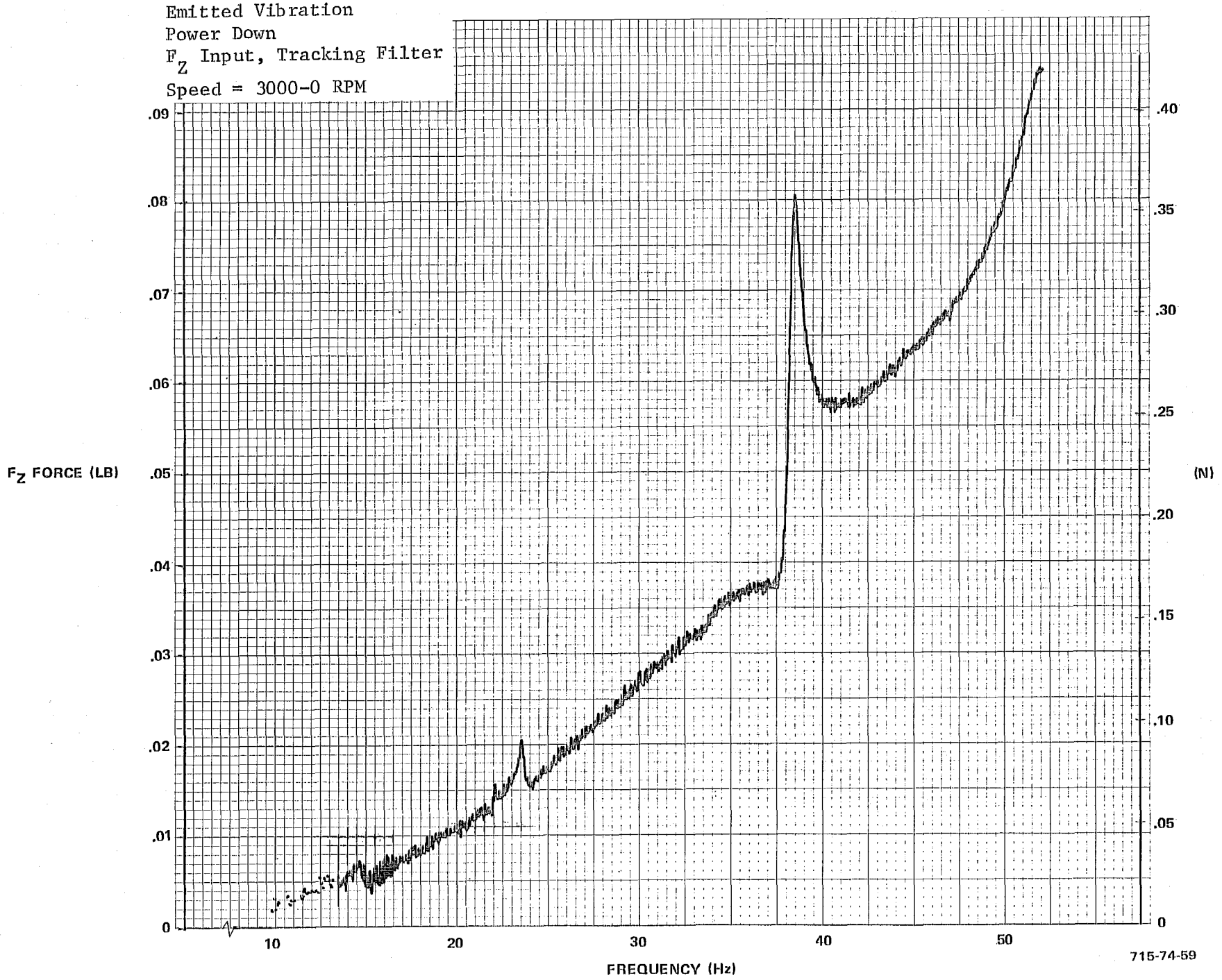

Figure 5.3-13
HEAO RWA Tests
Emitted Vibration
Runup
T_X Input, Tracking Filter
Speed = 0-3000 RPM

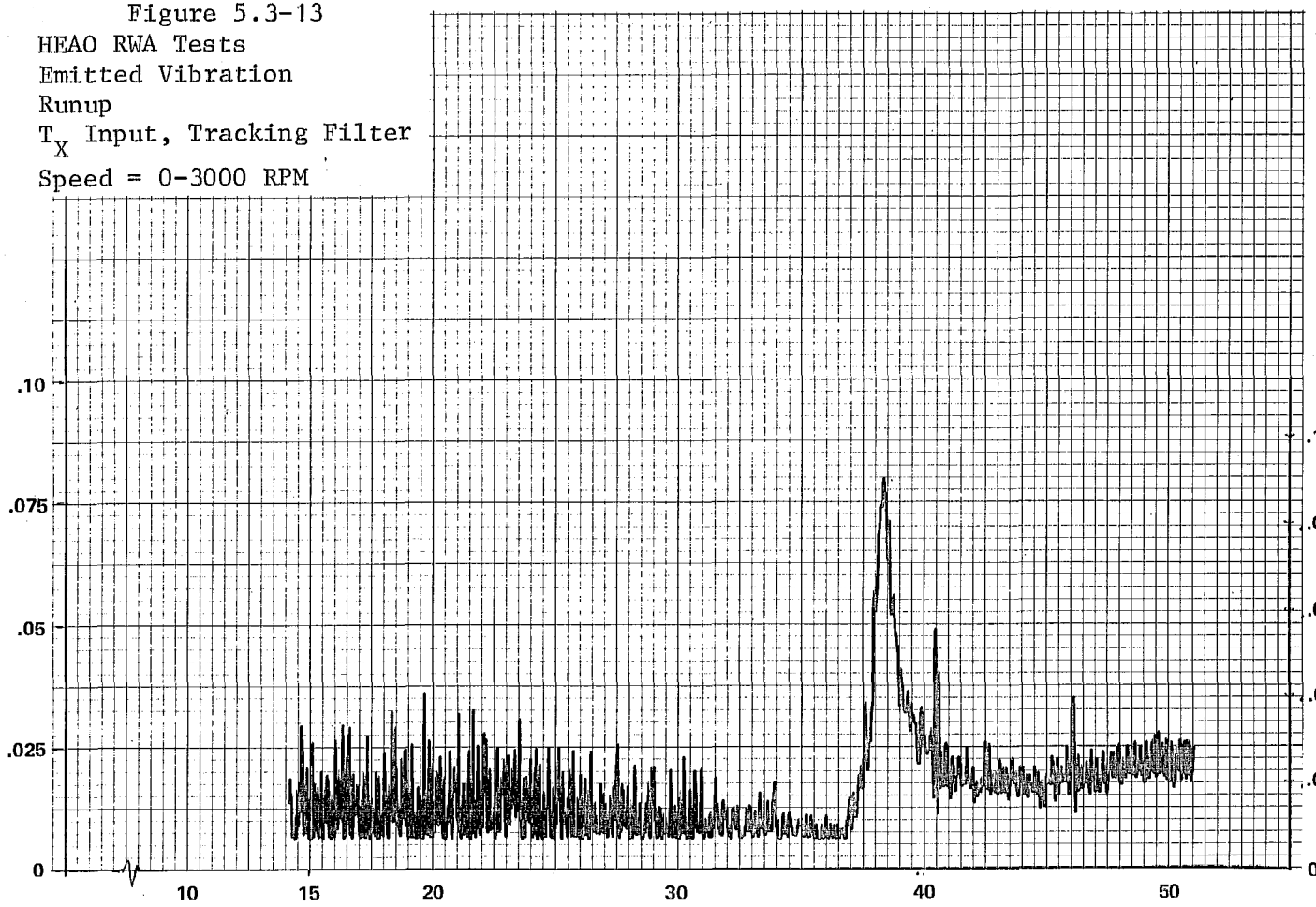

T_X TORQUE (IN.-LB)

(N-M) X 10

FREQUENCY (Hz)

Figure 5.3-14
HEAO RWA Tests
Emitted Vibration
Power Down
T_Y Input, Tracking Filter
Speed = 3000-0 RPM

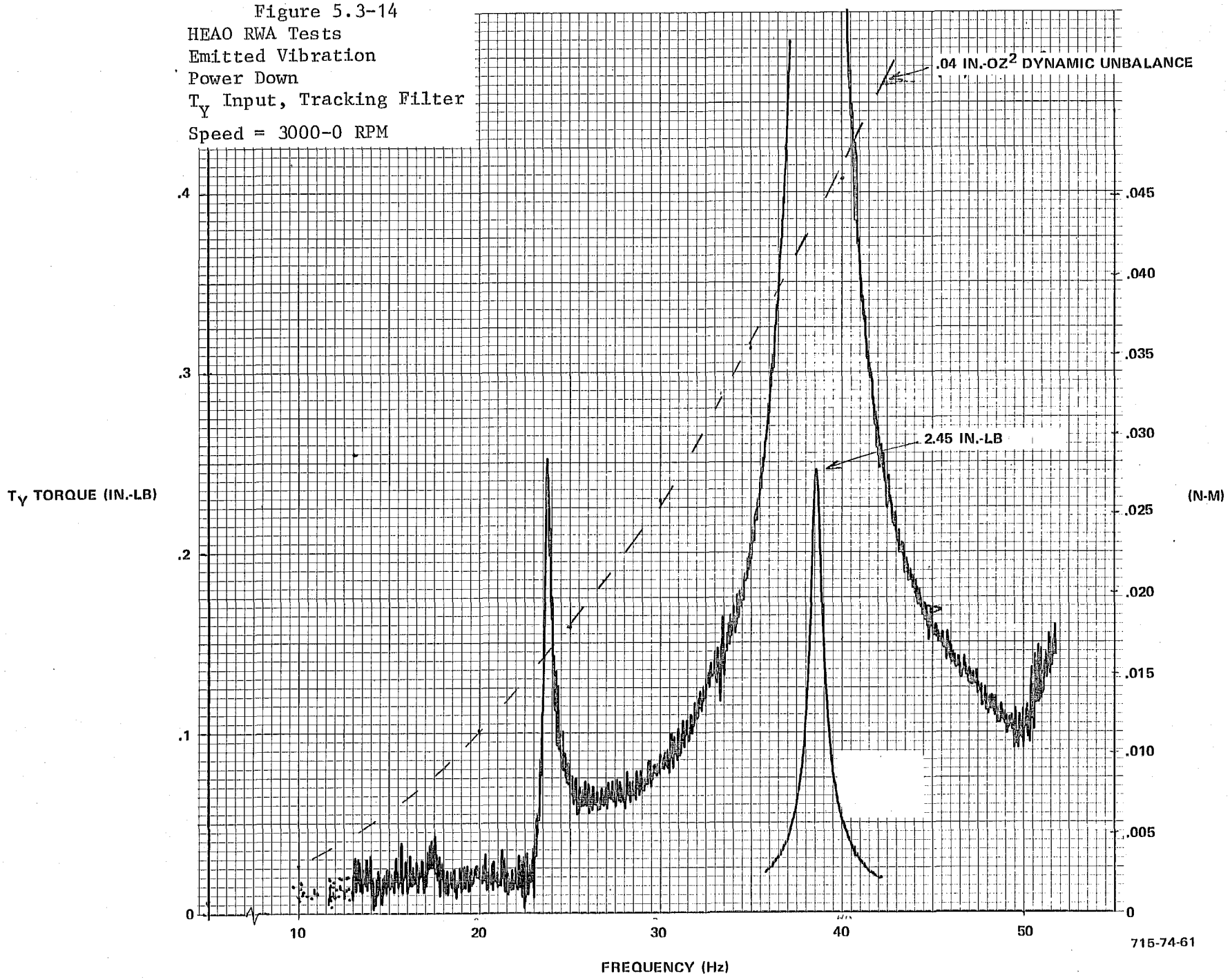

Figure 5.3-15
HEAO RWA Tests
Emitted Vibration
Power Down
T_Z Input, Tracking Filter
Speed = 3000-0 RPM

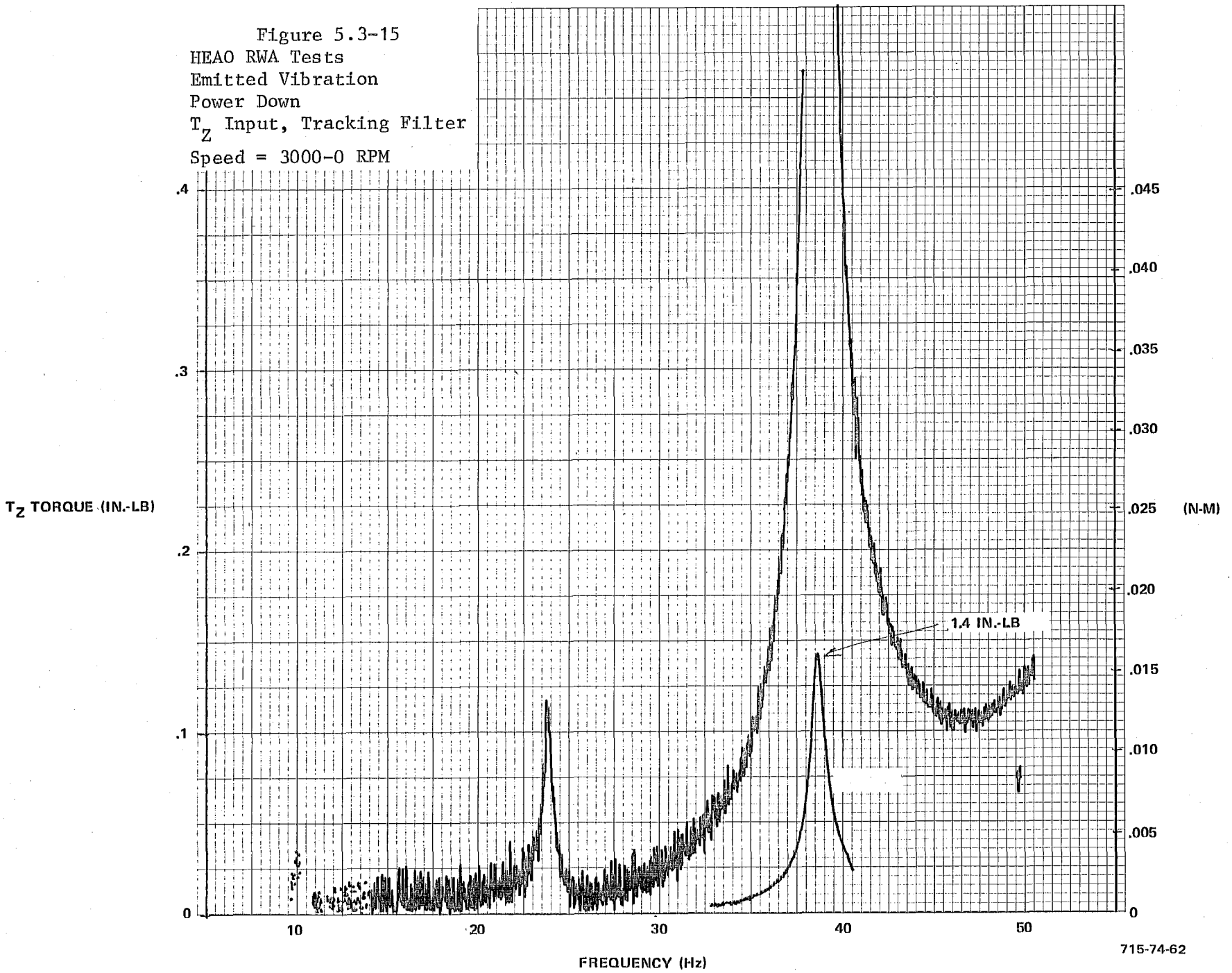

Figure 5.3-7 shows the force along the spin axis, F_x. The 38-Hz resonance is present, but two other additional frequencies can be seen. One is at 23.5 Hz and the other at 40.5 Hz. The 40.5 Hz is not present in the rundown data shown in Figure 5.3-10. This also is consistent with the radial force data in Figures 5.3-8, -9, -11, and -12. It is suspected that both the 23.5 Hz and 40.5 Hz resonances are somehow related to the ac induction motor excitation frequency since runups were done at a 160-Hz excitation frequency and rundowns at a 100-Hz frequency. It is also interesting to note that the F_y force exhibits a null at the 38-Hz resonance and the F_z force, also radial, exhibits a peak (Figures 5.3-8 and 5.3-9). Figure 5.3-8 shows that the reduction in force when the motor is shut off is approximately 17 percent.

Figures 5.3-14 and -15, the radial axis torques, show the largest degree of 23.5-Hz resonance, but it is still small compared to the 38-Hz component at 2.45 inch-pounds for F_y and 1.4 inch-pounds for F_z. A dashed curve corresponding to the .04 oz-in.^{2} dynamic unbalance measured on the balance machine is superimposed on Figure 5.3-14. There isn't a very good match to the data; an unbalance value of .015 oz-in.^{2} appears to fit the data better.

Constant Speed - Figures 5.3-16 through 5.3-23 show the frequency spectrums of forces and torques for the HEAO RWA when running at a constant speed. Data for four speeds are shown in the report: 500, 1000, 1500, and 3000 rpm. The data was taken using the same procedure and equipment as discussed in Paragraph 5.2 for the FSC MWA.

Since low speed RWA operation is being considered for the LST, a run was conducted at 500 rpm. The wheel speed fundamental is 8.3 Hz and gets masked by the 7.5- to 8.0-Hz fixture isolation resonance, but the excitation of higher frequency components can be determined from the data.

The force data at 500 rpm, Figure 5.3-16, shows very little activity except for a slight peak at 71 Hz. The torque data, Figure 5.3-17, shows more activity with peaks occuring in the 55- to 75-Hz region for T_y and T_z. As in the force response, the principal peak is at 71 Hz. Note the absence of wheel speed harmonics.

At 1000 rpm, Figures 5.3-18 and -19, the forces and torques at the wheel speed frequency, 16.7 Hz, can be identified. A component at 50 Hz is also very apparent and may be a third harmonic. At 1500 rpm, however, no third harmonic

Figure 5.3-16
HEAO RWA Tests
Emitted Vibration
Constant Speed
1 Min Peak Hold
Speed = 500 RPM

Figure 5.3-17
HEAO RWA Tests
Emitted Vibration
Constant Speed
1 Min Peak Hold
Speed = 500 RPM

Figure 5.3-18
HEAO RWA Tests
Emitted Vibration
Constant Speed
1 Min Peak Hold
Speed = 1000 RPM

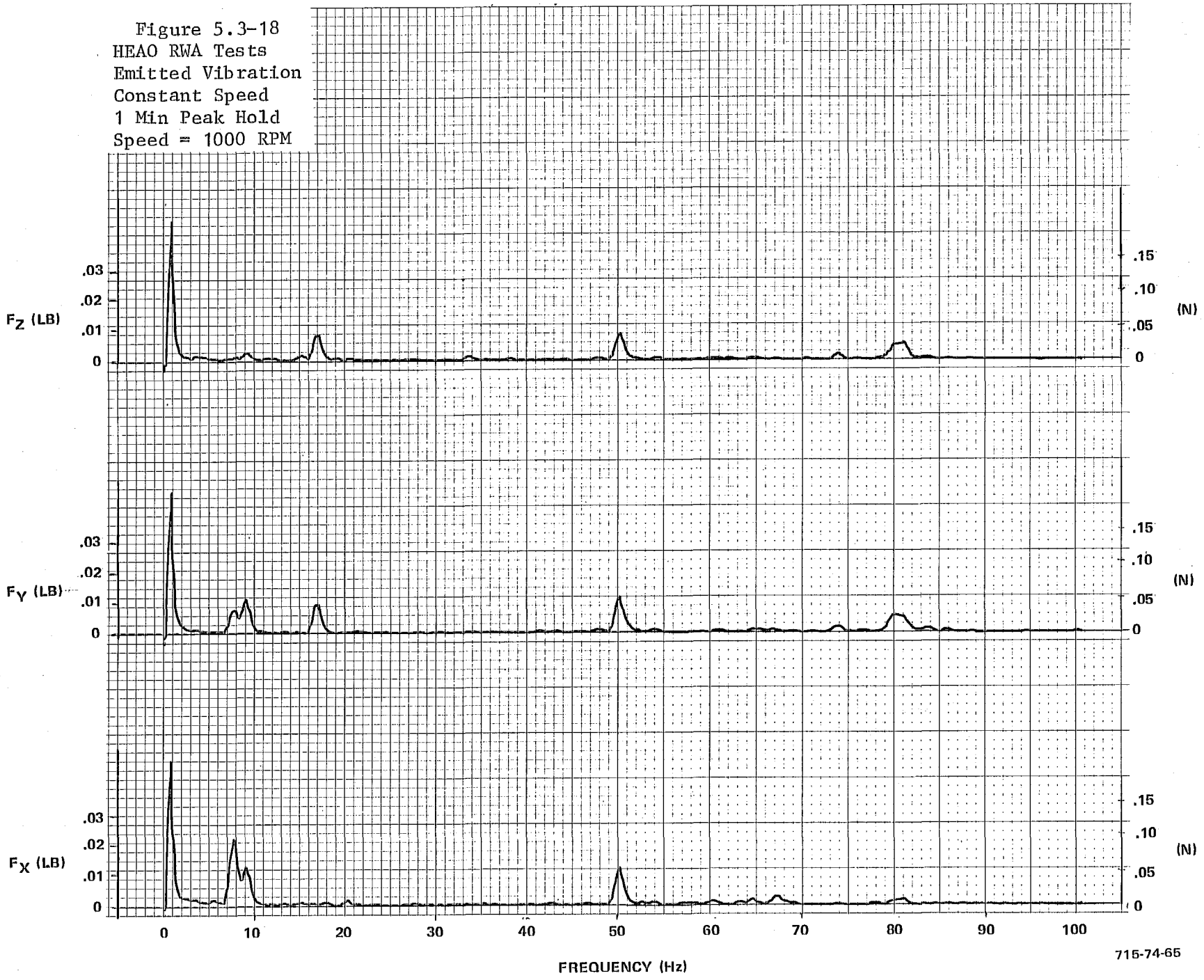

Figure 5.3-19
HEAO RWA Tests
Emitted Vibration
Constant Speed
1 Min Peak Hold
Speed = 1000 RPM

715-74-66

Figure 5.3-20
HEAO RWA Tests
Emitted Vibration
Constant Speed
1 Min Peak Hold
Speed = 1500 RPM

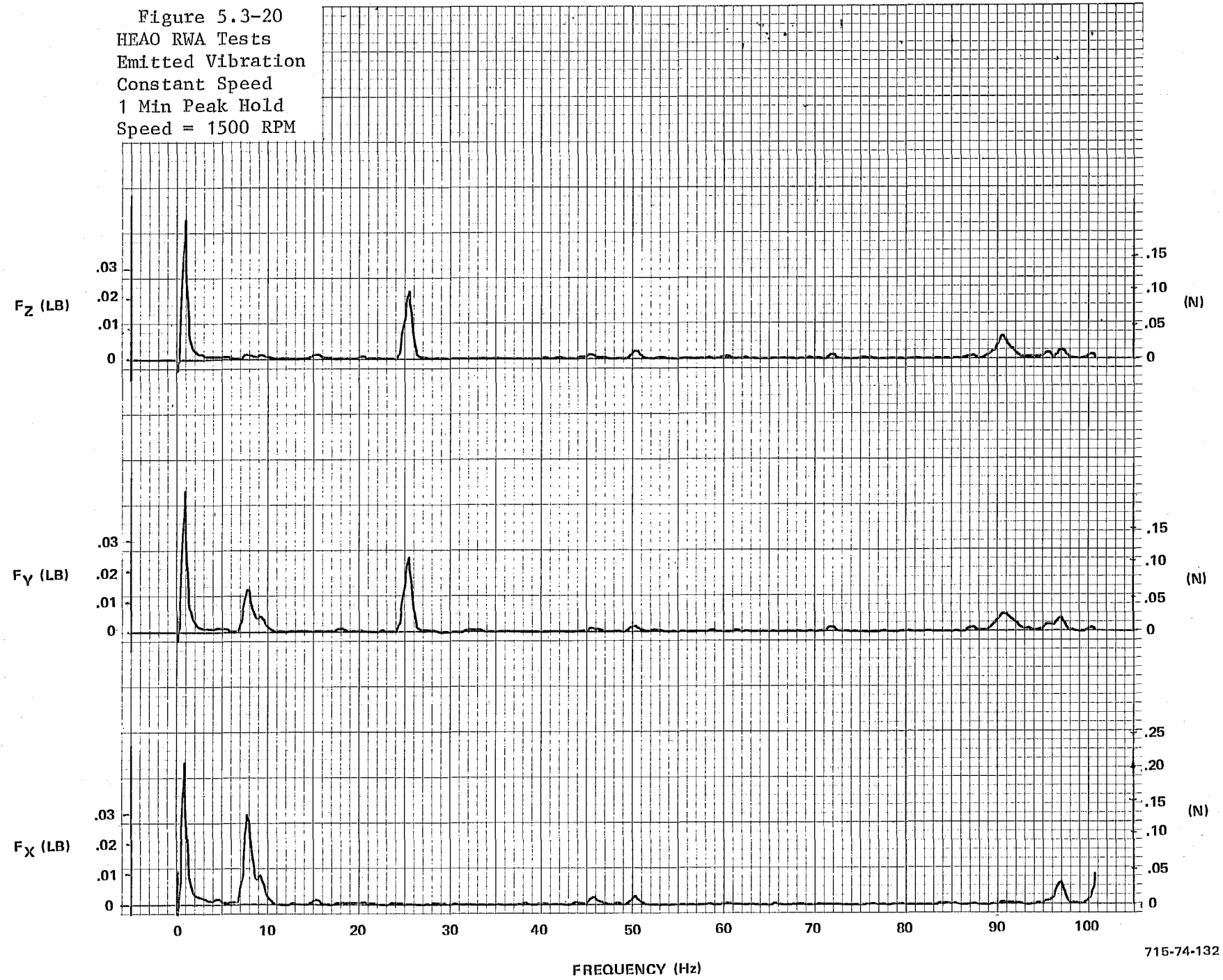

715-74-132

Figure 5.3-21
HEAO RWA Tests
Emitted Vibration
Constant Speed
1 Min Peak Hold
Speed = 1500 RPM

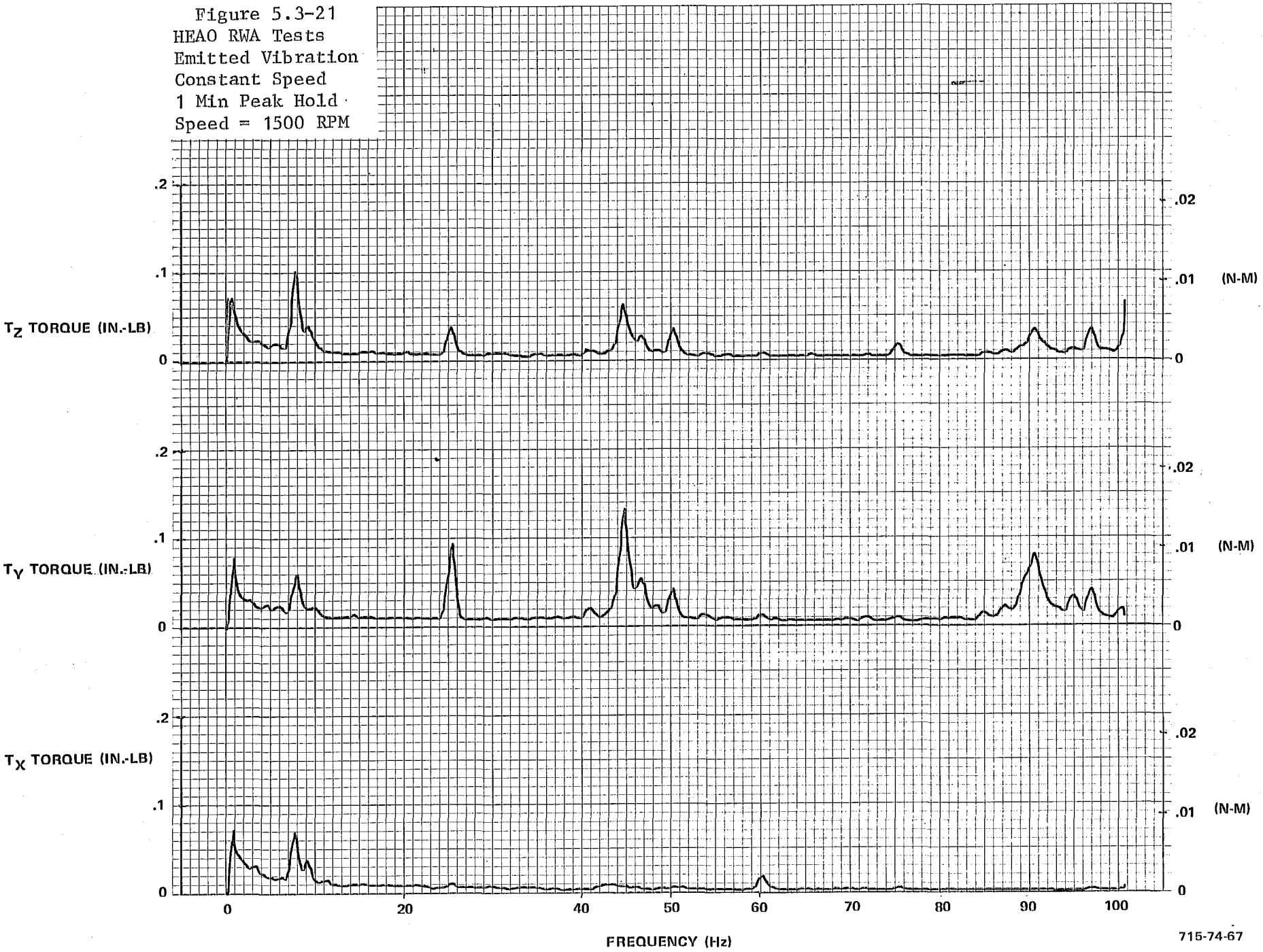

Figure 5.3-22
HEAO RWA Tests
Emitted Vibration
Constant Speed
1 Min Peak Hold
Speed = 3000 RPM

715-74-68


Figure 5.3-23
HEAO RWA Tests
Emitted Vibration
Constant Speed
1 Min Peak Hold
Speed = 3000 RPM
T_Z (IN.-LB)
T_Y (IN.-LB)
T_X (IN.-LB)
.2
.1
0
.02
.01
(N-M)
0
10
20
30
40
50
60
70
80
90
100
FREQUENCY (Hz)
715-74-69

is present. Figures 5.3-20 and 5.3-21 show the responses at 1500 rpm and the wheel speed component at 25 Hz is evident. A radial torque component at 45 Hz is also present and exceeds the wheel speed component.

At 3000 rpm, Figures 5.3-22 and -23, the wheel speed component is predominant for both the forces and torques. A small second harmonic at 100 Hz is present and a small 101H bearing retainer component at 19 Hz. Note how quiet the torque response is between 55 and 90 Hz at 3000 rpm compared to the same region at 1000 rpm.

5.4 MMB TEST RESULTS

The 38 tests performed on the Model Magnetic Bearing (MMB) Wheel on the hard mount vibration fixture are listed in Table 5.4-1. The curves necessary to show the pertinent vibration signatures of the MMB have been selected and are included in this section. Note that the orientation of the MMB spin axis is horizontal, not vertical like the ball bearing wheels, and therefore the MMB axial response is along the test fixture Y axis.

Calibration - Figures 5.4-1 through 5.4-3 show some typical dynamic calibration runs. A freely suspended .25-pound force exciter was used, as described in Paragraph 5.2, to input sinusoidal forces into the unit. The MMB rotor was not magnetically suspended for this test, and was resting on its backup ball bearings. This provided a very rigid MMB unit, and this can be seen in the calibration data which has no resonance until 150 Hz. It will be recalled that the FSC and HEAO calibration data showed a 120- and 65-Hz resonance, respectively, due to the rotor web/rim resonance. This data is a good representation of the hard mount fixture resonances since the MMB is acting as an essentially solid mass.

Figure 5.4-1 shows the three force responses to a F_x (spin axis) input. The data shows no significant cross coupling and a fixed output in the desired, F_x, axis over the 20- to 120-Hz range. Likewise, Figures 5.4-2 and 5.4-3 show an approximately constant output in the input axis and no cross coupling.

Peak Hold Runup and Rundown - Figures 5.4-4 and 5.4-5 show the emitted forces and moments respectively for the MMB during a runup from 0 to 5000 rpm (wheel frequency 0 to 83.3 Hz). The radial force responses in Figure 5.4-4 show a resonance at 30 and 34 Hz in the F_x and F_z axis, after which the force is constant at approximately .2 Lb. As explained in the appendix, this is a typical

Figure 5.4-1
Magnetic Bearing Tests
Emitted Vibration
Fixture Calibration
F_X Input = .25 lbf
Speed = 0 RPM

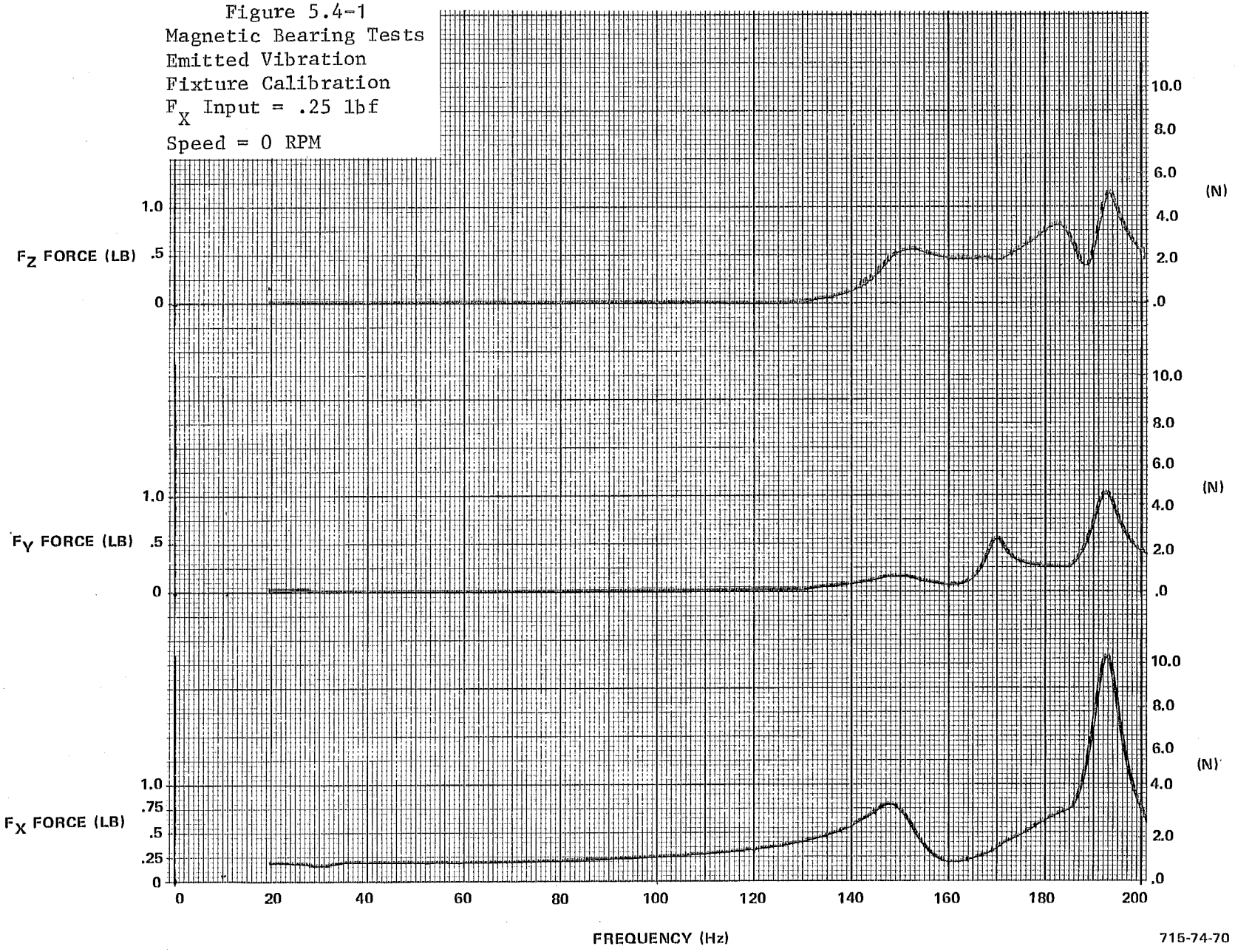

715-74-70

Figure 5.4-2
Magnetic Bearing Tests
Emitted Vibration
Fixture Calibration
T_X Input = 1 in.-lbf
Speed = 0 RPM

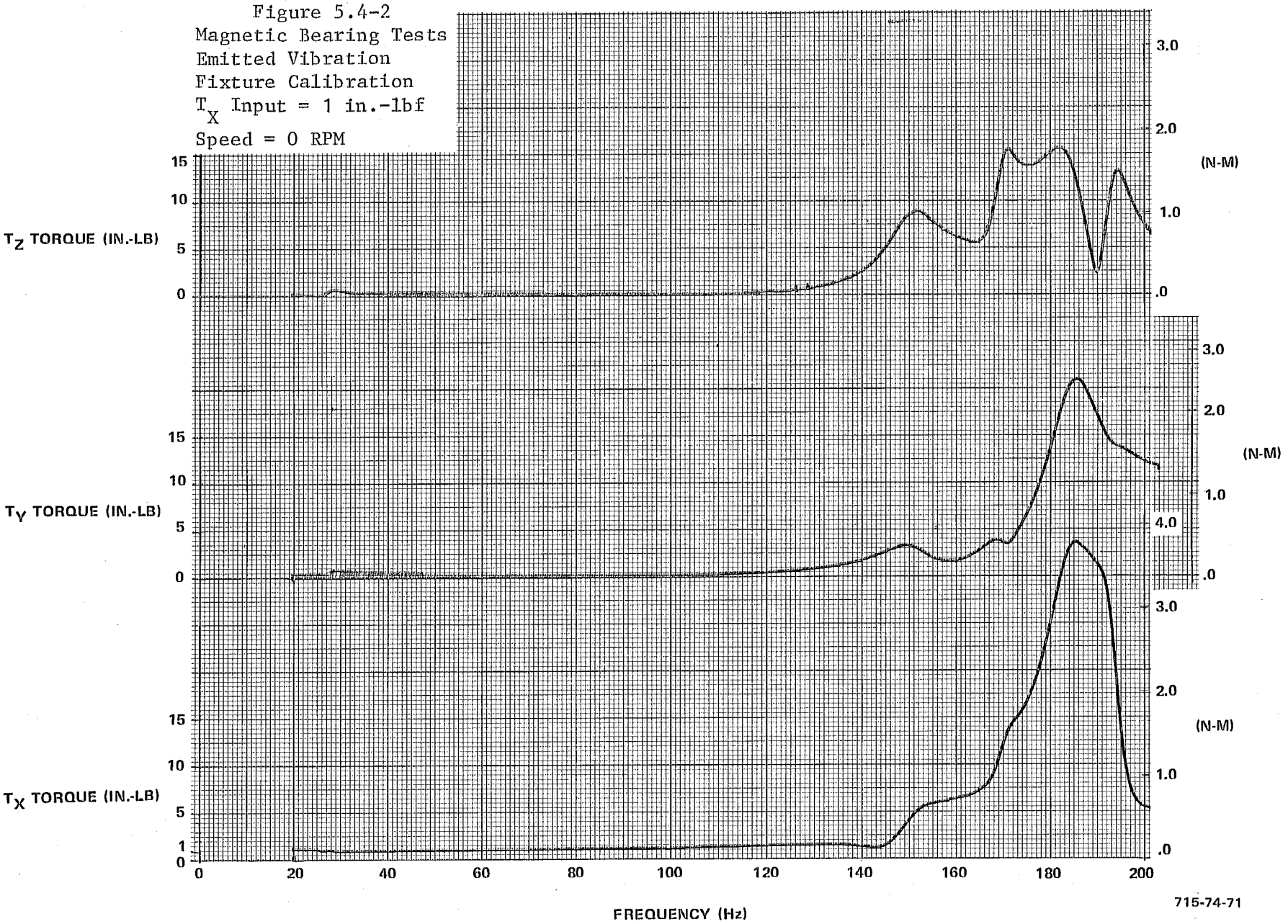

Figure 5.4-3
Magnetic Bearing Tests
Emitted Vibration
Fixture Calibration
T_Z Input
Speed = 0 RPM

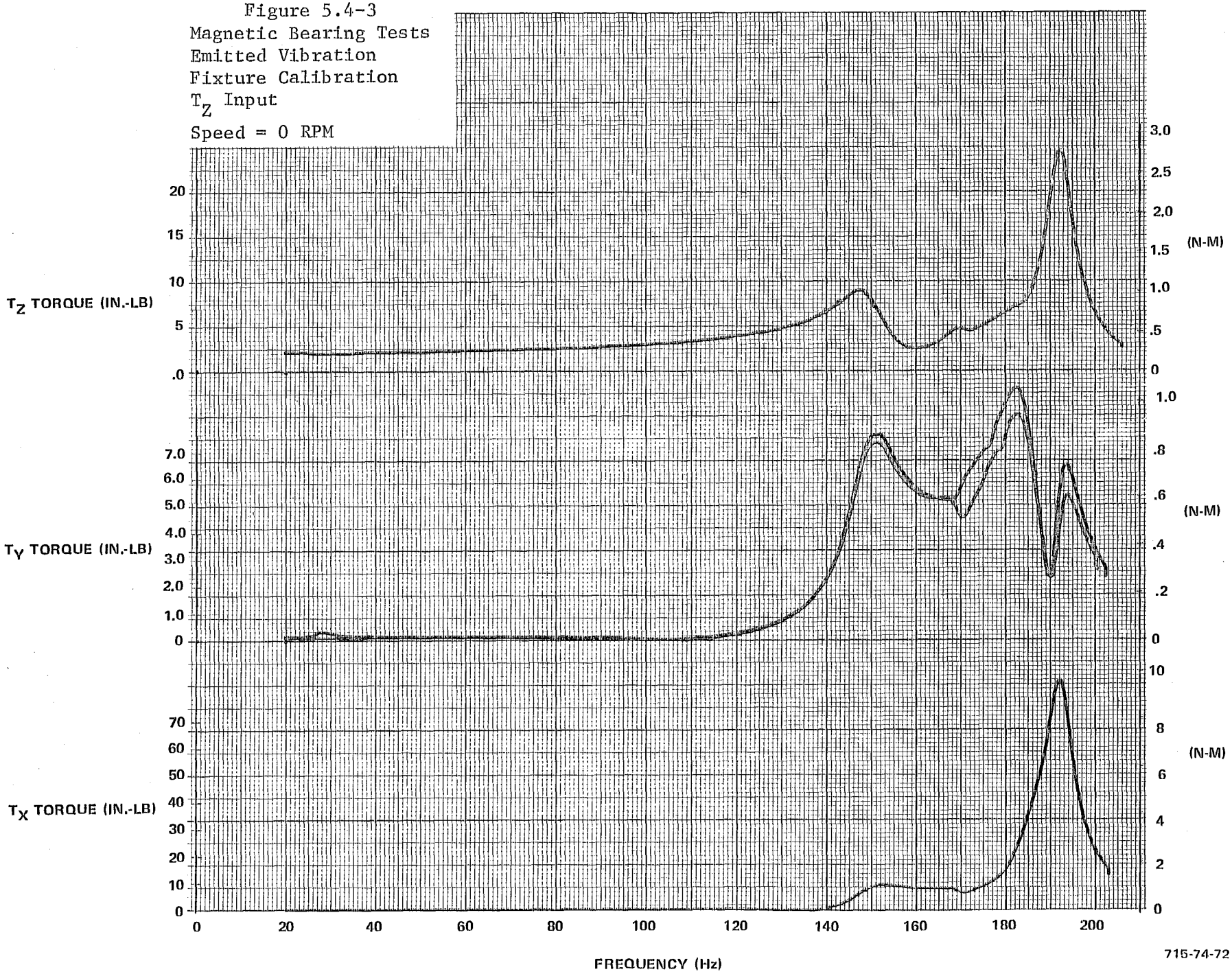

715-74-72

Figure 5.4-4
Magnetic Bearing Tests
Emitted Vibration
Runup
Peak Hold
Speed = 0-5000 RPM

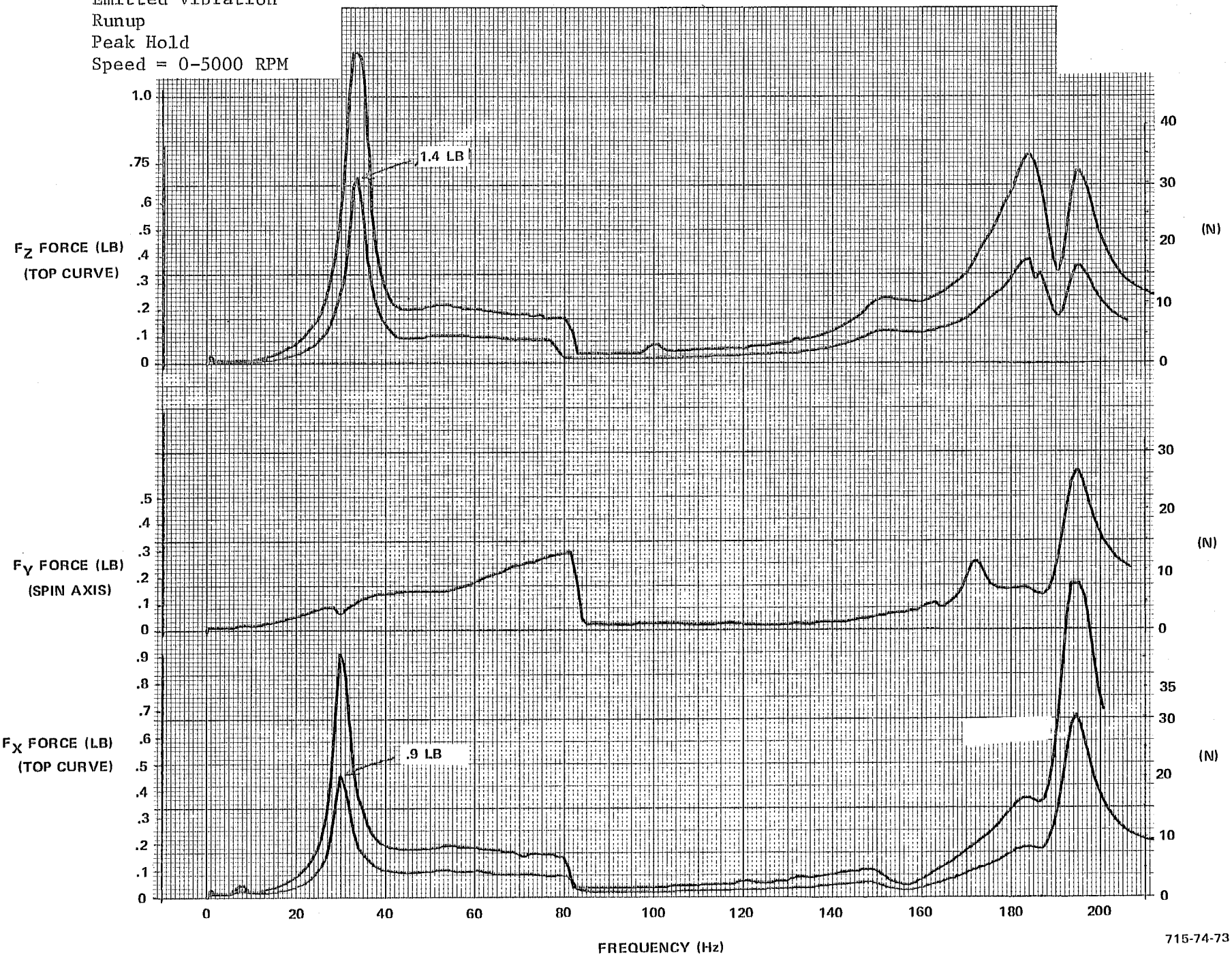

715-74-73

Figure 5.4-5
Magnetic Bearing Tests
Emitted Vibration
Runup
Peak Hold
Speed = 0-5000 RPM

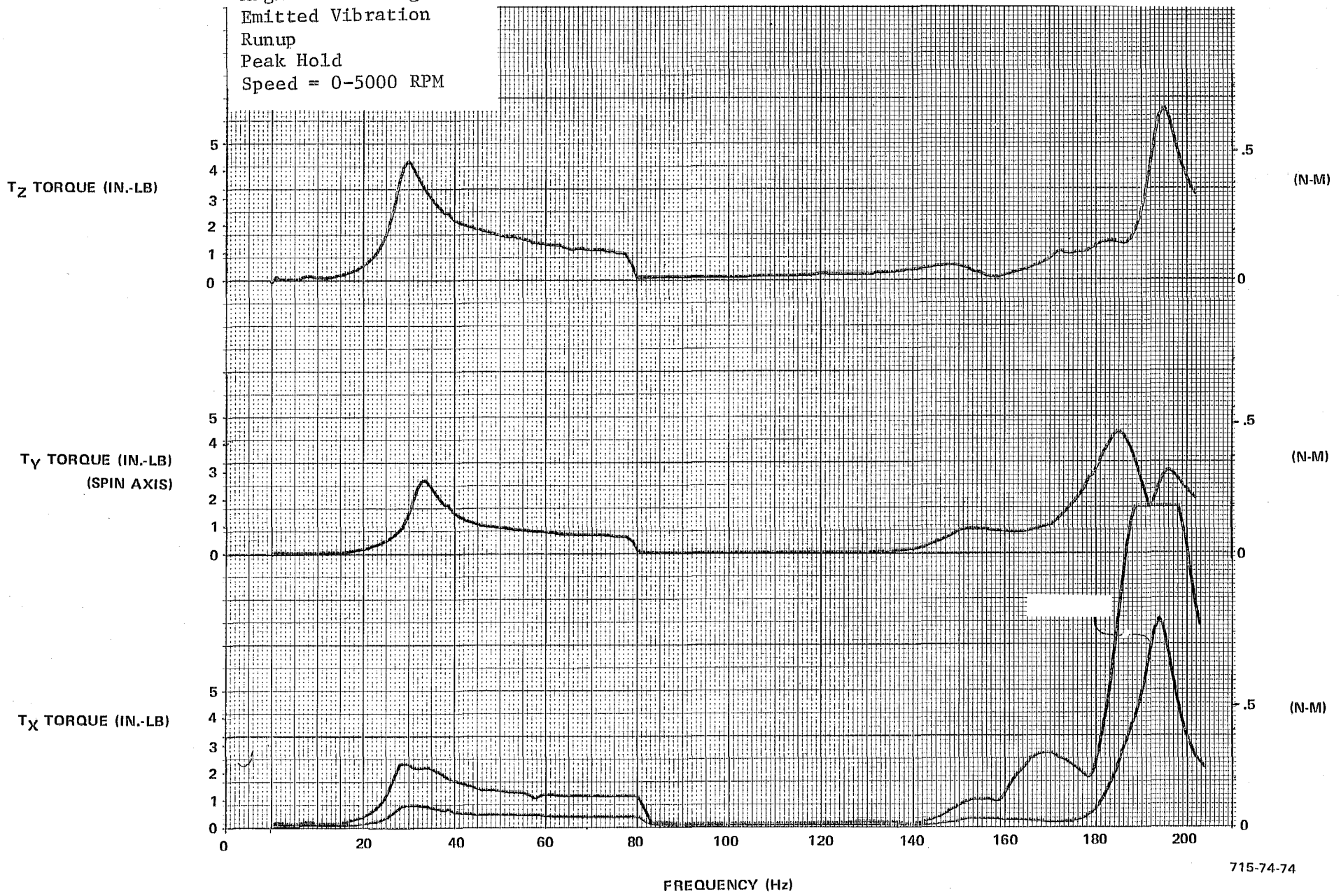

response for a wheel after passing through its critical resonance. The spin axis force, F_y, increases linearly with speed. At 5000 rpm the axial force is .3 pound compared to the radial force of only .2 pound.

The three-torque responses reach a peak at approximately 30 to 34 Hz and they level off at a lower amplitude at about 70 Hz. This, again, is typical of a wheel after passing through a critical frequency resonance.

Figures 5.4-6 and 5.4-7 show the emitted forces and moments, respectively, for an MMB rundown from 5000 to 0 rpm. The results are very similar to the run-up data. Note how quiet the data is beyond the wheel speed (83 to 140 Hz) compared to the results on the ball bearing wheels.

Tracking Filter Runup - Figures 5.4-8 and 5.4-9 show the forces and torques, respectively, for a runup of the MMB from 0 to 5000 rpm while using a tracking filter tuned to wheel speed. The responses are similar to those obtained with the peak hold mode runup; the radial force peaks are 1.20 and 1.06 pounds in the F_z and F_x axes, respectively. Again, the different frequency resonance is evident in the two radial axes. The torques are also similar to the peak hold mode data. The peak spin axis torque here is 3.0 in-lb compared to 2.8 in-lb (Figure 5.4-5) in the peak hold mode.

Constant Speed Runs - Figures 5.4-10 through 5.4-15 depict the emitted vibration signatures at 1500, 3000, and 5000 rpm. This data shows harmonics existing at multiples of the wheel speed. In Figure 5.4-10, a fundamental force component is present in all axes at 24.4 Hz with second, third and fourth harmonics evident at lower amplitudes. Similar harmonics can be seen in the torque curves in Figure 5.4-11 out to the sixth harmonic (146 Hz). The remaining curves show similar responses with the 34-Hz radial resonance prominent for a speed of 3000 rpm. At 5000 rpm only the fundamental frequency is evident in the 20- to 100-Hz range. The magnetic bearing has no lower retainer frequency and exhibits a very quiet response at frequencies below wheel speed. Note that at all speeds the maximum force is along the spin axis and at wheel speed is about twice as large as the radial force.

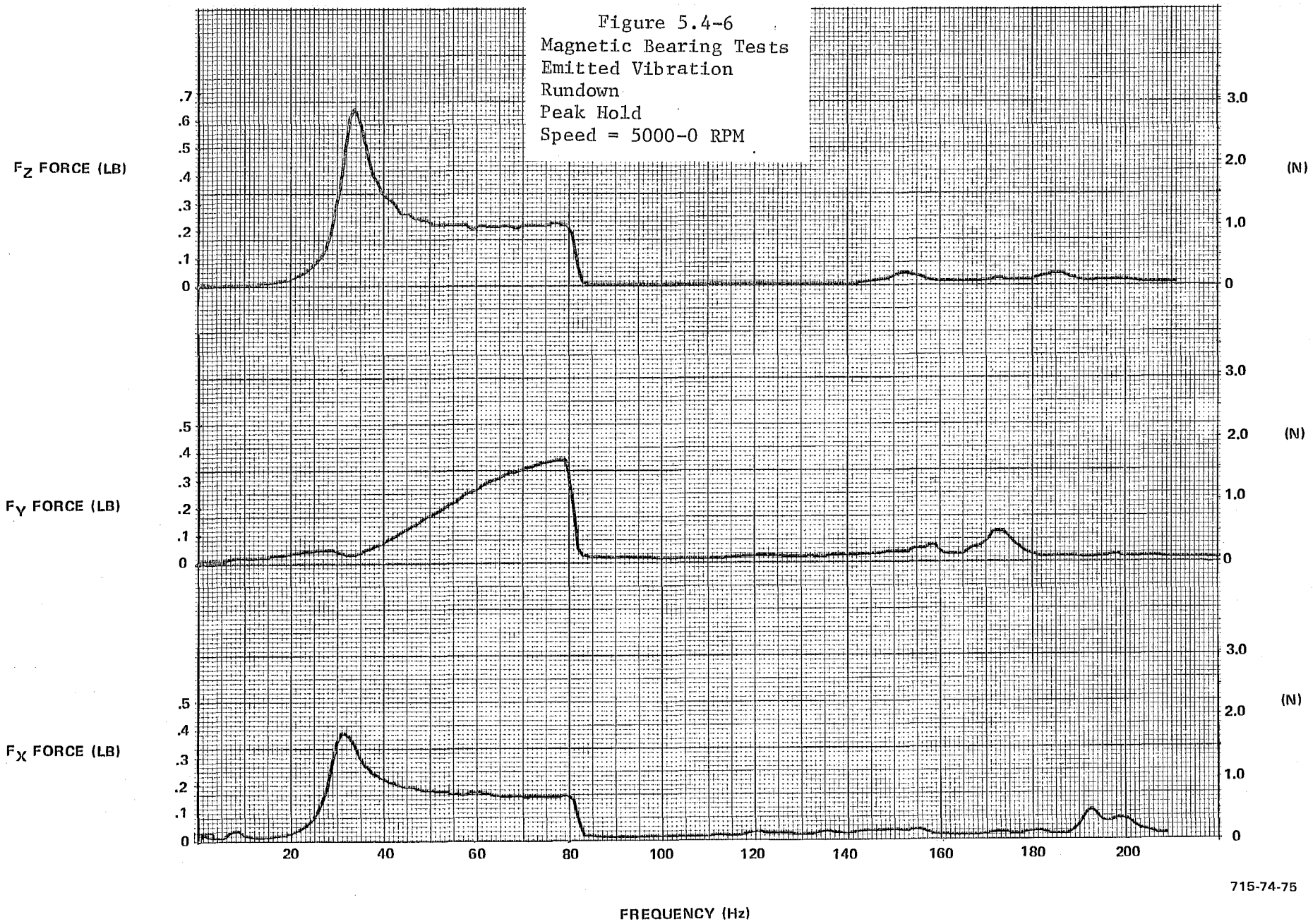
Figure 5.4-6
Magnetic Bearing Tests
Emitted Vibration
Rundown
Peak Hold
Speed = 5000-0 RPM
F_Z FORCE (LB)
F_Y FORCE (LB)
F_X FORCE (LB)
.7
.6
.5
.4
.3
.2
.1
0
3.0
2.0
1.0
(N)
20
40
60
80
100
120
140
160
180
200
FREQUENCY (Hz)
715-74-75

Figure 5.4-7
Magnetic Bearing Tests
Emitted Vibration
Rundown
Peak Hold
Speed = 5000-0 RPM

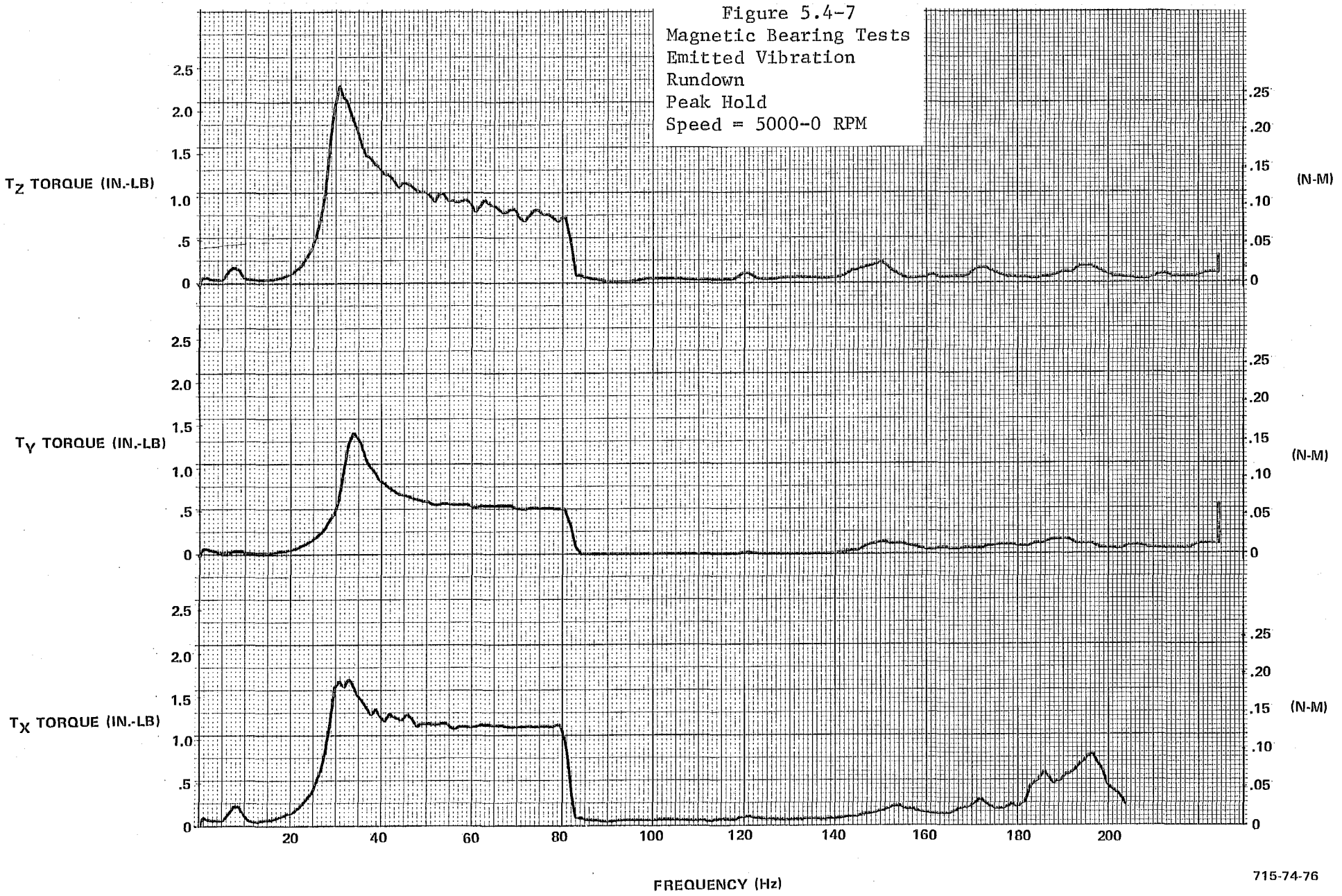

715-74-76

Figure 5.4-8
Magnetic Bearing Tests
Emitted Vibration
Runup
Tracking Vibration
Speed = 0-5000 RPM

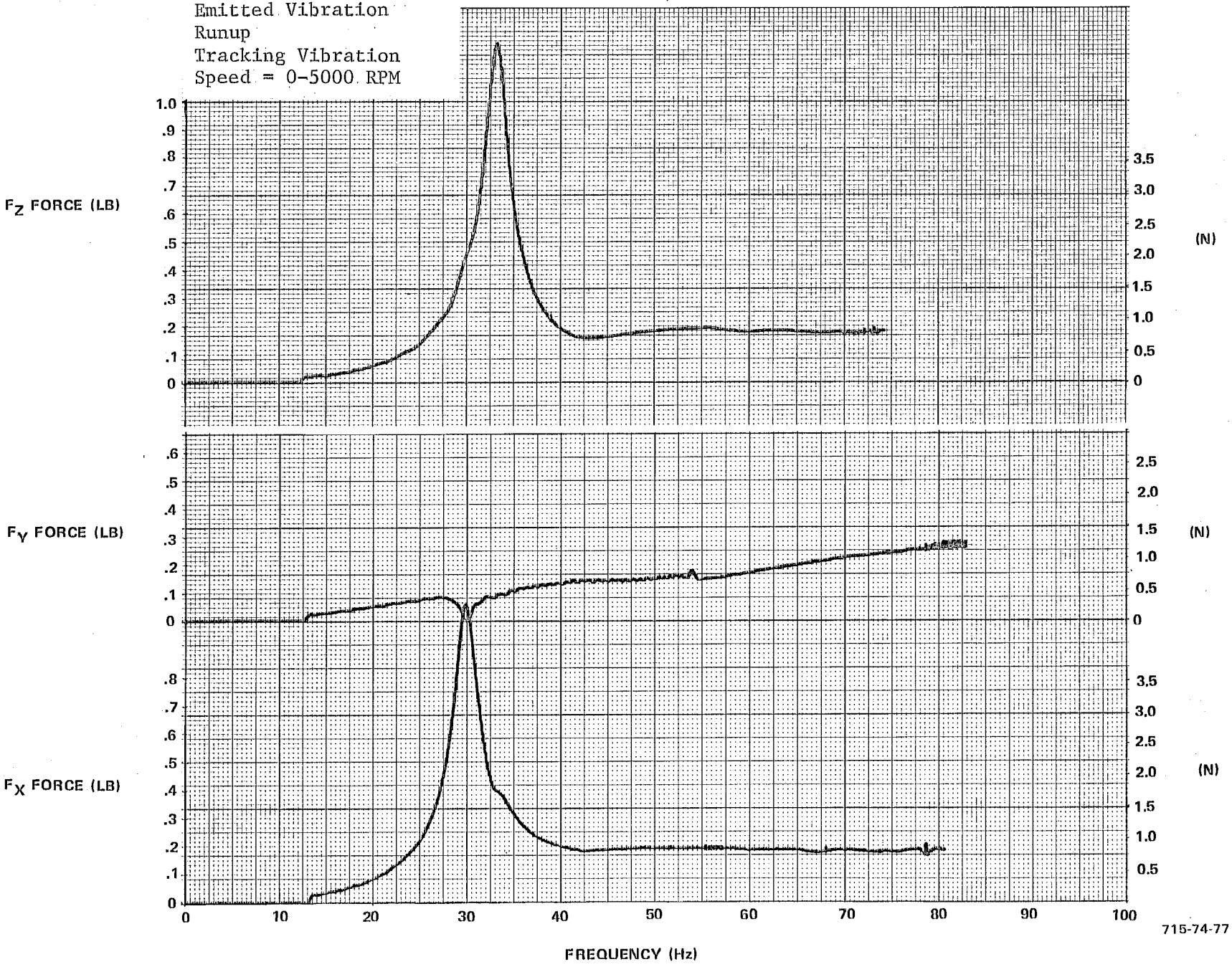

715-74-77

Figure 5.4-9
Magnetic Bearing Tests
Emitted Vibration
Runup
Tracking Filter
Speed = 0-5000 RPM

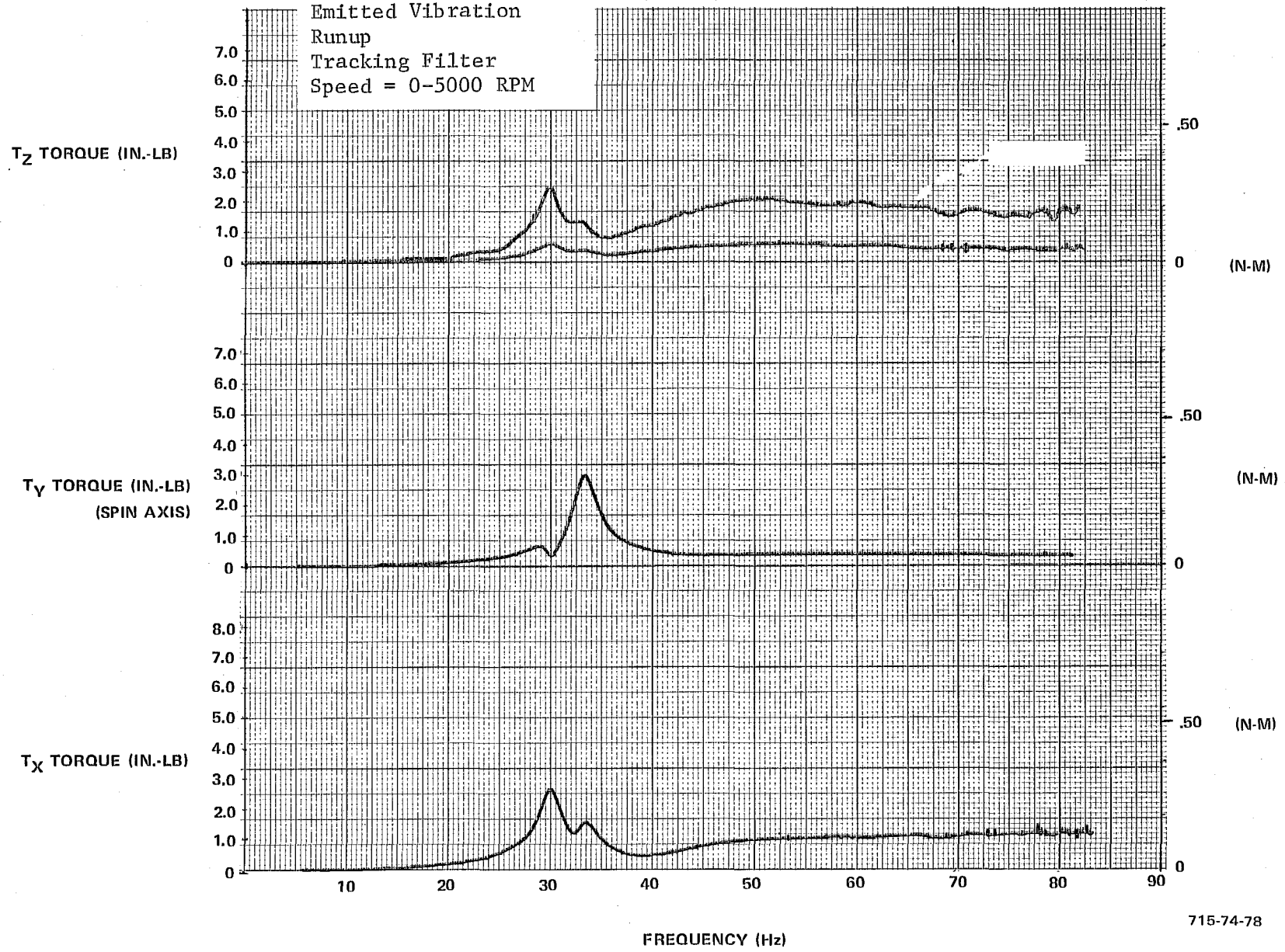

Figure 5.4-10
Magnetic Bearing Tests
Emitted Vibration
Constant Speed
1 Min Peak Hold
Speed = 1500 RPM

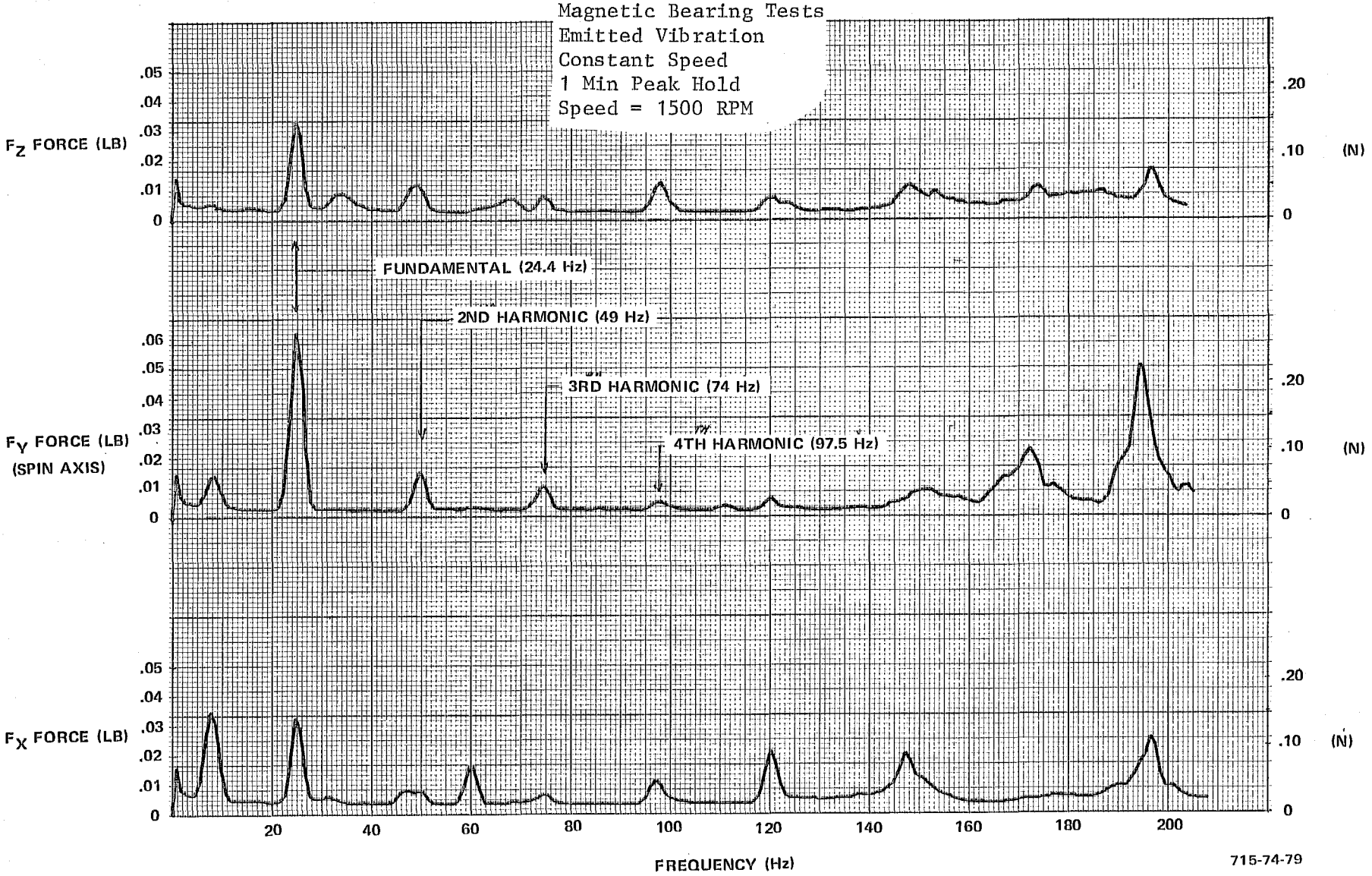

715-74-79

Figure 5.4-11
Magnetic Bearing Tests
Emitted Vibration
Constant Speed
1 Min Peak Hold
Speed = 1500 RPM

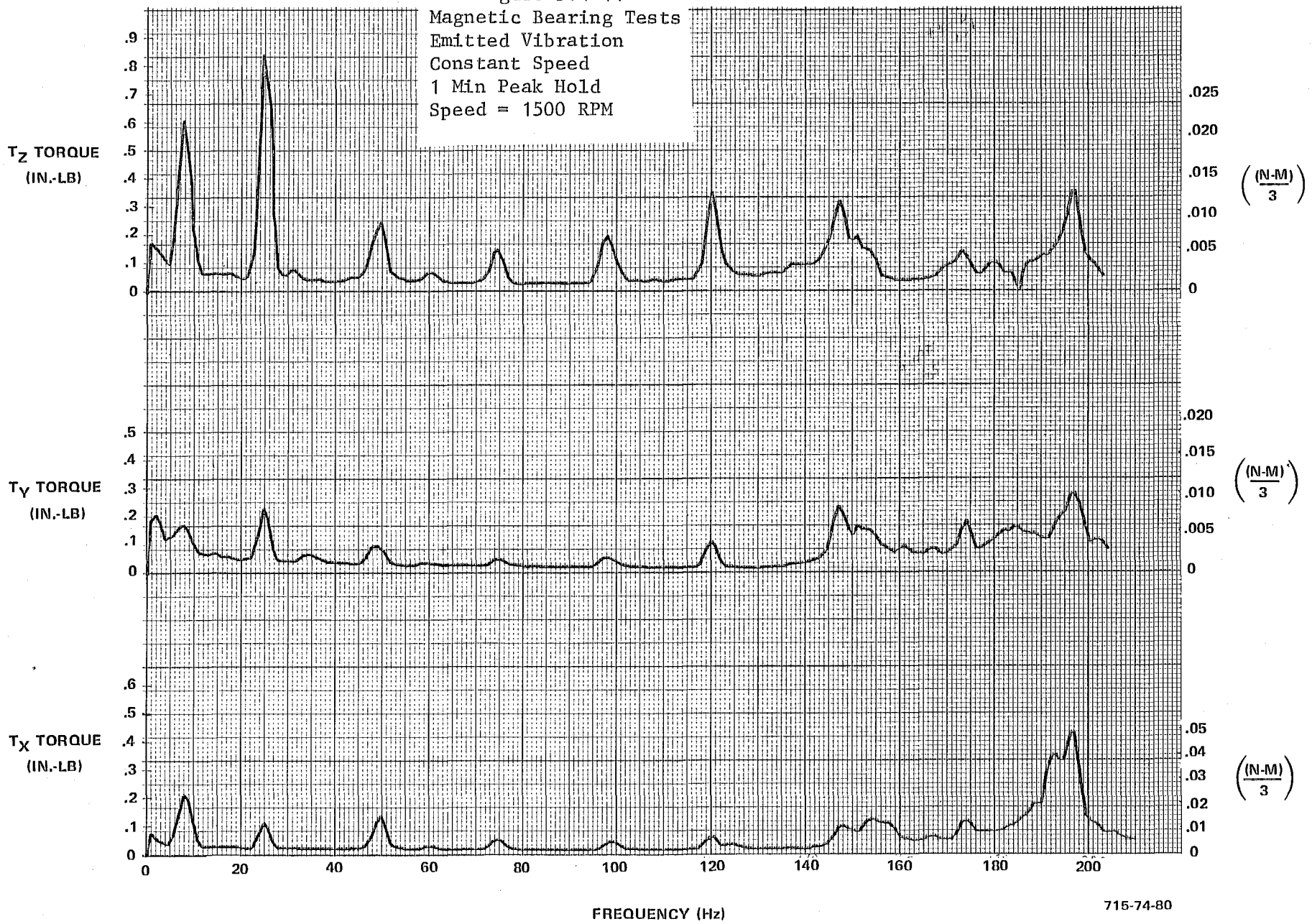

Figure 5.4-12
Magnetic Bearing Tests
Emitted Vibration
Constant Speed
1 Min Peak Hold
Speed = 3000 RPM

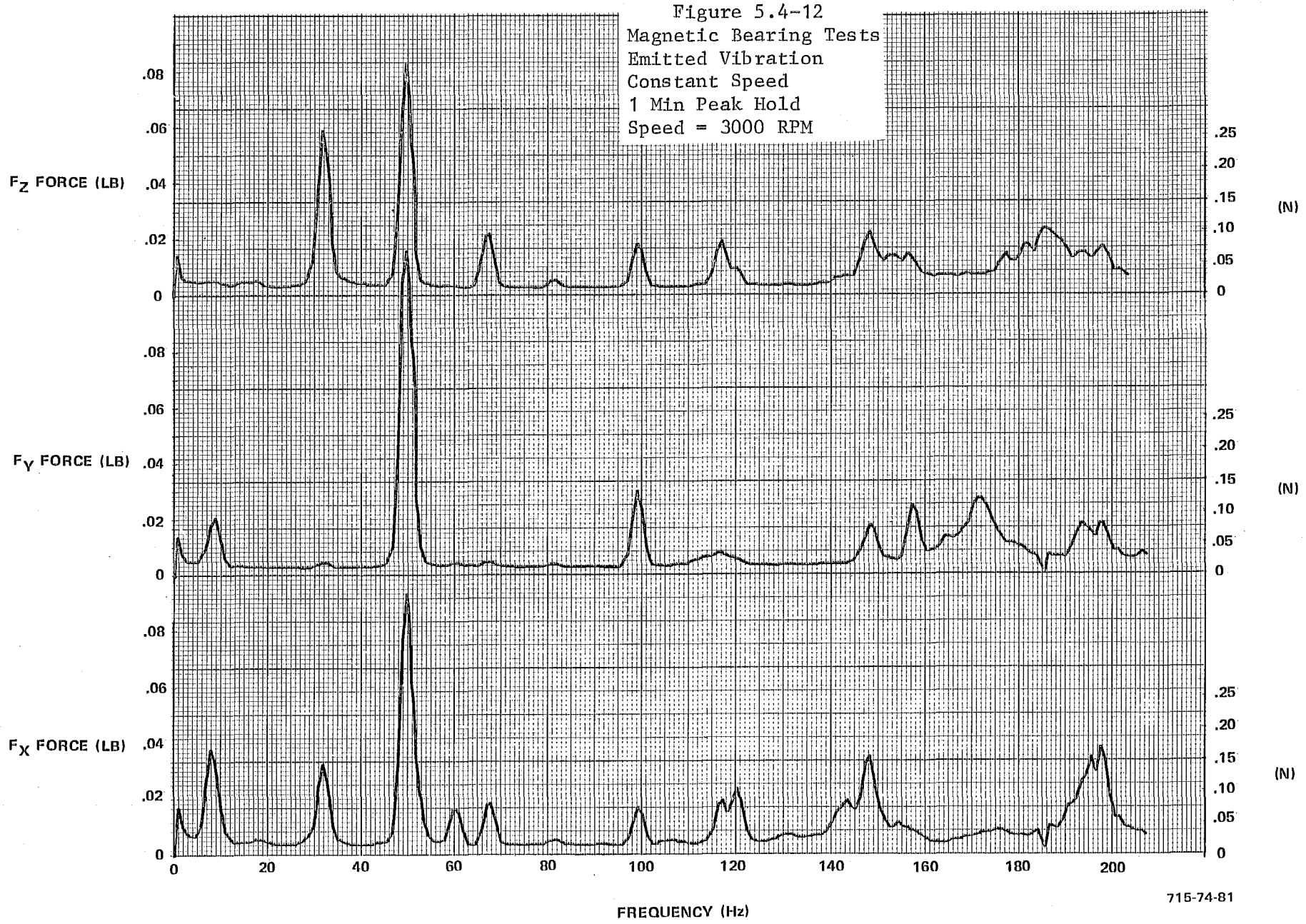

715-74-81

Figure 5.4-13
Magnetic Bearing Tests
Emitted Vibration
Constant Speed
1 Min Peak Hold
Speed = 3000 RPM

Figure 5.4-14
Magnetic Bearing Tests
Emitted Vibration
Constant Speed
1 Min Peak Hold
Speed = 5000 RPM

715-74-83

Figure 5.4-15
Magnetic Bearing Tests
Emitted Vibration
Constant Speed
1 Min Peak Hold
Speed = 5000 RPM

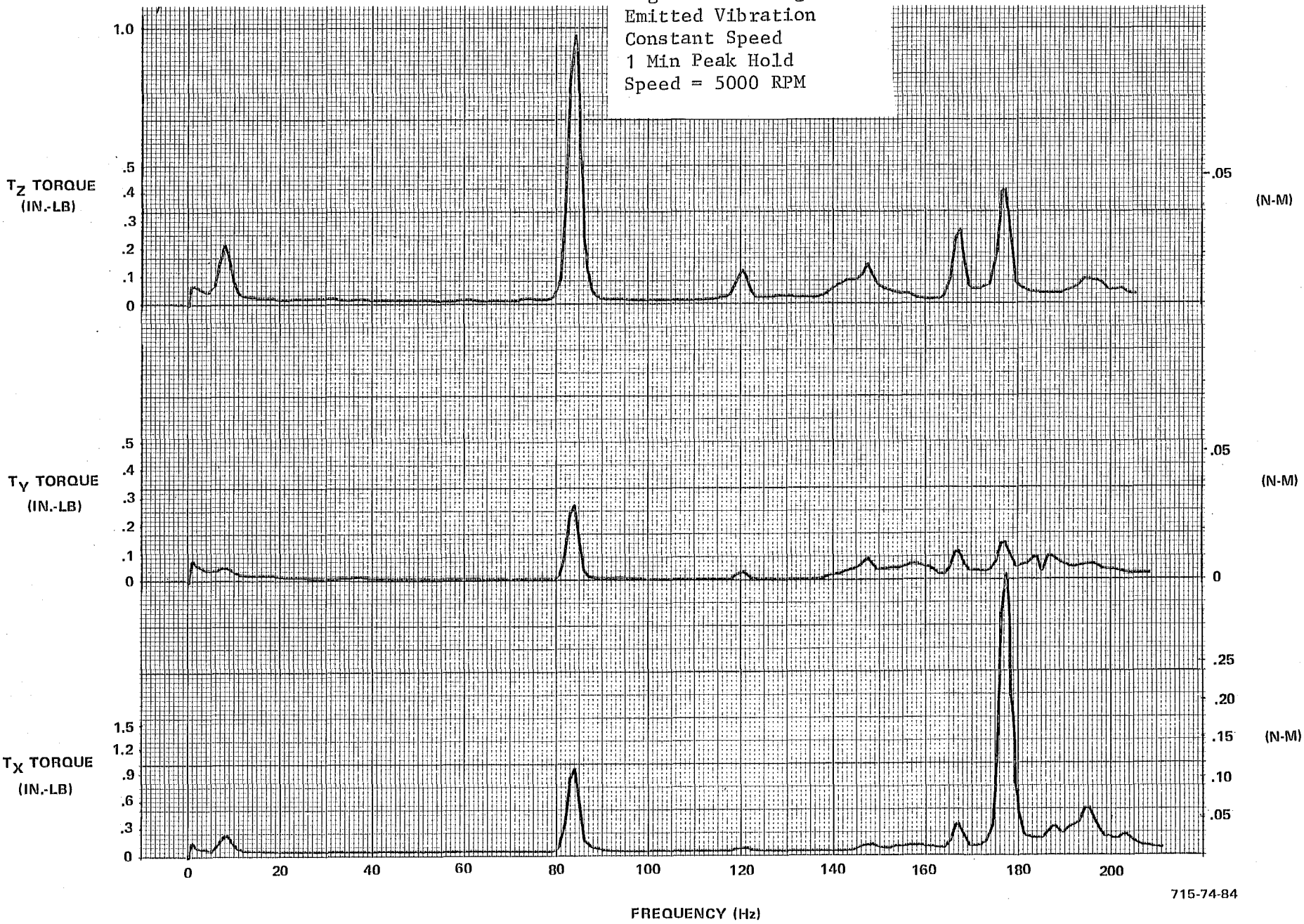

TABLE 5.4-1

MAGNETIC BEARING TESTS

Run No.	Response Axis						Rotor Speed (rpm)	Type of Run
	F_x	F_y	F_z	T_x	T_y	T_z		
*1	X	X	X				0	Fixture Calibration, F_x Input
2				X	X	X	0	Fixture Calibration, F_x Input
3	X	X	X				0	Fixture Calibration, F_y Input
4				X	X	X	0	Fixture Calibration, F_y Input
5	X	X	X				0	Fixture Calibration, F_z Input
6				X	X	X	0	Fixture Calibration, F_z Input
7	X	X	X				0	Fixture Calibration, T_x Input
*8				X	X	X	0	Fixture Calibration, T_x Input
9	X	X	X				0	Fixture Calibration, T_y Input
10				X	X	X	0	Fixture Calibration, T_y Input
11	X	X	X				0	Fixture Calibration, T_z Input
*12				X	X	X	0	Fixture Calibration, T_z Input
13	X	X	X				1000	Constant Speed (1 minute peak hold)
14				X	X	X	1000	Constant Speed (1 minute peak hold)
*15	X	X	X				1500	Constant Speed (1 minute peak hold)
*16				X	X	X	1500	Constant Speed (1 minute peak hold)
17	X	X	X				2000	Constant Speed (1 minute peak hold)
18				X	X	X	2000	Constant Speed (1 minute peak hold)
19	X	X	X				2500	Constant Speed (1 minute peak hold)
20				X	X	X	2500	Constant Speed (1 minute peak hold)
*21	X	X	X				3000	Constant Speed (1 minute peak hold)
*22				X	X	X	3000	Constant Speed (1 minute peak hold)
23	X	X	X				3500	Constant Speed (1 minute peak hold)
24				X	X	X	3500	Constant Speed (1 minute peak hold)
25	X	X	X				4000	Constant Speed (1 minute peak hold)
26				X	X	X	4000	Constant Speed (1 minute peak hold)
27	X	X	X				4500	Constant Speed (1 minute peak hold)
28				X	X	X	4500	Constant Speed (1 minute peak hold)
*29	X	X	X				5000	Constant Speed (1 minute peak hold)

* = Denotes that run is included in this report.

TABLE 5.4-1 (cont)

MAGNETIC BEARING TESTS

Run No.	Response Axis						Rotor Speed (rpm)	Type of Run
	F_x	F_y	F_z	T_x	T_y	T_z		
*30				X	X	X	5000	Constant Speed (1 minute peak hold)
*31	X	X	X				0-5000	Runup, Peak Hold
*32				X	X	X	0-5000	Runup, Peak Hold
*33	X	X	X				0-5000	Runup, Tracking Filter
*34				X	X	X	0-5000	Runup, Tracking Filter
*35	X	X	X				5000-0	Rundown, Peak Hold
*36				X	X	X	5000-0	Rundown, Peak Hold
37	X	X	X				5000-0	Rundown, Tracking Filter
38				X	X	X	5000-0	Rundown, Tracking Filter

5.5 COMPARATIVE TEST RESULTS

Many comparisons between the three momentum wheels tested can be made from the test data presented in Paragraphs 5.2, 5.3 and 5.4. Two types of comparisons are made in this paragraph: the HEAO and FSC wheel signatures and the FSC and MMB characteristic curves. This provides a comparison between two ball bearing wheels of very similar design, but different size, and between a ball and magnetic bearing wheel model.

HEAO-FSC Comparison - Figure 5.5-1 shows the radial and axial forces emitted from the two wheels. The HEAO radial force is higher, corresponding to the static unbalance difference between the wheels: .001 ounce-inch for FSC and .005 ounce-inch for HEAO. Both wheels exhibit a large peak force at their gyroscopic resonant frequency. These force frequencies have been identified and predicted in the analysis, but the force amplitudes cannot be predicted accurately by analysis. These are highly undamped resonances, and establishing a confident prediction will require more detailed analysis and study of the HEAO type RWA design.

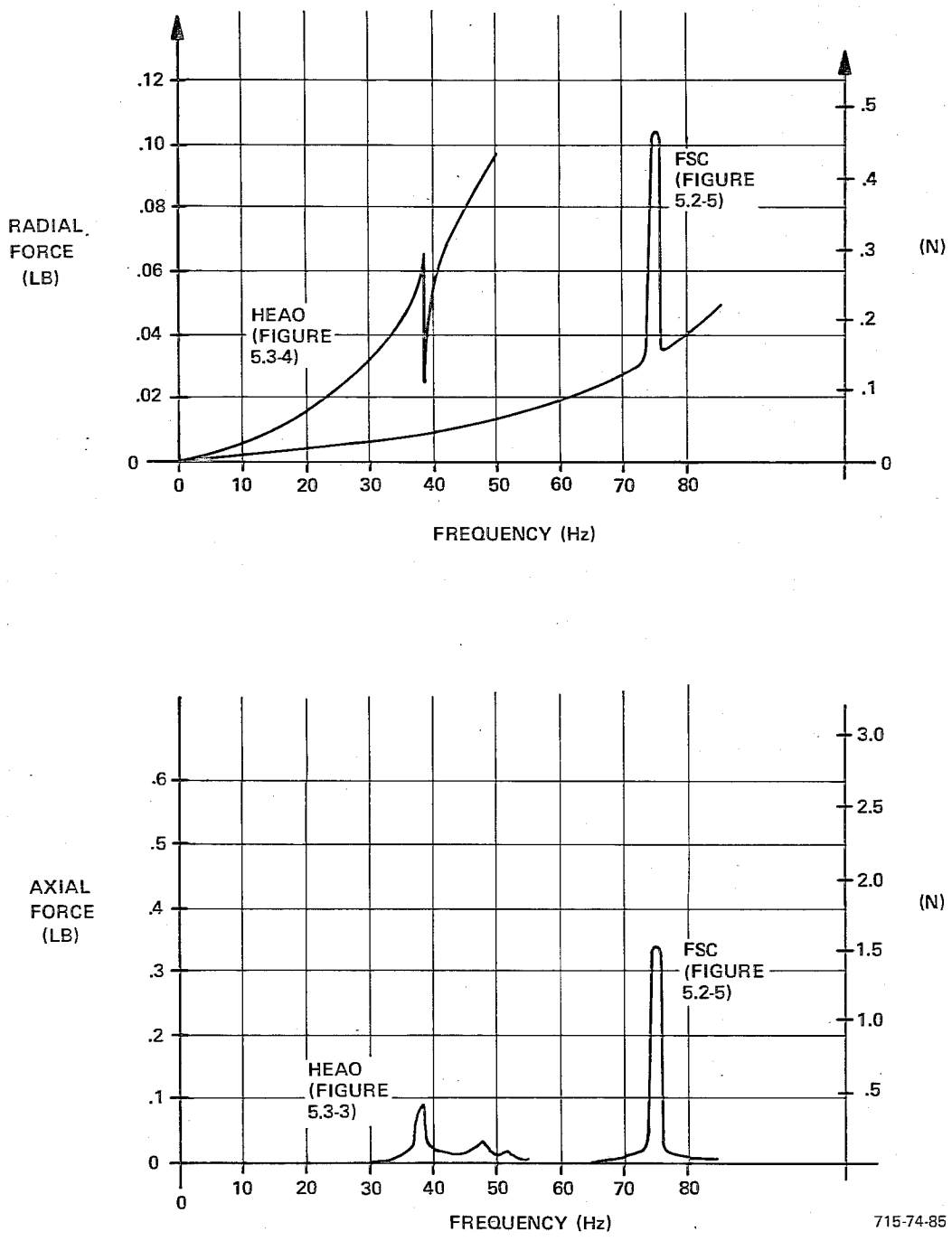

Figure 5.5-1
Reaction Wheel Force Comparison

The axial forces are very low, except for the gyroscopic resonant frequency where a force exceeding the radial force is present.

Figure 5.5-2 shows the radial and axial torques emitted from the two wheels. The radial torques are very low, except at the gyroscopic resonant frequency and at one additional frequency (23 Hz) in the HEAO RWA. As stated above, the frequencies are predictable from existing models, but the peak amplitudes are not predictable presently. The HEAO radial peak torque is 2.4 in-lb and the FSC peak torque is 1.4 in-lb.

The axial torque amplitude of the two wheels is significantly different at the gyroscopic resonance. The HEAO torque is less than one tenth the FSC level; no known reason exists for this difference.

FSC-MMB Comparison - Figures 5.5-3 and 5.5-4 show the emitted force and torque vibrations respectively, from the FSC RWA and the MMB wheel. Both the force and torque values for the MMB exceed those of the FSC except when the FSC unit has a gyroscopic resonance at 75 hertz.

This comparison, although interesting, is similar to comparing "apples and oranges". The FSC is a complete reaction wheel with housing and large rotor inertia, specifically designed as a flight unit. Whereas, the MMB was never intended to be a reaction wheel; its momentum is less than 1 ft-lb-sec at 5000 RPM. Instead it was built as a test fixture for a magnetic bearing suspension with a test rotor and no housing or means of evacuation was present. The data shows some characteristics of the magnetic bearing itself, such as the radial resonance, but to get a valid comparison of ball to magnetic bearing reaction wheels a magnetic bearing reaction wheel designed with a large inertia rotor and evacuated housing would have to be tested. Unfortunately, no such wheel was available for test during this study.

5.6 DATA ANALYSIS

This section presents the results of dynamic analysis on the data obtained during the hard-mount test of the FSC, HEAO, and MMB wheels. Since the most prominent and largest amplitude phenomena in the data for all wheels were dynamic resonances within the 0- to 130-Hz frequency range of interest, the analysis effort was directed at identifying and explaining the causes for these phenomena. In most cases good agreement between test data and analysis exists for identifying the frequencies; however, predicting the amplitudes is another matter. To

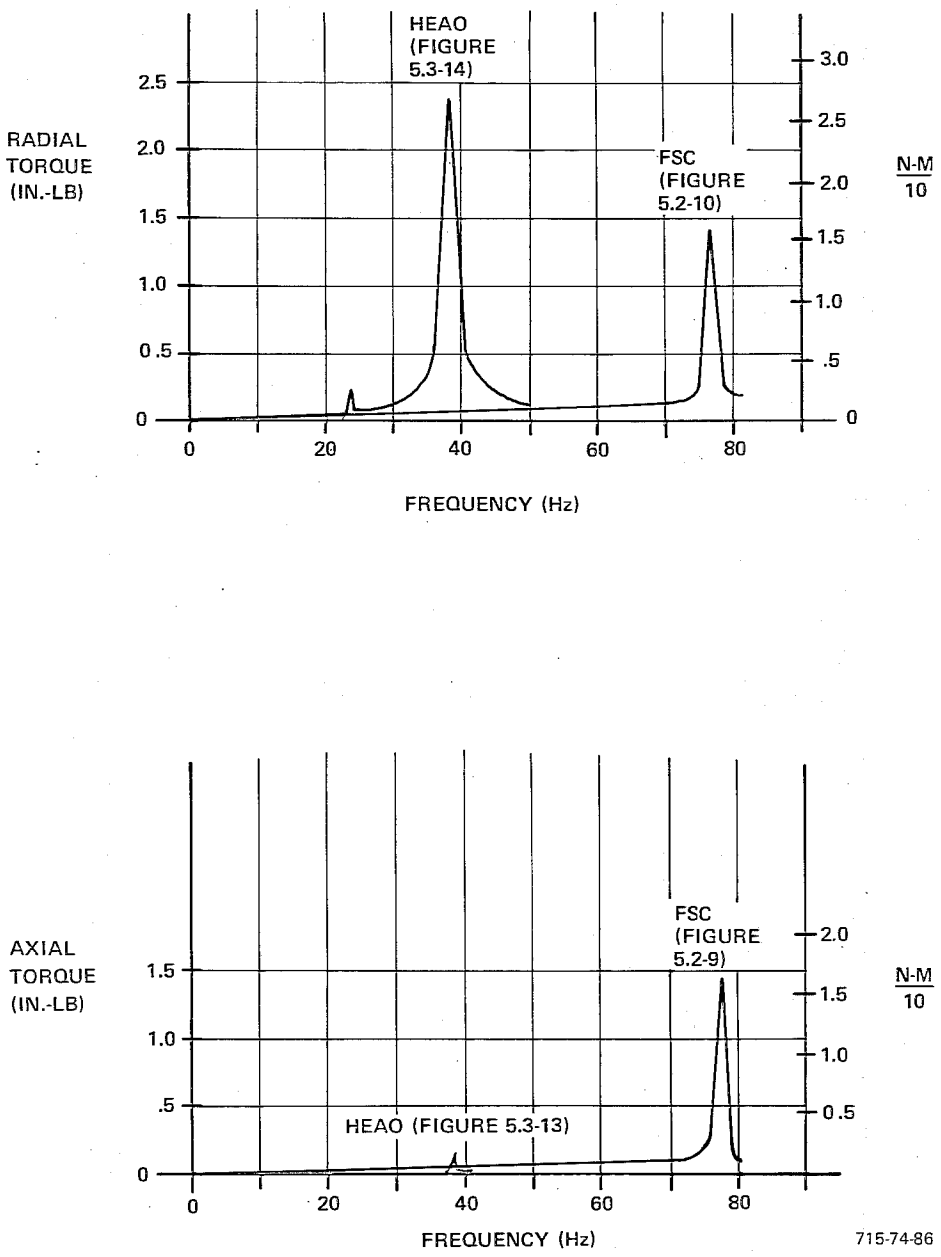

Figure 5.5-2
Reaction Wheel Torque Comparison

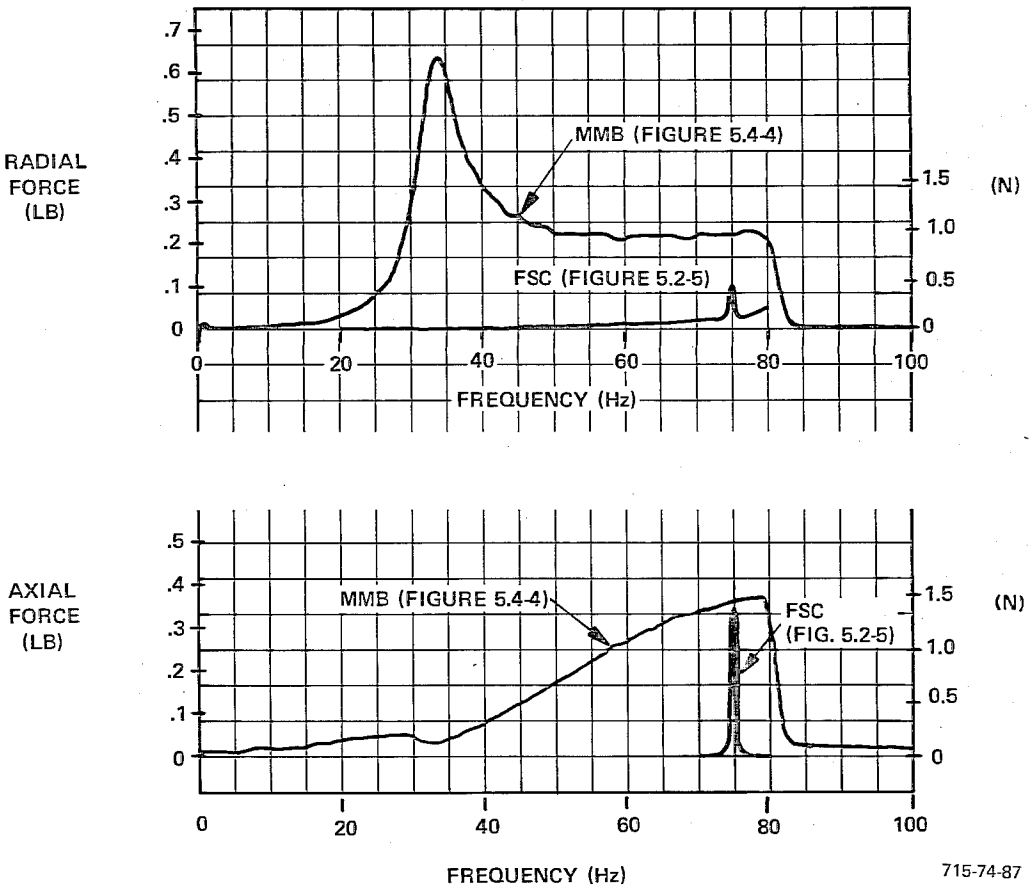

Figure 5.5-3
FSC/MMB Force Comparison

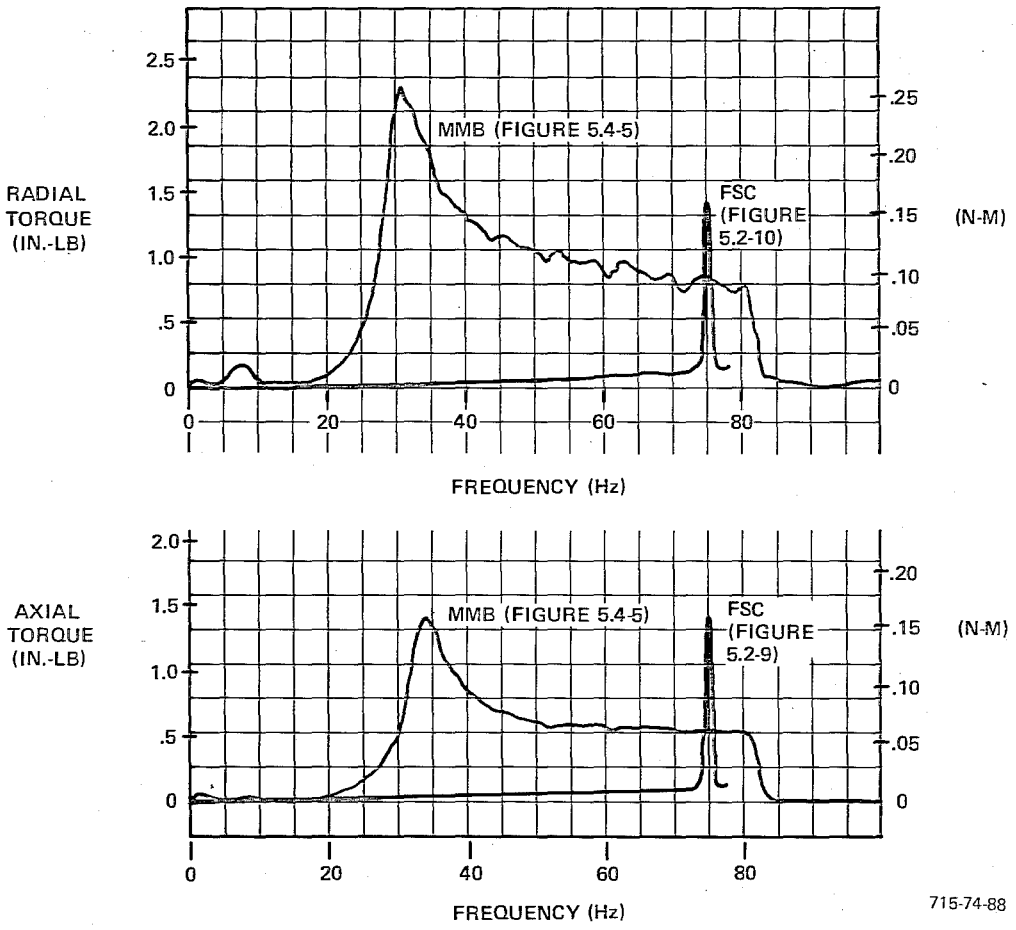

Figure 5.5-4
FSC/MMB Torque Comparison

accurately predict the amplitudes of the dynamic resonances requires a good model for microinch damping factors in the reaction wheel case and structure, as well as other more complex second order effects which have not been analyzed or measured to date. Therefore, within the scope of this study, no attempt was made at matching the amplitudes of resonant peaks against analysis; the only effort was to match the frequencies.

The appendix, Rotational Dynamic Theory, describes the rotational static and dynamic fundamentals in a lucid manner, describing the effects of static unbalance, dynamic unbalance, and axial bearing runout and how they affect disk- and shaft-shaped rotors differently. This section uses the theory developed with a computer program and additional analysis of static vibration data to identify and explain the test data. The static (nonrunning) vibration test data is first used to identify pertinent resonances within the unit. This is possible since during vibration testing ten accelerometers are placed at various locations within the unit such as on the rotor rim, rotor web, motor case, bearing cartridge, case top, etc. By noting the amplitude and phase frequency responses for each accelerometer, a good understanding of the important resonances are obtained. In some cases, such as for the MMB where test data was not available, a calculation was performed using the design drawings. The derived spring constants and masses obtained from this effort were then input to a Sperry digital computer program which is used for both RWA and CMG dynamic analysis. Since the reaction wheel has no gimbal axis, many of the equations simplify considerably. The results of this computer run were then compared to the test data in Sections 5.2 through 5.4 to determine the level of agreement. In the analysis, such things as motor case and bearing dynamics were neglected in favor of looking at the lower frequency (0- to 80-Hz) dynamics. To get better agreement with test data these second order factors, as well as structural damping, will have to be considered in the future.

5.6.1 Fleet Sat Com Reaction Wheel Assembly

Static Vibration Data Analysis - Three different resonances can be associated with the rotor and rotor suspension in the FSC RWA. During vibration testing the resonances were identified as a cross-axis torsional resonance at 120 Hz, an axial resonance at 550 Hz, and a radial resonance at 620 Hz. Other resonances encountered were modes involving the housing as the flexible element,

and these were not applicable. To confirm the accelerometer data which indicated the various rotor web modes, calculations were performed to ensure the modes measured were fully understood before analysis of dynamic data (wheel running) was undertaken.

The lowest frequency resonance (120 Hz) was of the most interest, as it was felt this was the resonance which the gyroscopics moved to 75 Hz during runup. The web was modelled as a thin shell (Figure 5.6-1) and a computer program was used to determine the influence coefficients between the applied forces and deflections. The web torsional stiffness from this analysis is indicated in Table 5.6-1 with the other FSC parameters used for the data analysis.

The calculation frequencies of Table 5.6-2, using the web stiffnesses and rotor rim mass and rotor transverse inertia, correlate well with the measured data. The calculated frequency for the radial resonance assumed infinitely stiff spin bearings which yielded a higher resonant frequency than was actually present. No data was available for the spin bearing radial stiffness, but, as was shown in the rotor dynamics section, the location of the compliance in the radial direction does not affect the results for the wheel running. Thus, an equivalent spring was calculated based on the vibration data and used for the dynamic data analysis.

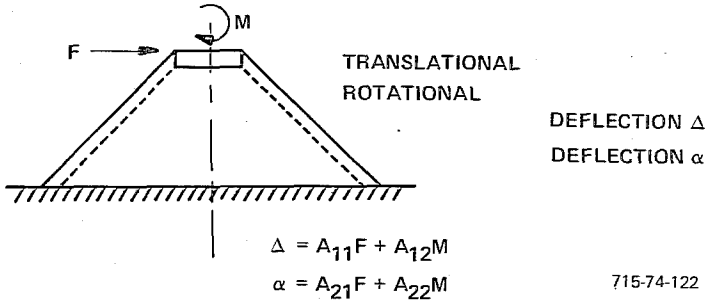

Figure 5.6-1
FSC RWA Thin Shell Web Model for
Torsional Spring Constant Calculation

TABLE 5.6-1

FLEET SAT COM PARAMETERS

Parameter	Value		Units	
Rotor Inertia Along Spin Axis	.0291	.0214	$n\text{-}m\text{-}sec^2$	$ft\text{-}lbf\text{-}sec^2$
Rotor Transverse Inertia	.0151	.0112	$n\text{-}m\text{-}sec^2$	$ft\text{-}lbf\text{-}sec^2$
Rotor Mass	2.402	.1646	kg	slugs
Rim Mass	1.780	.122	kg	slugs
Measured Web Axial Stiffness	1.751×10^7	1.2×10^6	n-m	lbf/ft
Calculated Web Torsional Stiffness	9825	7246	n-m/rad	ft-lbf/rad
Measured Rotor (web and shaft)	1.95×10^8	1.337×10^7	n-m	lbf/ft

TABLE 5.6-2

MEASURED AND PREDICTED RESONANCES FOR FLEET SAT COM

Resonance Description	Measured Frequency	Calculated Frequency
Static Torsional Resonance	120 Hz (754 rad/sec)	128 Hz (804 rad/sec)
Static Radial Resonance	620 Hz (3895 rad/sec)	1650 Hz (10,367 rad/sec)
Static Axial Resonance	550 Hz (3456 rad/sec)	493 Hz (3098 rad/sec)
Torsional Resonance During Runup	75 Hz (471 rad/sec)	70 Hz (440 rad/sec)

FSC Dynamic Vibration Data Analysis - With the three modes discussed above related to the rotor and its suspension, a computer program used the resonant frequencies in conjunction with Equations A-3 and A-7 to simulate the rotor dynamics during runup. This program used the resonant frequencies measured during static testing along with the transverse rotor inertia and rotor mass to calculate torsional and radial spring constants. This was accomplished by using the characteristic equations for A-3 and A-7 with $\omega_s = 0$ to calculate the torsional stiffness ($\dot{K}_R$) and the radial stiffness (K_R). The computer program is also capable of performing the above calculations with coupling between the radial and torsional modes due to cg offsets, rotor web geometry, etc, but this feature was not used in order to keep the results uncomplicated with second order effects. The program provided for inputting static unbalance forces, dynamic unbalance torques and a sinusoidal torque vector along a transverse direction fixed with respect to an inertial reference frame. Tektronix Computer graphic plot routines provided Bode plots for these three different excitations.

The plots of angular rotation and linear translation for the FSC are shown in Figure 5.6-2 through 5.6-4. The initial values of the output variable and its phase depend on the magnitude of the exciting force or torque and its phase and are not the items of concern here. Rather, the important information displayed in the curves is the location of resonant peaks and the slopes of the curves. As seen in Figure 5.6-2, the resonance of 70 Hz due to a fixed torque vector (axial runout) agrees closely with the data in Table 5.6-2 and Figure 5.2-9 for the actual measured resonance of 75 Hz. Figure 5.6-3 indicates that for a disc rotor there is no critical speed. Figure 5.6-4 is the static unbalance plot with a critical frequency of 620 Hz. This frequency is beyond the range of frequencies recorded for the data and was not seen.

As discussed in the rotor dynamics appendix, the fixed (nonrotating) torque disturbance may be caused by ball bearing axial runout. Further work is necessary to accurately identify its cause. The conformation of the 75-Hz resonance by the computer simulations indicates that the 120-Hz static vibration torsional mode becomes a 75-Hz resonance with the wheel running. This resonance is the only resonance in the region of interest from 0 to 150 Hz. As noted in the appendix, this resonance is not excited by pure dynamic unbalance, but some other cause with a body fixed torque at wheel speed. Two possible methods are available for reducing the effects of the 75-Hz torsional resonance. The forcing function

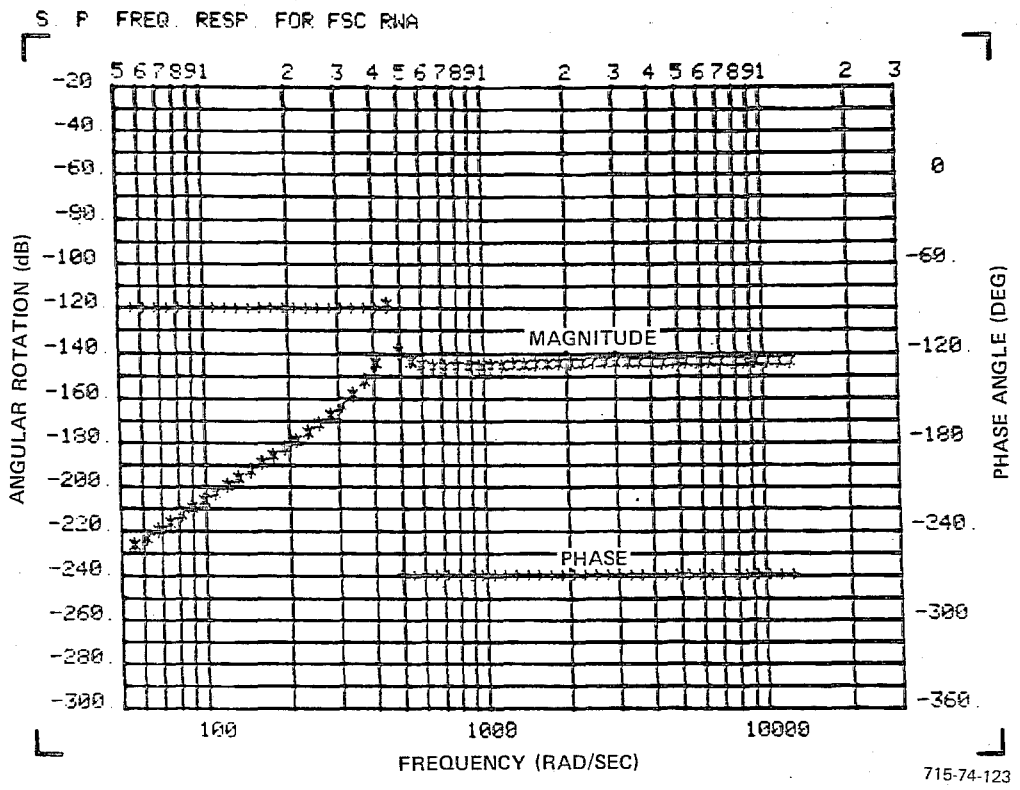

Figure 5.6-2
Fixed Torque Vector Response for FSC RWA

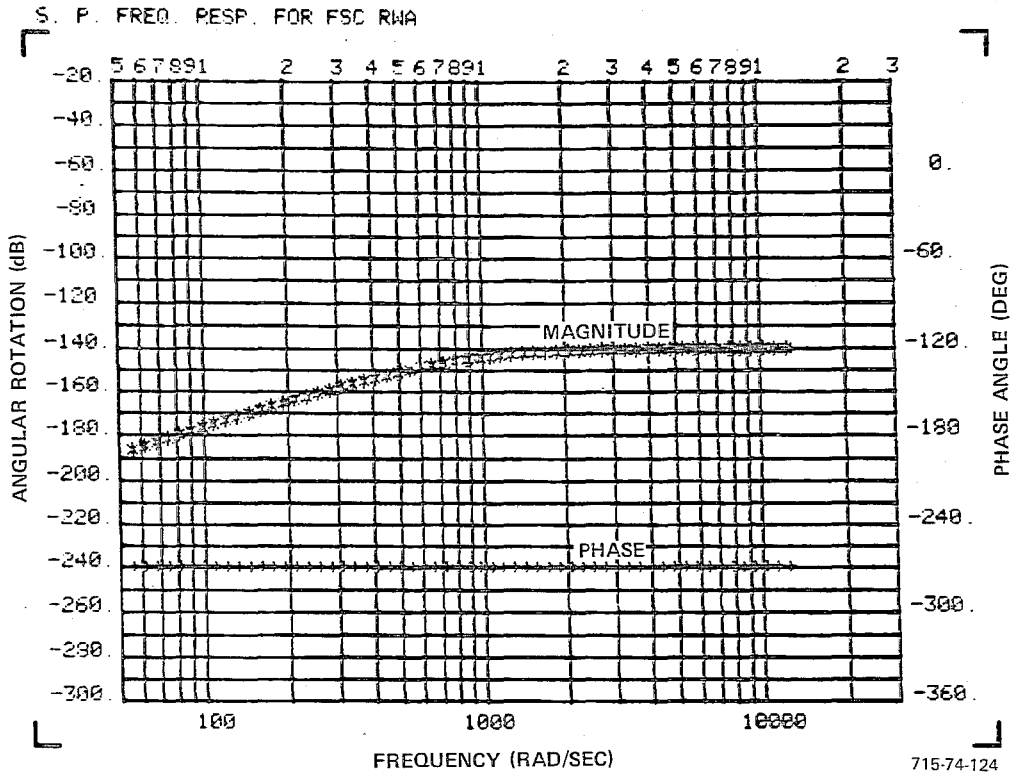

Figure 5.6-3
Dynamic Imbalance Response for FSC RWA

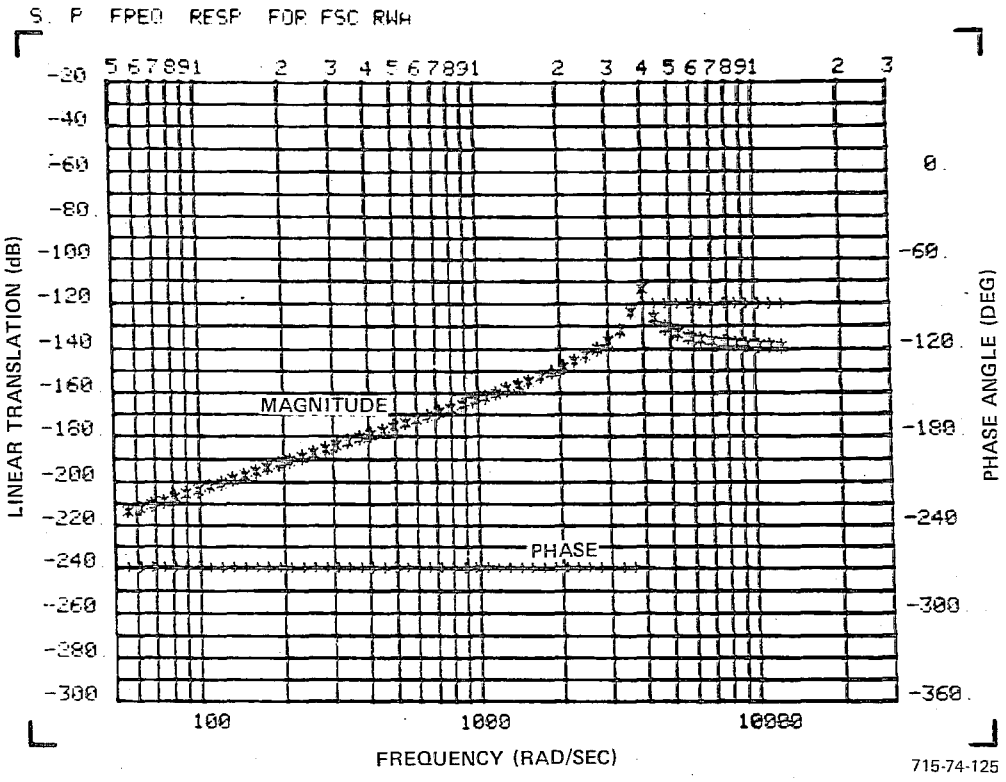

Figure 5.6-4
Static Imbalance Response for FSC RWA

to the wheel could be reduced by improving the bearing axial runout and using closer tolerances on the housing cg location, if this is actually the cause. A simpler approach, however, may be to stiffen the rotor web, thereby moving the resonance to a higher frequency. Such stiffening would require a small additional weight but may greatly improve the vibration characteristics of the FSC MWA in the 0- to 130-Hz region.

5.6.2 HEAO Reaction Wheel Assembly

Static Vibration Data Analysis - The parameters for the HEAO reaction wheel assembly are listed in Table 5.6-3, with measured and predicted resonance values in Table 5.6-4. Since this wheel is of a very similar design to the FSC wheel, the same rotor dynamics are present. The high predicted value for the static torsional resonance is probably due to the total rotor torsional stiffness being lower than that of just the rotor web due to additional compliance in the rotor shaft and bearings. The radial static resonance was difficult to extract from the vibration data due to many other housing and stator modes within this frequency range. However, once again, the resonance within the range of interest was a torsional rotor mode.

TABLE 5.6-3

HEAO PARAMETERS

Parameters	Value		Units	
Rotor Inertia Along Spin Axis	.196	.144	$n\text{-}m\text{-}sec^2$	$ft\text{-}lbf\text{-}sec^2$
Rotor Transverse Inertia	.113	.083	$n\text{-}m\text{-}sec^2$	$ft\text{-}lbf\text{-}sec^2$
Rotor Mass	7.76	.532	kg	slugs
Measured Web Torsional Stiffness	1.28×10^5	2.03×10^4	n-m/rad	ft-lbf/rad
Measured Web Radial Stiffness	3.22×10^7	2.21×10^6	n-m	lbf/ft

TABLE 5.6-4

MEASURED AND PREDICTED RESONANCES FOR HEAO

Resonance Description	Measured Frequency	Calculated Frequency
Static Torsional Resonance	65 Hz (408 rad/sec)	79 Hz (496 rad/sec)
Static Radial Resonance	Undetermined	324 Hz (2036 rad/sec)
Torsional Resonance During Runup	38 Hz (239 rad/sec)	39 Hz (245 rad/sec)

Dynamic Vibration Data Analysis - The computer plots for matching resonances during runup for the HEAO RWA have the same general shape as the FSC plots due to both wheels using similar disc type rotors. The predicted torsional resonance of 39 Hz, shown in Figure 5.6-5, due to a fixed torque excitation correlated well with the measured value of 38 Hz as in Figure 5.3-6. As with FSC, rotor web stiffening may move this resonance to a higher frequency.

5.6.3 Model Magnetic Bearing Wheel

Static Vibration Data Analysis - The parameters for the MMB are listed in Table 5.6-5, with resonances listed in Table 5.6-6. The static radial resonance is closely predicted using the measured radial spring constant and rotor weight. The absence of a measured or calculated torsional spring constant prevented predicting the torsional resonant frequency. It should be noted that due to the characteristics of the magnetic bearings, a calculation of torsional stiffness due to radial springs located at the bearings will yield a much greater value of torsional stiffness than is actually present. This is caused by a restoring force located at each bearing, and accurate prediction of this effect is being investigated.

Dynamic Vibration Data Analysis - The MMB rotor is a shaft rotor, and as explained in the rotor dynamics appendix it will exhibit a torsional resonance excited by dynamic unbalance. The calculated frequency as seen in Figure 5.6-6 matches the torsional resonance measured at 30 Hz. In addition, the radial resonance prediction agrees well with the measured value as shown in Figure 5.6-7. It appears from the dynamic data that the fixed torque excitation present in the FSC and HEAO RWA was not present, as this resonance calculated at 22 Hz

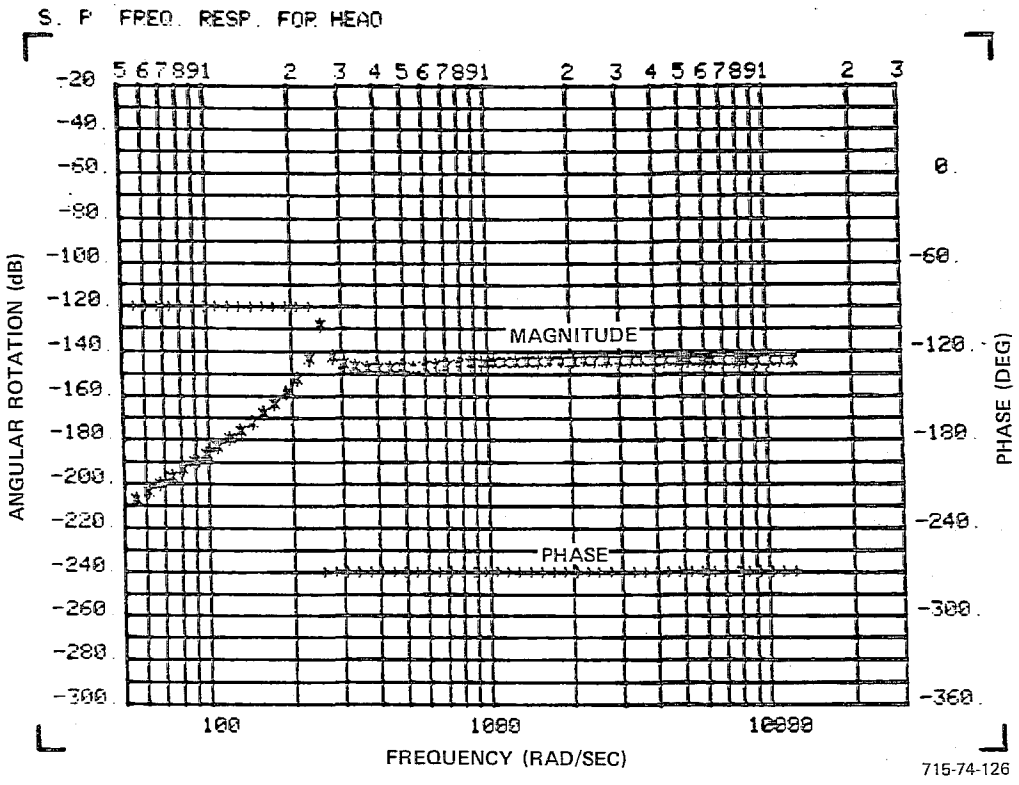

Figure 5.6-5
Fixed Torque Vector Plot for HEAO

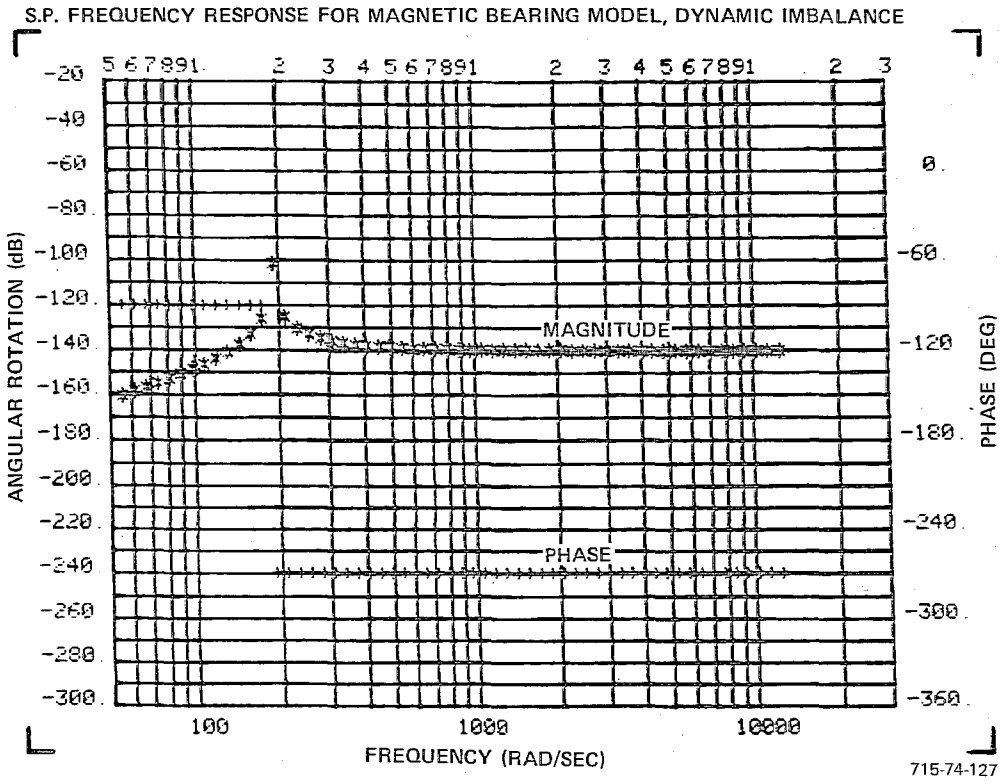

Figure 5.6-6
Dynamic Imbalance Response for Magnetic Bearing Model

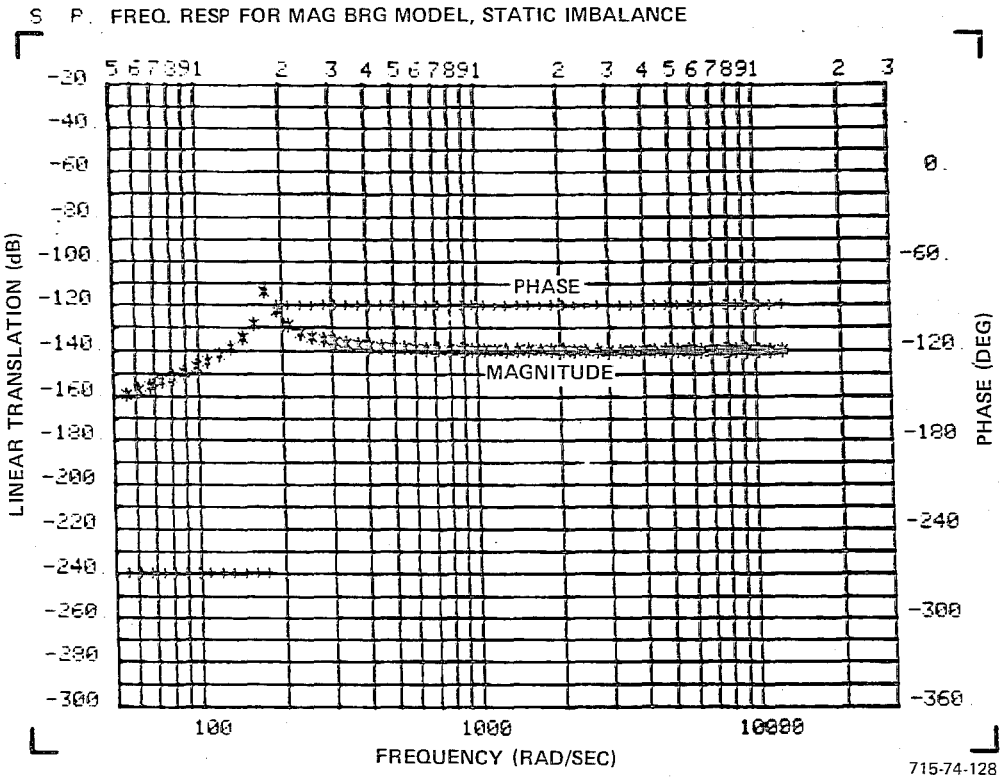

Figure 5.6-7
Static Imbalance Response for Magnetic Bearing Model

was not present in the measured data during runup. Since the torsional and static resonances are excited by rotor unbalance, improving the rotor balance would decrease the torques and forces exerted by the rotor at resonance. Another method would be to increase the torsional and radial stiffness and move the resonances to higher frequencies. Due to the characteristics of the magnetic bearings, the addition of eddy current damping could also be added to decrease the resonant amplitudes.

TABLE 5.6-5

MODEL MAGNETIC BEARING PARAMETERS

Parameters	Value		Units	
Rotor Inertia Along Spin Axis	.018	.0013	n-m-sec^2	lbf-ft-sec^2
Rotor Transverse Inertia	.0058	.0043	n-m-sec^2	lbf-ft-sec^2
Rotor Mass	1.704	.1168	kg	slugs
Radial Stiffness	5.779 x 10^4	3960	n-m	lbf/ft

TABLE 5.6-6

MEASURED AND PREDICTED RESONANCES FOR MODEL MAGNETIC BEARING

Resonance Description	Measured Frequency	Calculated Frequency
Static Radial Resonance	28 Hz (176 rad/sec)	29 Hz (182 rad/sec)
Static Torsional Resonance	25 Hz (157 rad/sec)	Not calculated
Torsional Resonance During Runup	30 Hz (189 rad/sec)	30 Hz (189 rad/sec)
Radial Resonance During Runup	30 Hz (189 rad/sec)	29 Hz (182 rad/sec)

SECTION 6.0

INITIAL (FREELY SUSPENDED) VIBRATION TESTS

Some LST pointing error studies have considered the possibility of isolating the reaction wheels from the vehicle structure to reduce the emitted vibration from reaction wheel to spacecraft. This type mounting allows the reaction wheel case to move freely at frequencies greater than the isolator cut-off frequency. To evaluate the effect of this mounting technique on the reaction wheel emitted vibrations, a set of special tests was initially performed on the MMB and FSC wheels in which the wheels were hung on very weak springs. Accelerometers were mounted on the case of the units to measure the vibration in the axial and radial directions.

During the study the LST vehicle design was modified such that the Optical Telescope Assembly (OTA) became isolated from the Support System Module (SSM) and vibration isolation of the reaction wheels was de-emphasized in favor of hard mounting. This change tended to make the freely suspended test less critical; therefore, when the HEAO RWA was available for only a limited time, a decision was made to bypass the freely suspended HEAO tests in favor of the hard mount tests described in Section 5.0. Another effect of this RWA isolation de-emphasis was to reduce the amount of analysis devoted to the freely suspended data and to concentrate on explaining the hard mount data. Consequently, this section does not include as much data or discussion as for the hard mount tests, although a similar amount of data for each wheel tested was acquired and will be available, if necessary, for future study.

6.1 TEST SETUP DESCRIPTION

The reaction wheels were freely suspended from overhead by three or four weak springs and instrumented with two accelerometers (Columbia, type 1107-3) as shown in Figures 6.1-1 and 6.1-2. The accelerometers were mounted in different orientations, as shown, to measure the linear and angular accelerations along and perpendicular to the spin axis. The accelerometers are direct reading high level dc types whose output was processed by operational amplifiers and then applied to the dynamic analyzer. A Spectral Dynamics 101B Analyzer and 330 Real-Time Analyzer were used. The resonant frequencies of the test setups were measured, and are listed in Table 6.1-1.

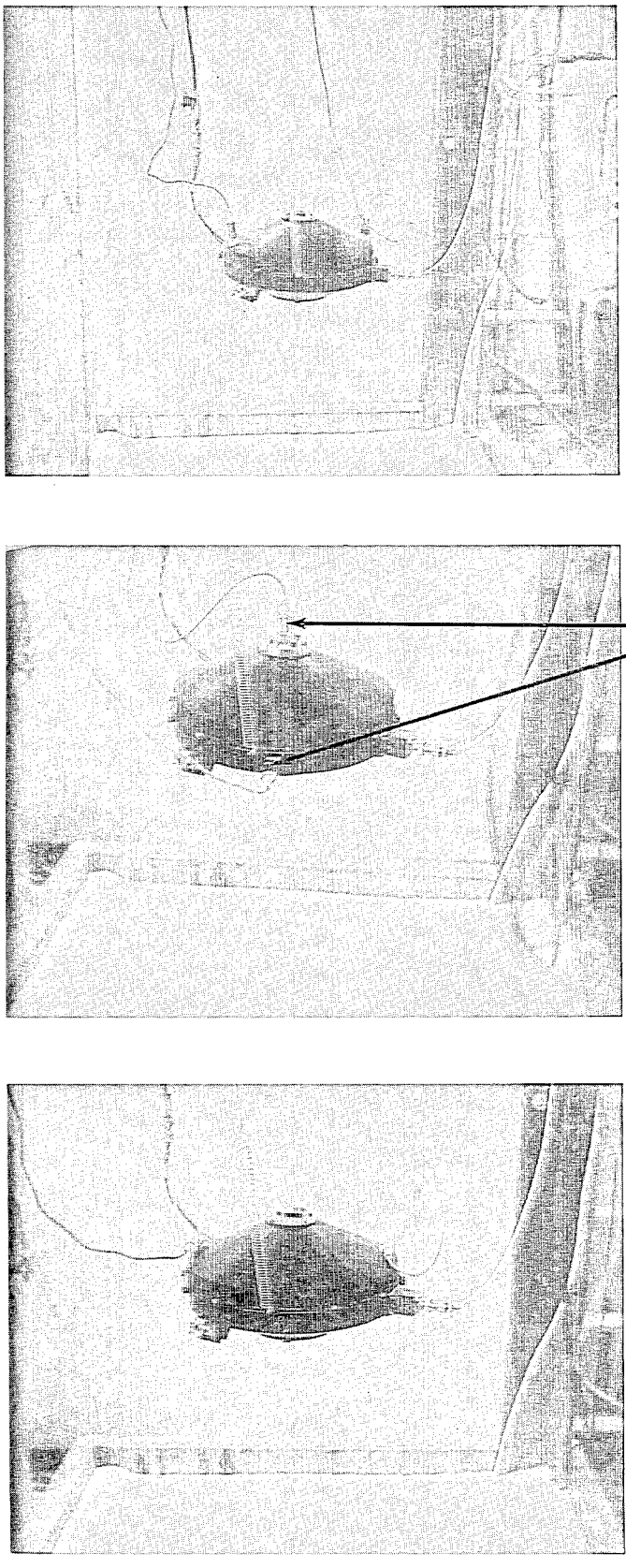

Figure 6.1-1
Fleet Sat Com
Test Setup

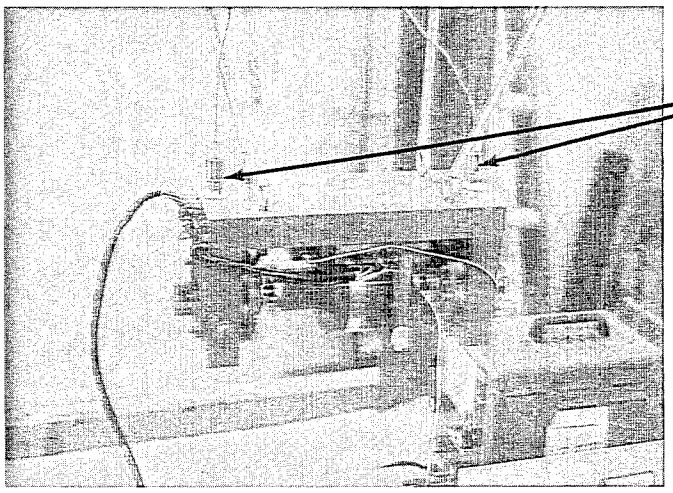

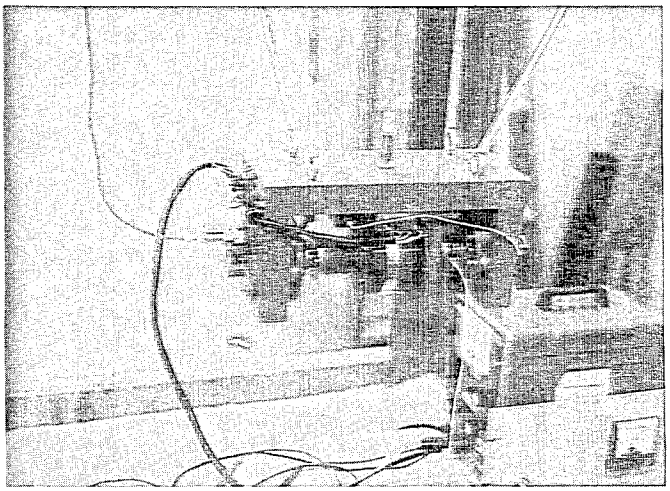

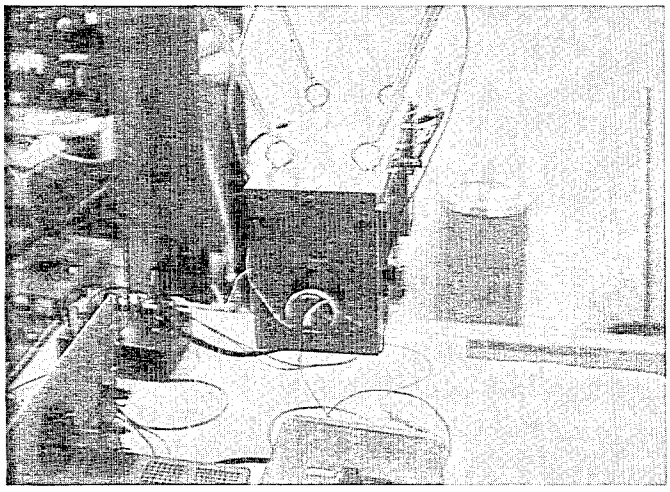

715-74-2

Figure 6.1-2
Mag Brg Wheel
Test Setup

TABLE 6.1-1

TEST SYSTEM RESONANT FREQUENCIES

Parameter	Frequency (Hz)
Fleet Sat Com (Figure 6.1-1)	
Cross Axis Angular	1.2
Cross Axis Linear	.8
Spin Axis Angular	2.3
Spin Axis Linear	1.8
Model Magnetic Bearing (Figure 6.1-2)	
Cross Axis Angular	2.2
Cross Axis Linear	1.2
Spin Axis Angular	3.3
Spin Axis Linear	.8

6.2 FLEET SAT COM TEST RESULTS

Figures 6.2-1 through 6.2-11 show some typical responses obtained from the freely suspended tests. Tables 6.2-1 and 6.2-2 list all the tests that were performed; the first set of tests used an especially quiet set of spin bearings and probably represents an atypical, optimistic case. Therefore, to give data more representative of a typical RWA, another set of bearings was put into the FSC and some data repeated. The second set of tests are called FSC-2, and data is presented in Figures 6.2-8 through 6.2-11.

The response is plotted in g's rms and therefore needs some conversion to obtain linear force and angular torque. The linear force is derived from

$$F = W \ddot{y} \qquad (6.2\text{-}1)$$

where

F = linear force (lbf)

$\ddot{y}$ = acceleration (g's)

W = weight (lb)

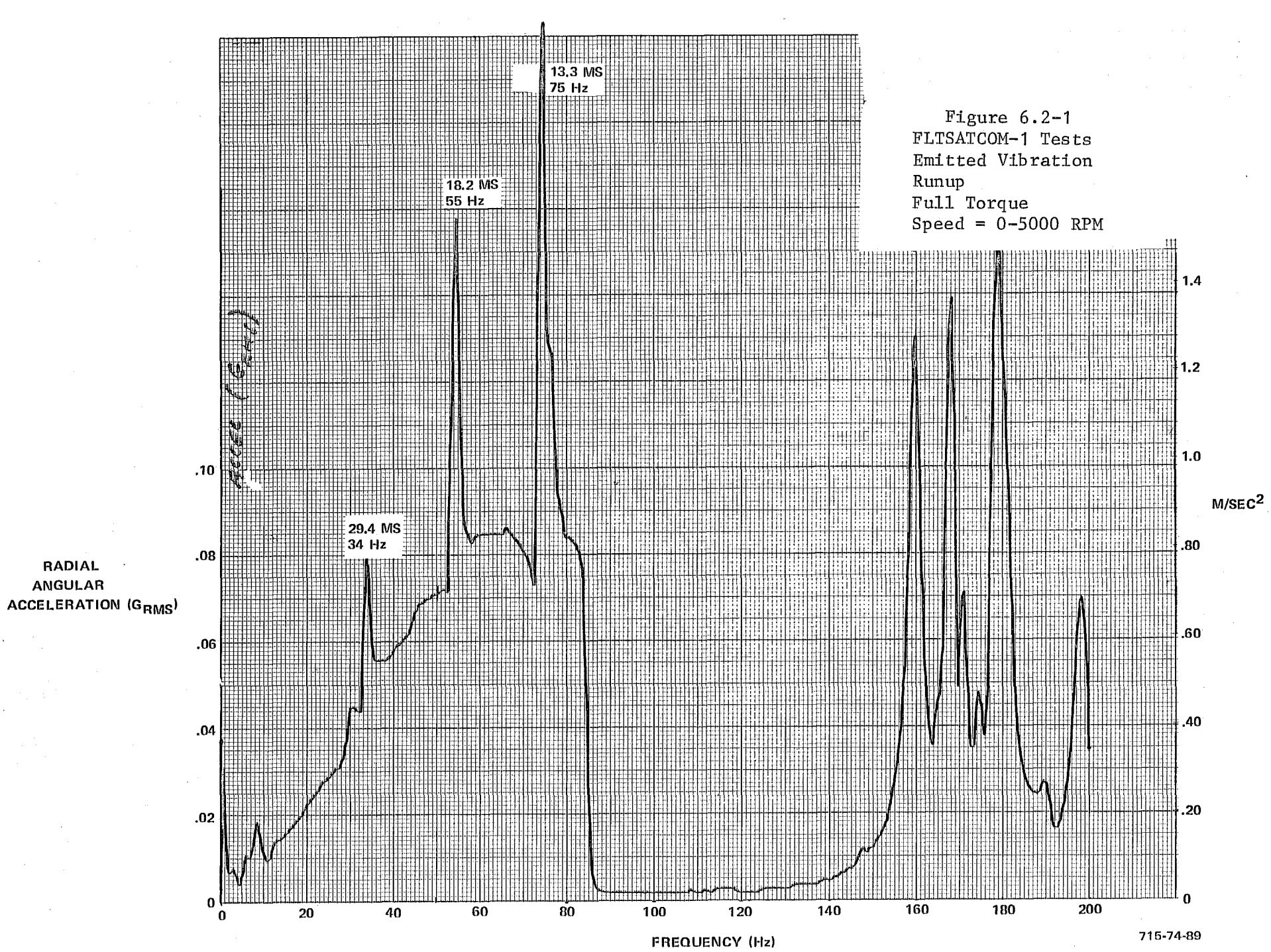

Figure 6.2-1
FLTSATCOM-1 Tests
Emitted Vibration
Runup
Full Torque
Speed = 0-5000 RPM

Figure 6.2-2
FLTSATCOM-1 Tests
Emitted Vibration
(3) Cross Axis Angular Acceleration
1 Min Peak Hold
Speed = 2000, 3500, 4000 RPM

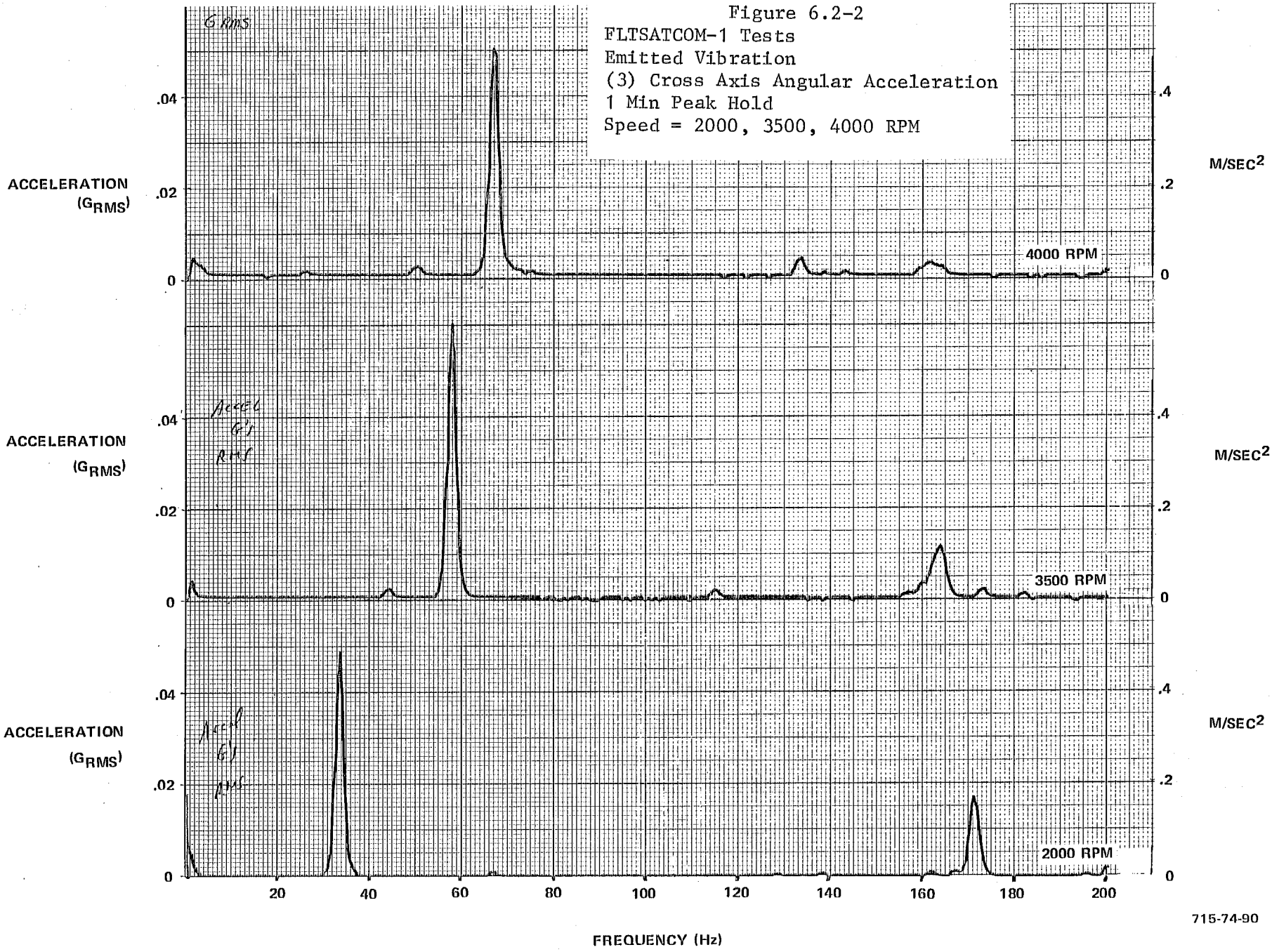

715-74-90

Figure 6.2-3


FLTSATCOM-1 Tests
Emitted Vibration
(4) Cross Axis Angular Acceleration
Speed = 4500, 5000, 3000, 2500 RPM
2500
3000
5000
4500
.04
.02
0
.4
.2
M/SEC2
ACCELERATION (GRMS)
20
40
60
80
100
120
140
160
180
200
FREQUENCY (Hz)
715-74-91

Figure 6.2-4
FLTSATCOM-1 Tests
Emitted Vibration
(3) Cross Axis Angular Acceleration
Speed = 2000, 1500, 1000 RPM

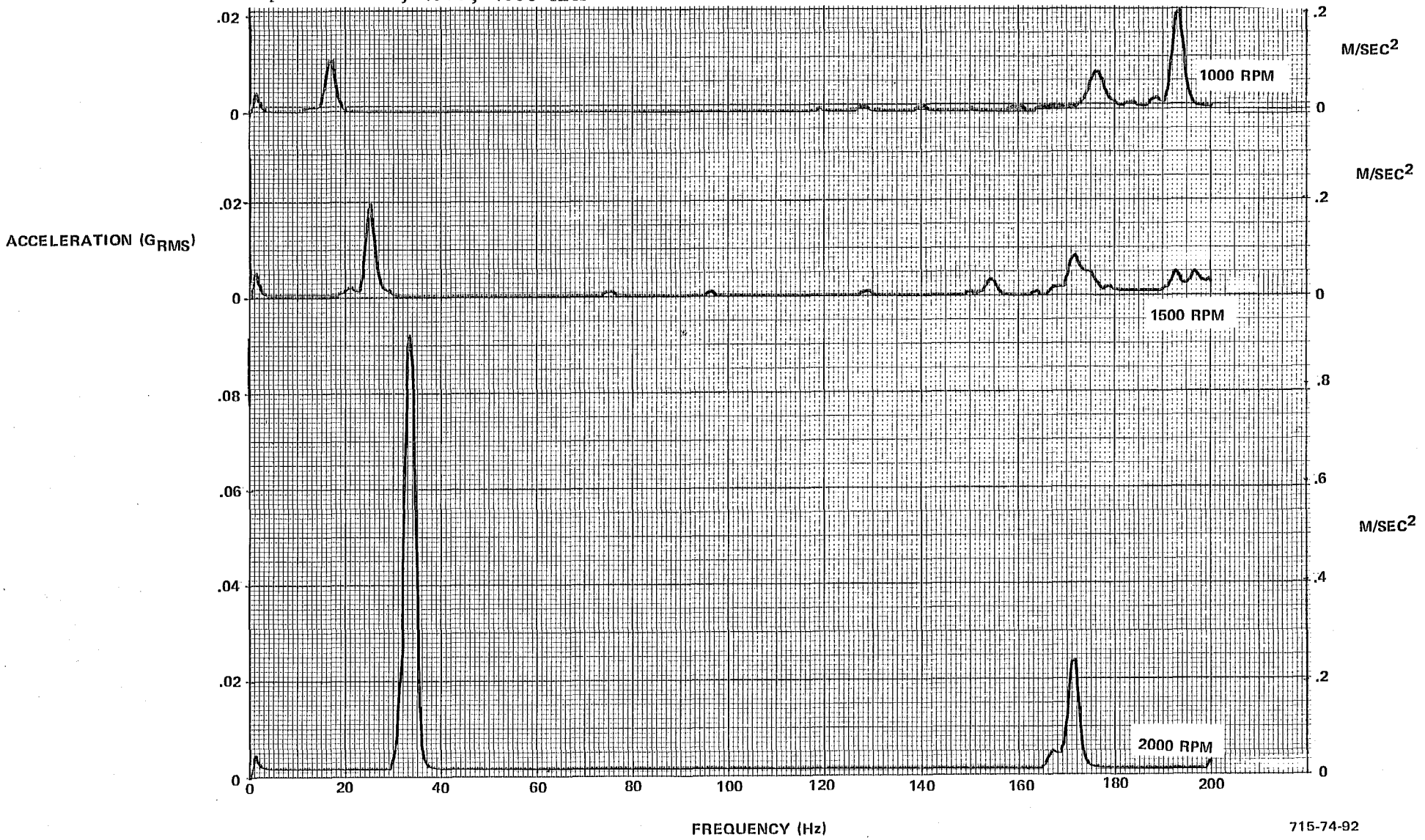

715-74-92

Figure 6.2-5
FLTSATCOM-1 Tests
Emitted Vibration
Runup
Peak Hold
Speed = 0-5000 RPM

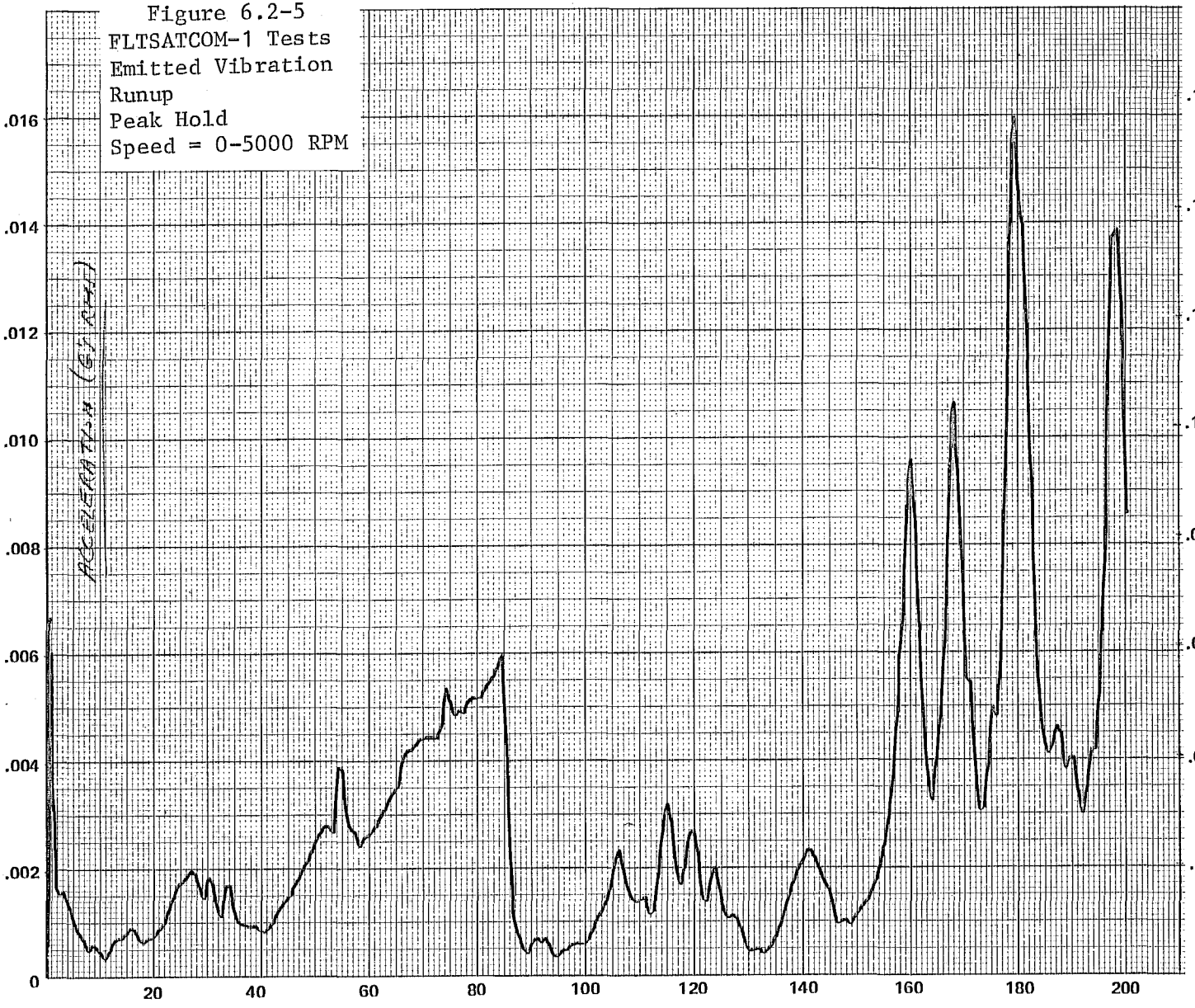

RADIAL LINEAR ACCELERATION (G_{RMS})

715-74-93

Figure 6.2-6
FLTSATCOM-1 Tests
Emitted Vibration
Rundown
Speed = 5000-0 RPM

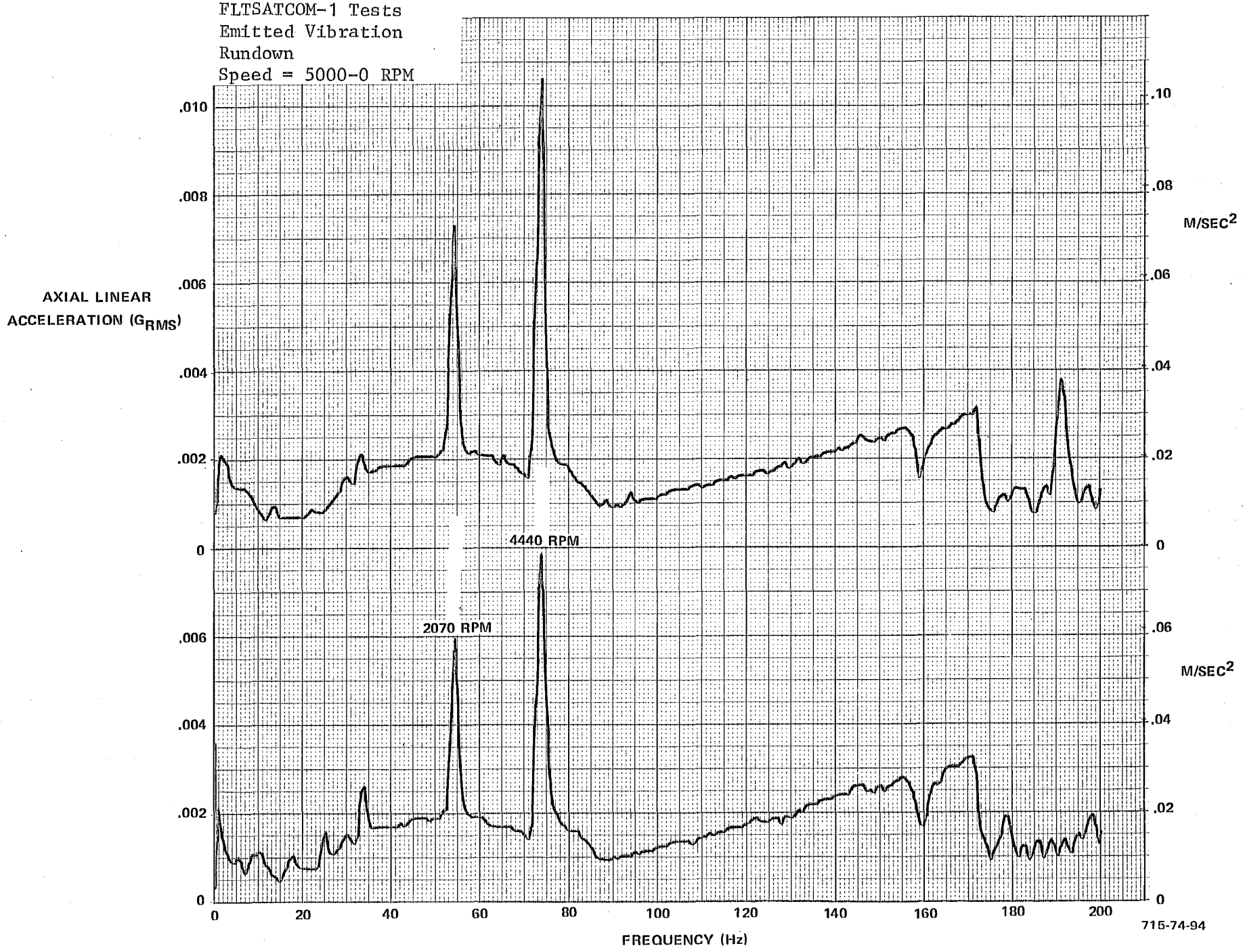

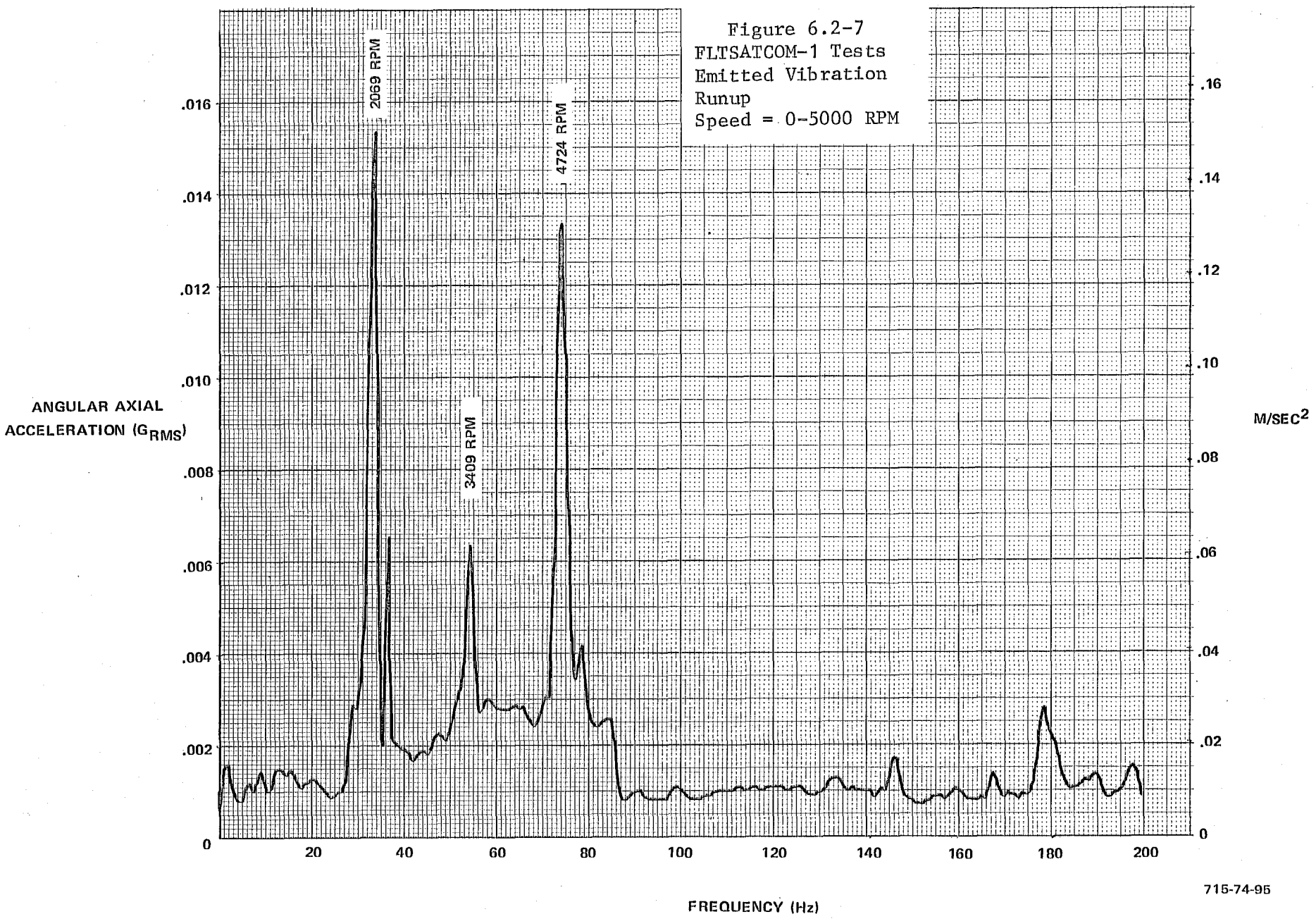
Figure 6.2-7
FLTSATCOM-1 Tests
Emitted Vibration
Runup
Speed = 0-5000 RPM
2069 RPM
3409 RPM
4724 RPM
ANGULAR AXIAL
ACCELERATION (G_{RMS})
.016
.014
.012
.010
.008
.006
.004
.002
0
.16
.14
.12
.10
.08
.06
.04
.02
0
M/SEC^2
20
40
60
80
100
120
140
160
180
200
FREQUENCY (Hz)
715-74-95

Figure 6.2-8
FLTSATCOM-2 Tests
Emitted Vibration
Rundown
Wheel Speed Tracking Filter
Speed = 5000-0 RPM

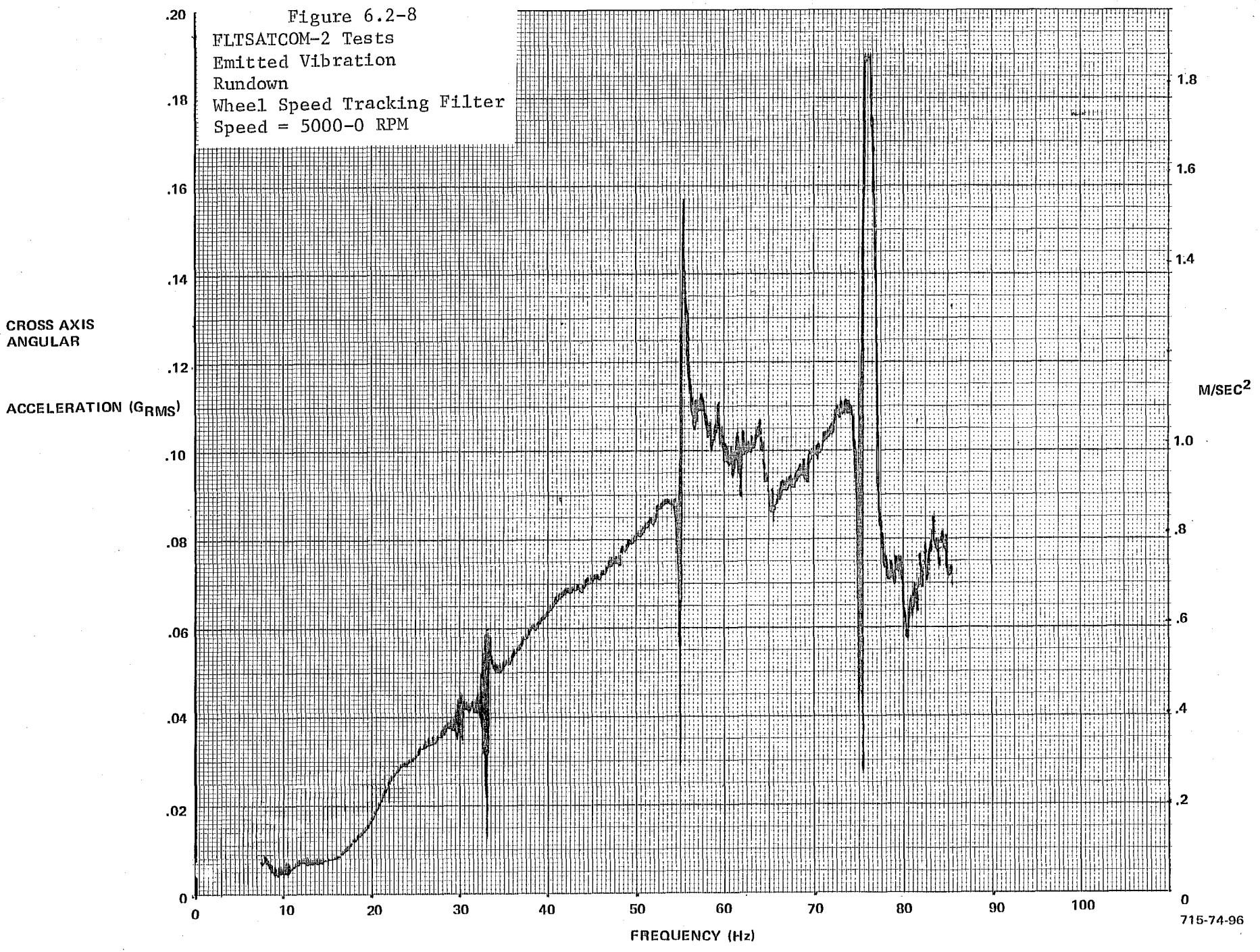

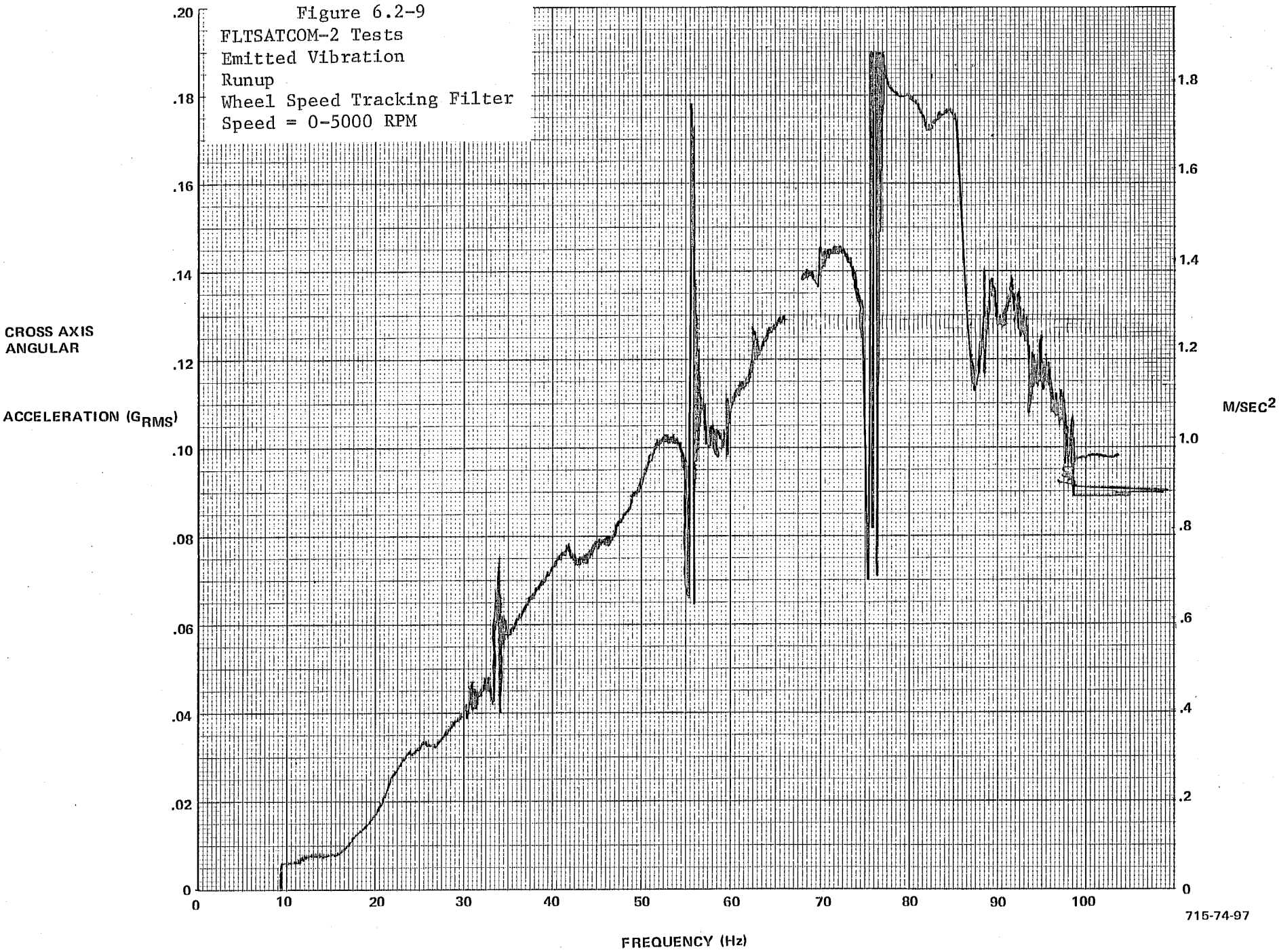
Figure 6.2-9
FLTSATCOM-2 Tests
Emitted Vibration
Runup
Wheel Speed Tracking Filter
Speed = 0-5000 RPM
CROSS AXIS
ANGULAR
ACCELERATION (G_{RMS})
.20
.18
.16
.14
.12
.10
.08
.06
.04
.02
0
1.8
1.6
1.4
1.2
1.0
.8
.6
.4
.2
0
M/SEC^2
0
10
20
30
40
50
60
70
80
90
100
FREQUENCY (Hz)
715-74-97

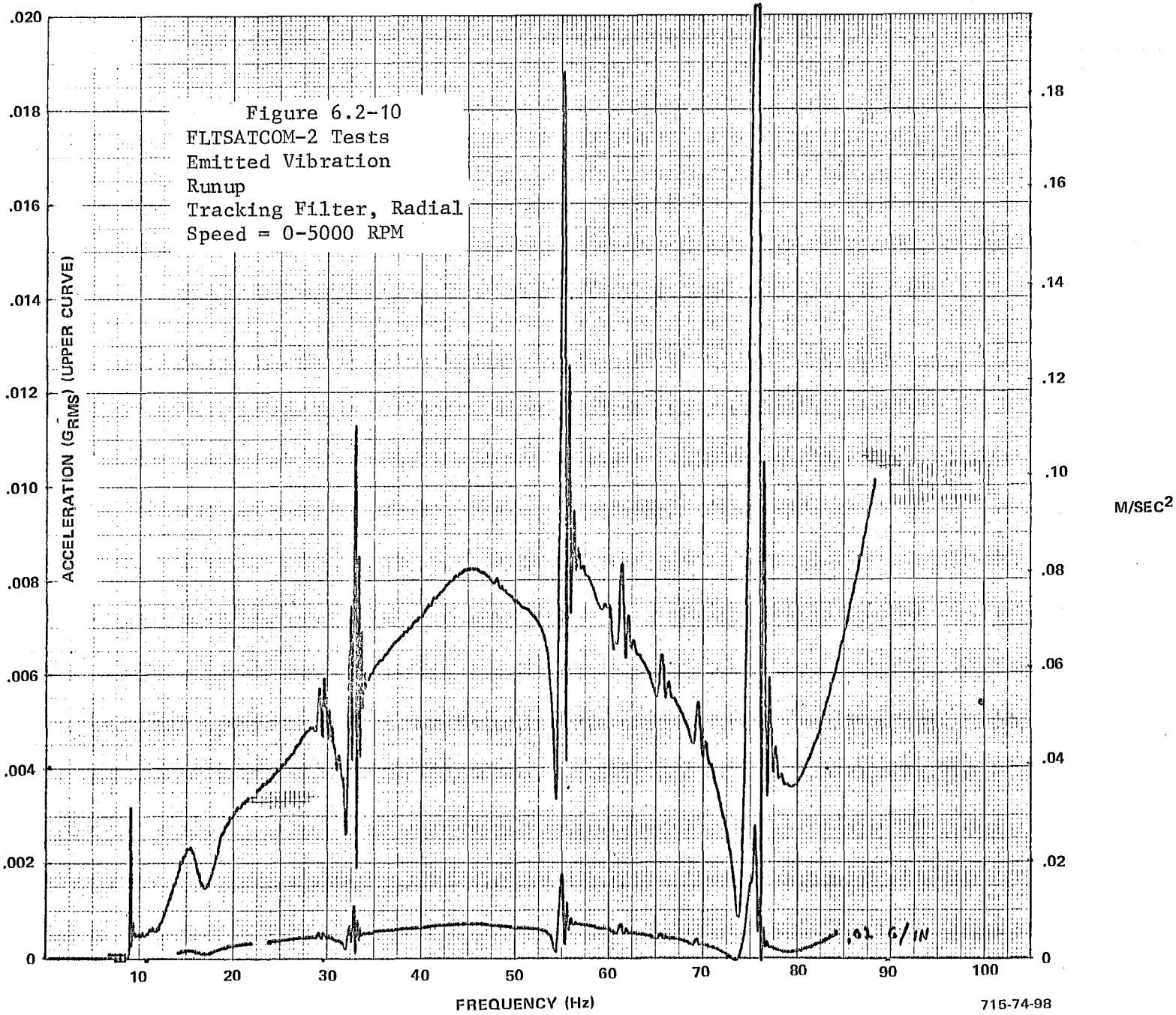
Figure 6.2-10
FLTSATCOM-2 Tests
Emitted Vibration
Runup
Tracking Filter, Radial
Speed = 0-5000 RPM
ACCELERATION (G_{RMS}) (UPPER CURVE)
.020
.018
.016
.014
.012
.010
.008
.006
.004
.002
0
.18
.16
.14
.12
.10
.08
.06
.04
.02
0
M/SEC^2
10
20
30
40
50
60
70
80
90
100
FREQUENCY (Hz)
.02 G/IN
715-74-98

Figure 6.2-11

FLTSATCOM-2 Tests
Emitted Vibration
Runup
Wheel Speed Tracking Filter, Axial
Speed = 0-5000 RPM

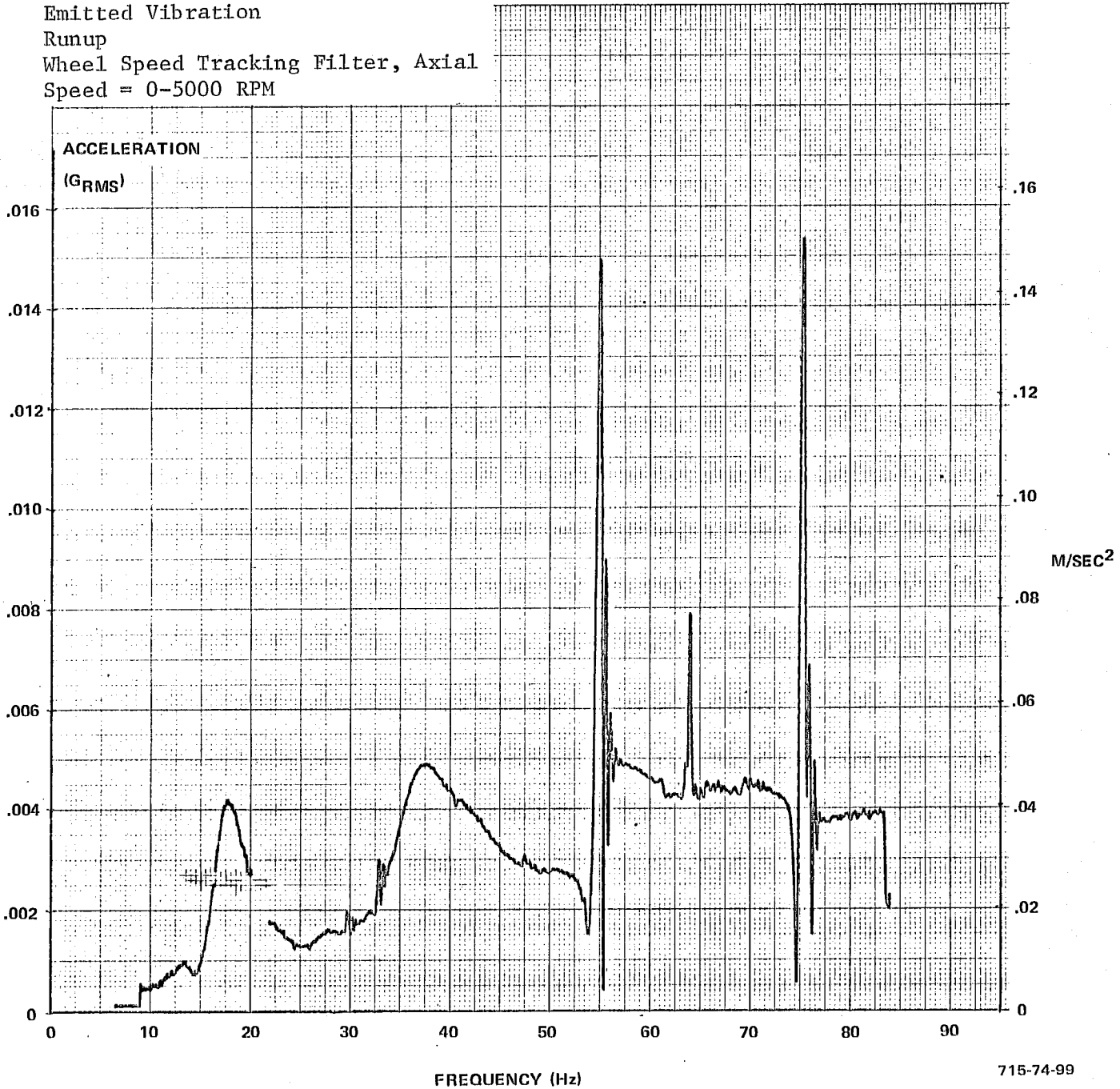

The FSC RWA weight is 12.3 lbm and therefore

$$\boxed{F = 12.3\ \ddot{y}}$$

or in newtons:

$$\boxed{F = 54.7\ \ddot{y}}$$

The angular torque is derived from:

$$T = 32.2\ \left(\frac{I}{D}\right)\ \ddot{y} \qquad (6.2\text{-}2)$$

where

T = angular torque (ft-lb)

I = moment of inertia ($ft\text{-}lb\text{-}sec^2$)

D = distance between accelerometers (ft)

$\ddot{y}$ = acceleration measured by the two accelerometer couple (g's)

For the FSC tests the distance, D, is 10.5 inches, and the inertias of interest are:

$$\text{Cross Axis Inertia} = I_{xx} = .026\ ft\text{-}lb\text{-}sec^2$$

$$\text{Spin Axis Inertia} = I_{zz} = .040\ ft\text{-}lb\text{-}sec^2$$

giving a cross axis torque of:

$$\boxed{T_{xx} = T_{yy} = .95\ \ddot{y}}$$

and spin axis torque of:

$$\boxed{T_{zz} = 1.45\ \ddot{y}}$$

or in newton-meters,

$$T_{xx} = T_{yy} = 1.28\ \ddot{y}$$

$$T_{zz} = 1.97\ \ddot{y}$$

Figures 6.2-1, 6.2-8, and 6.2-9 show the characteristic cross-axis, angular accelerations. Figure 6.2-1 is a peak hold mode runup, and the others used a tracking filter. Note the three resonant peaks at 34, 55, and 75 Hz. These are characteristic of the freely suspended FSC runs and are believed to be caused by rotor/case dynamic interaction. In Figure 6.2-1 three peaks can also be seen between 150 and 190 Hz, probably caused by reaction wheel case structural excitation. Note also at the 123-Hz frequency, where the rotor web resonance exists for a nonspinning hard mounted FSC, no activity is present.

Figures 6.2-2 through 6.2-4 show the cross-axis angular accelerations at various constant speeds from 1000 to 5000 rpm.

Figures 6.2-5 and 6.2-6 show cross-axis linear and spin-axis linear acceleration during a runup from 0 to 5000 rpm (0 to 83.3 Hz). Note the large peaks at 55 and 75 Hz along the spin or axial axis.

Figure 6.2-7 shows the angular acceleration about the spin axis, and the three characteristic frequencies are present here also.

Figures 6.2-10 and 6.2-11 show the linear responses in the cross axis and along the spin axis respectively during a 0 to 5000 rpm runup.

TABLE 6.2-1

FLEET SAT COM-1 TESTS

Run No.	Response Axis				Rotor Speed (rpm)	Type of Run
	Axial (Spin Axis)		Radial (Cross Axis)			
	Linear	Angular	Linear	Angular		
*1				X	0-5000	Runup, full torque
*2			X		2000, 3500, 4000	(3) Cross Axis Angular Acceleration (1 minute peak hold)
*3			X		4500, 5000, 3000, 2500	(4) Cross Axis Angular Acceleration
*4				X	2000, 1500, 1000	(3) Cross Axis Angular
5				X	5000-0	Rundown, motor off, peak hold
6				X	3000	Comparison, real time to dynamic analyzer
7				X	0-5000	Runup, 1/2 torque
8				X	5000-0	Rundown, 1/2 torque
9				X	2700	Runup, rundown, 1/2 torque
*10			X		0-5000	Runup, peak hold
11			X		5000-0	Rundown, radial accel
*12	X X				5000-0 0-5000	Rundown Runup, peak hold
13	X		X		1000, 1500, 2000	Radial, axial
14	X		X		2500, 3000, 3500	Radial, axial
15	X		X		4000, 4500	Radial, axial
16	X		X		5000	Radial, axial
17			X		5000-0	Rundown, motor off, radial

* = Denotes a graph of this run is included in the report.

TABLE 6.2-1 (cont)

FLEET SAT COM-1 TESTS

Run No.	Response Axis				Rotor Speed (rpm)	Type of Run
	Axial (Spin Axis)		Radial (Cross Axis)			
	Linear	Angular	Linear	Angular		
18	X				5000-0	Rundown, motor off, axial
19	X				5000-0	Rundown, full torque
*20		X			0-5000	Runup
21		X			5000-0	Rundown, motor off
22		X			1974, 4477, 3226	Motor off, (peak hold 1 minute)

TABLE 6.2-2

FLEET SAT COM-2 TESTS

Run No.	Response Axis				Rotor Speed (rpm)	Type of Run
	Axial (Spin Axis)		Radial (Cross Axis)			
	Linear	Angular	Linear	Angular		
*1				X	5000-0	Rundown, wheel speed tracking filter
*2				X	0-5000	Runup, wheel speed tracking filter
3				X	5000-1714	Rundown, peak hold
4				X	1000, 2000	(2) Cross axis angular
5				X	3000, 5000	(2) Cross axis angular
6				X	2000	Cross axis peak hold
*7	X		X		0-5000	Runup, tracking filter, radial
*8	X		X		0-5000	Runup, wheel speed tracking filter, axial
9	X		X		3000 3000	axial radial
10	X		X		5000 5000	radial axial

6.3 MODEL MAGNETIC BEARING TEST RESULTS

Figures 6.3-1 through 6.3-5 show some typical responses obtained by freely suspending the MMB from overhead on a set of four weak springs. Table 6.3-1 lists all the tests performed on the MMB.

The responses are plotted in g's rms, and require a conversion to obtain force and torque values. The linear force is derived using Equation 6.2-1 and yields:

$$\boxed{F = 31.4\ \ddot{y}} \quad (lb_f)$$

or

$$\boxed{F = 140\ \ddot{y}} \quad (n)$$

Likewise, the angular torques are derived using Equation 6.2-2 and gives a cross-axis torque of:

$$T_{yy} = 32.2\left(\frac{.13}{.833}\right)\ddot{y}$$

$$\boxed{T_{yy} = 5\ \ddot{y}} \quad (ft\text{-}lb_f)$$

or

$$\boxed{T_{yy} = 6.8\ \ddot{y}} \quad (n\text{-}m)$$

for a torque about the spin axis, use:

$$T_{zz} = 32.2\left(\frac{.042}{.478}\right)\ddot{y}$$

$$\boxed{T_{zz} = 2.8\ \ddot{y}} \quad (ft\text{-}lb_f)$$

or

$$\boxed{T_{zz} = 3.8\ \ddot{y}} \quad (n\text{-}m)$$

Figure 6.3-1
Magnetic Bearing Tests
Emitted Vibration
Motor On, Speed 0-5000 RPM
Motor Off, Speed 5000-0 RPM
Cross Axis Angular

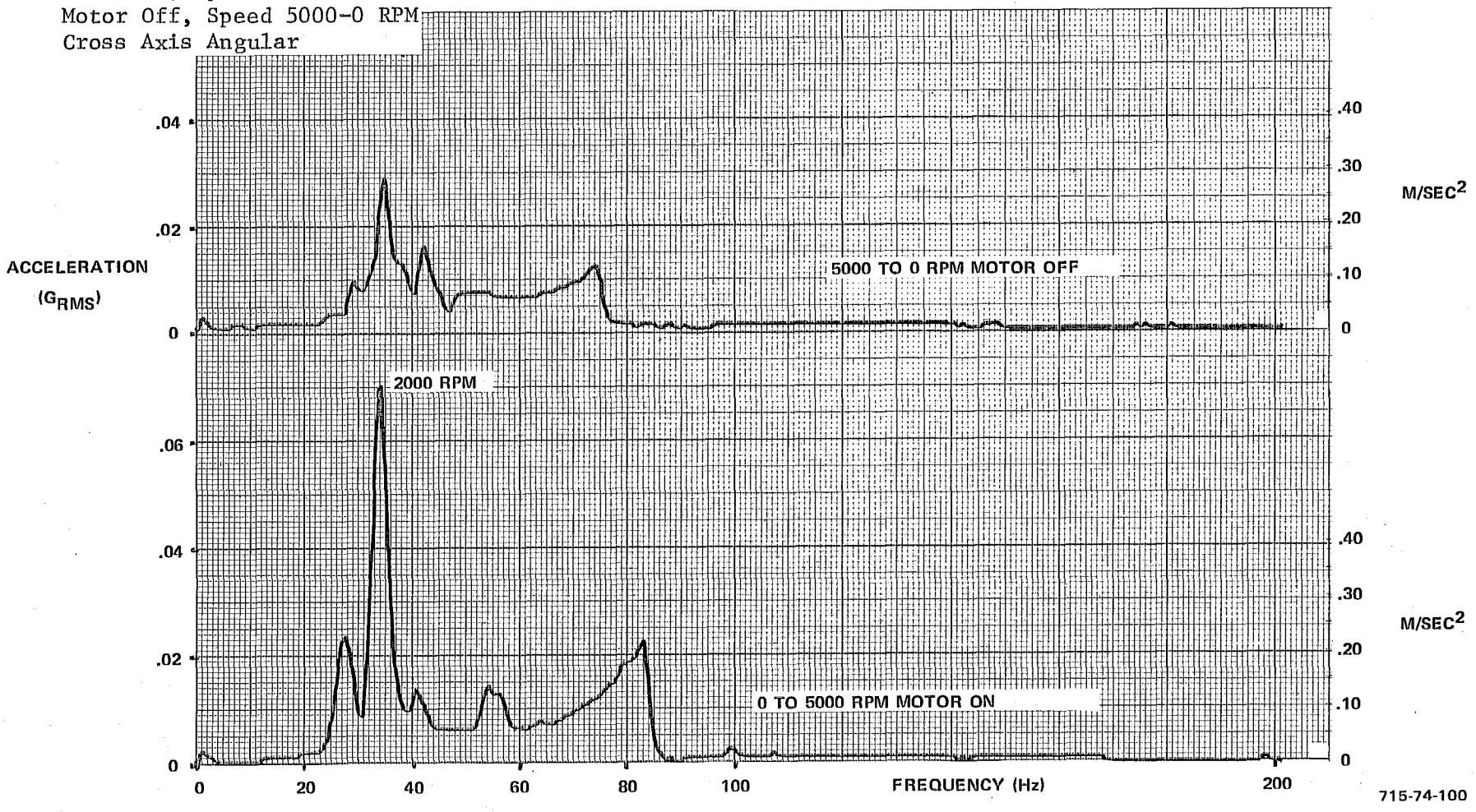

Figure 6.3-2
Magnetic Bearing Tests
Emitted Vibration
Motor On, Speed 0-5000 RPM
Motor Off, Speed 5000-0 RPM
Axial Linear

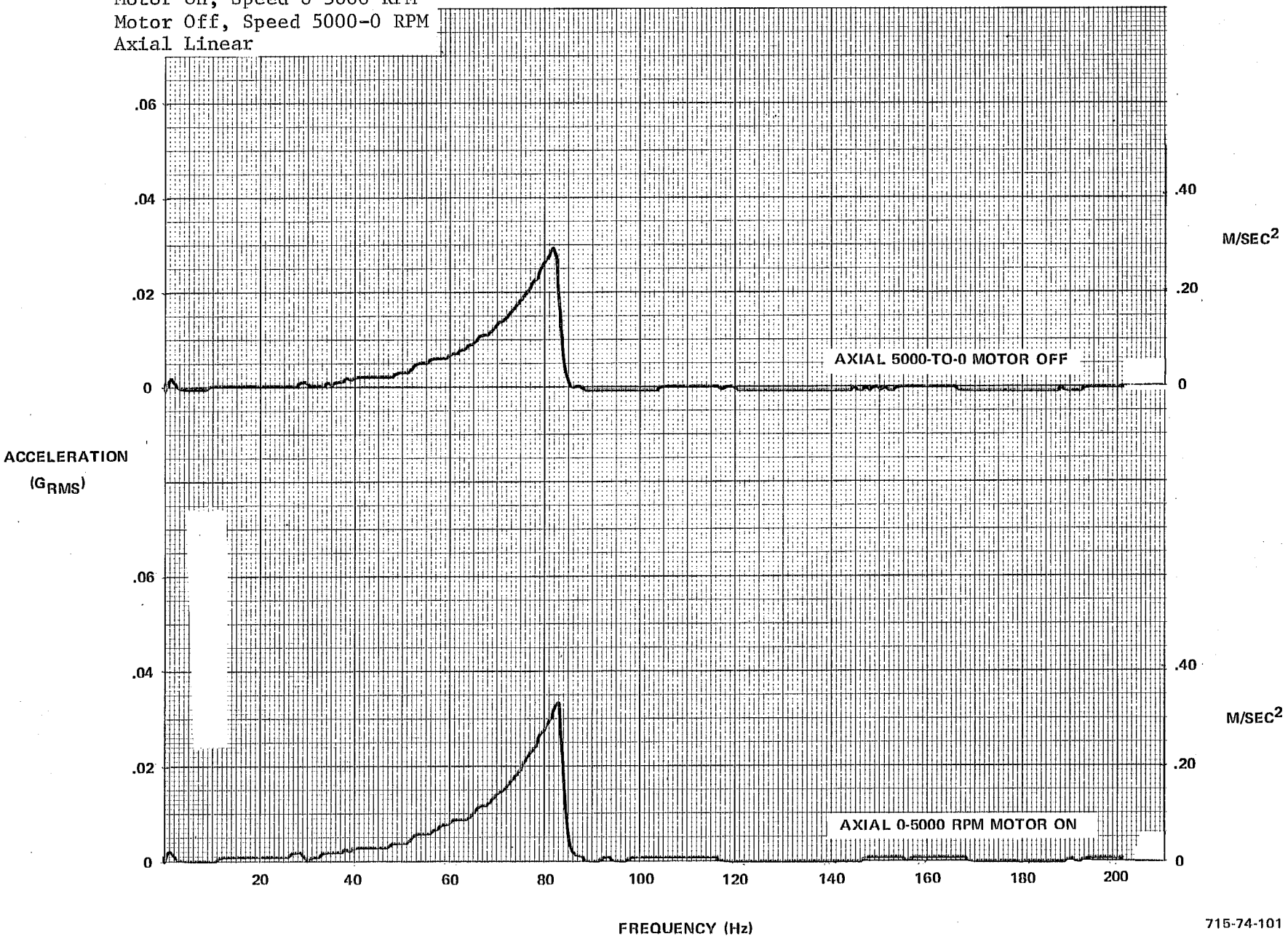

715-74-101

Figure 6.3-3
Magnetic Bearing Tests
Emitted Vibration
Motor On
Spin Axis Angular
Speed = 0-5000 RPM

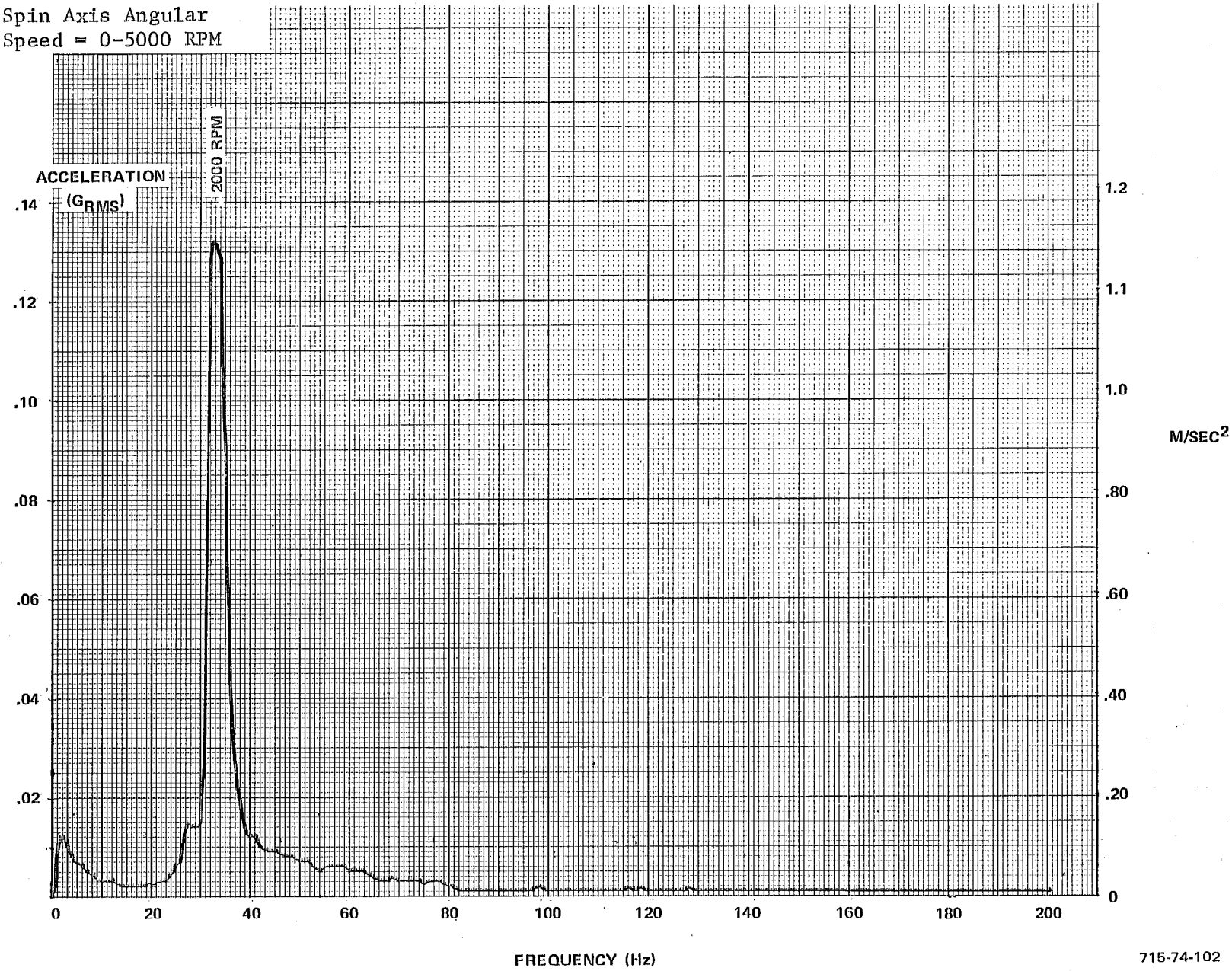

715-74-102

Figure 6.3-4
Magnetic Bearing Tests
Emitted Vibration
Axial
Radial
Speed = 4000, 3500 RPM

715-74-103

Figure 6.3-5
Magnetic Bearing Tests
Emitted Vibration
Cross Axis Angular
Speed = 5000, 4500, 4000, 3500, 3000, 2500 RPM

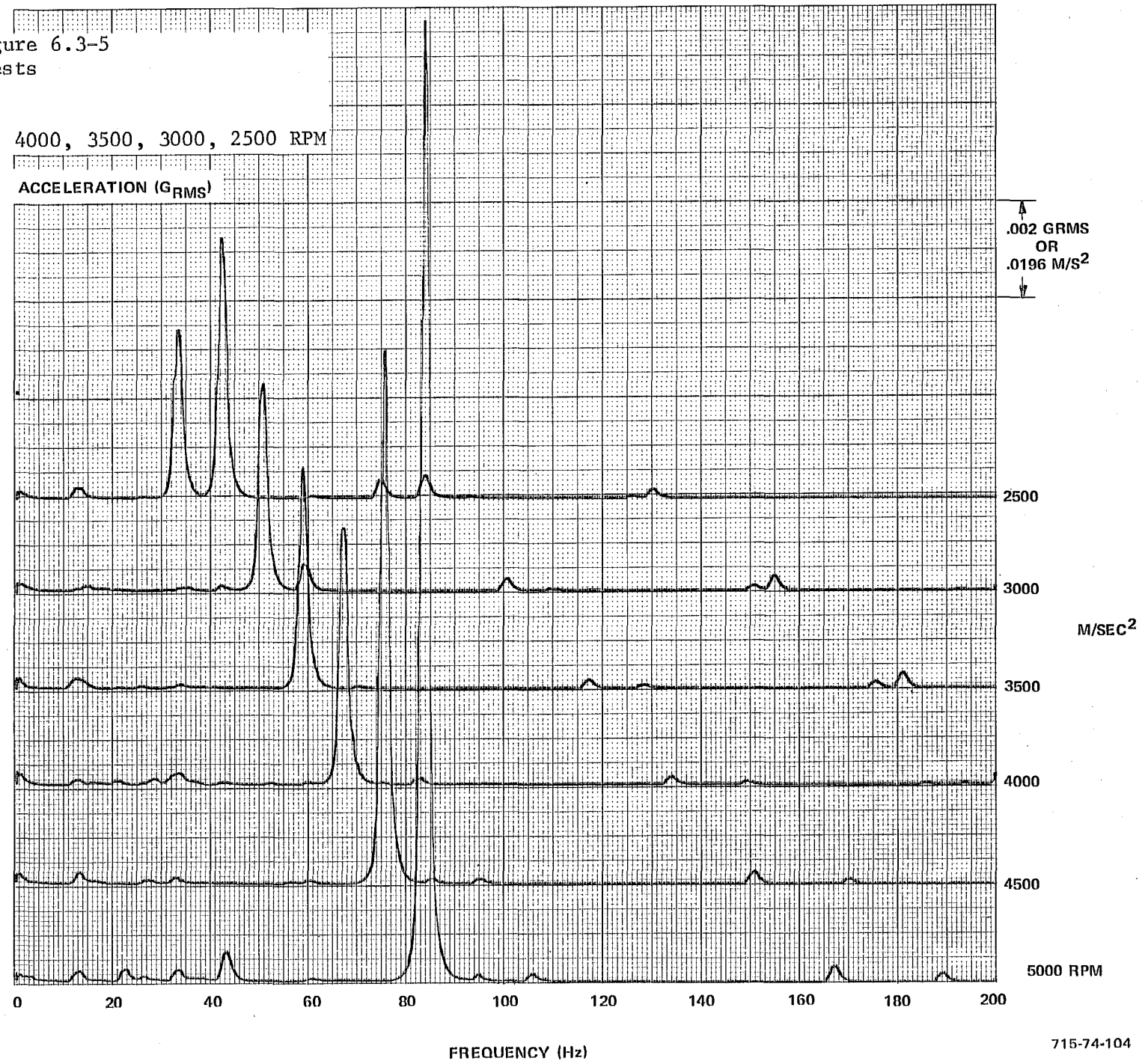

715-74-104

Figure 6.3-1 shows the cross-axis, angular response during a runup to 5000 rpm and coastdown from 5000 rpm of the MMB. Note the angular axis resonance at 34 Hz caused by the radially soft magnetic bearing spring, and the quiet response beyond the maximum wheel speed frequency (83.3 Hz). Figure 6.3-2 shows the linear acceleration along the spin axis during a runup. Figure 6.3-3 shows the angular acceleration about the spin axis, and a very large peak at 34 Hz is evident.

The remaining two curves show constant speed runs at speeds from 2500 to 5000 rpm. Figure 6.3-4 shows the linear acceleration response along the spin (axial) and cross (radial) axis. Figure 6.3-5 shows the cross-axis angular acceleration.

TABLE 6.3-1

MAGNETIC BEARING TESTS

Run No.	Response Axis				Rotor Speed (rpm)	Type of Run
	Axial (Spin Axis)		Radial (Cross Axis)			
	Linear	Angular	Linear	Angular		
*1			X		5000, 4500, 4000, 3500, 3000, 2500	Cross axis angular
2				X	2000, 1500, 1000	(4) Cross axis angular
3	X				5000	(2) Axial, .026/in. and .002 g/in.
4			X		4500, 5000	(2) Radial
5	X				4500	Axial
*6	X		X		4000, 3500	Axial, radial
7	X		X		3000, 2500	Real time analysis and dynamic analysis, 3000 rpm, radial, axial
8	X		X		1000, 1500, 2000	Radial, axial
9		X			2500, 3000, 3500, 4000, 4500, 5000	Spin axis angular
10		X			1000, 1500, 2000	Spin axis angular
*11	X				0-5000	Motor on, spin axis angular
12		X			5000-0	Motor on
13		X			5000-0	Motor off, spin axis angular
*14				X	0-5000 5000-0	Motor on Motor off, cross axis angular

* = Denotes that curve is included in this report.

TABLE 6.3-1 (cont)

MAGNETIC BEARING TESTS

Run No.	Response Axis				Rotor Speed (rpm)	Type of Run
	Axial (Spin Axis)		Radial (Cross Axis)			
	Linear	Angular	Linear	Angular		
*15	X				0-5000 5000-0	Motor on Motor off, axial
16			X		5000-0 0-5000	Power off, radial Motor on, radial
17			X		0-5000 5000-0	Runup, rundown, 1/2 gm unbalance peak hold mode
18			X		5000, 3000, 2000	1/2 gm unbalanced, peak hold mode (1 minute)
19			X		0-5000	Balanced, peak hold; motor on (7.33V and 30V) motor off (real time peak hold)
20			X		0, 2000, 3000, 5000	Balanced, peak hold mode (1 minute)
21			X		0-5000	Runup, wheel speed tracking filter, 1/2 gm unbalance
22			X		0-5000, 5000-0	Runup, rundown, 1/2 gm unbalance wheel speed tracking filter
23			X		0-5000 5000-0	Runup, rundown; balanced wheel speed tracking filter
24			X		0, 5000, 3000, 2000	1/2 gm unbalance, cross axis angular acceleration
25			X		2000, 3000 5000	Cross axis, balanced

SECTION 7.0

PREDICTIONS FOR AN LST SIZE RWA

This section makes an engineering prediction of the emitted vibration which will be generated from a Sperry ball bearing and magnetic bearing reaction wheel sized to meet the existing LST RWA requirements. It is emphasized that this is an engineering best guess, based on data taken during this study, the present understanding of reaction wheel dynamics, and past experience with precision balancing of large control moment gyros. Before more accurate predictions can be made, further detailed study, analysis and modeling of the reaction wheel case, rotor, motor, and bearing interactions is necessary.

7.1 BASELINE LST RWA REQUIREMENTS

The design of the LST Attitude Control System is still evolving during the prime contractor Phase B studies, and various size reaction wheels are being considered during the design tradeoffs and iterations. For this study a baseline design has been selected which Sperry feels is representative of what eventually may be required for the LST. It is essentially a 44 foot-pound-second (60 n-m-s) reaction wheel which runs at a maximum speed of 1500 rpm (25 Hz wheel speed frequency). Table 7.1-1 lists the principal requirements.

Since various vehicle designs are being considered, no firm requirement exists for the level of emitted vibration necessary; the only ground rules used here are to keep it as low as possible and have no resonances in the control pointing frequency range of 0 to 15 Hz. Weight and power will be important considerations eventually, but at present the forcing parameter is low emitted vibrations.

TABLE 7.1-1

PERFORMANCE REQUIREMENTS OF LST BASELINE RWA

Parameter	Value		Units	
Maximum Speed	±312	±3000	rad/sec	rpm
Maximum Speed During Pointing	±156	±1500	rad/sec	rpm
Momentum at Maximum Speed	120	88.6	n-m-s	ft-lb-sec
Rotor Inertia	.384	.283	$n\text{-}m\text{-}s^2$	$ft\text{-}lb\text{-}sec^2$
Reaction Torque Over Speed Range	.50	71	n-m	oz-in.
Torque Resolution	.05	.05	percent	percent
Torque Linearity Over Speed	3	3	percent	percent
Emitted Vibration				
Forces (X, Y, and Z Axis)	TBD	TBD	n	lb_f
Torques (X, Y, and Z Axis)	TBD	TBD	n-m	$in.\text{-}lb_f$
Weight (Including electronics)	TBD	TBD	kg	lbm
Power at Maximum Speed and Torque	TBD	TBD	Watts	Watts
Power at Constant Speed = 156 rad/sec	TBD	TBD	Watts	Watts

7.2 LST BALL BEARING RWA

The ball bearing RWA which will meet the LST Baseline requirements has a design that evolves from the same family as the FSC and HEAO RWA. A similar housing, rotor, and bearing system can be used. The principal differences from the HEAO would be:

- Enlarge the rotor diameter (and housing) to allow for twice the rotor inertia and an efficient rotor design.
- Stiffen the rotor web to put the gyroscopic resonance at a high frequency.
- Replace the ac induction motor with a higher torque brushless dc motor.
- Add electronics integral with the wheel housing, if one central control electronic unit is not used.

The predicted characteristics of this design are listed in Table 7.2-1 and Figure 7.2-1.

TABLE 7.2-1

PERFORMANCE CHARACTERISTICS OF LST BALL BEARING RWA

Parameter	Value		Units	
Maximum Speed during Pointing	±156	±1500	rad/sec	rpm
Momentum at Pointing Speed	60	44.3	n-m-s	ft-lb-sec^2
Reaction Torque Over Speed Range	.50	71	n-m	oz-in.
Torque Resolution	.05	.05	percent	percent
Torque Linearity Over Speed	3	3	percent	percent
Drag Torque at Maximum Speed	.01	1.5	n-m	oz-in.
Type of Motor	Brushless dc			
Bearing Type	Barden 101-H Angular Contact Duplex Pair (DF)			
Total Weight (Including Electronics)	24.5	54	kg	lbm
Rotor Weight	17.3	38	kg	lbm
Rotor Outer Diameter	.43	17	m	in.
Power at Maximum Speed and Torque	112	112	Watts	Watts
Run Power at 156 rad/sec	5	5	Watts	Watts
Emitted Vibrations	See Figures 7.2-1 and 7.2-2			

The prediction of static and dynamic unbalance is not extremely involved, but is the best estimate at present. It is based on the static radial unbalance force given in the appendix by:

$$F_R = M_R \epsilon \omega^2$$

and the dynamic torque:

$$T = (I_w - I_T) \phi \omega^2$$

The two terms ϵ and ϕ can be thought of as corresponding to shifts in the bearing-defined spin axis relative to the principal axis of the rotor; ϵ corresponding to a parallel translation of some microinches, and ϕ corresponding to an angular rotation of some microradians. If these factors are considered to be constant between reaction wheels when the same type bearings (101H) and suspension system are used (probably a good first guess), then the radial force is proportional to the rotor masses at a given speed and the cross axes torques are proportional to the difference inertias, or almost proportional to the polar inertia for a similar shape rotor. Using this type of extrapolation from the FSC to HEAO RWA, the static unbalance is predicted to be four times as large in the HEAO; it was measured as being five times as large. The dynamic unbalance is predicted to be six times larger in the HEAO, and was measured to be four times greater.

Using this same prediction technique to extrapolate from HEAO to the LST design gives:

$$\text{Static Unbalance} = .011 \text{ oz-in.}$$

$$\text{Dynamic Unbalance} = .08 \text{ oz-in.}^2$$

Another factor to keep in mind when using these values for LST predictions is that environmental shifts will change these initial balance figures. Balance stability is an entire subject in itself and requires detailed testing and analysis before a confident prediction can be made of balance or microinch shifts caused by such things as launch vibrations, temperature change, time, and duty cycle hysteresis. At the present level of understanding, a budget of three times the above initial balance values should be added for the effects of balance instability.

The gyroscopic unbalance frequency is predicted from the equation developed in the appendix:

$$\omega = \sqrt{\frac{K_R}{I_T + I_w}} \quad \text{(rad/sec)}$$

Assuming that the torsional rotor web spring constant will be stiffened to be twice the present HEAO value of 20,330 foot-pounds per radian, and that the total inertia will double for the LST design, results in obtaining the same resonant frequency of 38 Hz. This should be well beyond the anticipated pointing

operation frequency range of 0 to 15 Hz so that no problem is encountered while fine pointing. The peak amplitude is increased by two times over the HEAO measured values, since the rotor mass is larger by approximately two.

The predicted force and torque values for the LST Ball Bearing RWA are shown in Figures 7.2-1 and 7.2-2.

7.3 LST MAGNETIC BEARING RWA

When predicting the emitted vibration from an LST magnetic bearing reaction wheel, an additional difficulty is encountered beyond that present for ball bearing wheel predictions. The added factor is the large design difference in the rotor and housing from the MMB to an actual reaction wheel. The MMB used a shaft rotor with a very stiff, U-shaped test housing, whereas an LST magnetic bearing reaction wheel would have a disk-shaped rotor, similar to the HEAO webbed rotor and a thin-walled housing within which a vacuum could be maintained. These differences will change the dynamics from the MMB and possibly add additional resonances. Of course, a design objective would be to keep any housing or rotor web-related resonances out of the frequency region of interest. Keeping this added complexity factor in mind, we now proceed to consider some design options for an LST magnetic bearing wheel.

Looking at the test data for the MMB and the LST RWA requirements, the first obvious question is: where should the angular resonance be located? The higher the frequency required for the angular resonance, the stiffer the bearing must be radially, and consequently the bearing will be larger and heavier. An alternate solution might be to design the bearing stiffness very low and intentionally set the resonance at a very low frequency, say 5 Hz. In this way advantage can be taken of the magnetic bearing's low drag torque by running the rotor at a much higher speed and reducing the rotor and RWA mass. However, two problems arise in this approach -- first, the peak resonant frequency forces and damping must be well controlled and predictable, and second, a lower limit exists to bearing radial stiffness since it is required to support the rotor weight in a 1g earth gravity field. A third design option would be to use a radially active and axially passive, or an all axis-active bearing system. The principal disadvantage of this appraoch is the added complexity (a factor of two or three times for the sensors and electronics) needed to control the added degrees of freedom. With an axial active-radial passive system, only a simple single axis control electronic channel is required.

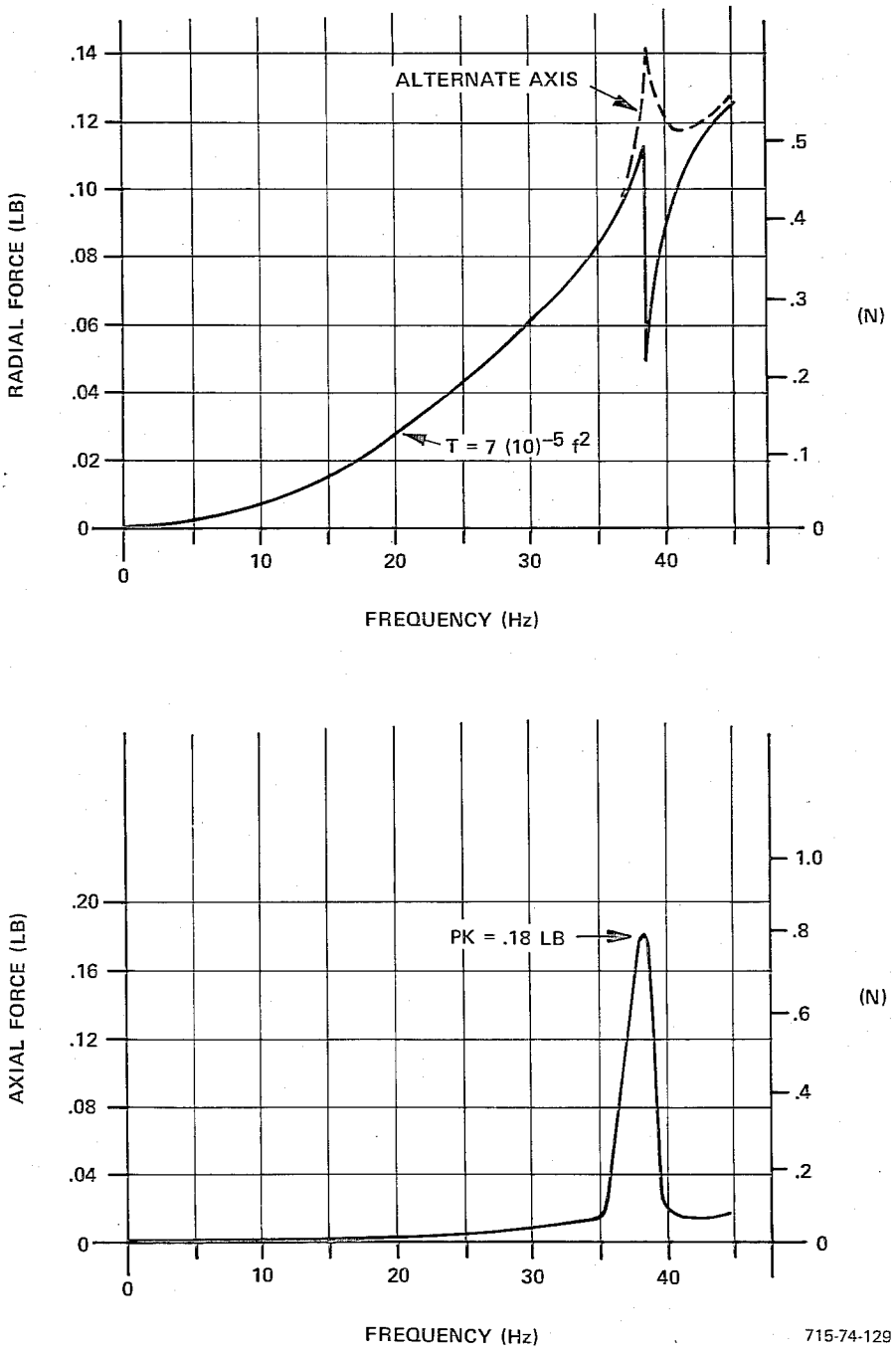

Figure 7.2-1
Predicted LST RWA Forces (Initial)

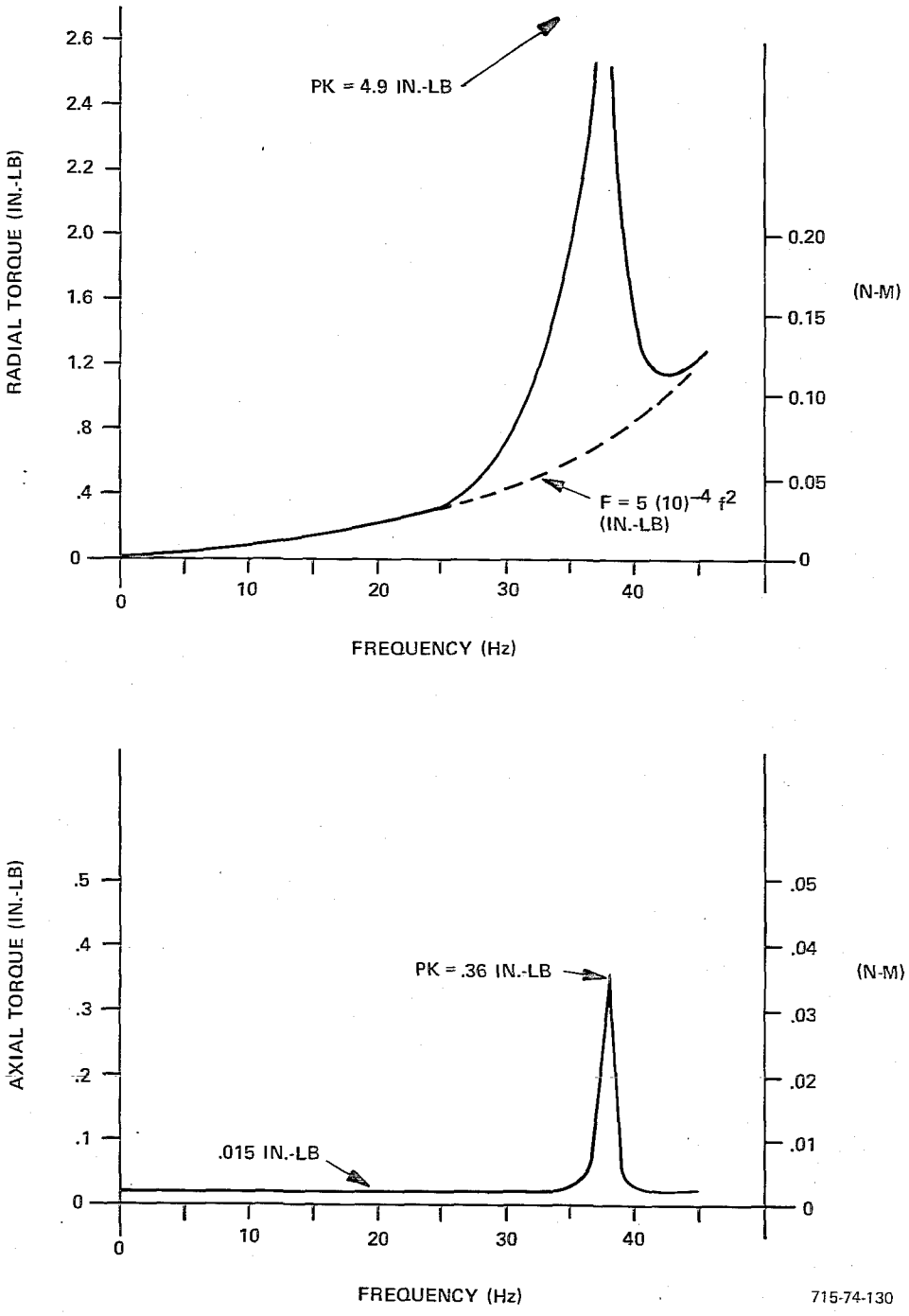

Figure 7.2-2
Predicted LST RWA Torques (Initial)

Considering the various options, it was decided for this prediction to consider an RWA with its angular resonance above the operating frequency range using a radially passive magnetic bearing. For sizing, a rotor similar to the LST ball bearing rotor design was selected. This rotor weights 38 pounds, has an outer diameter of 17 inches, and has a speed of 1500 rpm at 45 ft-lb-sec momentum. The radial bearing stiffness is the principal design concern and must be sized for the following considerations:

- Operating Attitude - The rotor weight must be supported with the spin axis horizontal or vertical, and functional requirements must be met in both 0g and 1g environments.

- Cross-Axis Rate - The specified rate must be sustained without touchdown, e.g., during vehicle maneuvering.

- $\overline{H}$-Vector Misalignment - The angular stiffness must be sufficient to limit the misalignment under specified rates during operation.

- Resonances - The radial, angular and gyroscopic resonances must be above the wheel speed frequencies which will be used during fine pointing. A lower frequency limit of 38 Hz has been selected.

The first and last factors are the important considerations for LST, since the cross-axis rates are very low and H-vector alignment is not critical.

The radial stiffness per bearing to meet the weight, and radial and angular gyroscopic frequency limits are 3285, 3390 and 6834 pounds per inch respectively. It can therefore be seen that the angular resonance sizes the bearing. A bearing with a similar stiffness, 5000 pounds per inch, has been built and tested at Sperry to support a 60-pound rotor for a Magnetic Bearing Momentum Wheel. The bearing stators weighed 44 pounds total and the bearing rotors weighed 12 pounds.

Figure 7.3-1 shows a cross sectional view of an LST RWA type design. A segmented spin motor is shown and has been used at Sperry on other magnetic bearing designs. Weight is saved using this approach, since the motor rotor is made part of the RWA rotor and saves adding more rim mass. A three-loop

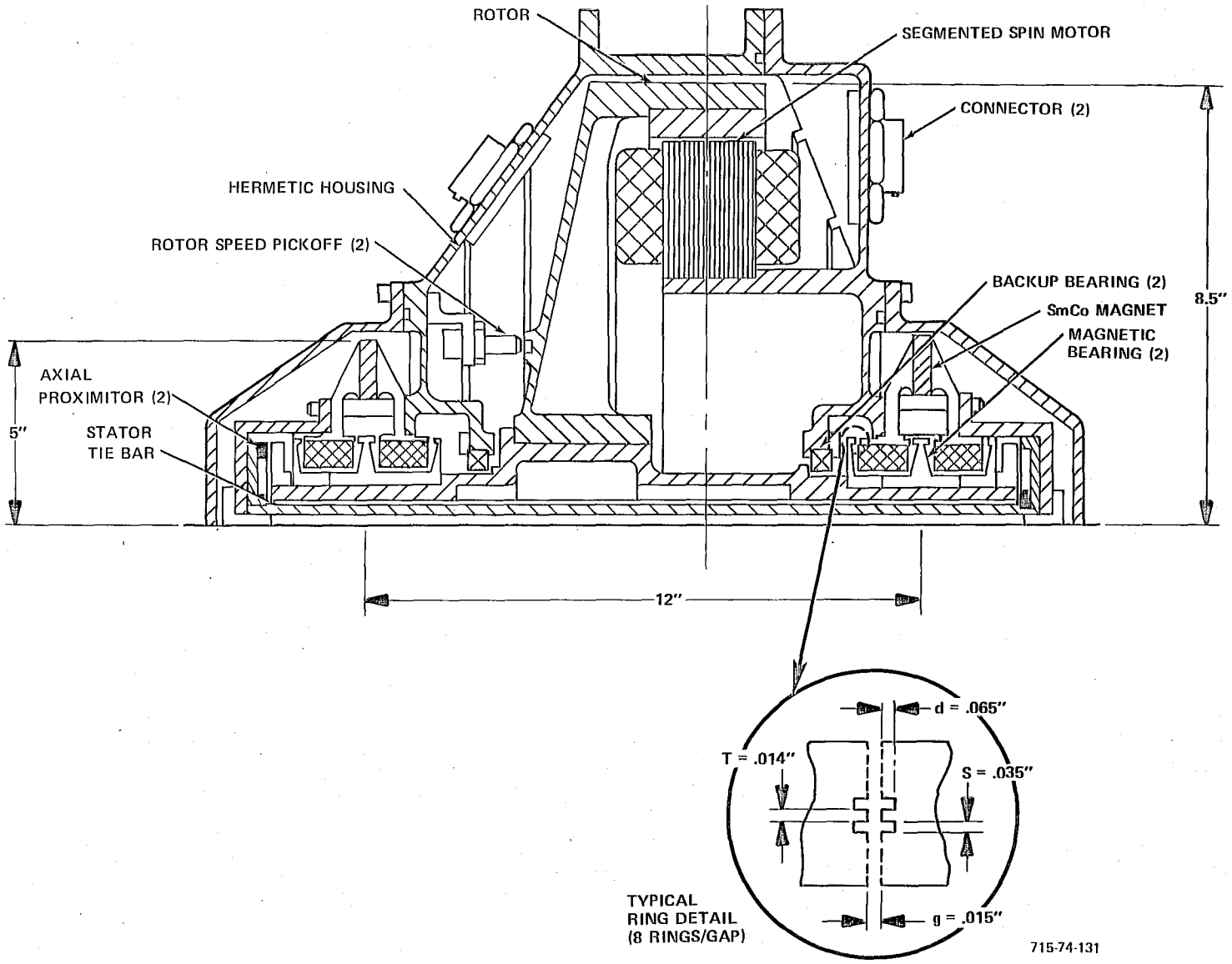

Figure 7.3-1
Magnetic Bearing RWA Cross Section

samarium cobalt magnetic bearing is used with a 12-inch bearing span; a detail of the annular teeth arrangement is also shown. Table 7.3-1 lists the principal characteristics of this type of design.

The emitted vibration shown in Figures 7.3-2 and 7.3-3 are based on achieving the following balance:

$$\text{Static Unbalance} = .02 \text{ oz-in.}$$

$$\text{Dynamic Unbalance} = .16 \text{ oz-in.}^2$$

These values are derived from the levels expected for the ball bearing wheel with an additional budget added for uncertainties caused by the magnetic bearing axis location repeatability and stability.

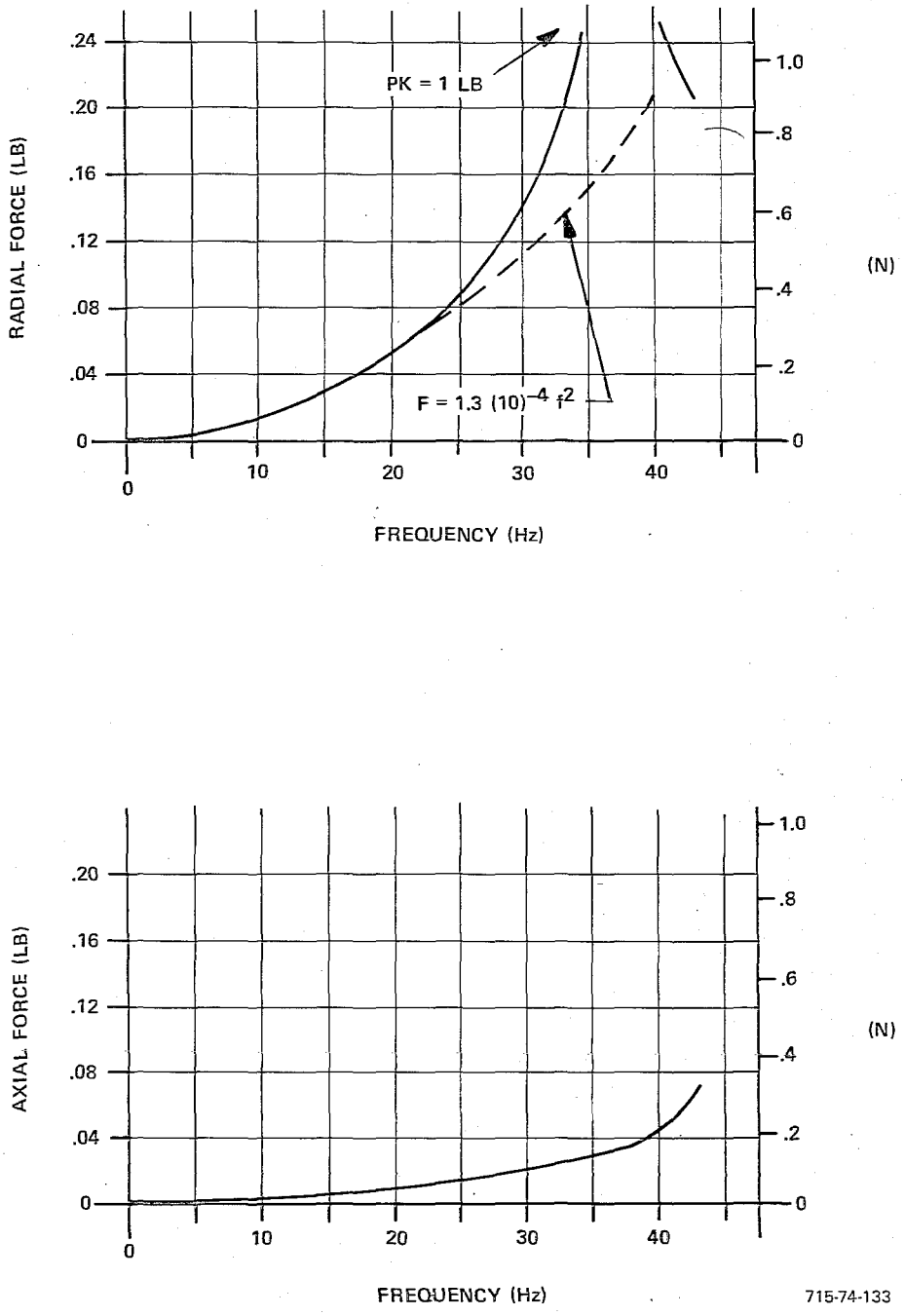

Figure 7.3-2
Predicted LST Magnetic Bearing RWA Forces (Initial)

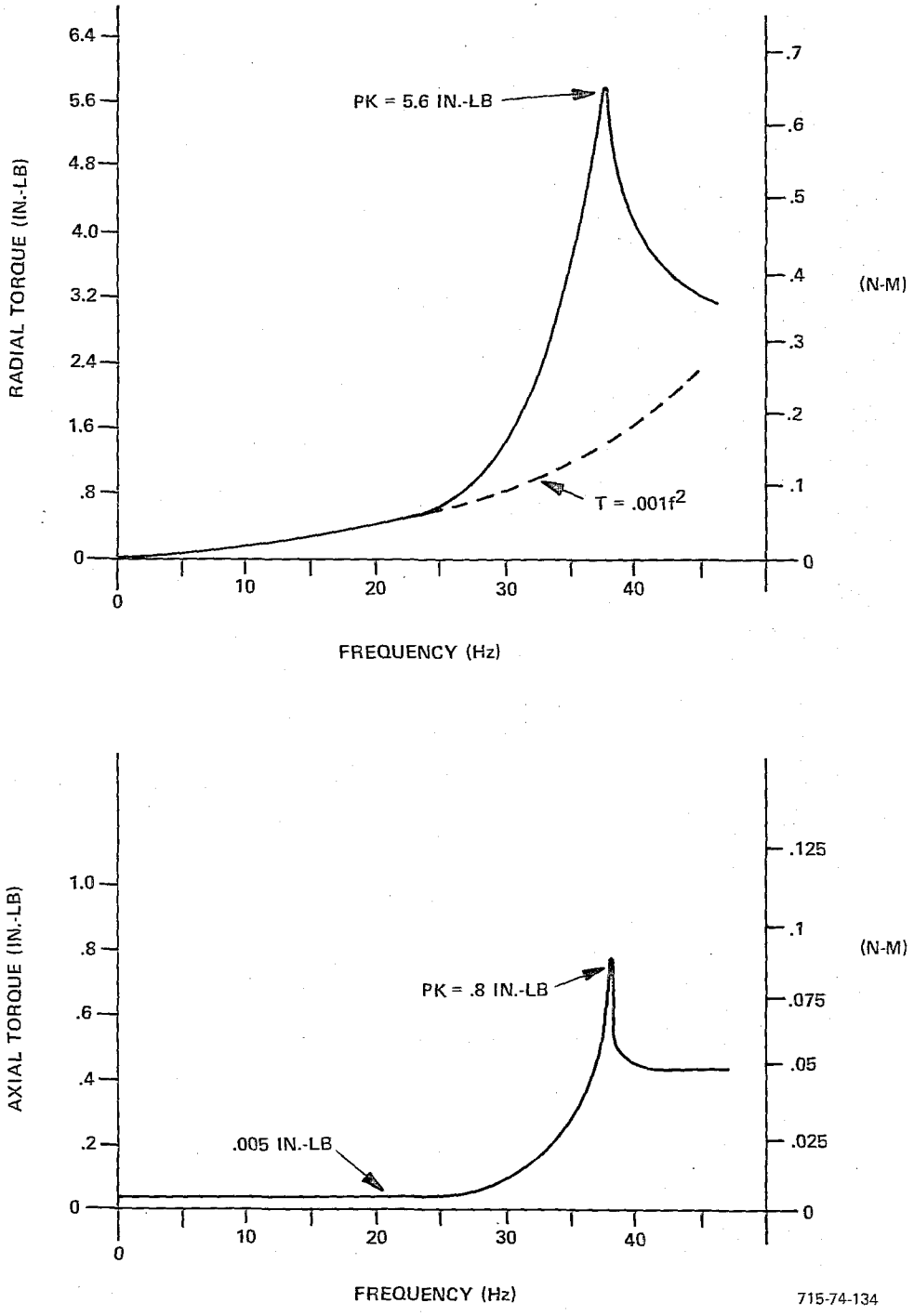

Figure 7.3-3
Predicted Magnetic Bearing Torques (Initial)

TABLE 7.3-1

PERFORMANCE CHARACTERISTICS OF LST MAGNETIC BEARING RWA

Parameter	Value		Units	
Maximum Speed during Pointing	±156	±1500	rad/sec	rpm
Momentum at Pointing Speed	60	44.3	n-m-s	ft-lb-sec^2
Reaction Torque Over Speed Range	.50	71	n-m	oz-in.
Torque Resolution	.05	.05	percent	percent
Torque Linearity Over Speed	3	3	percent	percent
Drag Torque at Maximum Speed	.00085	.12	n-m	oz-in.
Type of Motor	Brushless dc			
Bearing Type	Magnetic Three Loop Samarium Cobalt			
Total Weight (Including Electronics)	44	97	kg	lbm
Bearing Weight	16.1	35	kg	lbm
Rotor Weight	17.3	38	kg	lbm
Rotor Outer Diameter	.43	17	m	in.
Power at Maximum Speed and Torque	110	110	Watts	Watts
Run Power at 156 rad/sec	3	3	Watts	Watts
Emitted Vibrations	See Figures 7.3-2 and 7.3-3			

SECTION 8.0

HEAO 101H BEARING PRE-BREAKAWAY FRICTION TEST

The characterization of friction inside the so-called breakaway region is essential to the prediction of zero speed performance in a reaction wheel which is going from positive to negative speed or vice-versa. A precision pre-breakaway friction measurement system was developed at Sperry to provide a direct recording of the friction-stiffness/hysteresis characteristics of typical mechanical and electromechanical components used in momentum exchange devices. Motors, slip rings, gimbal bearings, and spin bearings have been tested on this fixture.

The test results presented in this section are for a duplex pair of Barden 101H ball bearings. These bearings, which are used for spin axis suspension in the Model 400 RWA, FSC, HEAO and other reaction wheels have extremely low static friction and friction stiffness. It was necessary, therefore, to compensate for the fixture flexure stiffness in the data analysis.

8.1 TEST FIXTURE AND PROCEDURE

A block diagram and mechanical schematic of the test fixture are presented in Figures 8.1-1 and 8.1-2 respectively. The test fixture basically consists of a torque motor-driven shaft mounted on flexural pivots with a 5-inch measurement arm attached to it. The flexural pivots have a stiffness of 1.16 foot-pounds per radian which is generally well below the stiffness of most test specimens. A noncontacting electronic micrometer capable of measuring motions of .2 microinch is used to sense the rotational displacement of the 5-inch measurement arm. The torque motor is a toroidally wound, limited angle brushless dc device with negligible cogging and hysteresis torques.

The rotating part of the test specimen (bearing inner race) is mounted to the shaft. The nonrotating part is fixed to the housing. Fixturization is provided that simulates the intended mounting configuration of the test specimen. This is important, since alignment and preload can significantly affect friction characteristics.

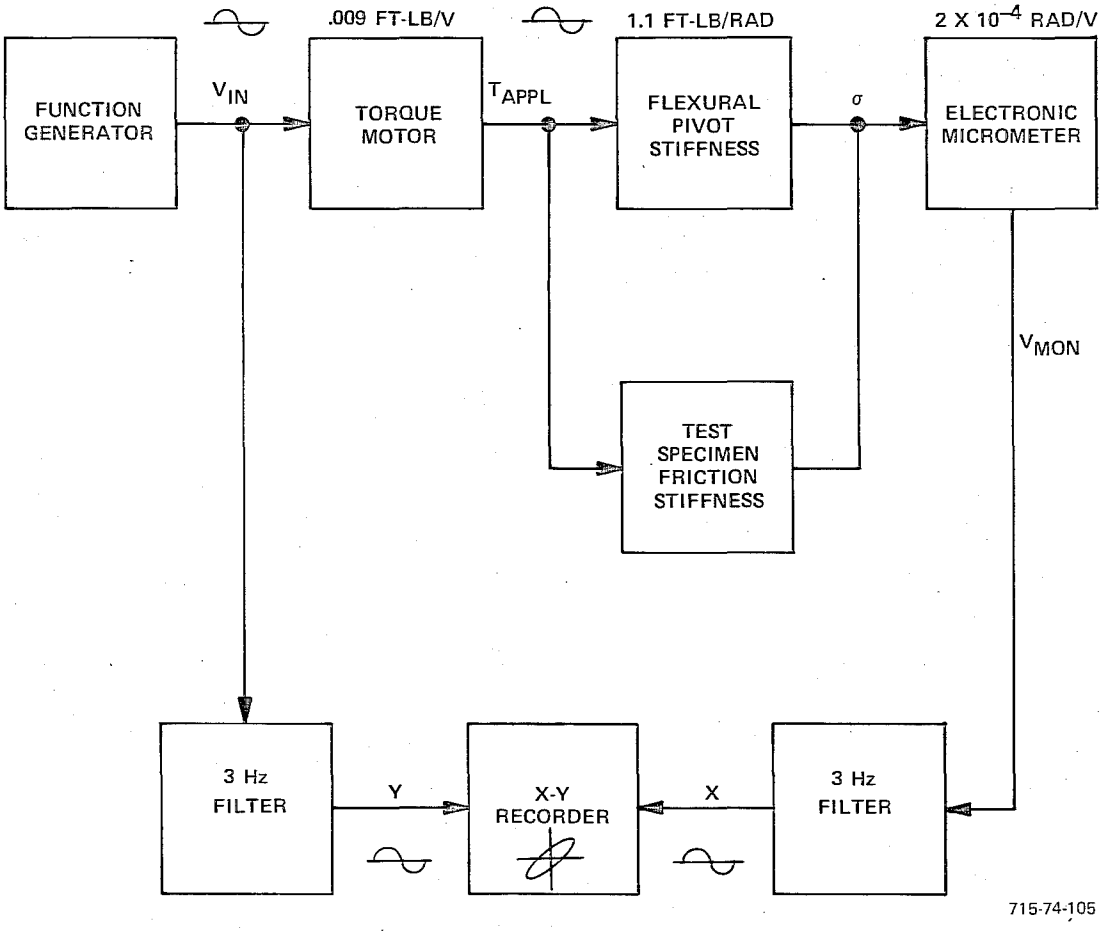

Figure 8.1-1
Friction Characterization Test Fixture Block Diagram

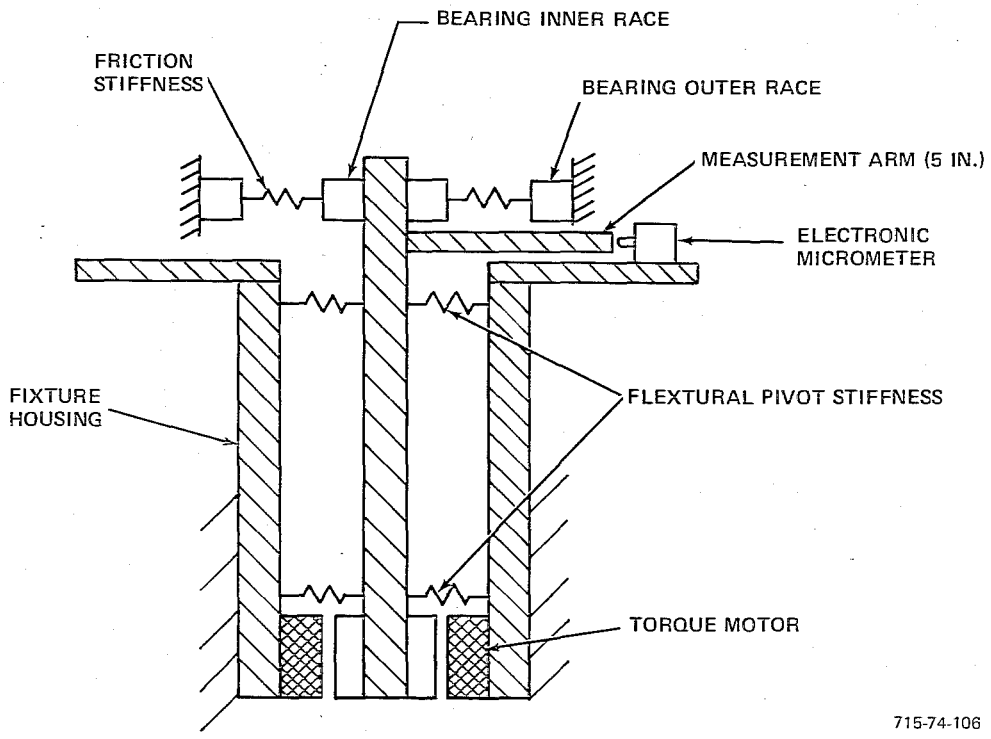

Figure 8.1-2
Test Fixture Mechanical Schematic

To measure the friction/stiffness characteristics, the torque motor is driven with a .02-Hz sine wave from the function generator. This low frequency ensures that inertial and viscous torques will be negligible compared to the spring restoring torques of the test specimen. The torque motor has a measured torque constant of 9.12×10^{-3} foot-pounds per volt. The torque motor input voltage is monitored on the Y axis and an X-Y plotter after first passing through a 3-Hz filter to eliminate extraneous noise in the system. The output of the electronic micrometer (scale factor = 2×10^{-4} radians per volt) is also passed through a 3-Hz filter before being displayed on the X axis of the X-Y plotter.

Table 8.1-1 identifies the specific test equipment, mounting fixtures and test articles used in these tests. Figure 8.1-3 shows photographs of the test fixture and bearing set under test.

TABLE 8.1-1

FRICTION TEST HARDWARE IDENTIFICATION

Test Specimen	Two - duplex pairs of Barden 101H ball bearings	
	Set 1	Set 2
Preload	12 lb	12 lb
Lubricant	Andok-C Grease	V-79 Oil
Mounting Fixtures	5100-11085 Shaft Hub	
	5100-11083 101 Bearing Cartridge, Part A	
	5100-11082 101 Brace, Part A	
	5100-11081 101 Brace, Part B	
	5100-11080 101 Brace Bracket	
	5100-11084 101 Bearing Cartridge, Part B	
	5100-21037 Friction Characterization Fixture	
Function Generator	Wavetek Model 142, S/N 11592	
Electronic Micrometer	Lion Model 30, S/N 1005 with 1X probe, S/N 1173	
X-Y Plotter	HP Model 7045A, S/N 12301	

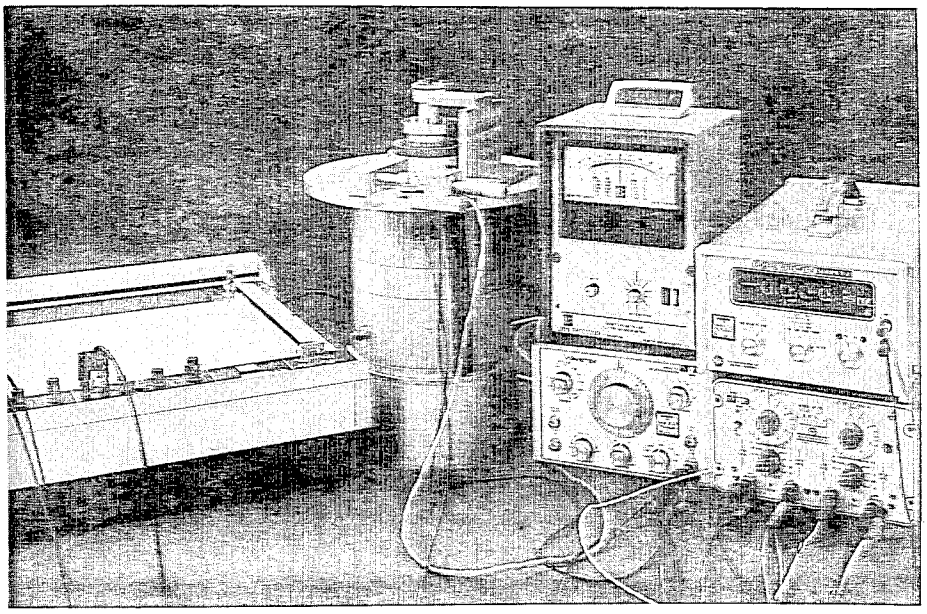

Friction Fixture Test Setup

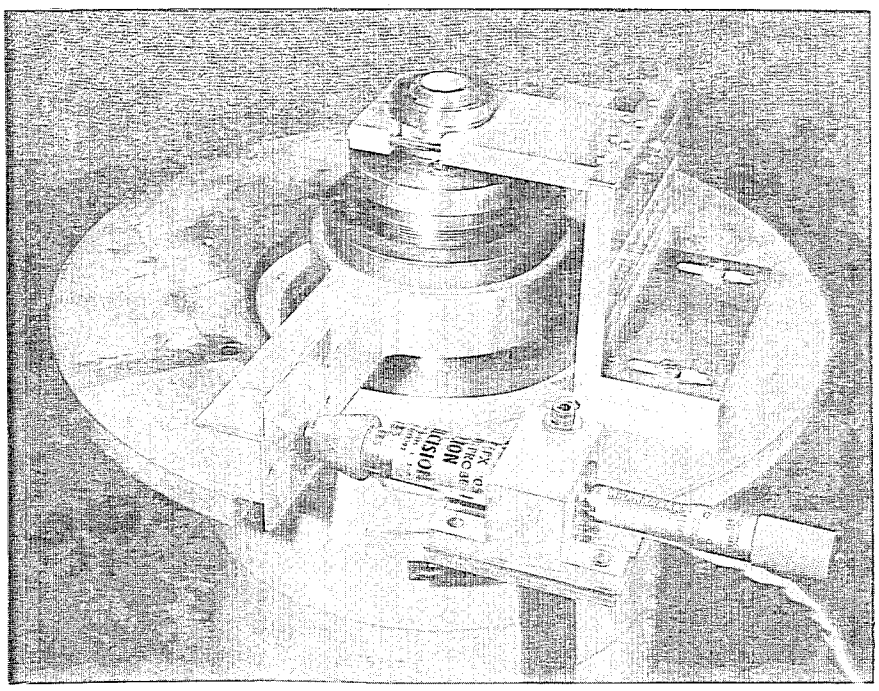

715-74-107

Figure 8.1-3
Bearings Mounted on Friction Test Fixture Using .1X Probe

8.2 TEST DATA AND CONCLUSIONS

Some friction characteristic plots are shown in Figures 8.2-1 through 8.2-8. For each of four positions of the bearing outer race (identified by 1 through 4, spaced approximately 90 degrees apart) two plots were made, one with low torque motor input and one with high input. Two plots were also made on each figure with different amplitude inputs to the torque motor.

The plotter pen was allowed to make approximately one complete loop before it was lifted. As stated before, the loop was made with a sinusoidal rate of .02 Hz, with both the angular displacement and input torque signals filtered by a 3-Hz low pass filter before being displayed on the X-Y plotter.

The following conclusions can be drawn from this data:

- The 101H ball bearing set at very low speed behaves as a continuous nonlinear spring element opposing shaft rotation. Torsional stiffness is very low (less than 5 foot-pounds per radian).

- A breakaway phenomenon occurs at very low torque (between 50 and 300×10^{-6} foot-pounds), beyond which the spring-restoring torque remains approximately constant. A second friction increase occurs when the retainers begin to ride against the outer races. Since this occurs at an angular deflection beyond the measurement range of the fixture, it was not possible to characterize this phenomenon.

- No significant difference in the pre-breakaway friction was noted between the two bearing sets tested, one of which contained Andok-C grease and the other V-79 oil.

8.3 FRICTION MODEL

A simple friction model, which has been found adequate for many computer simulations, is shown in Figure 8.3-1. As the deflection increases, the springs act together to provide a high stiffness. Above breakaway, the integrator is saturated and the only restoring force is that due to the fixture flexural stiffness, which is not part of the bearing friction model. If the direction of rotation is reversed, the saturated integrator immediately returns to its linear region, thereby imposing the maximum (highest stiffness) resistance to motion.

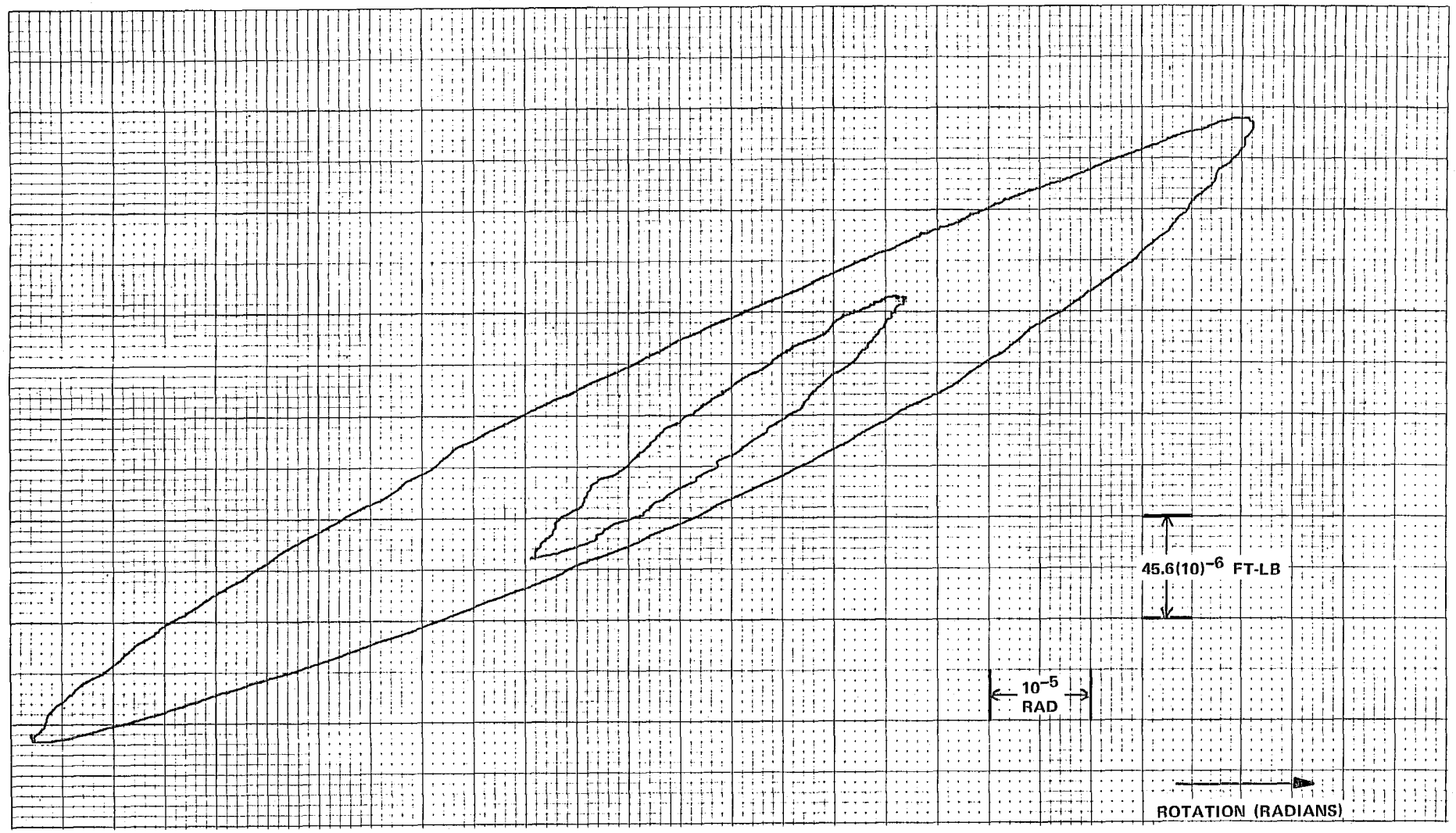

Figure 8.2-1
Pre-Breakaway Friction, 6/16/75
101H Bearing Set No. 1
Position No. 1
Vertical Scale = 45.6 x 10^{-6} ft-lb/in.
Horizontal Scale = 10 x 10^{-6} rad/in.
Vertical Scale = 61.8 x 10^{-6} N-m/in.

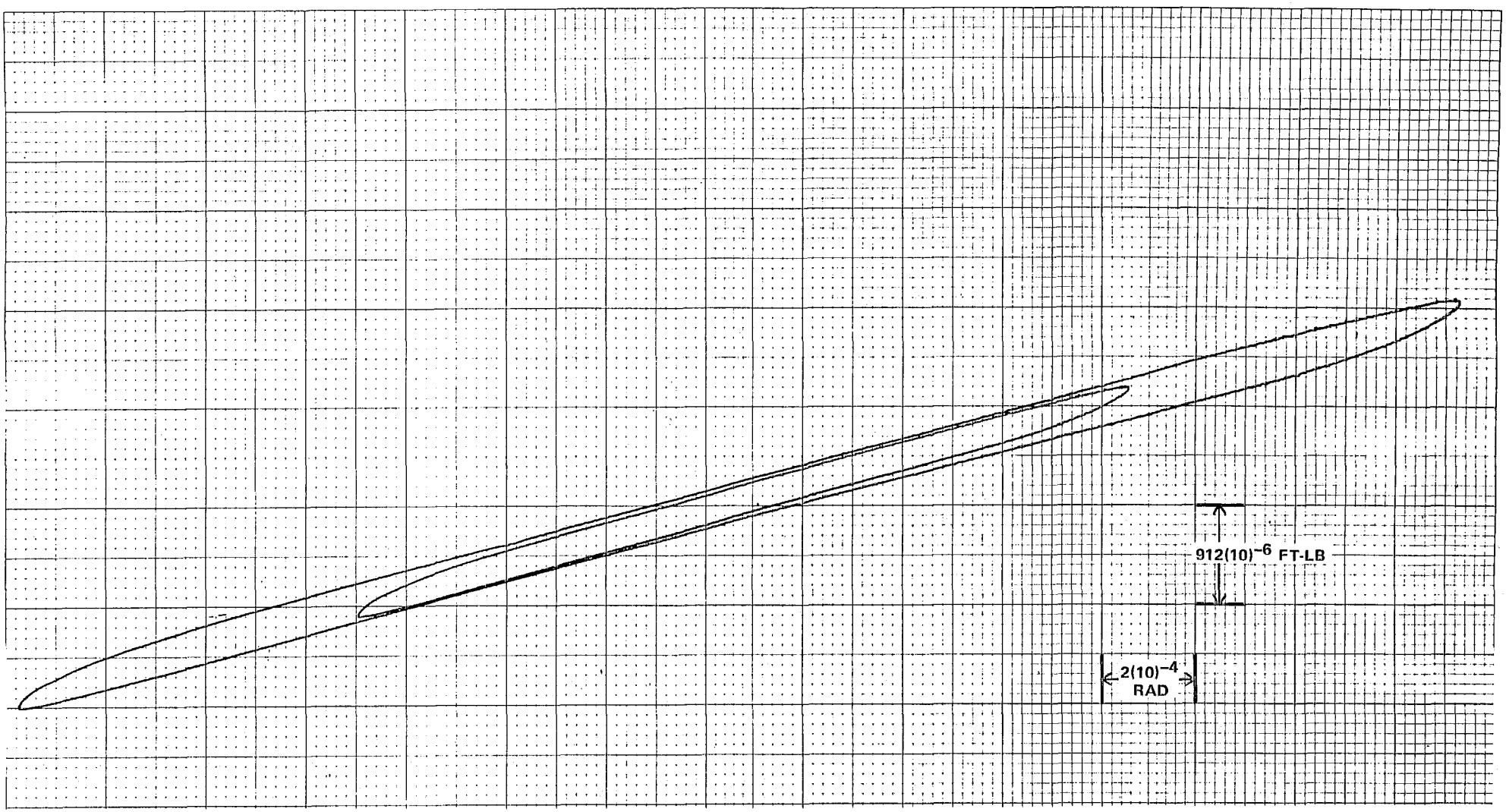

Figure 8.2-2
Pre-Breakaway Friction, 6/16/75
101H Bearing Set No. 1
Position No. 1
Vertical Scale = 912 x 10^{-6} ft-lb/in.
Horizontal Scale = 200 x 10^{-6} rad/in.
Vertical Scale = 1.24 x 10^{-3} N-m/in.

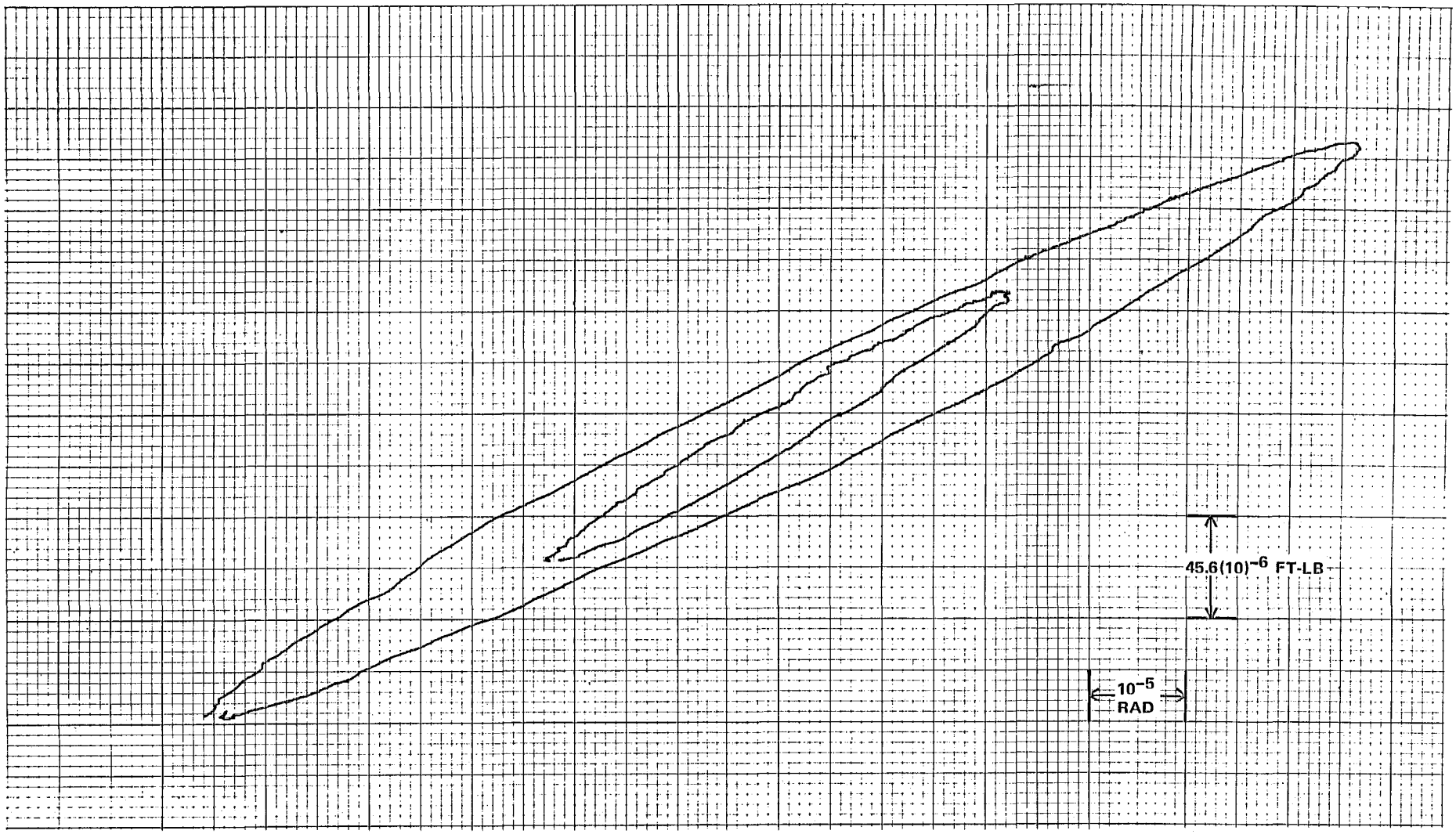

Figure 8.2-3
Pre-Breakaway Friction, 6/16/75
101H Bearing Set No. 1
Position No. 2
Vertical Scale = 45.6 x 10^{-6} ft-lb/in.
Horizontal Scale = 10 x 10^{-6} rad/in.
Vertical Scale = 61.8 x 10^{-6} N-m/in.

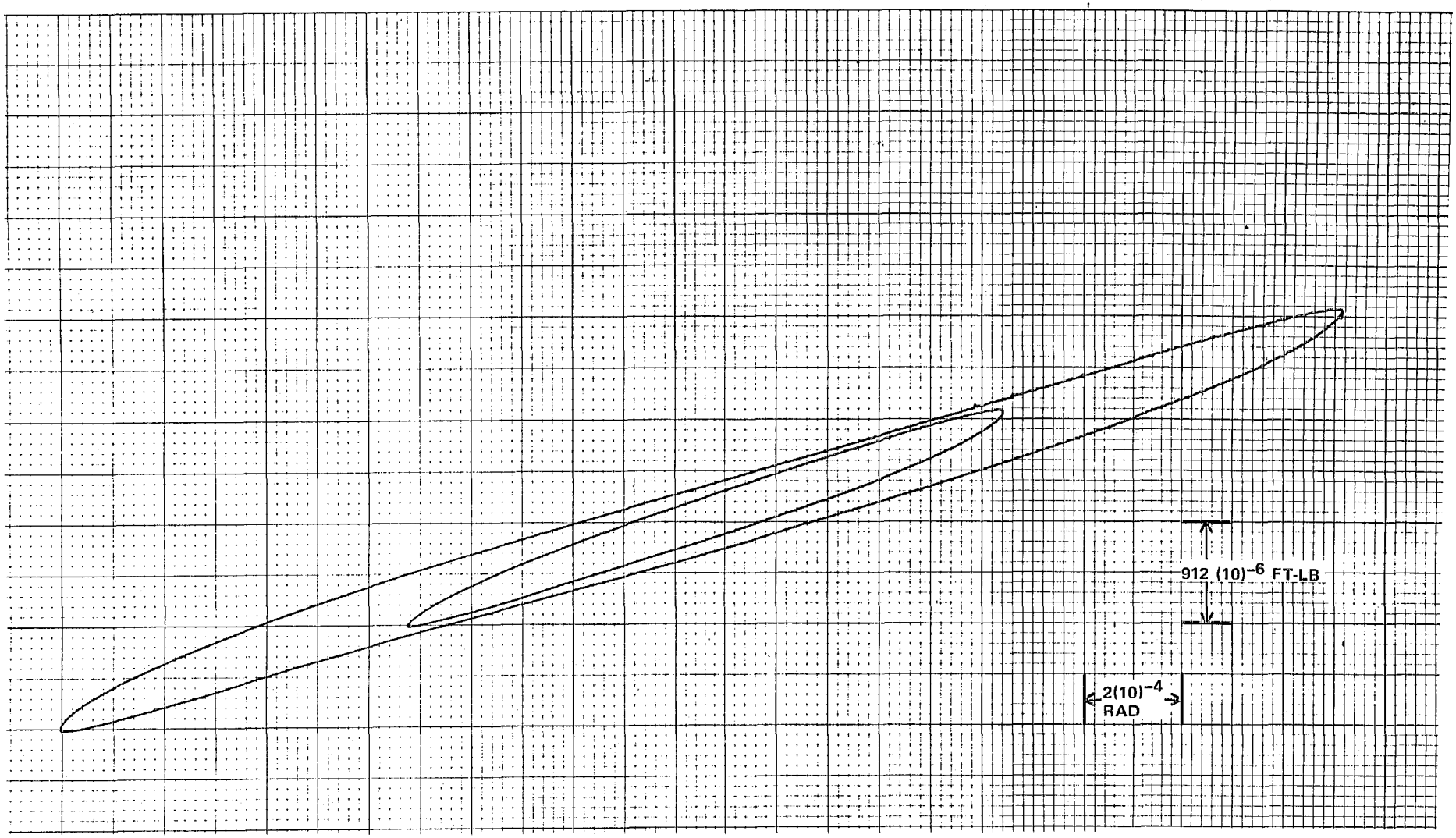

Figure 8.2-4
Pre-Breakaway Friction, 6/16/75
101H Bearing Set No. 1
Position No. 2
Vertical Scale = 912 x 10^{-6} ft-lb/in.
Horizontal Scale = 200 x 10^{-6} rad/in.
Vertical Scale = 1.24 x 10^{-3} N-m/in.

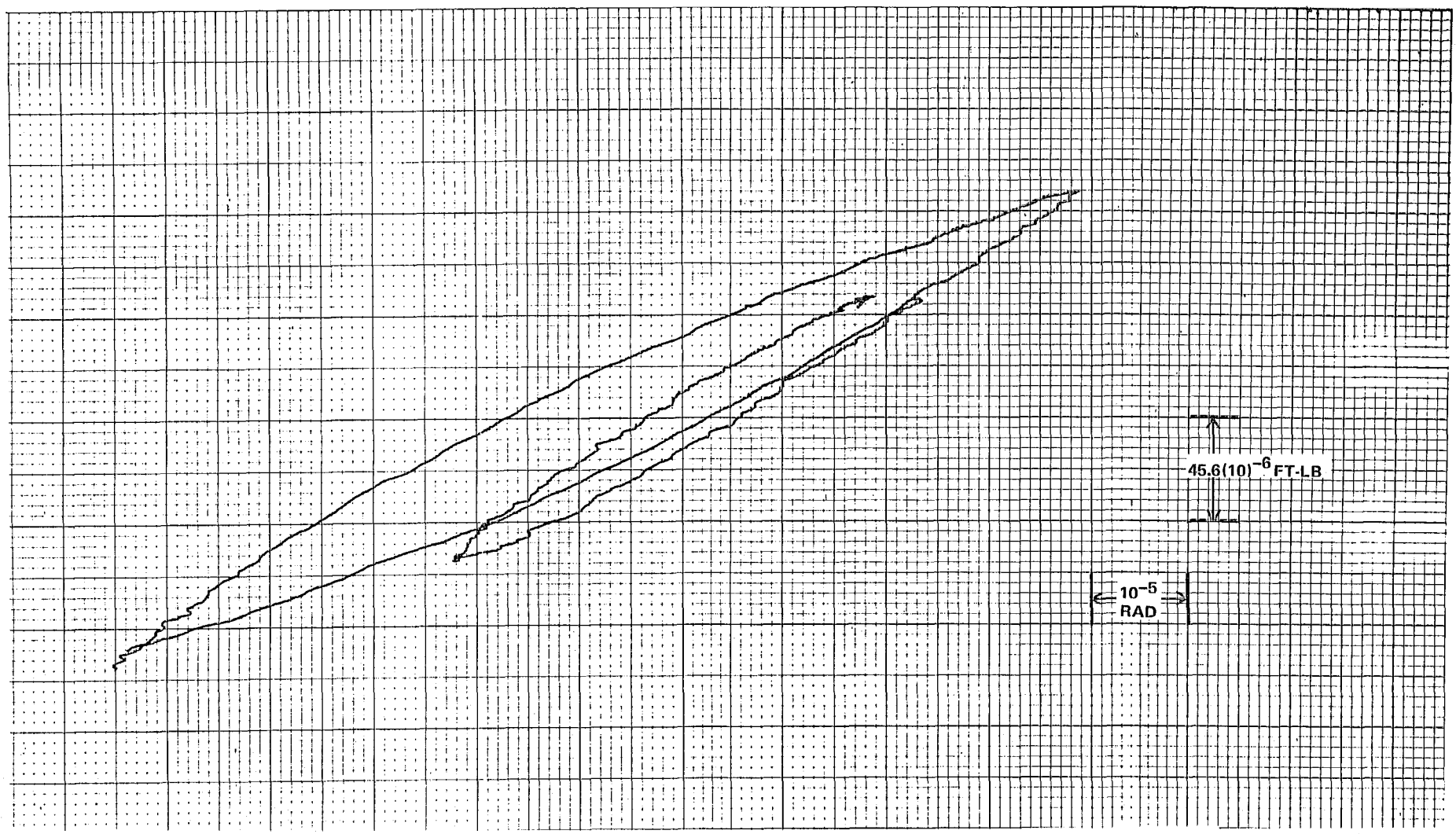

Figure 8.2-5
Pre-Breakaway Friction, 6/16/75
101H Bearing Set No. 2
Position No. 1
Vertical Scale = 45.6 x 10^{-6} ft-lb/in.
Horizontal Scale = 10 x 10^{-6} rad/in.
Vertical Scale = 61.8 x 10^{-6} N-m/in.

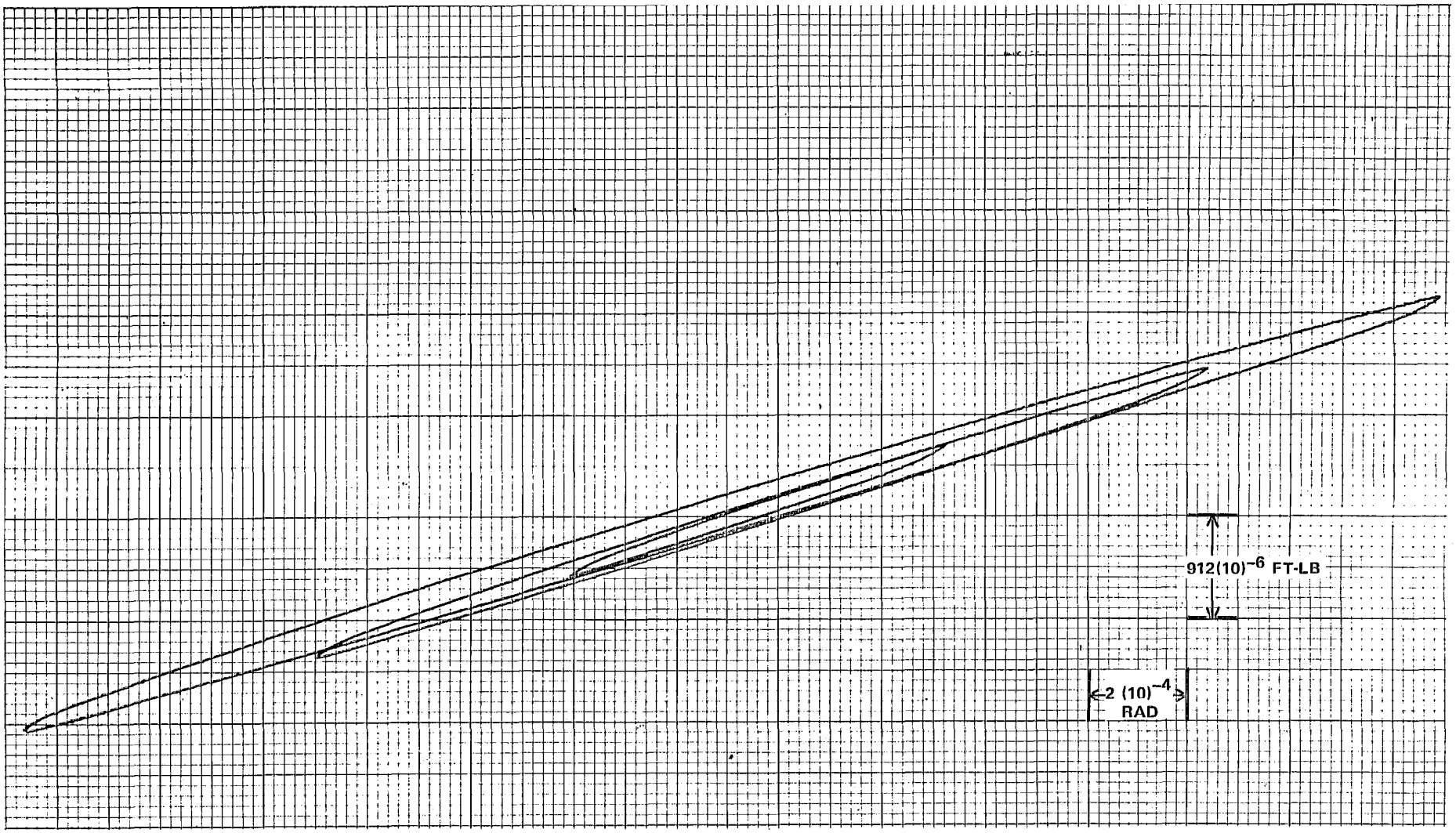

Figure 8.2-6
Pre-Breakaway Friction, 6/16/75
101H Bearing Set No. 2
Position No. 1
Vertical Scale = 912 x 10^{-6} ft-lb/in.
Horizontal Scale = 200 x 10^{-6} rad/in.
Vertical Scale = 1.24 x 10^{-3} N-m/in.

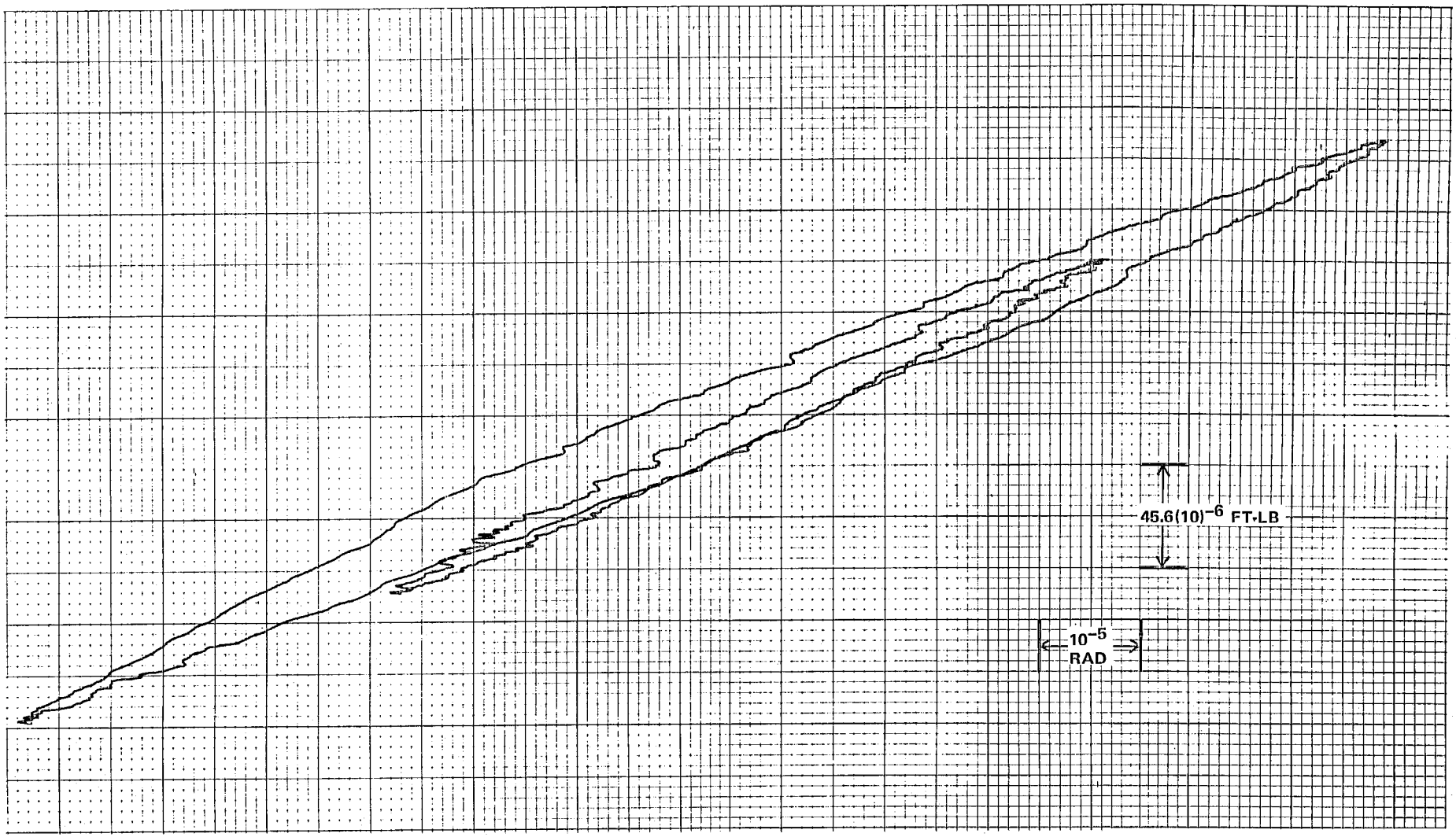

Figure 8.2-7
Pre-Breakaway Friction, 6/16/75
101H Bearing Set No. 2
Position No. 2
Vertical Scale = 45.6 x 10^{-6} ft-lb/in.
Horizontal Scale = 10 x 10^{-6} rad/in.
Vertical Scale = 61.8 x 10^{-6} N-m/in.

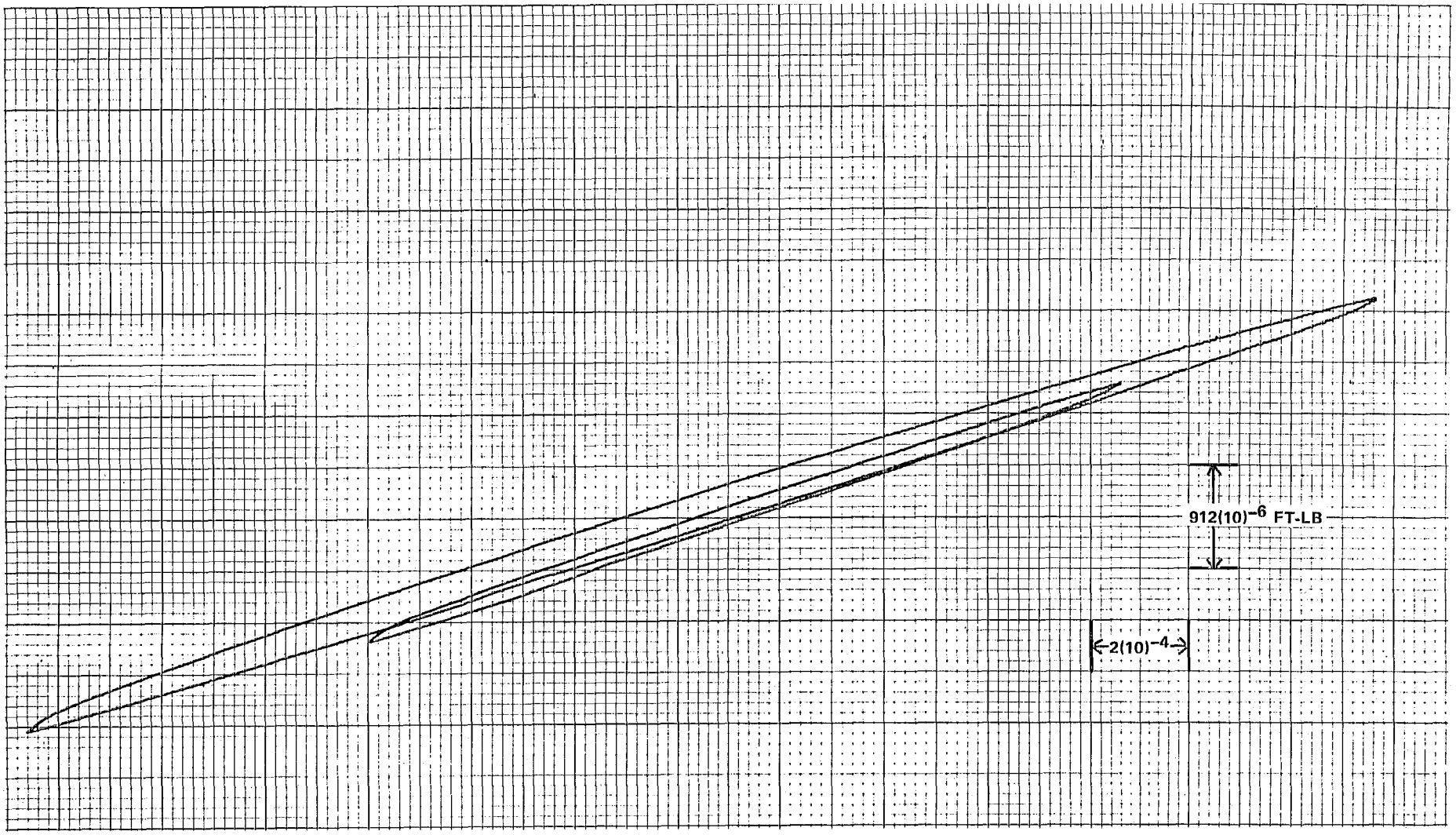

Figure 8.2-8
Pre-Breakaway Friction, 6/16/75
101H Bearing Set No. 2
Position No. 2
Vertical Scale = 912 x 10^{-6} ft-lb/in.
Horizontal Scale = 200 x 10^{-6} rad/in.
Vertical Scale = 1.24 x 10^{-3} N-m/in.

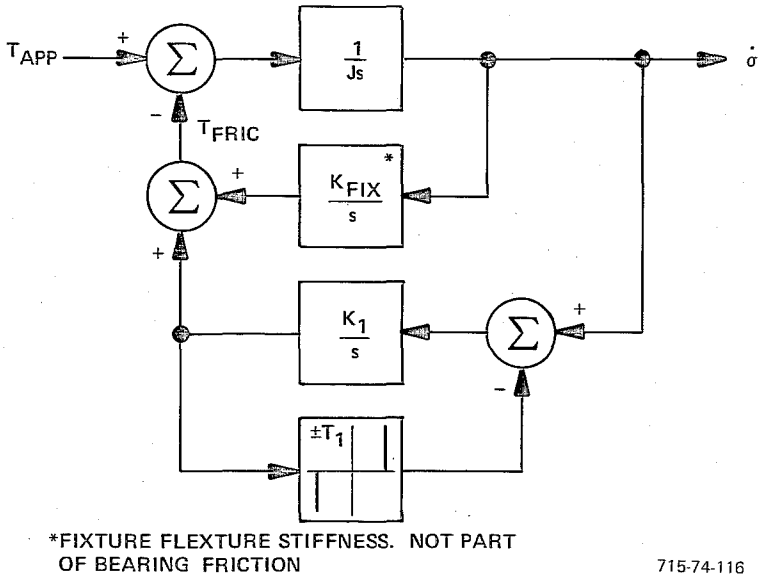

Figure 8.3-1
Limited Spring Friction Model
(* Not Part of Test Article Friction)

This results in the generation of a hysteresis loop in the friction torque/deflection curve. Additional limited springs may be included to provide a closer match with the continuous friction characteristic. Figure 8.3-2 indicates typical friction characteristics realized using this model (including the fixture flexure stiffness).

The data measured on the 101 bearing sets can only be approximated with this simple model. A conservative (worst case) friction model based on the maximum stiffness and breakaway torque levels observed in the data is defined by:

$$K_1 = 4.31 \text{ ft-lb/rad}$$

$$T_1 = 300 \times 10^{-6} \text{ ft-lb}$$

$$K_{fix} = 1.16 \text{ ft-lb/rad (fixture)}$$

The single limited-spring model has been of use for predicting worse case performance. A more accurate (but complex) model which provides a smooth curve fit to the continuous friction stiffness data is shown in Figure 8.3-3. This representation is based on a square law relation between stiffness and torque as discussed in Reference 1. The parameters were determined as indicated in Figure 8.3-4. This plot applies for positive angular rate. For negative rate, the stiffness characteristic would be a mirror image of that shown, increasing rather than decreasing from left to right.

A considerable spread of the stiffness data is indicated in Figure 8.3-4 between those points reduced from different test plots and identified by the different plot symbols. The curve shown represents an approximate square-law fit to all the data. The model given in Figure 8.3-3 was simulated using the square-law parameters $a_1 = 1.38 \times 10^8$ foot-pound per radian per $(\text{ft-lb})^2$, $a_2 = 85 \times 10^{-6}$ foot-pounds and $T_1 = 90 \times 10^{-6}$ foot-pounds. A typical result is shown in Figure 8.3-5 for a peak applied torque of 10^{-4} foot-pounds. The model agrees reasonably well with much of the measured data.

---

(1) A Solid Friction Model by P. R. Dahl, Aerospace Corp, Report No. TOR-0158 (3107-8)-1, May 1968.

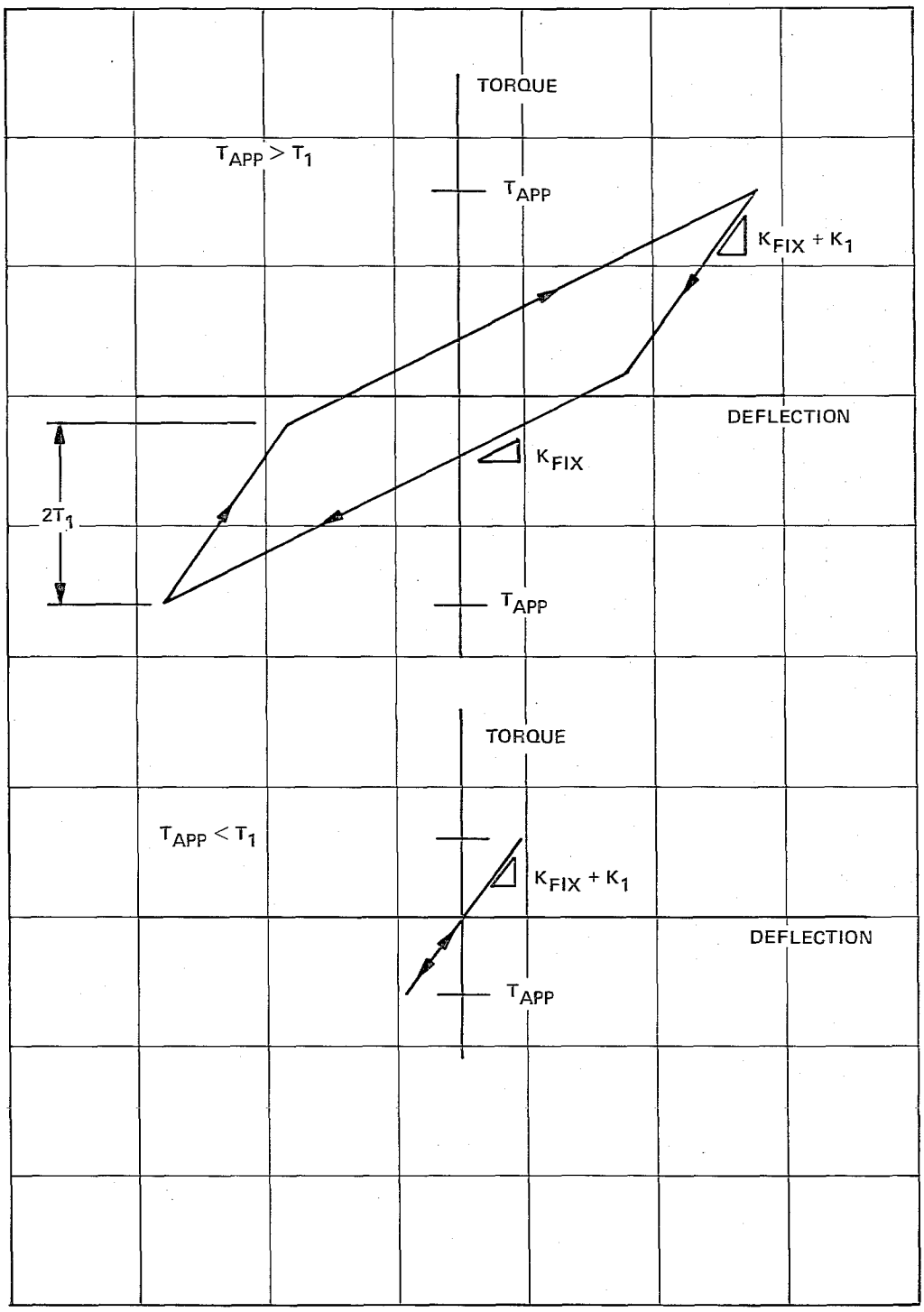

Figure 8.3-2
Typical Friction Characteristics of Limited Spring Model

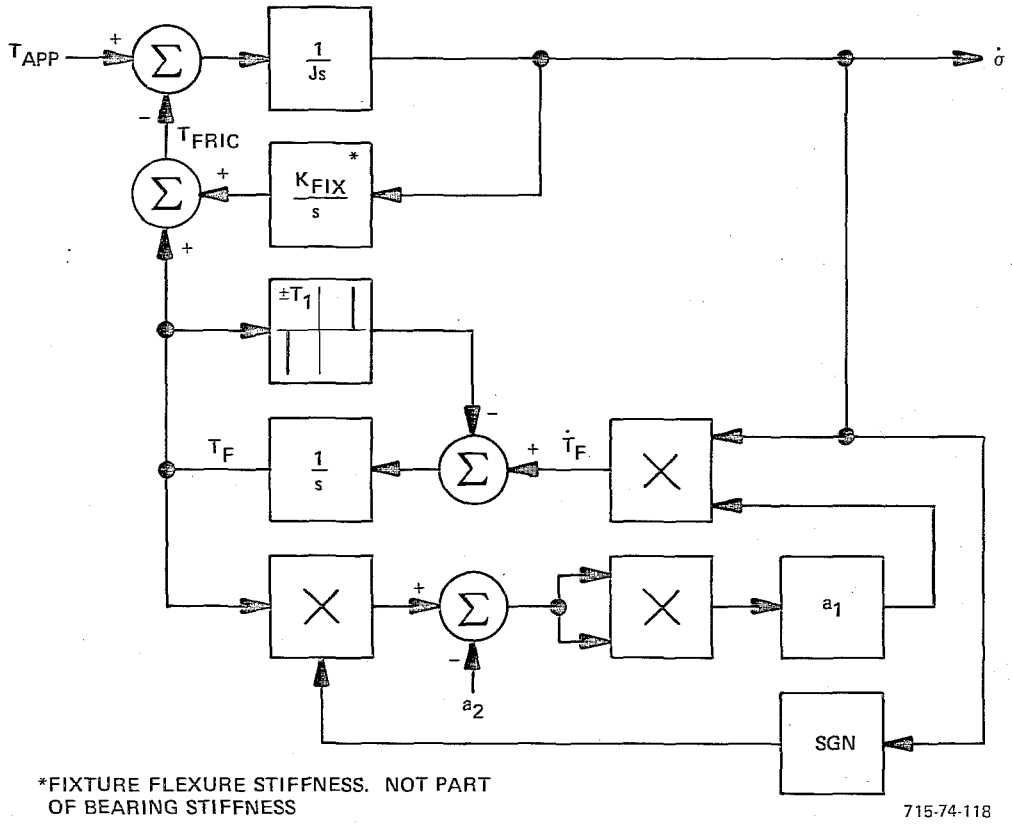

Figure 8.3-3
Square-Law Friction Model

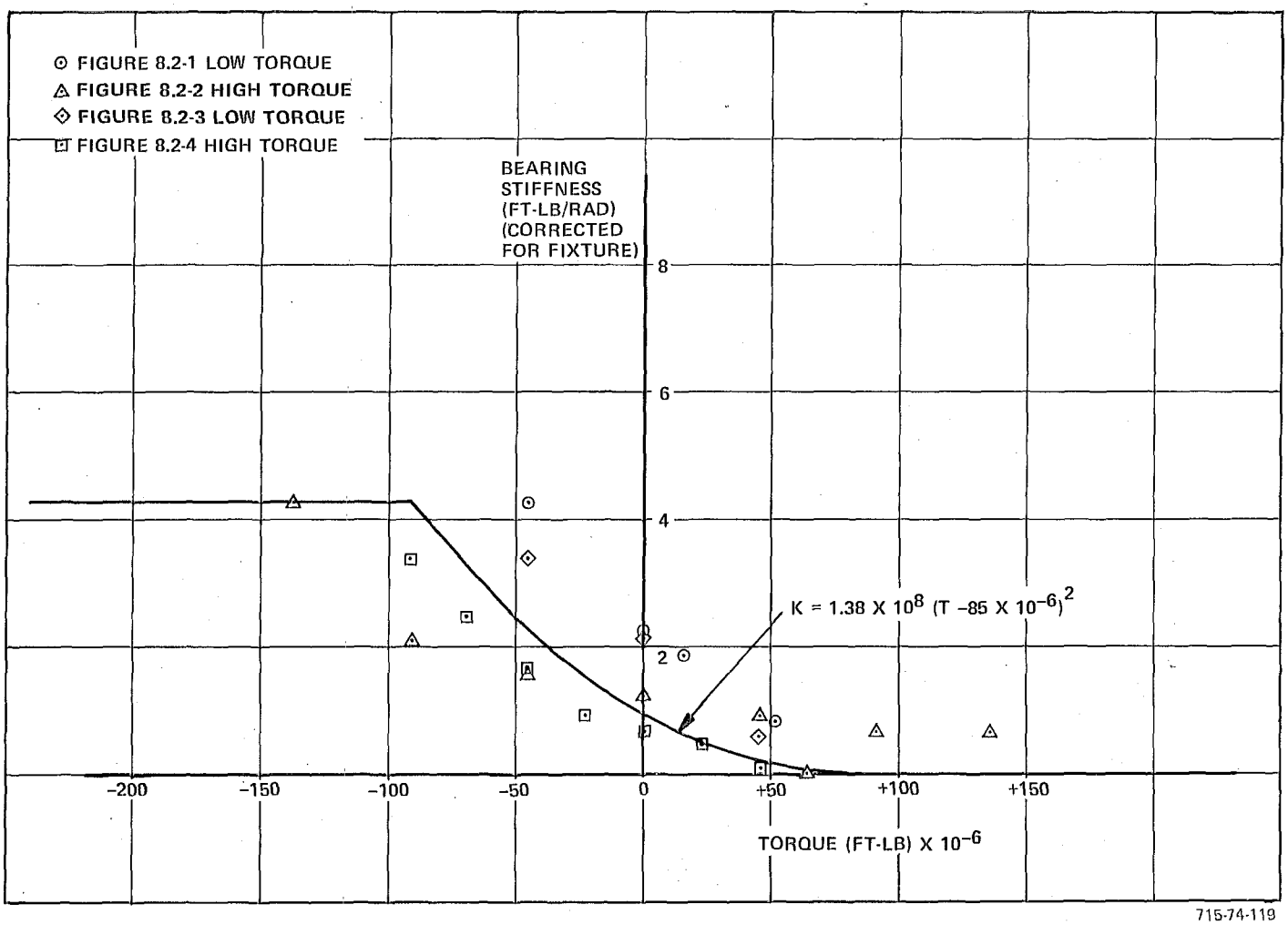

Figure 8.3-4
Square-Law Fit to 101H Friction Data

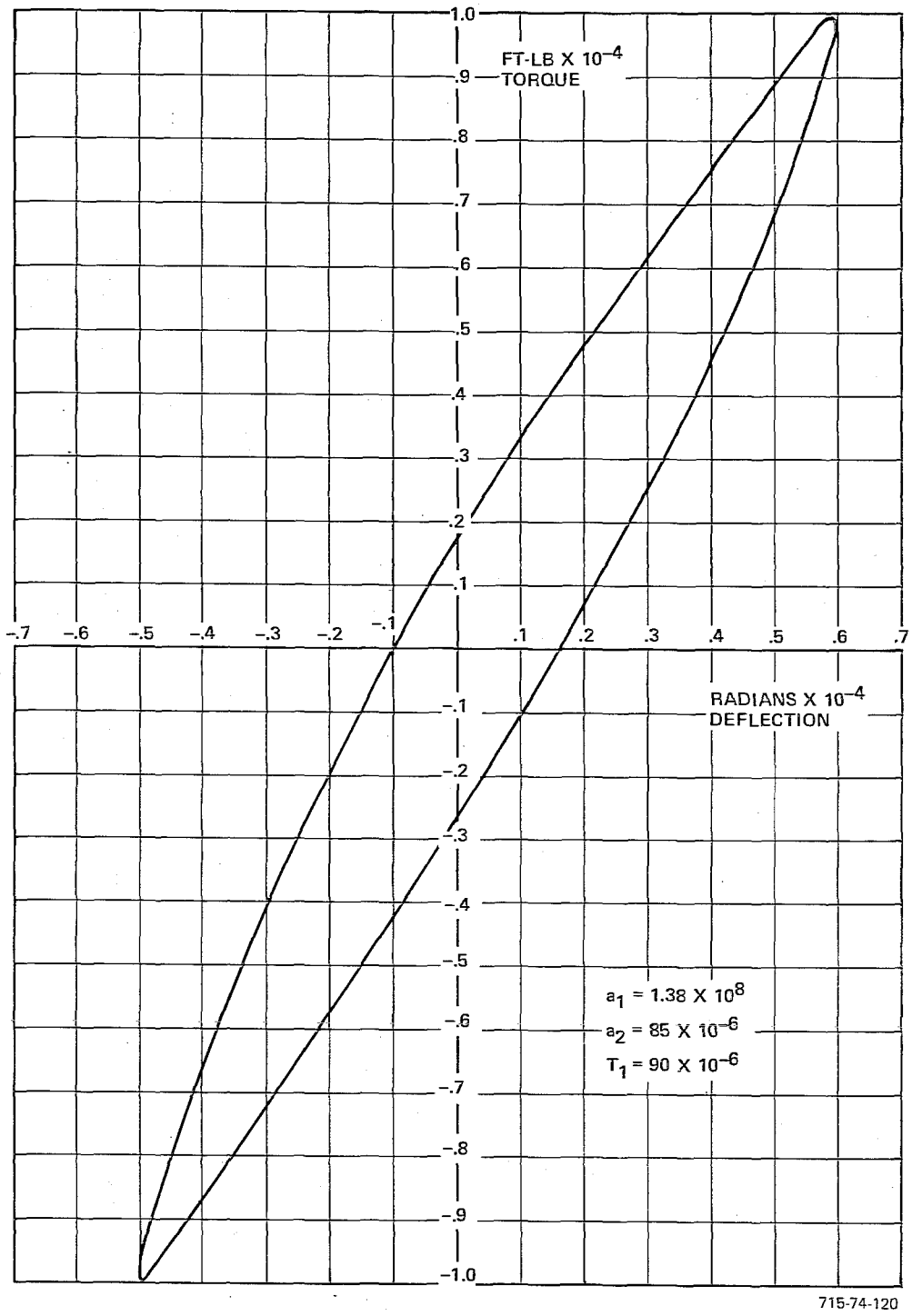

Figure 8.3-5
Typical Square-Law Friction Characteristic for 101H Bearing Set

In summary, it is possible to establish two models based on the test data:

Model 1: An approximate model (Figure 8.3-1) for the pre-breakaway friction consisting of a single limited angle spring. The maximum spring rate and limit are:

$$K_1 = 4.31 \text{ ft-lb/rad}$$

$$T_1 = 300 \times 10^{-6} \text{ ft-lb}$$

Model 2: A more complete model based on Dahl's work consisting of a limited square-law spring with a rate direction sensitive stiffness. Typical parameter values for this model are

$$a_1 = 1.38 \times 10^{8} \text{ ft-lb/rad per (ft-lb)}^2$$

$$a_2 = 85 \times 10^{-6} \text{ ft-lb}$$

$$T_1 = 90 \times 10^{-6} \text{ ft-lb}$$

APPENDIX

ROTATIONAL DYNAMICS

Any rotor has three principal axes of inertia, which intersect at the rotor mass center. The maximum principal axis of inertia is the axis about which the inertia of the rotor is a maximum; in Figure A.1-1, the z axis, and in Figure A.1-2, either the x or y axes are maximum principal axes. The minimum principal axis is the axis about which the rotor inertia is a minimum; in Figure A.1-1, either the x or y axes, and in Figure A.1-2 the z axis, are minimum principal axes.

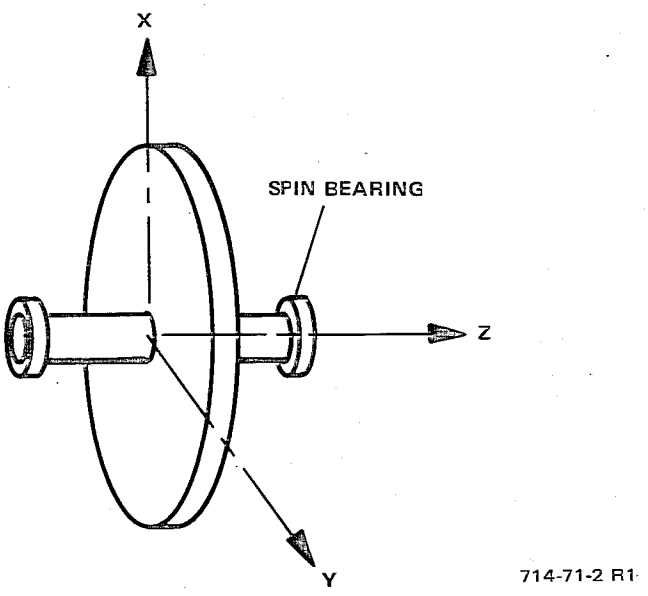

Figure A.1-1
Thin Disk Rotor

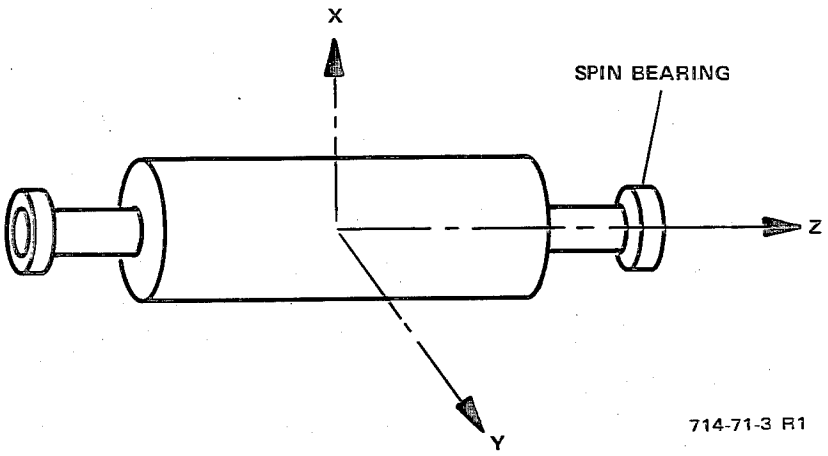

Figure A.1-2
Cylindrical Rotor

2.3

A perfectly balanced rotor is one whose axis of rotation exactly coincides with a principal inertia axis. If the axis of rotation is parallel to but not coincident with a principal axis, pure static imbalance exists in the rotor. For the symmetrical rotors shown in Figures A.1-1 and A.1-2, this static imbalance produces rotor fixed radial forces at the spin bearings which are equal to and in phase with each other, resulting in an oscillatory radial force being applied to the spin bearing support structure.

If the axis of rotation passes through the cg of the rotor but is not parallel to a principal axis, pure dynamic imbalance exists in the rotor. This dynamic imbalance results in rotor fixed radial forces at the spin bearings which are equal to but out of phase with each other, resulting in an oscillatory couple being applied to the spin bearing support structure.

Real rotors have both static and dynamic unbalance. Analytically, it is easiest to consider each type of unbalance separately, and superimpose them to obtain their combined effects.

A.1 Static Unbalance and Translational Dynamics

Figure A.1-3 is a mechanical schematic of a rotor suspended by two spin bearings which are constrained by equal radial stiffnesses and damping. The z axis is selected to coincide with the nominal rotor spin axis and the x, y axes are in the plane of the rotor cg. These axes are inertially fixed. The rotor center of mass is offset from the z axis by a small distance, ϵ, selected to lie along the x axis at time 0 (rotor not rotating).

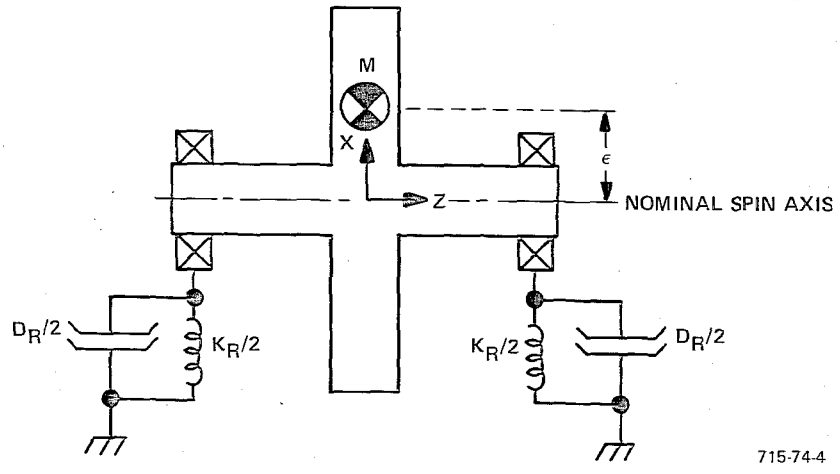

Figure A.1-3
Statically Unbalanced Rotor at Rest

With the rotor spinning at speed ω_s radians per second, the springs deflect as shown in Figure A.1-4. If x_s and y_s are the deflections of the spin axis, the center of mass is given by:

$$x_c = x_s + \epsilon \cos \omega_s t$$
$$y_c = y_s + \epsilon \sin \omega_s t \qquad \text{(A-1)}$$

and the equations of motion for the mass center are:

$$M\ddot{x}_c = -K_R x_s - D_R \dot{x}_s$$
$$M\ddot{y}_c = -K_R y_s - D_R \dot{y}_s \qquad \text{(A-2)}$$

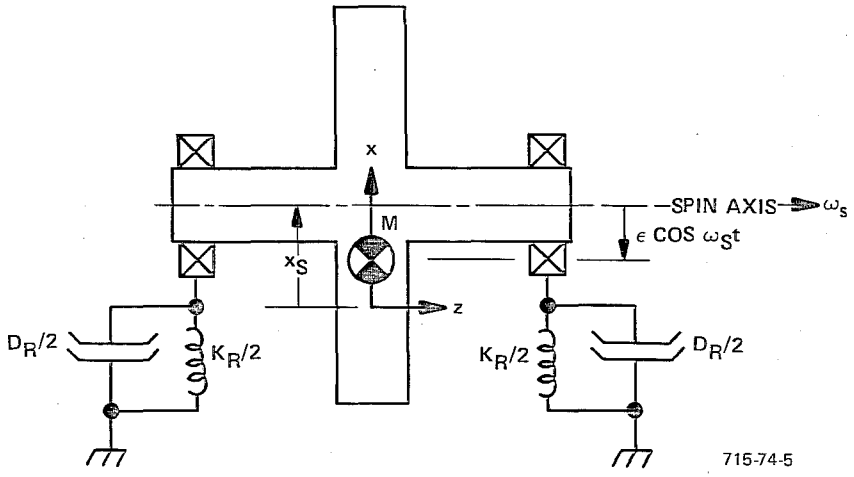

Figure A.1-4
Statically Unbalanced Spinning Rotor

Combining equations (A-1) and (A-2) and Laplace transforming yields the equations of motion for this system:

$$\left(Ms^2 + D_R s + K_R\right) x_s(s) = M\epsilon\omega_s^2 \left(\frac{s}{\omega_s}\right) u(s)$$
$$\left(Ms^2 + D_R s + K_R\right) y_s(s) = M\epsilon\omega_s^2 \, u(s) \qquad \text{(A-3)}$$

where

$$u(s) = \frac{\omega_s}{s^2 + \omega_s^2} = \mathcal{L}\left(\sin \omega_s t\right)$$

The term, $M\epsilon\omega_s^2$, appearing on the right side of these equations, is known as the static unbalance force and generally has the units of pounds force. Other frequently used terms for static unbalance are $M\epsilon$, usually given in ounce-inches, or just ϵ, specified in microinches. The static unbalance force is of constant amplitude and is fixed in the rotor. Therefore, the nonrotating x, y components of this force are sinusoidal at the spin frequency. It should be noted that the force transmitted to the large mass under the wheel is not the static unbalance force but is related to the deflection of the bearings and the supporting stiffness and damping:

$$F_{xs} = K_R x_s + D_R \dot{x}_s$$
$$F_{ys} = K_R y_s + D_R \dot{y}_s \qquad \text{(A-4)}$$

Figure A.1-5 is a block diagram of the statically unbalanced rotor dynamics. Both x and y axis dynamics are identical and uncoupled. The same unbalance force is applied to each axis but in quadrature.

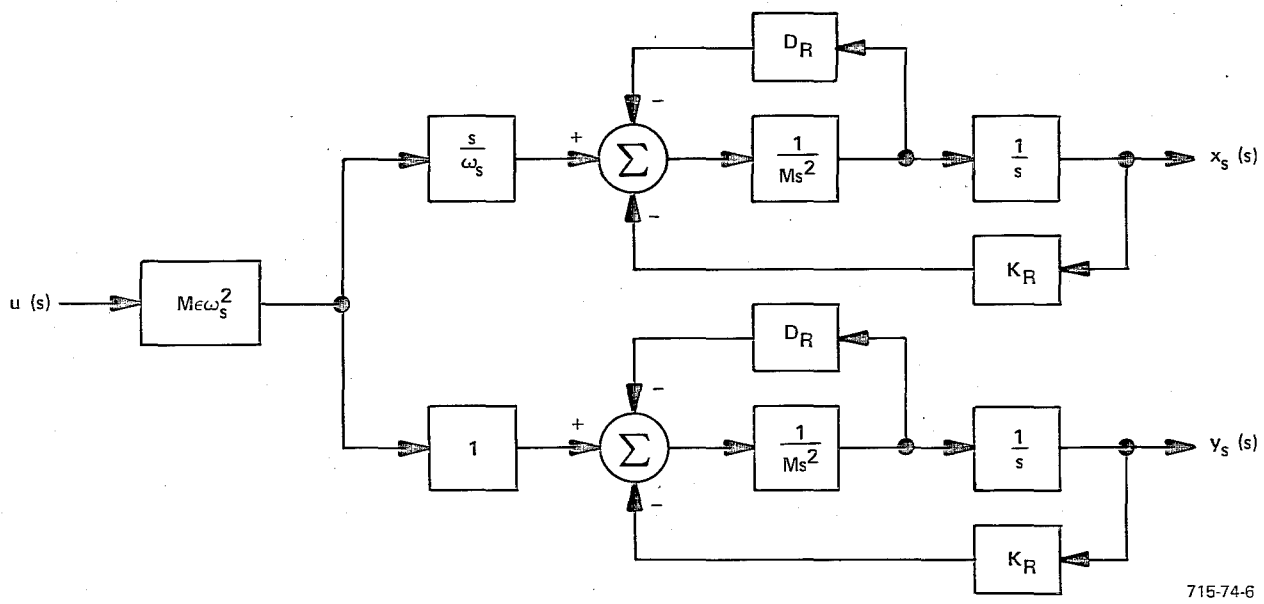

Figure A.1-5
Block Diagram of Statically Unbalanced Rotor Dynamics

For a constant cg eccentricity, ϵ, the static unbalance force increases as the square of rotor speed, and the spin axis deflection is given by:

$$\frac{x_s(s)}{u(s)} = \frac{M\epsilon\omega_s s}{Ms^2 + D_R s + K_R}$$

$$\frac{y_s(s)}{u(s)} = \frac{M\epsilon\omega_s^2}{Ms^2 + D_R s + K_R} \qquad \text{(A-5)}$$

Since the unbalance force is sinusoidal, the amplitude and phase of these deflections are obtained by setting $s = j\omega_s$. Figure A.1-6 shows the response as a function of rotor speed. If the structural damping, D_R, is neglected, these deflections may be multiplied by the constant, K_R, to obtain the force transmitted to the mounting interface.

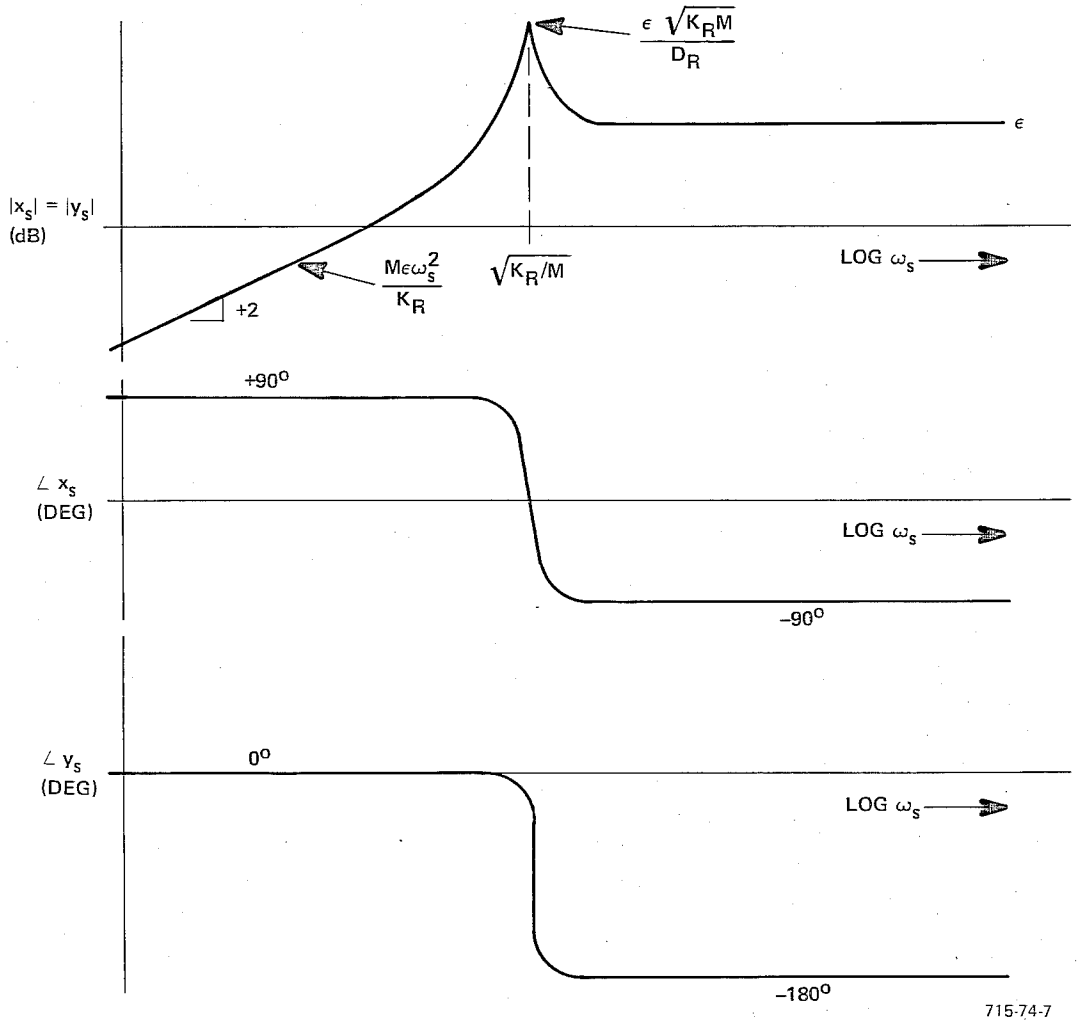

Figure A.1-6
Deflection vs Rotor Speed of a Statically Unbalanced Rotor

The deflection is shown to increase proportional to speed squared until the resonant frequency $\sqrt{\frac{K_R}{M}}$ is reached. This same resonance is present when the rotor is not turning and the wheel is vibrated by an external force. Above this speed the deflection approaches an asymptote equal to the eccentricity, ϵ, as the rotor spins about its true center of mass.

Figure A.1-7 illustrates the motion of the rotor as viewed from one of the spin bearings.

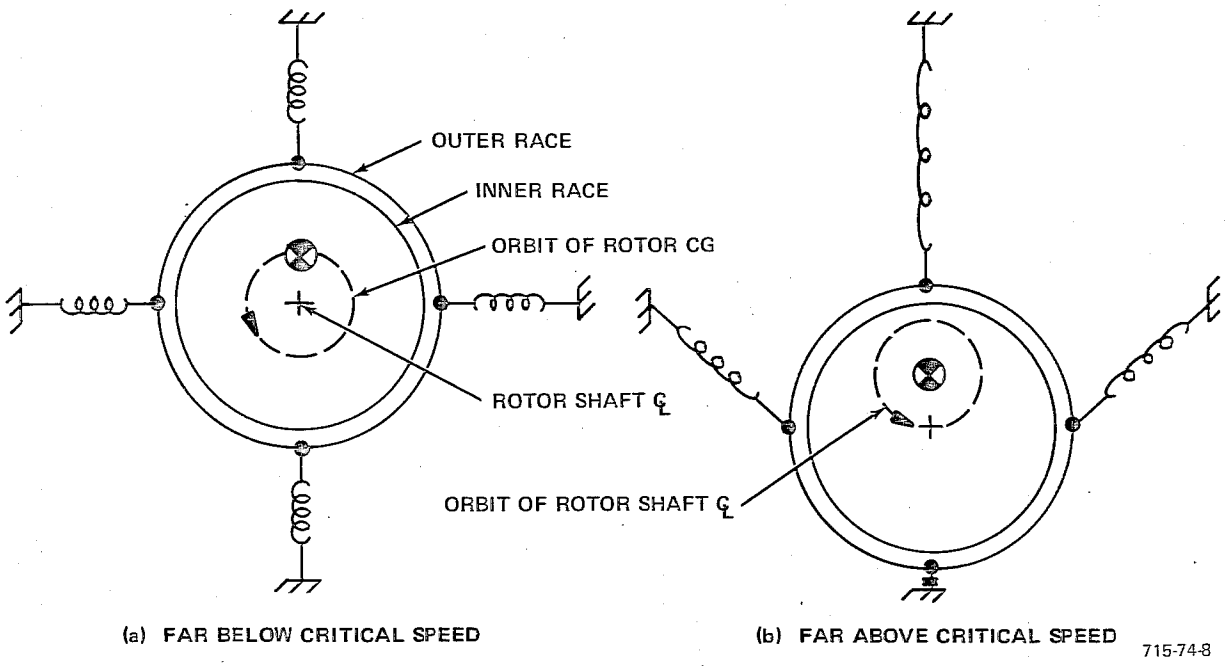

Figure A.1-7
End View of Statically Unbalanced Rotor Motion

The above analysis was based on the arrangement of Figure A.1-3 in which the compliance and damping were lumped into two equal elements on the nonrotating side of the spin bearings. In many cases, however, the compliance occurs mainly in the rotating members (rotor web or shaft, etc) and the question arises as to whether this modifies the dynamics. Consideration of Figures A.1-8 and A.1-9 shows that the equations of motion are exactly the same as with nonrotating

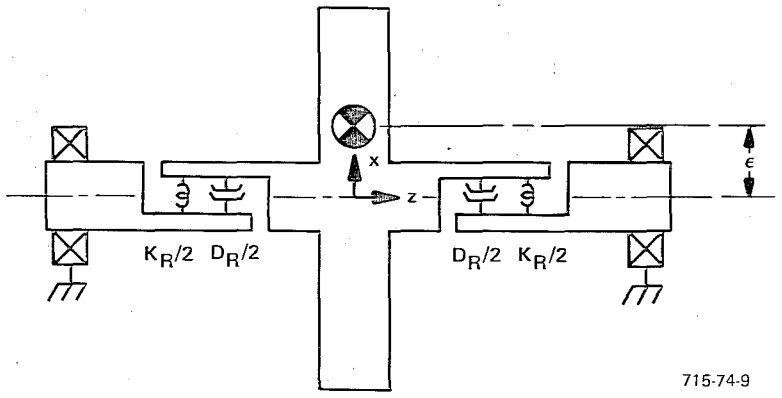

Figure A.1-8
Statically Unbalanced Rotor at Rest - Rotating Compliance

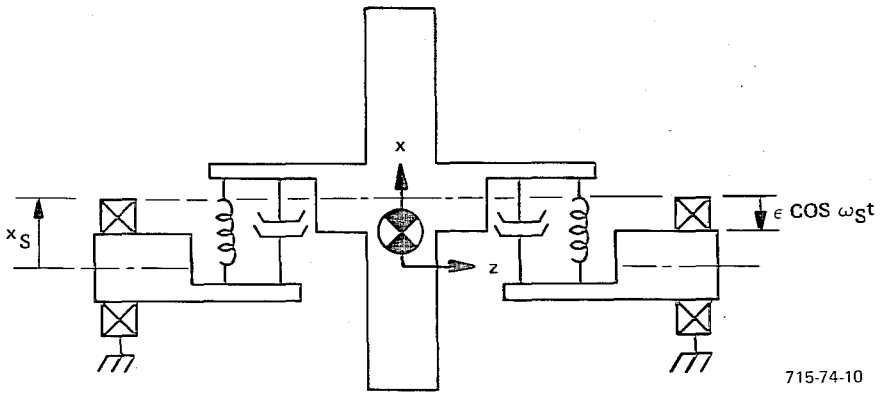

Figure A.1-9
Statically Unbalanced Spinning Rotor - Rotating Compliance

compliance if x_s and y_s are defined as the deflections of the rotor (not bearing) spin axis relative to the inertial x, y, z reference system. The mass center is given by (Cf Equation A-1):

$$x_c = x_s + \epsilon \cos \omega_s t$$

$$y_c = y_s + \epsilon \sin \omega_s t \qquad \text{(A-6)}$$

A.2 Dynamic Unbalance and Rotational Dynamics

Figure A.1-10 is a mechanical schematic of a dynamically unbalanced rotor suspended by equal stiffnesses under each spin bearing. The x, y, z axes are inertially fixed with origin at the rotor cg and z aligned with the nominal spin axis when the rotor is not spinning. The principal axis of the rotor is assumed to be misaligned with the nominal spin axis by a small angle, ϕ, defined to be in the x, z plane at time = 0.

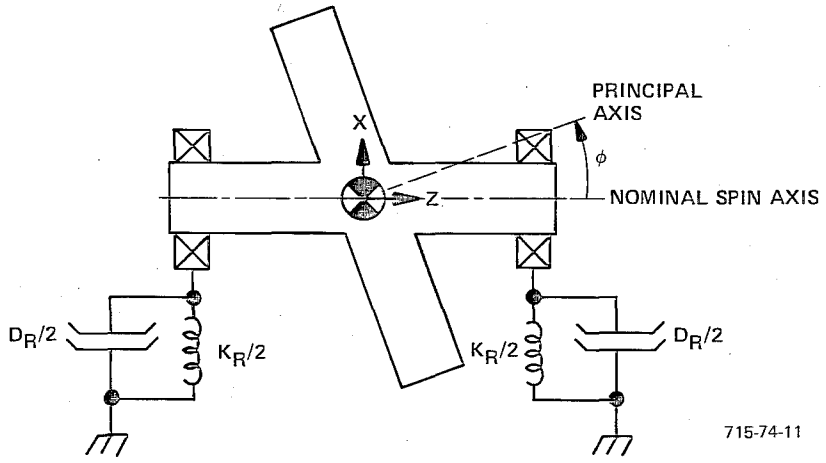

Figure A.1-10
Dynamically Unbalanced Rotor at Rest

With the rotor spinning at speed ω_s, the rotor deflects about the x and y axes as indicated in Figure A.1-11.

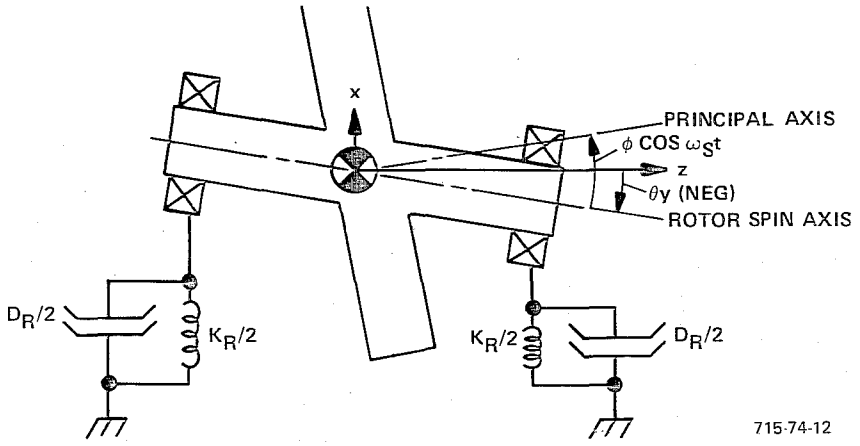

Figure A.1-11
Dynamically Unbalanced Spinning Rotor

Under the assumption that the transverse inertia of the rotor is the same in all directions in the x-y plane, the equations of motion for this system may be written in Laplace notation:

$$\left(I_T s^2 + D_R' s + K_R'\right)\theta_x + I_w \omega_s s\, \theta_y = \left(I_w - I_T\right)\omega_s^2 \left(\frac{s}{\omega_s}\right)\phi\ u\ (s)$$

$$-I_w \omega_s s\, \theta_x + \left(I_T s^2 + D_R' s + K_R'\right)\theta_y = \left(I_w - I_T\right)\omega_s^2\, \phi\ u\ (s) \qquad \text{(A-7)}$$

where

I_w = Moment of inertia of rotor about spin axis

I_T = Moment of inertia of rotor about axes transverse to spin axis

θ_x, θ_x = Rotation of spin axis about x and y axes

K_R' = Torsional stiffness = $\dfrac{L^2 K_R}{2}$

D_R' = Torsional damping = $\dfrac{L^2 D_R}{2}$

L = Bearing span

The term $(I_w - I_T)\ \omega_s^2\ \phi$ on the right side of Equation (A-7) is the dynamic unbalance torque, and generally has the units of inch-pounds. Other frequently used terms for dynamic imbalance are $(I_w - I_T)\ \phi$ usually given in ounce-inches^2 or simply ϕ in microradians. The dynamic imbalance torque has constant magnitude and is fixed in the rotor. Its x, y components, therefore, are sinusoidal at the spin frequency. The magnitude of this torque is proportional to the difference in inertias $(I_w - I_T)$. The sign of this term is opposite for a disk $(I_w > I_T)$ and a cylindrical $(I_w < I_T)$ rotor, and its magnitude would be zero for a spherical rotor $(I_w = I_T)$.

The dynamic imbalance may also be expressed in terms of the cross product of inertia or an equivalent pair of mass imbalances at the rim. In Figure A.1-12 the dynamic imbalance is produced by adding equal weights at the rim edges to a perfectly balanced rotor. The cross product of inertia, by definition, is:

$$I_{xy} = \frac{mDW}{4} \tag{A-8}$$

If the x and z axes are rotated about the y axis such that z' coincides with the principal axis, the cross product of inertia $I_{x'z'}$ is zero. Using the rules for rotation of the inertia tensor, the required rotation angle ϕ may be determined. (See, for example, Shames, Engineering Machanics-Dynamics, pp 477-480.)

$$\phi = \frac{I_{xz}}{I_w - I_T} = \frac{mDW}{4\ (I_w - I_T)} \tag{A-9}$$

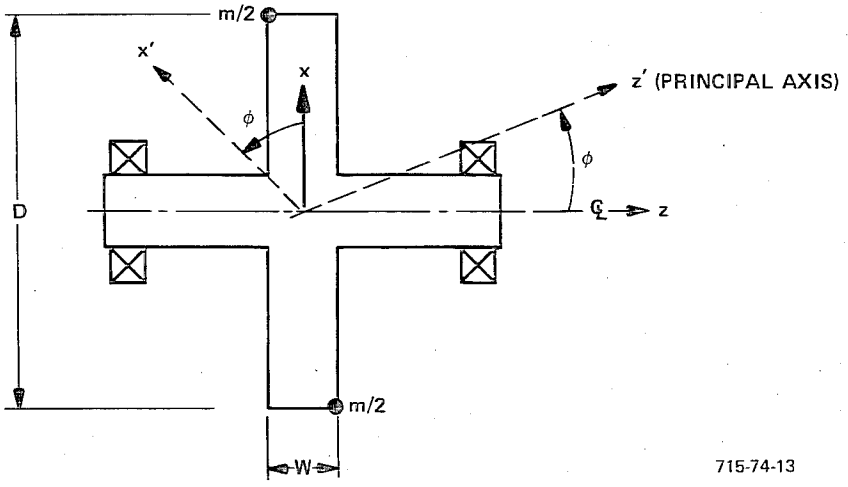

Figure A.1-12
Equivalent Rim Weights Producing Dynamic Unbalance

In summary, the dynamic unbalance torque magnitude may be expressed as:

$$T_u = (I_w - I_T)\ \phi\ \omega_s^2 = I_{xz}\ \omega_s^2 = \frac{mDW}{4}\ \omega_s^2 \qquad \text{(A-10)}$$

The moment transmitted to the mounting structure is not equal to the unbalance torque, but is related to the angular deflections and rates:

$$\begin{aligned} M_{xs} &= K'_R\ \theta_{xs} + D'_R\ \dot{\theta}_{xs} \\ M_{ys} &= K'_R\ \theta_{ys} + D'_R\ \dot{\theta}_{ys} \end{aligned} \qquad \text{(A-11)}$$

A block diagram of the rotational dynamics excited by dynamic imbalance is shown in Figure A.1-13. The two rotational axes are cross coupled by the angular momentum ($I_w\ \omega_s$).

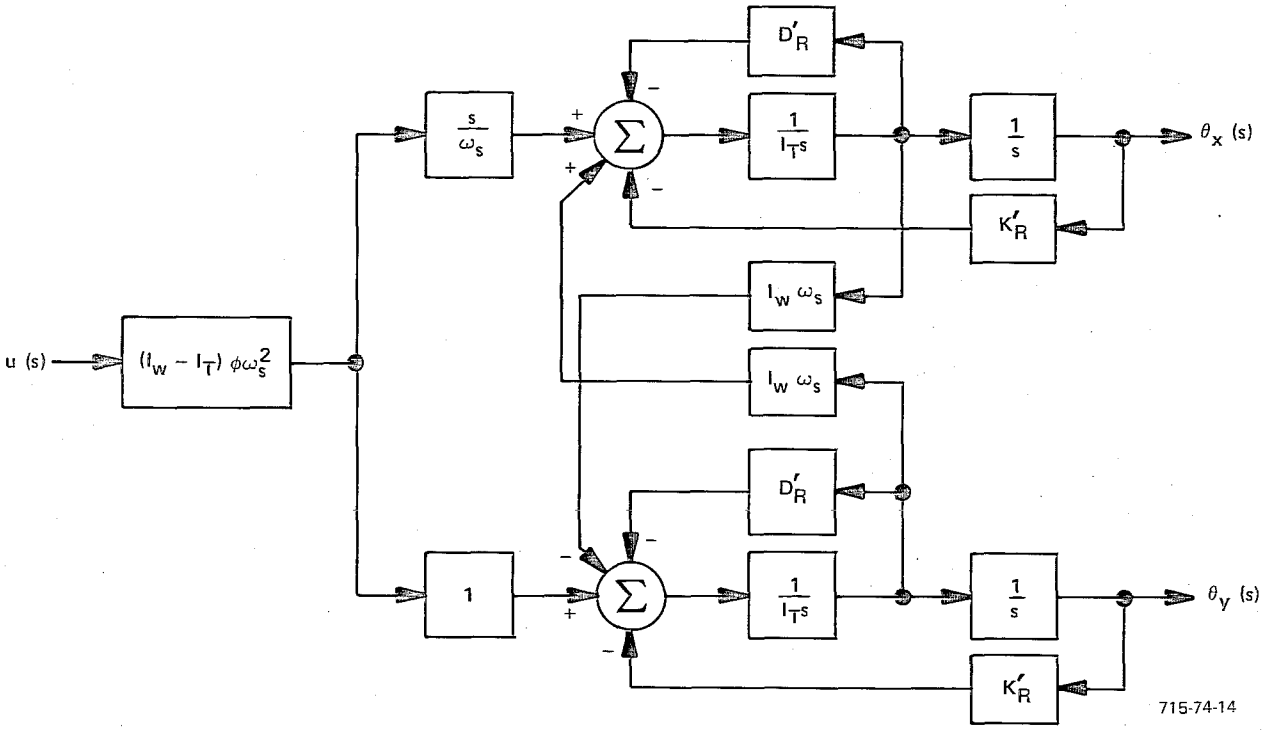

Figure A.1-13
Block Diagram of Dynamically Unbalanced Rotor Dynamics

For a constant axis misalignment, ϕ, the dynamic unbalance torque increases as the square of rotor speed, and the angular deflection of the spin axis is given by:

$$\frac{\theta_x(s)}{u(s)} \approx \frac{\left(I_w - I_T\right)\phi\omega_s s\left(I_T s^2 - I_w \omega_s^2 + K_R'\right)}{I_T^2 s^4 + \left(2K_R' I_T + I_w^2 \omega_s^2\right)s^2 + K_R'^2}$$

$$\frac{\theta_y(s)}{u(s)} = \frac{\left(I_w - I_T\right)\phi\,\omega_s^2\left(I_T s^2 + I_w s^2 + K_R'\right)}{I_T^2 s^4 + \left(2K_R' I_T + I_w^2 \omega_s^2\right)s^2 + K_R'^2} \qquad \text{(A-12)}$$

For simplicity, the structural damping coefficients are neglected in the above equations. Interpretation of the dynamics represented by Equation (A-12) may be approached two ways. First, the transfer functions may be considered in the conventional manner with coefficients of s assuming different values as the rotor speed ω_s is varied. The poles and zeros may then be obtained by factoring:

Poles of $\theta_{x/u}$, $\theta_{y/u}$

$$\omega_\Delta = \frac{I_w \omega_s}{2I_T} \pm \sqrt{\left(\frac{I_w \omega_s}{2I_T}\right)^2 + \frac{K_R'}{I_T}} \qquad \text{(A-13)}$$

Zeros of $\theta_{x/u}$

$$\omega_x = 0, \sqrt{\frac{K_R'}{I_T} - \omega_s^2\left(\frac{I_w}{I_T}\right)} \qquad \text{(A-14)}$$

Zeros of $\theta_{y/u}$

$$\omega_y = \sqrt{\frac{K_R'}{I_T + I_w}} \qquad \text{(A-15)}$$

In Figure A.1-14 the pole frequency is plotted against the spin frequency. At zero speed the pole frequency is that of the torsional vibration mode, $\sqrt{\frac{K_R'}{I_T}}$. As the rotor runs up, this mode splits into an upper and lower frequency pair. The lower frequency poles approach zero while the upper poles approach $\left(\frac{I_w}{I_T}\right)\omega_s$.

Intersection of these frequencies with the line $\omega = \omega_s$ represents a critical speed where the deflection theoretically becomes infinite. The lower pole always intersects this line at the frequency $\sqrt{\frac{K'_R}{I_T + I_w}}$ while the upper set of poles do not intersect at all if the transverse inertia is less than the polar inertia as in a disk rotor. For a cylindrical rotor, an intersection occurs at the frequency $\sqrt{\frac{K'_R}{I_T - I_w}}$.

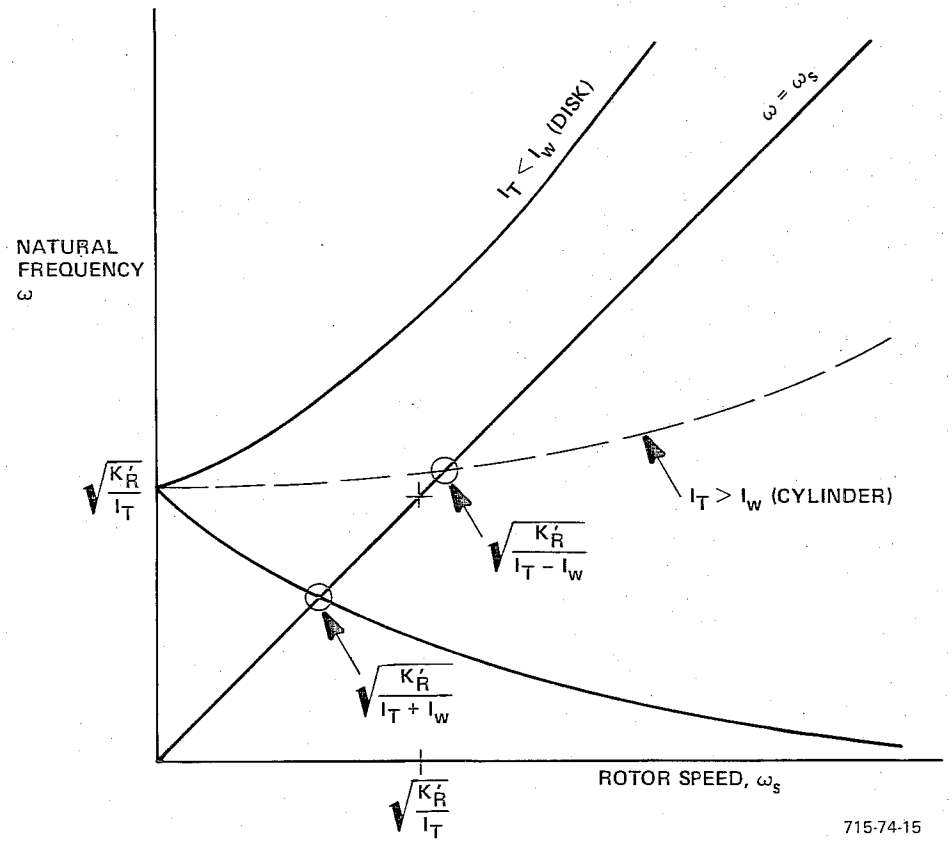

Figure A.1-14
Variation of Pole Natural Frequency with Rotor Speed

The $\theta_{x/u}$ zero natural frequency given by Equation (A-14) is plotted in Figure A.1-15.

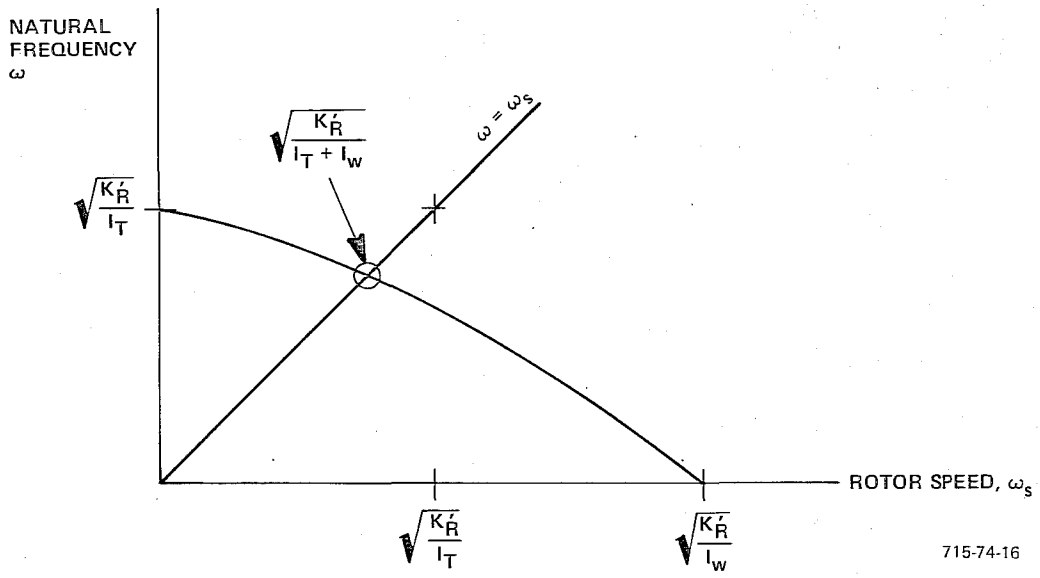

Figure A.1-15
Variation of $\theta_{x/u}$ Zero Natural Frequency with Rotor Speed

This zero starts from the same torsional vibration frequency and crosses the wheel speed line at the frequency $\sqrt{\frac{K'_R}{I_T + I_w}}$. Equation (A-15) states that the zeros of $\theta_{y/u}$ are fixed and at $\sqrt{\frac{K'_R}{I_T + I_w}}$. Comparing the various critical frequencies it can be seen that the lower critical speed resonance is always cancelled by a zero during rotor rumup while the existence of an upper critical speed depends on the rotor shape. It is important to note, however, that the pole/zero cancellation only implies that the resonance will not be excited by the rotor dynamic unbalance torque. The resonance (pole) still exists and may be excited by other torques as discussed later.

An alternate approach to the interpretation of Equation (A-12) is based on recognizing that the unbalance torque is sinusoidal and at rotor frequency. Therefore, the substitution $s = j\omega_s$ may be made, and the resulting ratio of polynomials in ω_s may be factored.

$$\left.\frac{\theta_x}{u}\right|_{s=j\omega_s} = \frac{j\phi\,\omega_s^2\left(\omega_s^2 - \dfrac{K'_R}{I_T + I_w}\right)}{\left(\omega_s^2 - \dfrac{K'_R}{I_T - I_w}\right)\left(\omega_s^2 - \dfrac{K'_R}{I_T + I_w}\right)}$$

$$\left.\frac{\theta_y}{u}\right|_{s=j\omega_s} = \frac{\phi\,\omega_s^2\left(\omega_s^2 - \dfrac{K'_R}{I_T + I_w}\right)}{\left(\omega_s^2 - \dfrac{K'_R}{I_T - I_w}\right)\left(\omega_s^2 - \dfrac{K'_R}{I_T + I_w}\right)} \qquad \text{(A-16)}$$

Again, a pole-zero cancellation occurs at the lower critical speed. Figure A.1-16 plots the magnitude and phase of the shaft angular rotations against rotor speed. Both θ_x and θ_y responses are identical except for a 90-degree phase shift. The deflections increase with the square of speed up to the frequency $\sqrt{\dfrac{K'_R}{|I_T - I_w|}}$. A sharp resonance occurs if the rotor is of the cylindrical type, $I_T > I_w$. Above this speed the deflection becomes constant and equal to the misalignment angle, ϕ. This corresponds to rotation of the rotor about its (misaligned) principal axis.

A pictorial illustration of the rotor angular motions during runup is given in Figures A.1-17 and A.1-18. Figure A.1-17 shows a disk rotor unbalanced by rim weights above and below the speed $\sqrt{\dfrac{K'_R}{I_T - I_w}}$ at two rotor angles (θ_R). Examination of the torques produced by the unbalance weights indicates a gradual increase in the θ_y deflection to ϕ with no peaking or phase reversal as the speed increases. Throughout the speed range, the unbalance torque T_u is such as to force the principal axis to turn toward the spin axis. The low speed rotation is determined by the spin bearing center line alignment, while at high speeds rotation is about the principal axis.

The unbalance torque shown in Figure A.1-18 for the cylindrical rotor is in a direction to increase the misalignment between the principal axis and the spin axis. As speed is increased, the rotor deflection increases due to this torque until the critical speed is reached. Above this frequency, the phase of the deflection reverses, causing the principal axis to move toward the spin axis. Eventually, the motion indicated in Figure A.1-18c) and d) results, and the rotor spins about its principal axis.

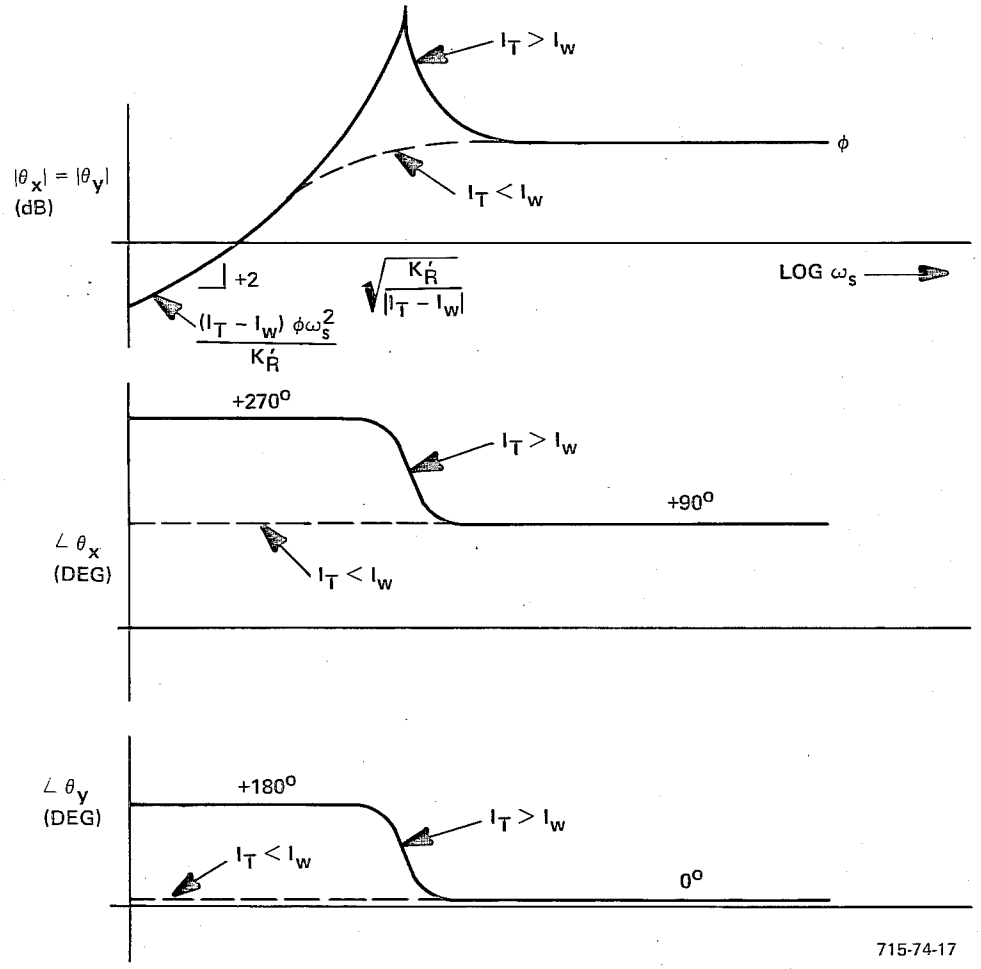

Figure A.1-16
Angular Deflection vs Rotor Speed of a Dynamically Unbalanced Rotor

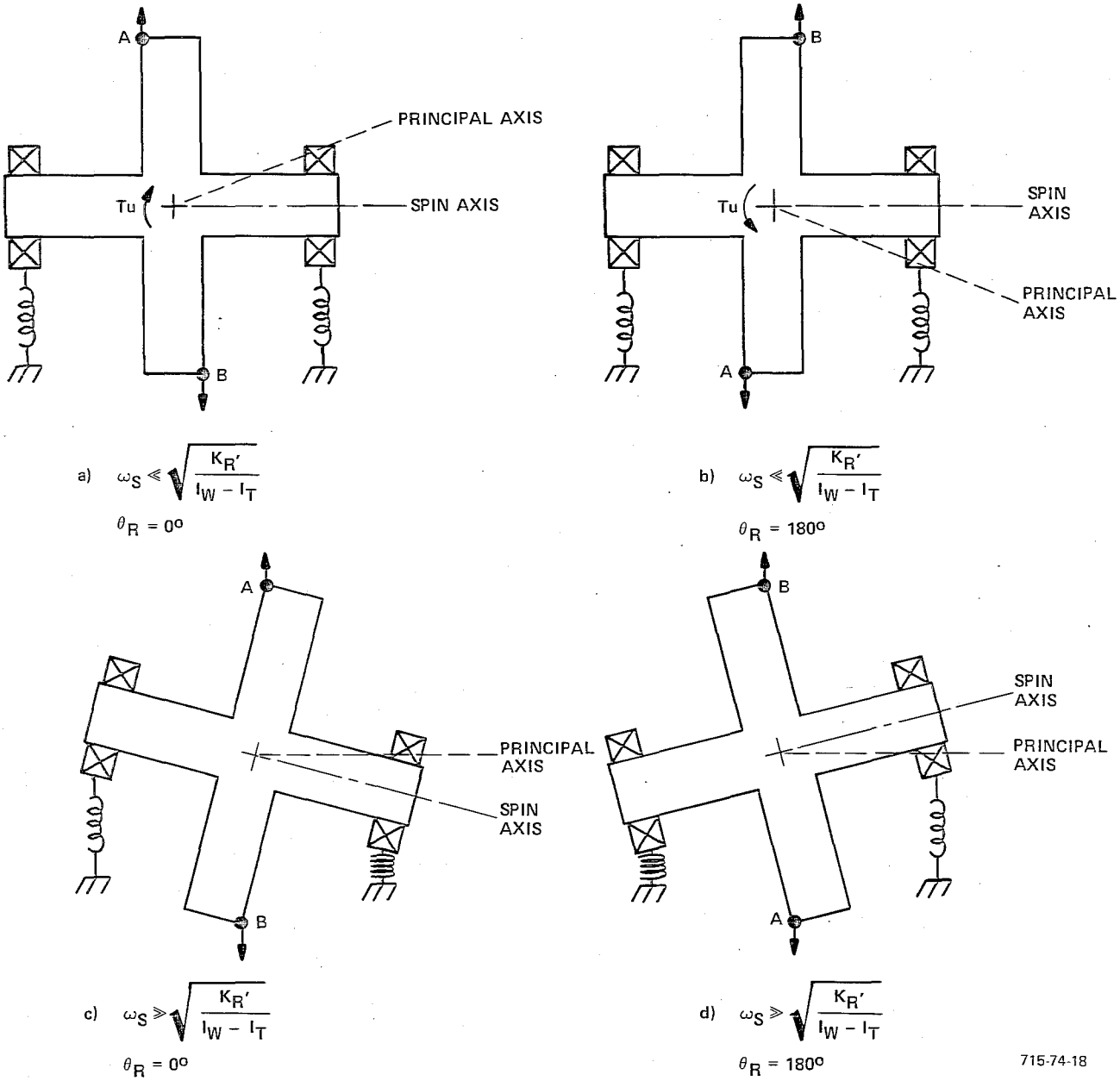

Figure A.1-17
Dynamically Unbalanced Disk Rotor Motion

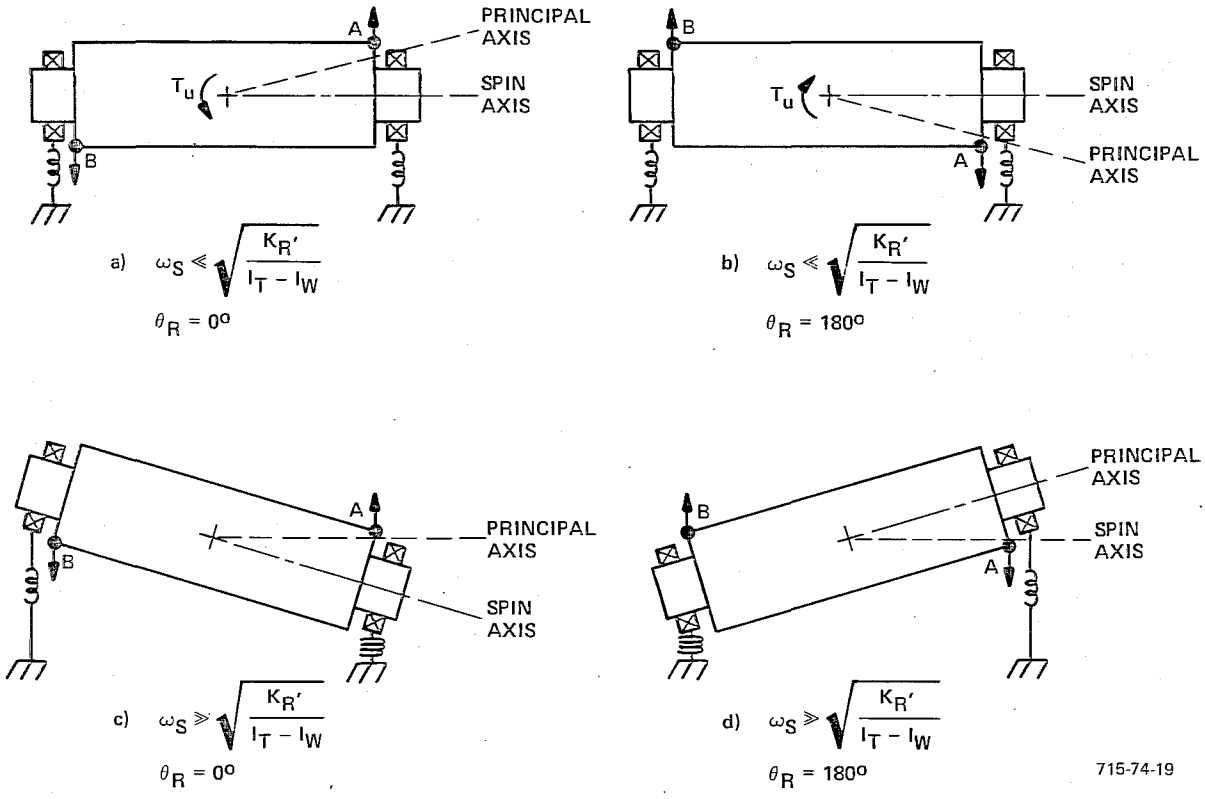

Figure A.1-18
Dynamically Unbalanced Cylindrical Rotor Motion

A.3 Axial Runout and Rotational Dynamics

If a sinusoidal torque at wheel speed exists along the x_s or y_s direction, but not both equally in quadrature, the lower critical speed resonance discussed in the preceding section will be excited. Axial spin bearing runout coupled through the housing dynamics can produce such a torque.

Figures A.1-19 and A.1-20 illustrate the origin of the axial runout force. If the spin bearings are considered as thrust bearings and both inner and outer races are misaligned to the spin axis, one ball will be squeezed more than the others. Elastic testoring forces will cause the inner race, and hence rotor, to move axially such that the loading on the tight ball causes a force balance within the suspension system. As indicated in the figure, the resulting motion of the rotor will be sinusoidal and at the rotor speed.

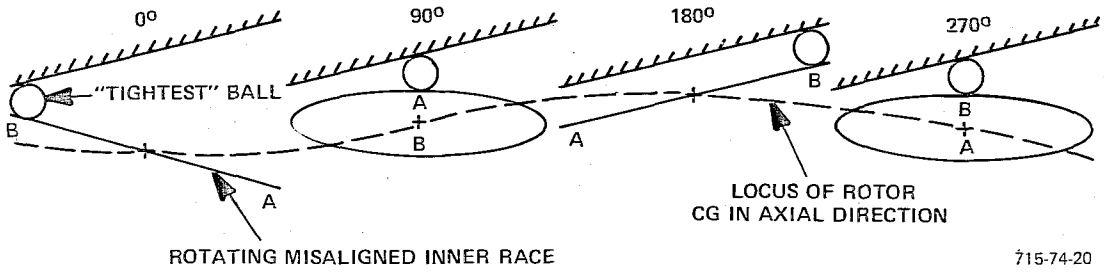

Figure A.1-19
Axial Rotor Vibration Due to Raceway Misalignment

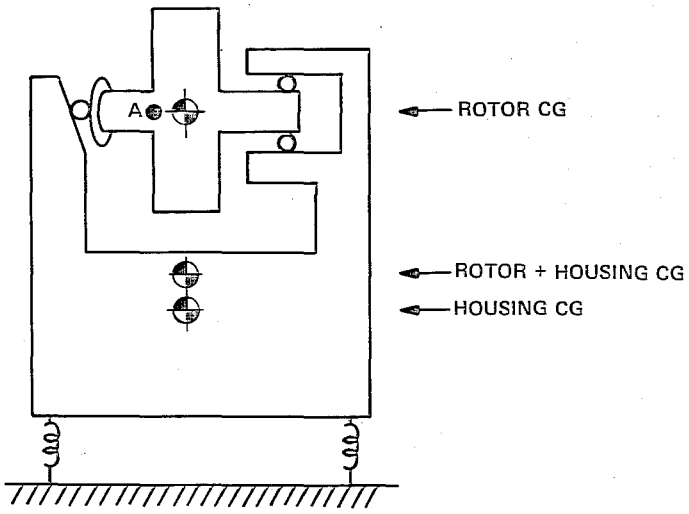

a) ROTOR STOPPED, $\theta_R = 0^o$

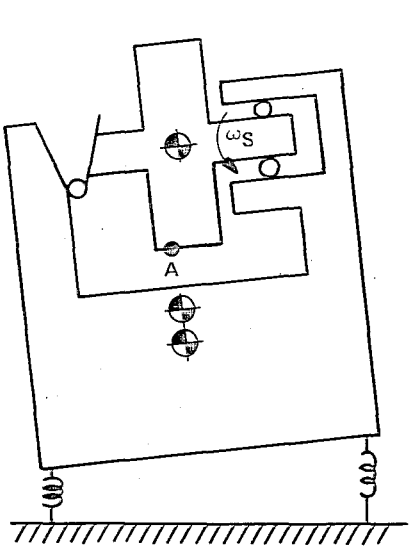

(b) ROTOR SPINNING, $\theta_R = 90^o$

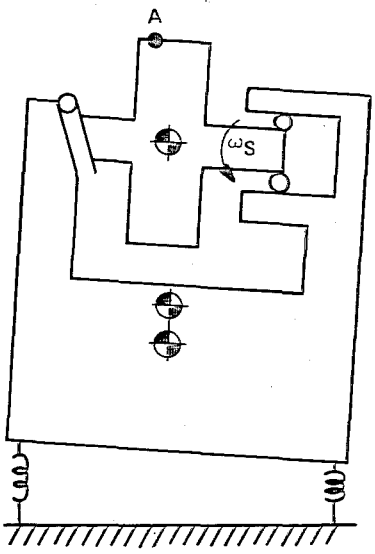

(c) ROTOR SPINNING, $\theta_R = 270^o$

715-74-121

Figure A.1-20
Mechanical Schematic Showing Rocking Motion
of Rotor and Housing Due to Axial Runout

The force resulting from an axial deflection, δ, of the rotor is:

$$F_A = M\delta\omega_s^2 \sin \omega_s t \tag{A-17}$$

The rotor housing, which has been considered fixed up to now, is restrained by finite stiffnesses and has some center of mass offset relative to the line of action of the axial force. This will result in motion of the housing, which in turn impresses a reaction torque on the spin bearings. The dynamics of this motion have not been developed yet, but as a first approximation, the torque may be considered related to the axial force by a constant, K.

Equation (A-7) provides the dynamics; however, the right hand side is replaced by the radial torque due to axial runout:

$$\begin{aligned} \left(I_T s^2 + D_R' s + K_R'\right)\theta_x + I_w \omega_s s\, \theta_y &= KM\delta\omega_s^2\, u\,(s) \\ -I_w \omega_s s\, \theta_x + \left(I_T s^2 + D_R' s + K_R'\right)\theta_y &= 0 \end{aligned} \tag{A-18}$$

As in the preceding section, structural damping may be neglected and factored transfer functions derived from these equations as a function of the rotor speed:

$$\left.\frac{\theta_x}{u}\right|_{s=j\omega_s} = \frac{-I_T KM\delta\omega_s^2\left(\omega_s^2 - \dfrac{K_R'}{I_T}\right)}{\left(\omega_s^2 - \dfrac{K_R'}{I_T - I_w}\right)\left(\omega_s^2 - \dfrac{K_R'}{I_T + I_w}\right)\left(I_T^2 - I_w^2\right)}$$

$$\left.\frac{\theta_y}{u}\right|_{s=j\omega_s} = \frac{jI_w KM\delta\omega_s^4}{\left(\omega_s^2 - \dfrac{K_R'}{I_T - I_w}\right)\left(\omega_s^2 - \dfrac{K_R'}{I_T + I_w}\right)\left(I_T^2 - I_w^2\right)} \tag{A-19}$$

The magnitude of the θ_x, θ_y deflection is plotted in Figure A.1-21 assuming constant runout, δ. Note that the lower critical speed resonance is present in both axes for either disk or cylindrical shaped rotors.

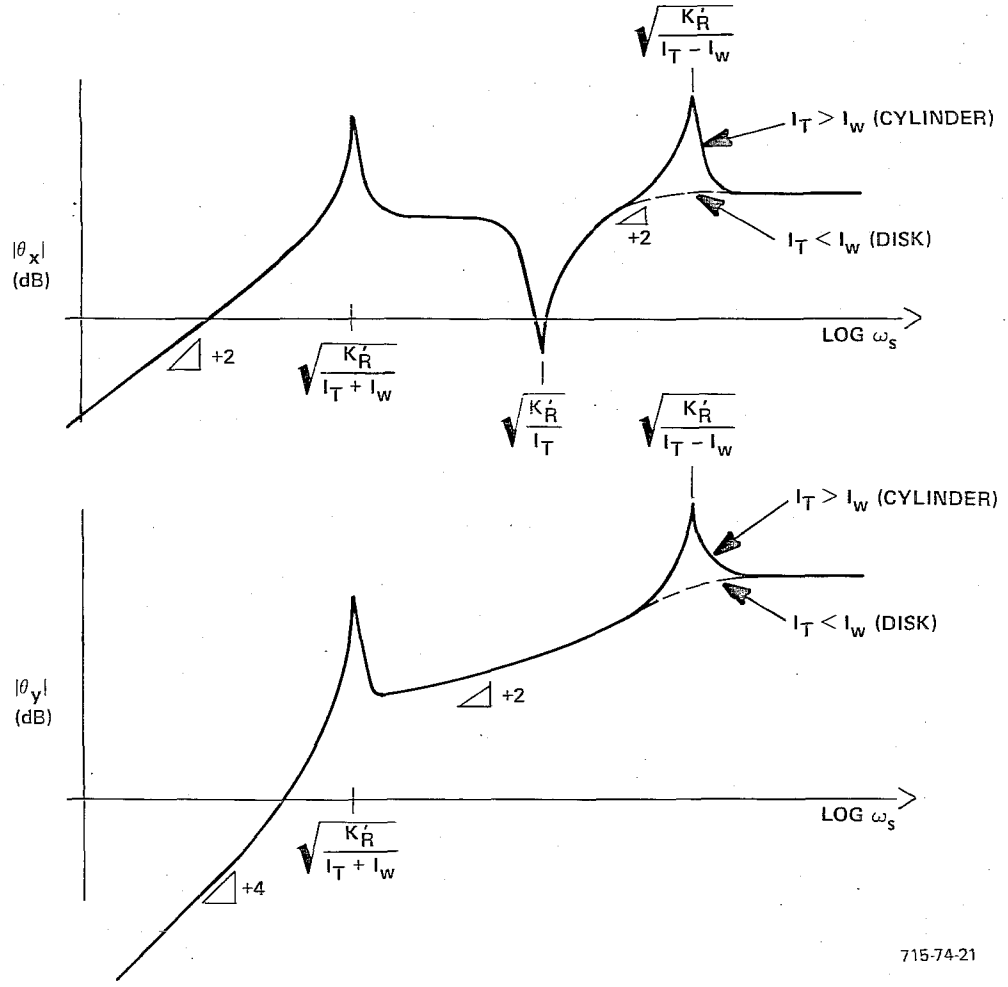

Figure A.1-21
Angular Deflection vs Rotor Speed for
Rotational Vibration Excited by Axial Runout